

The Vapour Sensing Capabilities of Organic Field-Effect Transistors

by

Lee Hague



**The
University
Of
Sheffield.**

A thesis submitted in partial fulfilment for the
degree of Doctor of Philosophy

in the
Faculty of Science
Department of Physics and Astronomy

June 2012

To my grandma,
whose love and support has gotten me this far

Abstract

The work in this doctoral thesis is mainly concerned with the detection of volatile organic vapours (analytes) using organic field-effect transistors (OFETs) as transducers, in some cases using a ‘sensitiser layer’ on top of the devices to improve their response to certain analytes; some work has also been carried out using a gold nano-particle chemi-resistor to detect amine vapour and the development of an aqueous sensing system is also discussed. It was found that the porphyrins PtOEP (platinum (II) octaethyl porphyrin) and PtEP-I (Etioporphyrin-I) could be used as organic semiconductors and that PtOEP was sensitive to isopropanol (IPA) and acetone vapours; PtOEP was also used to successfully sensitise a pentacene OFET to ethylene vapour at low ppm concentrations. Pentacene OFETs were found to be sensitive to octylamine (an amine), ethylethanoate (an ester), formamide (an amide) and ethylene (an alkene); through the use of a 2:1 molar ratio blend of the calixarene calix[8]arene (calixarene 2) and the porphyrin 5,10,15,20-Tetrakis (3,4-bis (2-ethylhexyloxy) phenyl)-21H,23H-porphyrinato cobalt (II) (Co-EHO) as a sensitiser layer, it was possible to introduce sensitivity to both octanal (an aldehyde) and octan-2-one (a ketone) into a pentacene OFET; the calixarene: 5,17-(34-nitrobenzylideneamino)-11,23-di-*tert*-butyl-25,27-diethoxycarbonyl-methyleneoxy-26,28dihydroxycalix[4]arene (calixarene 1) was also be used to improve OFET recovery after exposure to ethylethanoate and formamide, but some sensor response was lost in the process. The n-type organic semiconductor PDI8-CN₂ (*N,N'*-bis (*n*-octyl)- dicyanoperylene-3,4:9,10-bis(dicarboximide)) was found to be sensitive to octylamine vapour, but the nature of its response seems to indicate some kind of amine base-doping mechanism is at work within the device, analogous to the acid doping possible with p-type semiconductors. Gold nano-particles were found to be sensitive to octylamine vapour as the amine group has an affinity for gold and coats the nano-particles, increasing the resistance of the nano-particle film. Creating a water gated P3HT (poly(3-hexylthiophene-2,5-diyl)) OFET without the electro-chemical doping normally experienced by such devices was found to be possible through the use of a calixarene 1 barrier layer, paving the way for the development of an aqueous sensing system.

Contents

1	Introduction	1
1.1	Physics of Organic Semiconductors	1
1.1.1	Charge Carrier Injection into an Organic Semiconductor and the Origin of Contact Resistance	2
1.2.2	Charge Carrier Transport in an Organic Semiconductor.....	6
1.1.2.1	Mobility.....	7
1.1.2.2	Current Density.....	10
1.2	Organic Chemistry.....	12
1.2.1	Organic Structure and Bonding.....	12
1.2.1.1	The Shapes of Organic Molecules	12
1.2.1.1.1	Polymers	14
1.2.1.2	Carbon-Carbon Bonding (Orbital Hybridization)	17
1.2.1.3	Molecular Orbital Approach	19
1.2.1.4	Basic Organic Molecules and Functional Groups.....	21
1.2.2	Functional Organic Materials.....	27
1.2.2.1	Low Molecular Weight Organic Semiconductors	27
1.2.2.1.1	Pentacene	27
1.2.2.1.2	<i>N,N'</i> -bis (<i>n</i> -octyl)- dicyanoperylene-3,4:9,10-bis(dicarboximide) (PDI8-CN ₂)	27
1.2.2.1.3	5,6,11,12-Tetraphenylnaphthacene (Rubrene)	28
1.2.2.1.4	Buckminsterfullerene (C ₆₀).....	28
1.2.2.1.5	[6,6]-Phenyl-C ₆₁ -butyric acid methyl ester (C ₆₀ PCBM).....	29
1.2.2.1.6	6,13-Bis(triisopropylsilyl)ethynylpentacene (TIPS-pentacene).....	29
1.2.2.2	Semiconducting Polymers and Oligomers	30
1.2.2.2.1	Poly(3-hexylthiophene-2,5-diyl) (P3HT).....	30
1.2.2.2.2	Poly(2,5-bis(3-hexadecylthiophen-2-yl)thieno[3,2-b]thiophene) (pBTTT)	31
1.2.2.2.3	Poly[[N,N9-bis(2-octyldecyl)-naphthalene-1,4,5,8-bis(dicarboximide)-2,6-diyl]-alt-5,59-(2,29-bithiophene)] (P(NDI2OD-T2)).....	31
1.2.2.3	Synthetic Metals	32
1.2.2.4	Core Shell Nano-Particles.....	33
1.2.3	Macrocycles	34
1.2.3.1	Porphyrins	34
1.2.3.2	Phthalocyanines.....	35
1.2.3.3	Calixarenes	36

1.2.4	Organic Reactions and Interactions	37
1.2.4.1	A Basic Primer on Chemical Reaction Conditions and Mechanisms.....	37
1.2.4.2	Van der Waals Interactions.....	39
1.2.4.3	Hydrogen Bonding Interactions	41
1.3	Organic Field-Effect Transistors	41
1.3.1	Structure and Construction of an Organic Field-Effect Transistor.....	44
1.3.1.1	Standard Electrode Structures.....	45
1.3.1.2	Substrate Material and Electrode Adhesion Promotion.....	46
1.3.1.3	Gate Contact and Gate Insulation.....	46
1.3.1.3.1	Water-Gated Organic Field-Effect Transistors and the Electric Double Layer.....	48
1.3.1.4	Surface Modification.....	51
1.3.1.5	Choice of Organic Semiconductor and Source/Drain Contact Material	53
1.3.1.6	Sensitiser Layers.....	53
1.3.2	Electrical Behaviour of Organic Field-Effect Transistors	54
1.3.2.1	The Output Characteristic.....	57
1.3.2.2	The Saturated Transfer Characteristic	59
1.3.2.3	Dynamic Properties of Organic Field-Effect Transistors	60
1.4	Thermodynamics	61
1.4.1	Vapour Pressure and Liquid-Vapour Equilibrium	61
1.4.2	Reaction and Recovery of Organic Materials under Vapour Exposure	62
1.5	Vapour Response Mechanisms in Organic Field-Effect Transistors.....	64
1.6	Conventional Vapour Sensing Systems.....	65
1.6.1	Mass Spectroscopy	66
1.6.2	Metal Oxide based Resistor Sensors.....	66
1.7	Vapour Sensing Systems using Organic Materials	66
1.7.1	Optical Spectroscopy	67
1.7.2	Quartz Crystal Microbalance (QCM) Sensors.....	67
1.7.3	Core-Shell Nano-Particle Swelling Based Sensors.....	68
1.7.4	Organic Field-Effect Transistor and Organic Chemi-resistor Based Sensors	68
1.7.5.1	State of the Art: Amine Sensing	69
1.7.5.2	State of the Art: Aldehyde and Ketone Sensing.....	70
1.7.5.3	State of the Art: Ester Sensing	71
1.7.5.4	State of the Art: Ethylene Sensing	71
2	Experimental Methods	72

2.1	Cleaning Methods for Silicon Oxide Wafers	72
2.1.1	Chemical Cleaning.....	72
2.1.2	Ultra-Violet Generated Ozone Cleaning	72
2.2	Deposition Methods	73
2.2.1	Thermal Evaporation.....	73
2.2.2	Spin Coating	75
2.2.3	Langmuir-Blodgett Deposition Technique	76
2.2.4	Langmuir-Schaefer Deposition.....	80
2.2.5	Self-Assembly from Solution.....	80
2.3	Metal Anodisation.....	81
2.4	Contacting the Electrodes of a Organic Field-Effect Transistor	81
2.4.1	Contacting with a Carbon-Black Paint.....	81
2.4.2	Contacting with a Low-Melting Point Solder	82
2.5	Thermal Annealing Organic Semiconductors under Vacuum.....	83
2.6	Organic Field-Effect Transistor Characterisation	83
2.6.1	Measuring Output Characteristics	84
2.6.2	Measuring Transfer Characteristics	85
2.6.3	Gain Method Characterisation.....	86
2.6.4	Chemi-Resistor Characterisation	87
2.7	Organic Materials Used in this Work	88
3	Instrumentation and Equipment Developed for this Work.....	92
3.1	Electronic OFET Characterisation Schemes	92
3.1.1	Current to Voltage Converter Characterisation Scheme	92
3.1.2	555 Chip Based Characterisation Scheme	96
3.2	Vapour Exposure.....	98
3.2.1	Saturated Vapour Generation and Dilution	99
3.2.2	Gas Flow, Heating and Electrical Monitoring within the Exposure Chamber.....	102
4	Hydrophobic Surface Modification Studies	105
5	Sensing Results.....	108
5.1	Porphyrin and Phthalocyanine Based Organic Field-Effect Transistor Vapour Sensors ...	108
5.1.1	Material Screening Studies	108
5.1.2	Platinum Octaethylporphyrin	115
5.1.2.1	Transistor Characteristics.....	115
5.1.2.2	Vapour Sensing Results.....	118

5.1.3	Platinum Etioporphyrin-I.....	122
5.1.3.1	Transistor Characteristics.....	123
5.1.3.2	Vapour Sensing Results.....	124
5.2	Pentacene Based Organic Field-Effect Transistor Vapour Sensors.....	137
5.2.1	Non-Sensitised Pentacene Organic Field-Effect Transistors	138
5.2.1.1	Transistor Characteristics.....	138
5.2.1.2	Amine Sensing Results Using the Gain Method Characterisation Scheme.....	149
5.2.1.3	Amine Sensing Results Using the Current to Voltage Converter Characterisation Scheme...	
	154
5.2.1.3.1	Determination of the Best Drive Voltage Function	154
5.2.1.3.2	The Influence of Contact Metal on Sensing Behaviour.....	156
5.2.1.3.3	Reusability Study on Pentacene Octylamine Sensors.....	158
5.2.1.3.4	Very Low Concentration Static-Environment Sensing	159
5.2.1.4	Ester Sensing Results	161
5.2.1.5	Amide Sensing Results	163
5.2.1.6	Ketone Sensing Results	165
5.2.1.7	Aldehyde Sensing Results	167
5.2.1.8	Ethylene Sensing Results.....	168
5.2.2	Sensitised Pentacene Organic Field-Effect Transistors.....	172
5.2.2.1	Calixarene Sensitised Transistors.....	172
5.2.2.1.1	Pre-Coating Transistor Characteristics.....	172
5.2.2.1.2	Post-Coating Transistor Characteristics	176
5.2.2.1.3	Amine Sensing Results	181
5.2.2.1.4	Ester Sensing Results	183
5.2.2.1.5	Amide Sensing Results	186
5.2.2.1.6	Ethylene Sensing Results.....	188
5.2.2.2	Calixarene : Porphyrin Blend Sensitised Transistors.....	193
5.2.2.2.1	Pre-Coating Transistor Characteristic	193
5.2.2.2.2	Post-Coating Transistor Characteristic.....	195
5.2.2.2.3	Ketone Sensing Results	196
5.2.2.2.4	Aldehyde Sensing Results	199
5.2.3	Pentacene Organic Field-Effect Transistor Lifetime Studies.....	201
5.3	N-Type Organic Field-Effect Transistor Vapour Sensors.....	204
5.3.1	Transistor Characteristics.....	204

5.3.2	Amine Sensing Results	208
5.4	Nano-Particle Based Chemi-Resistor Vapour Sensor.....	213
6	An Aqueous Sensing Platform Using Organic Field-Effect Transistors	215
6.1	Water Gated Pentacene Based Organic Field-Effect Transistors.....	215
6.2	Water Gated Poly(3-hexylthiophene-2, 5-diyl) Organic Field-Effect Transistors	216
7	Summary Conclusions and Future Work.....	225
8	Acknowledgements and Publications	227
	References	228
	Appendix 1 - Vapour Concentration Calculations.....	234

List of Figures

Figure 1. An example energy level diagram of electron and hole injection barriers from metal electrodes into an organic semiconductor with no applied bias. Φ , E_a and I_p are the electrode workfunction, semiconductor electron affinity and semiconductor ionisation potential as defined in the text.....	3
Figure 2. An example energy level diagram of electron and hole injection barriers from metal electrodes into an organic semiconductor with an applied bias. V is the applied potential difference and e the elementary charge.....	4
Figure 3. Energy diagrams showing band tilting (left), band bending (middle) and the effect of a self-assembled monolayer (right).....	6
Figure 4. The common molecular structural geometries found for 2-6 electron pairs, predicted through VSEPR theory. ^[27]	13
Figure 5. The view along the central C-C bond in ethane (Newman projection), showing the dihedral angle (left: $\theta = 10^\circ$, right: $\theta = 60^\circ$).....	14
Figure 6. The structure of a chain folded lamella. ^[31]	17
Figure 7. The structure of a spherulite. ^[31]	17
Figure 8. The orbital structure of single (left), double (middle) and triple (right) carbon-carbon bonds. The two blue areas form one π bond and the two green areas form a second.	18
Figure 9. The shapes of the hybrid orbitals for two to six electron pairs. ^[32]	19
Figure 10. The molecular orbital structure in O_2	21
Figure 11. The chemical structures of a generic alkane (top), alkene (middle) and alkyne (bottom).22	
Figure 12. The chemical structures of a generic primary (top), secondary (middle) and tertiary alcohol (bottom).	23
Figure 13. The chemical structures of a generic aldehyde (top), ketone (middle) and carboxylic acid (bottom).	23
Figure 14. The chemical structures of a generic primary (top), secondary (2nd from top) and tertiary amine (2nd from bottom) and nitrile (bottom).	24
Figure 15. The chemical structure of a generic ester and amide.	25
Figure 16. The chemical structures of a generic chloro- (top), fluoro- (2nd from top), bromo- (2nd from bottom) and iodo-group (bottom).	25
Figure 17. The chemical structure of a benzene ring.	26
Figure 18. The chemical structure of a pyridine ring.	26
Figure 19. The chemical structure of a pyrrole ring.	26
Figure 20. The chemical structure of a thiophene ring.	26
Figure 21. The chemical structure of pentacene.	27
Figure 22. The chemical structure of PDI8-CN ₂ (<i>N,N'</i> -bis (<i>n</i> -octyl)- dicyanoperylene-3,4:9,10-bis(dicarboximide)).	28
Figure 23. The chemical structure of Rubrene (5,6,11,12-Tetraphenylnaphthacene).	28
Figure 24. The chemical structure of C ₆₀ (Buckminsterfullerene).	29
Figure 25. The chemical structure of C ₆₀ PCBM ([6,6]-Phenyl-C ₆₁ -butyric acid methyl ester).....	29
Figure 26. The chemical structure of TIPS-pentacene (6,13-Bis(triisopropylsilyl)ethynyl)pentacene).30	
Figure 27. The chemical structure of P3HT (Poly(3-hexylthiophene-2,5-diyl)).	31

Figure 28. The chemical structure of pBTTT (Poly(2,5-bis(3-hexadecylthiophen-2-yl)thieno[3,2-b]thiophene)	31
Figure 29. The chemical structure of P(NDI2OD-T2) (Poly[[N,N9-bis(2-octyldodecyl)-naphthalene-1,4,5,8-bis(dicarboximide)-2,6-diyl]-alt-5,59-(2,29-bithiophene)]).....	32
Figure 30. The chemical structure of a thiol coated Au core-shell nano-particle.	34
Figure 31. The chemical structure of the basic porphyrin ring, showing two possible R-group configurations.	35
Figure 33. The chemical structures of a generic 8- (top) and a 4-member ring calixarene (bottom). 37	
Figure 34. A schematic diagram of an n-p-n type bipolar junction transistor.....	42
Figure 35. A cross-sectional diagram of an organic field-effect transistor.....	42
Figure 36. A photograph of a real pentacene OFET.....	44
Figure 37. Cross-sectional diagrams of the four possible OFET electrode structures (top: staggered electrode structures, bottom: coplanar electrode structures).....	45
Figure 38. A graphical representation of the Stern model of the electric double layer.....	50
Figure 39. A schematic of the EDL formation in a water gated OFET.....	51
Figure 40. Diagram of a SAM of OTS on Al ₂ O ₃ /SiO ₂ with a generic semiconductor.	52
Figure 41. An output characteristic showing the linear region and saturation region labelled for the -3V curve.	58
Figure 42. A saturated transfer characteristic with μ , V_T , V_o , S and the on/off ratio labelled.....	59
Figure 43. An example of a Langmuir trough.	76
Figure 44. A typical Langmuir isotherm: c = condensed mono layer (solid), e = expanded mono layer (liquid), g = gaseous.	78
Figure 45. Diagrams of a monolayer film on water (top) and the X- (left), Y- (middle) and Z-type (right) deposition types.....	79
Figure 46. A diagram of the contacting arrangement used in this work.	82
Figure 47. A picture of the Keithleys (top) and probeheads (bottom).	84
Figure 48. A screenshot of the output characteristic measurement program.....	85
Figure 49. A screenshot of the transfer characteristic measurement program.....	85
Figure 50. Circuit diagram of the gain method circuit.....	86
Figure 51. Square wave generator circuit diagram.....	88
Figure 52. The chemical structure of metallated EHO (5, 10, 15, 20-Tetrakis (3, 4-bis (2-ethylhexyloxy) phenyl)-21H, 23H-porphine), M = Co or Au.	89
Figure 53. The chemical structures of PtOEP (Platinum (II) 2,3,7,8,12,13,17,18-Octaethyl-21H,23H-porphine) (top) and PtEP-I (2,7,12,17-Tetraethyl-3, 8,13, 18-tetramethyl-21H,23H-porphine) (bottom).	89
Figure 54. The chemical structure of PPIXZn(II) (Zinc (II) 3,7,12,17-Tetramethyl-8,13-divinyl-2,18-porphinedipropionic acid).....	90
Figure 55. The chemical structure of Si(IV)PTSO (Silicon (IV) phthalocyanine bis (trihexylsilyloxide)).	90
Figure 56. The chemical structures of calixarene 1 (5,17-(34-nitrobenzylideneamino)-11,23-di- <i>tert</i> -butyl-25,27-diethoxycarbonyl-methyleneoxy-26,28dihydroxycalix[4]arene) (top) and calixarene 2 (calix[8]arene) (bottom).	91
Figure 57. Current to voltage converter circuit diagram.	93
Figure 58. An example p-type current to voltage converter trace.	94

Figure 59. An example p-type saturated transfer characteristic from current to voltage converter data.....	95
Figure 60. A circuit diagram of 555 circuit.....	96
Figure 61. Oscilloscope traces of the DISCHARGE connected (top) and disconnected (bottom) cases.....	98
Figure 62. A diagram of the gas flow system.....	100
Figure 63. A picture of the bubbler vessel.....	101
Figure 64. A picture of the mass-flow controller setup.....	102
Figure 65. A picture of the exposure chamber.....	104
Figure 66. SiO ₂ surface modification data.....	106
Figure 67. Al ₂ O ₃ surface modification data.....	107
Figure 68. Isotherms of 300µL and 1000µL spreading volume for Co-EHO.....	109
Figure 69. Isotherm of 300µL spreading volume for Au-EHO.....	110
Figure 70. Si(IV)PTSO 300µL spreading volume initial isotherm and recompression.....	112
Figure 71. Isotherm of 300µL spreading volume for PPIXZn(II).....	113
Figure 72. Isotherm of 300µL spreading volume for PtOEP.....	114
Figure 73. PtOEP 5 TR output and transfer characteristics.....	116
Figure 74. PtOEP 8 BL output and transfer characteristics.....	117
Figure 75. PtOEP 5 TR IPA raw sensing results (top) and five-point median (bottom). N.B. grey shaded areas indicate analyte exposure.....	119
Figure 76. PtOEP 5 TR IPA sensing results (drain current). N.B. grey shaded area indicates analyte exposure.....	120
Figure 77. PtOEP 8 BL acetone sensing results five-point median. N.B. grey shaded area indicates analyte exposure.....	121
Figure 78. PtOEP 8 BL acetone sensing results (drain current). N.B. grey shaded area indicates analyte exposure.....	122
Figure 79. PtEP-I 15 TL output and transfer characteristics.....	124
Figure 80. PtEP-I 15 TL 1% propylamine sensing results five-point median. N.B. grey shaded area indicates analyte exposure.....	126
Figure 81. PtEP-I 15 TL 1% propylamine sensing results (peak drain current evolution). N.B. grey shaded area indicates analyte exposure.....	127
Figure 82. PtEP-I 15 TL 5% propylamine sensing results five-point median. N.B. grey shaded area indicates analyte exposure.....	128
Figure 83. PtEP-I 15 TL 5% propylamine sensing results (peak drain current evolution). N.B. grey shaded area indicates analyte exposure.....	129
Figure 84. PtEP-I 15 TL 10% propylamine sensing results five-point median. N.B. grey shaded area indicates analyte exposure.....	130
Figure 85. PtEP-I 15 TL 10% propylamine sensing results (peak drain current evolution). N.B. grey shaded area indicates analyte exposure.....	131
Figure 86. PtEP-I 15 TL 30% propylamine sensing results five-point median. N.B. grey shaded area indicates analyte exposure.....	132
Figure 87. PtEP-I 15 TL 30% propylamine sensing results (peak drain current evolution). N.B. grey shaded area indicates analyte exposure.....	133
Figure 88. PtEP-I 15 TL 50% propylamine sensing results five-point median. N.B. grey shaded area indicates analyte exposure.....	134

Figure 89. PtEP-I 15 TL 50% propylamine sensing results (peak drain current evolution). N.B. grey shaded area indicates analyte exposure.....	135
Figure 90. PtEP-I 15 TL 100% propylamine sensing results five-point median. N.B. grey shaded areas indicate analyte exposure.....	136
Figure 91. PtEP-I 15 TL 100% propylamine sensing results (peak drain current evolution). N.B. grey shaded area indicates analyte exposure.....	137
Figure 92. Pentacene 4 TL output and transfer characteristics.....	139
Figure 93. Pentacene 9 BL output and transfer characteristics.....	140
Figure 94. Pentacene 10 BL output and transfer characteristics.....	141
Figure 95. Pentacene 17 TR output and transfer characteristics	142
Figure 96. Pentacene 21 TL output and transfer characteristics.....	143
Figure 97. Pentacene 24 BR output and transfer characteristics	144
Figure 98. Pentacene 31 BR output and transfer characteristics	145
Figure 99. Pentacene 45 TL output and transfer characteristics.....	146
Figure 100. Pentacene 55 BR output and transfer characteristics	147
Figure 101. Pentacene 4 TL 1% octylamine sensing results five-point median. N.B. grey shaded area indicates analyte exposure.	150
Figure 102. Pentacene 4 TL 1% octylamine sensing results (peak drain current evolution). N.B. grey shaded area indicates analyte exposure.....	151
Figure 103. Pentacene 4 TL 5% octylamine sensing results five-point median. N.B. grey shaded area indicates analyte exposure.	152
Figure 104. Pentacene 4 TL 5% octylamine sensing results (peak drain current evolution). N.B. grey shaded area indicates analyte exposure.....	153
Figure 105. Pentacene 9 BL 1% octylamine sensing results. N.B. grey shaded area indicates analyte exposure.	155
Figure 106. Pentacene 10 BL 1% octylamine sensing results. N.B. grey shaded area indicates analyte exposure.	156
Figure 107. Pentacene 17 TR 10% octylamine sensing results. N.B. grey shaded areas indicate analyte exposure.....	157
Figure 108. Pentacene 21 TL 1% octylamine cycles sensing results. N.B. grey shaded areas indicate analyte exposure.....	158
Figure 109. Pentacene 24 BR 100ppb / 1ppm octylamine and cyclohexane control sensing results.	160
Figure 110. Pentacene 31 BR variable % ethylethanoate sensing results. N.B. grey shaded areas indicate analyte exposure.....	162
Figure 111. Pentacene 45 TL variable % formamide sensing results. N.B. grey shaded areas indicate analyte exposure.....	164
Figure 112. Pentacene 55 BR variable % octan-2-one sensing results. N.B. grey shaded areas indicate analyte exposure.....	166
Figure 113. Pentacene 55 BR variable % octanal sensing results. N.B. grey shaded areas indicate analyte exposure.....	167
Figure 114. Pentacene 7 TL output and transfer characteristics.....	169
Figure 115. Pentacene 7 TL variable ppm ethylene sensing results. N.B. grey shaded areas indicate analyte exposure.....	170

Figure 116. Pentacene 7 TL variable ppm ethylene sensing results five-point median. N.B. grey shaded areas indicate analyte exposure.....	171
Figure 117. Pentacene 32 TR output and transfer characteristics.	173
Figure 118. Pentacene 44 BR output and transfer characteristics.	174
Figure 119. Pentacene 47 TL output and transfer characteristics.....	175
Figure 120. Pentacene 32 TR (post-coating) output and transfer characteristics.....	177
Figure 121. Pentacene 44 BR (post-coating) output and transfer characteristics.....	178
Figure 122. Pentacene 47 TL (post-coating) output and transfer characteristics.	179
Figure 123. Pentacene 47 TL variable % octylamine sensing results. N.B. grey shaded areas indicate analyte exposure.....	182
Figure 124. Pentacene 32 TR variable % ethylethanoate sensing results. N.B. grey shaded areas indicate analyte exposure.....	184
Figure 125. The percentage responses of both calixarene 1 coated and uncoated pentacene OFETs to ethylethanoate.	185
Figure 126. Pentacene 44 BR variable % formamide sensing results. N.B. grey shaded areas indicate analyte exposure.....	186
Figure 127. The percentage responses of both calixarene 1 coated and uncoated pentacene OFETs to formamide.	188
Figure 128. Pentacene-PtOEP 2 TL output and transfer characteristics.....	189
Figure 129. Pentacene-PtOEP 2 TL variable ppm ethylene sensing results. N.B. grey shaded areas indicate analyte exposure.....	190
Figure 130. Pentacene-PtOEP 2 TL variable ppm ethylene sensing results five-point median. N.B. grey shaded areas indicate analyte exposure.....	191
Figure 131. The percentage responses of both PtOEP coated and uncoated pentacene OFETs to ethylene.	192
Figure 132. Pentacene 50 TR output and transfer characteristics.	194
Figure 133. Pentacene 50 TR (post-coating) output and transfer characteristics.....	196
Figure 134. Pentacene 50 TR variable % octan-2-one sensing results. N.B. grey shaded areas indicate analyte exposure.....	197
Figure 135. The percentage responses of both Co-EHO : calixarene 2 blend coated and uncoated pentacene OFETs to octan-2-one.	198
Figure 136. Pentacene 50 TR variable % octanal sensing results. N.B. grey shaded areas indicate analyte exposure.....	199
Figure 137. The percentage responses of both Co-EHO : calixarene 2 blend coated and uncoated pentacene OFETs to octanal.	200
Figure 138. Pentacene 53 TL oscilloscope screen-shots.....	202
Figure 139. Pentacene 53 TL on-resistance vs. time plot.	203
Figure 140. PDI8-CN ₂ 1 TL output and transfer characteristics.	205
Figure 141. PDI8-CN ₂ 4 BR output and transfer characteristics.	206
Figure 142. PDI8-CN ₂ 6 BL output and transfer characteristics.	207
Figure 143. PDI8-CN ₂ 1 TL 1% octylamine sensing cycles. N.B. grey shaded areas indicate analyte exposure.	209
Figure 144. Pentacene 21 TL vs. PDI8-CN ₂ 1 TL 1% octylamine sensing. N.B. grey shaded areas indicate analyte exposure.	210
Figure 145. PDI8-CN ₂ 1 TL screenshot before 1% octylamine sensing.	211

Figure 146. PDI8-CN ₂ 1 TL screenshot after 1% octylamine sensing.....	211
Figure 147. PDI8-CN ₂ 1 TL screenshot and ‘off’ cycle subtraction directly after 1% octylamine sensing.....	212
Figure 148. Nano-particle octylamine sensing results ($R(0) = 60\text{k}\Omega$). N.B. grey shaded areas indicate analyte exposure.....	214
Figure 149. P3HT 18 BL and P3HT 10 BR screenshots, DI (top, $R_{\text{Box}} = 27\text{k}\Omega$) vs. tap water (bottom, $R_{\text{Box}} = 32\text{k}\Omega$).....	218
Figure 150. P3HT 10 BR screenshots, square wave and sine driven ($R_{\text{Box}} = 27\text{k}\Omega$).	220
Figure 151. P3HT 10 BR (top, $R_{\text{Box}} = 27\text{k}\Omega$) and P3HT 11 BR (coated) (bottom, $R_{\text{Box}} = 300\text{k}\Omega$) screenshots, square wave drive.....	222
Figure 152. P3HT 10 BR (top, $R_{\text{Box}} = 27\text{k}\Omega$) and P3HT 11 BR (coated) (bottom, $R_{\text{Box}} = 300\text{k}\Omega$) screenshots, sine wave drive.....	223
Figure 153. $\ln(\text{vapour pressure})$ against T^{-1} plot for IPA.....	234
Figure 154. $\ln(\text{vapour pressure})$ against T^{-1} plot for acetone.	235
Figure 155. $\ln(\text{vapour pressure})$ against T^{-1} plot for propylamine.....	235
Figure 156. $\ln(\text{vapour pressure})$ against T^{-1} plot for ethylethanoate.	236
Figure 157. $\ln(\text{vapour pressure})$ against T^{-1} plot for formamide.	236
Figure 158. $\ln(\text{vapour pressure})$ against T^{-1} plot for octanal.	237
Figure 159. $\ln(\text{vapour pressure})$ against T^{-1} plot for octan-2-one.....	237
Figure 160. $\ln(\text{vapour pressure})$ against T^{-1} plot for ethylene.	238
Figure 161. $\ln(\text{vapour pressure})$ against T^{-1} plot for cyclohexane.	238
Figure 162. $\ln(\text{vapour pressure})$ against T^{-1} plot for octylamine.	239

List of Tables

Table 1. Properties of some Common Gate Insulators, C _i values have been measured for the thicknesses indicated. ^[64-66]	48
Table 2. Mobility and threshold values for pentacene OFETs.	149
Table 3. Mobility and threshold values for pentacene OFETs before and after coating.	180
Table 4. Mobility and threshold values for PDI8-CN ₂ OFETs.	208
Table 5. The boiling points and concentrations of the analytes used in this thesis.	239

1 Introduction

The work described here is focused on the goal of finding and developing new materials and methods to detect organic vapours using transducers (a device that converts a physical change into an electrical signal) based around an organic field-effect transistor (OFET) architecture. This is by no means a new field of interest, it is indeed becoming one of the main areas of OFET research,^[1] along with active matrix addressing for displays^[2] and RFID (radio frequency identification) tags.^[3] Many research groups have developed organic vapour sensing devices: some based on OFETs,^[4, 5] others on chemi-resistors^[6] and some monitor the optical rather than electrical properties of organic materials to detect the presence of vapours.^[7, 8] The main advantage of moving from optical into electronic transducers is the ability to run electronic transducers with much lower power consumption, allowing the development of wireless sensor devices with on-board power supplies. The main qualities of a sensing device that make it desirable for commercialisation are: reliability, reusability, fabrication from industrially scalable procedures and most importantly suitability for the task it is designed to perform; in this case that would speak to the device's ability to detect vapours at low concentrations, below dangerous thresholds and human olfactory limits.

Described first is the physics, chemistry and electronics theory needed to understand the execution and implications of the work reported in later chapters.

1.1 Physics of Organic Semiconductors

To act as a semiconductor, an organic molecule must contain conjugation; conjugation refers to alternating single and double bonds along a carbon chain. In single bonded sp_3 hybridised carbon systems the gap between the energies of the σ bonding and anti-bonding orbitals is large meaning that the gap between the highest occupied molecular orbital (HOMO) and lowest unoccupied molecular orbital (LUMO) levels (band-gap) is large, this indicates that the material will act as an insulator and be transparent to visible light. In sufficiently large sp_2 hybridised systems, however, the π bonding – anti-bonding energy gap is smaller leading to semiconducting behaviour and absorption in the visible spectrum (see

section 1.2.1.2 for a discussion of hybridisation and section 1.2.1.3 for a discussion of bonding and anti-bonding orbitals).

Understanding of the nature of charge carriers and the physics surrounding their behaviour is pivotal to understanding the operation of organic (and inorganic) semiconductor based devices. Charge carriers exist in two distinct forms when considering the area of organic semiconductors; these are the electron and the hole polarons. Electron polarons are the result of the addition of a negatively charged electron to the lowest unoccupied molecular orbital (LUMO) level of a molecule of the semiconductor; the addition of the extra negative charge to the molecule causes the molecule to re-arrange its constituent atoms and orbitals to find a new minimum energy configuration. Hole polarons, however, result from the removal of an electron from (or creation of a hole in) the highest occupied molecular orbital (HOMO) level of a molecule; like the electron polaron, the addition of a charge on the molecule (positive in this case) causes a conformational change in the atoms and orbitals that make up the molecule to create a new minimum energy state: the hole polaron. Henceforth the convention of referring to electron and hole polarons as merely electrons and holes will be observed.

1.1.1 Charge Carrier Injection into an Organic Semiconductor and the Origin of Contact Resistance

One of the most fundamental issues in creating highly efficient organic semiconductor devices is achieving efficient charge carrier injection. Different types of devices have different injection requirements; here are described carrier injection mechanisms and methods commonly used to improve injection.

As mentioned previously electrons need to be injected into the LUMO level of the semiconductor (in the case of an n-type organic semiconductor) or holes need to be injected into the HOMO level (in the case of a p-type). The energy needed to remove an electron from the HOMO level into the vacuum level (and therefore to inject a hole) is given by the ionisation potential, while the energy gained by an electron when it is injected from the vacuum level into the LUMO level is given by the electron affinity. The difference between the work function of the injecting electrode and the ionisation potential / electron affinity

give the injection barriers that must be overcome in hole / electron injection (see **Figure 1**). The work function is defined as the energy required to remove an electron from a metallic material.

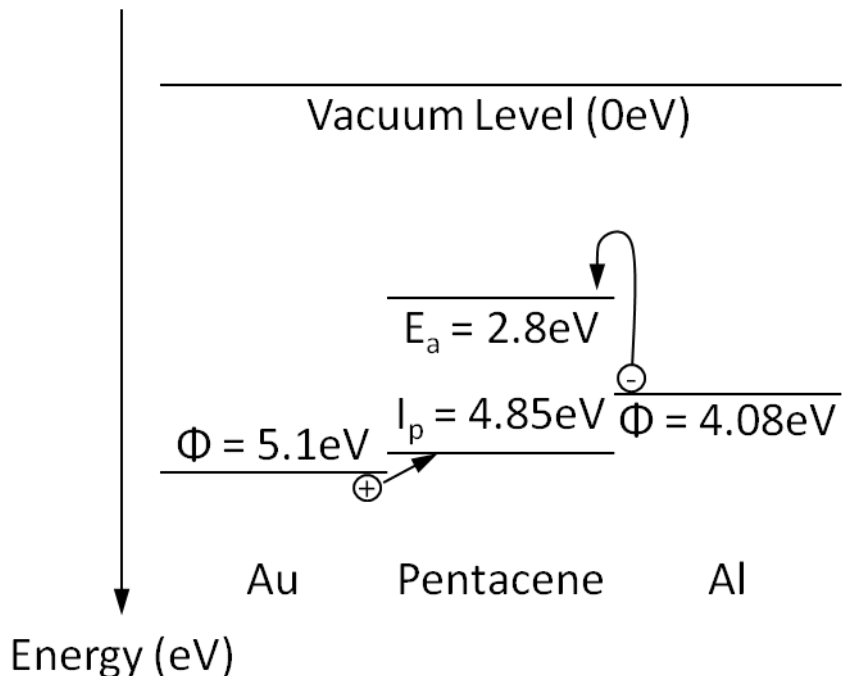


Figure 1. An example energy level diagram of electron and hole injection barriers from metal electrodes into an organic semiconductor with no applied bias. Φ , E_a and I_p are the electrode workfunction, semiconductor electron affinity and semiconductor ionisation potential as defined in the text.

It can inferred from **Figure 1** that the best metals for electron injection have low work function values and the best metals for hole injection have high work function values. The energy in **Figure 1** increases down the diagram as this is the energy required to remove an electron from a given level to the vacuum level.

When a potential is applied across the electrodes of a device the energy levels tilt meaning it is more energetically favourable for carriers at one side than the other, thus causing a net movement of carriers from one side of the device to the other (see **Figure 2**). The magnitude of the applied potential will determine the gradient of the energy levels.

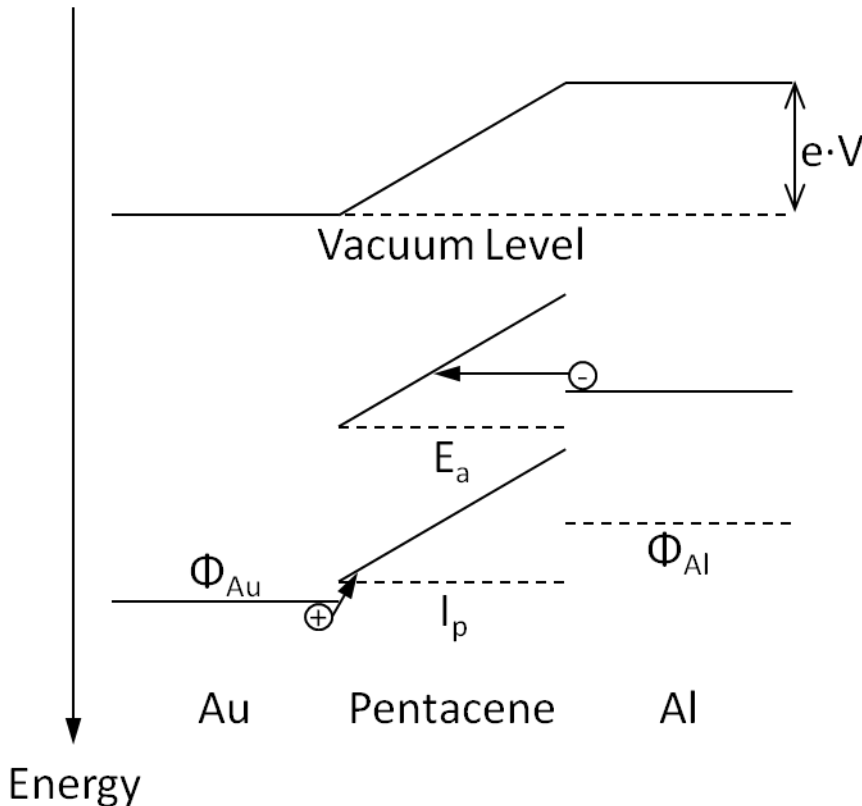


Figure 2. An example energy level diagram of electron and hole injection barriers from metal electrodes into an organic semiconductor with an applied bias. V is the applied potential difference and e the elementary charge.

There are two main mechanisms discussed when considering injection from a metal electrode into an organic semiconductor. These are the thermionic (or Schottky) emission and field emission (or Fowler-Nordheim tunnelling). The two mechanisms represent the two possibilities for dealing with a potential barrier: either gaining enough energy to go over the barrier (Schottky) or using quantum mechanical tunnelling to travel through the barrier (Fowler-Nordheim). Schottky emission is a highly temperature driven process and only weakly E-field dependent as described by the Richardson-Schottky equation (**Equation 1**).

$$\text{Equation 1.} \quad J_{RS} \propto T^2 \exp\left(-\frac{\Phi_B}{kT}\right) \cdot \exp\left(\frac{\beta_{RS} \sqrt{E}}{kT}\right)$$

where Φ_B is the potential barrier height, E is the E-field strength and β_{RS} is a constant.

In contrast Fowler-Nordheim tunnelling is heavily dependent on the E-field and independent of temperature; temperature can, however, assist in raising the carriers to higher excited states to make it easier for tunnelling to occur. To increase the probability of a tunnelling

event being possible, the width (not the height) of the potential barrier needs to be minimised; this can be achieved through moderation of the applied voltage (and therefore the E-field) see **Figure 2**. Fowler-Nordheim tunnelling is described by **Equation 2**, it can be seen from the mathematical descriptions of both mechanisms that this type of injection will be most prevalent at higher fields and larger barrier heights.

Equation 2.

$$J_{F-N} \propto \frac{E^2}{\Phi_B} \exp\left(-\frac{\gamma\Phi_B^{3/2}}{E}\right)$$

where γ is a constant.

As neither the Richardson-Schottky equation nor the Fowler-Nordheim were developed specifically for a metal/organic semiconductor interface Scott and Malliaras attempted to give a more realistic description of injection in their 1999 paper “Charge injection and recombination at the metal-organic interface”.^[9] But even this model neglects the contribution of tunnelling present at higher fields.

To improve the injection from a metal electrode sometimes a Schottky junction can be created between the metal and the semiconductor through doping of the semiconductor directly beneath the electrode. Rather than the band-tilting observed when a voltage is applied across a metal-semiconductor-metal system, band bending is observed in the Schottky junction; this is a consequence of the vast majority of the E-field being concentrated in the two doped areas next to the contacts and not being equally distributed throughout the semiconductor channel (see **Figure 3**). The band bending, as opposed to the tilting, leads to a smaller tunnelling barrier and therefore a greater current density contribution from Fowler-Nordheim-type injection. It has also been suggested that modification of the electrode surfaces by a polar self-assembled monolayer (SAM) can shift the workfunction of the electrode by moving its Fermi level as in **Figure 3**, effectively reducing the injection barrier into the organic semiconductor.^[10]

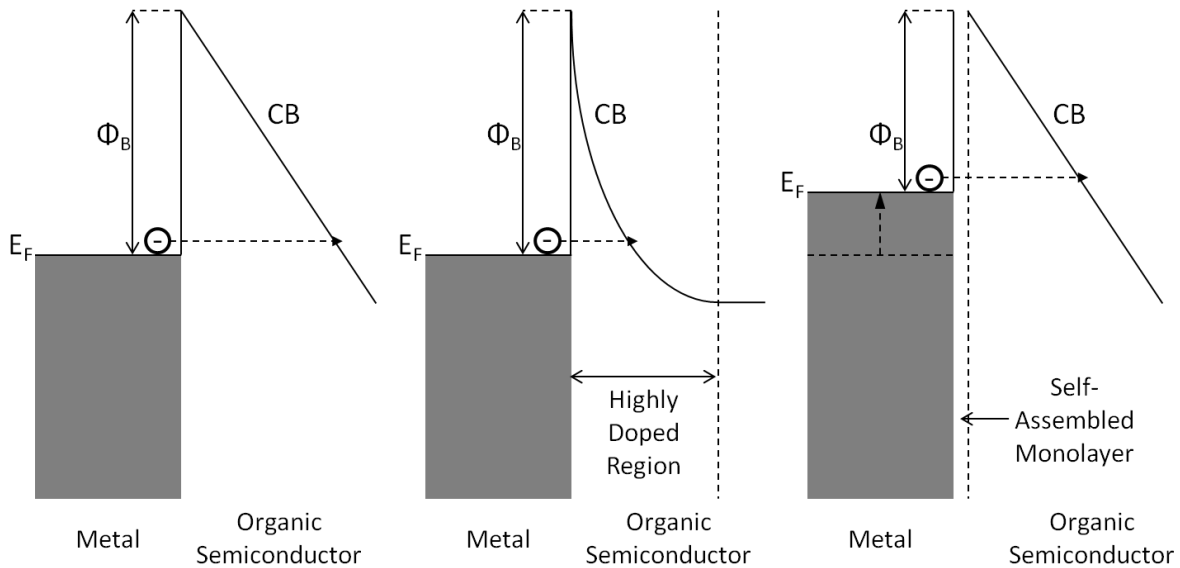


Figure 3. Energy diagrams showing band tilting (left), band bending (middle) and the effect of a self-assembled monolayer (right).

A Schottky junction has been realised in a pentacene OFET by Schroeder *et al* through the use of iron (III) chloride doping.^[11]

The best scenario is unhindered injection of carriers into the semiconductor from the electrodes, meaning that current would only be limited by transport across the bulk of the semiconductor; in this case the injection is said to be Ohmic.

1.2.2 Charge Carrier Transport in an Organic Semiconductor

The nature of charge carrier transport in organic semiconductors is a much debated subject, with many competing models trying to accurately describe experimental observations. It is thought that the degree of crystallinity and purity of a semiconductor determines the efficiency of the transport.

Organic semiconductors tend to be unipolar, that is they only transport either positive or negative charge carriers; the bandgaps of organic semiconductors (the energy difference between the HOMO and LUMO levels of the semiconductor) tend to be of the order of a couple of eV, but generally less than 4eV. A material that transports positive charge is known as a p-type^[12] and a material that transports negative charge is called an n-type.^[13, 14]

Materials that have low ionisation potentials tend to be p-types and materials that have high electron affinity tend to be n-types; inherent problems with p-types are that low

ionisation potentials tend to make them very susceptible to oxidation by atmospheric oxygen; n-types tend to form powerfully reducing radicals when acted upon by a positive potential while in a device, these radicals very readily react with atmospheric oxygen and water. Materials that transport both types of carriers do exist and are known as ambipolar semiconductors;^[14, 15] ambipolar materials, however, are very rare; work by Chua *et al*^[16] has shown that this is due to large densities of charge carrier traps at the semiconductor-insulator interface that selectively trap one type of carrier, in addition to the traps found in the bulk of the semiconductor. In the case of p-type materials it is thought to be the high number of hydroxyl (OH) groups present at the surface of many gate insulators that trap the electrons, preventing n-type conduction. Chua *et al* used a hydroxyl group free insulator and noticed n-type conduction in several p-type polymers. Charge carrier traps are a very important consideration when building an organic device as high levels of trap states can drastically change the behaviour of a device. Traps are in essence localised low energy states that tend to exist within the band-gap energy region. They tend to be carrier specific, i.e. there are electron traps and hole traps. Electrons can fall into traps from the “conduction band” of states (LUMO level), while holes can fall into traps from the “valence band” of states (HOMO level) and become immobilised; whilst immobilised the carriers are unable to transport charge and represent a centre of charge, which has a shielding effect, weakening the E-field strength within the semiconductor bulk. To release carriers from trap states an input of energy is required, this energy is generally thermal in nature. The filling and emptying of traps when the polarity of source and drain are reversed is one of the main causes of device hysteresis along with effects caused by mobile ions and defects.^[17] Hysteresis (“history dependence”) is behaviour displayed in some organic semiconductor devices where the current-voltage trace does not follow the same path when the voltage is increased as it does when the voltage is decreased.

1.1.2.1 Mobility

Carrier mobility is a measure of the average charge carrier velocity induced per unit E-field, described by **Equation 3**, it should be noted that while it appears that velocity scales linearly with E-field this is not the case as μ itself has an E-field dependence, as well as a charge carrier density dependence (discussed later).

Equation 3.

$$\langle v \rangle = \mu E$$

where $\langle v \rangle$ is average carrier velocity.

The units generally used for mobility are $\text{cm}^2\text{V}^{-1}\text{s}^{-1}$ and the mobilities found for organic semiconductors are generally several orders of magnitude smaller than for their inorganic counterparts; organic semiconductor mobilities tend to range from $\sim 10^{-6}$ to $\sim 10^2 \text{ cm}^2\text{V}^{-1}\text{s}^{-1}$ ^[18], with the more disordered amorphous materials tending to have the lower mobilities and as order increases in the semiconductors so does the mobility, the highest values, therefore, coming from the highly ordered crystalline semiconductors and single crystal devices. Attempts to model and predict mobility in organic systems are discussed hereafter.

The classical inorganic semiconductor band transport model relies on the fact that the orbitals of all the constituent atoms of the semiconductor overlap, creating coherent bands for the charge carriers to move through. The main feature of band transport is the temperature dependence of its mobility, which scales as $\mu \propto T^n$ (where n is generally positive) showing that mobility improves as temperature decreases. It has been suggested by Karl *et al.* that this behaviour is present in high purity molecular crystals of polyacene,^[19] this however has been disputed as the mean free path of the carriers is smaller than the intermolecular spacing of the molecules in the crystal at temperatures larger than 150K.^[20]

For well-ordered organic structures such as vacuum sublimed pentacene, a model has been suggested to explain the thermal dependence on mobility that is sometimes observed. This model is the multiple trapping and release (MTR) model,^[21] its main assertion being that the increase in mobility due to increase in temperature is due to the thermally activated release of carriers from trap states. The model assumes that there are localised trap states in existence near the transport band edge (HOMO level in p-types, LUMO in n-types), it assumes the trap states catch any nearby charge carrier with near 100% probability and it also assumes that the release of trapped carriers is purely thermally controlled. The effective charge carrier mobility in this model is described by **Equation 4**.

Equation 4.

$$\mu_{\text{eff}} = \mu_0 \alpha e^{-(E_c - E_t)/kT}$$

where μ_0 is the mobility, E_c is the transport band edge, E_t is the energy of the trap states and α is the ratio of trap density of states (DoS) to effective DoS at the transport band edge. It

can also be shown that $\mu_{eff} = \Theta\mu_0$, where Θ is the ratio of trapped carriers to total (trapped + free) carriers.^[21]

Disordered or amorphous semiconductor structures have been shown to have a thermally activated mobility and from experimental results seem to also have a field dependence given by $\ln(\mu) \propto E^{0.5}$. It is thought that charge carrier transport in amorphous materials proceeds via “hopping” transport, in which charge carriers perform thermally induced hops from the localised energy states of one molecule to the next to advance through the semiconductor bulk. The three most widely used and accepted hopping models are discussed here.

Hopping transport is sometimes described using a Poole-Frenkel (PF) like equation,^[21] as in **Equation 5**.

$$\text{Equation 5.} \quad \mu = \mu_0 e^{-(\Delta_0 - \beta\sqrt{E})/kT_{eff}}$$

where $T_{eff}^{-1} = T^1 - T^{*-1}$, $\mu_0 = \mu(T=T^*)$, Δ_0 is the energy barrier needed to be overcome and β is the PF factor. The problems with this model are firstly that T_{eff} has no physical meaning and secondly that the PF factor needed in this case is very different from the one predicted by PF theory.

An alternative hopping transport model is Bässler’s disorder model.^[22] Bässler theorises that due to the random nature of intermolecular interactions the density-of-states profile has a Gaussian distribution of energies with variance σ^2 , this is known as diagonal disorder. Transport in Bässler’s model is a random walk with a net path in the direction dictated by an applied field described by **Equation 6**.

$$\text{Equation 6.} \quad v = v_0 e^{-2\gamma\Delta R_{ij}} e^{-\Delta\varepsilon_{ij}/kT}$$

where v is the hopping frequency, v_0 is the “attempt-to-hop” frequency, ΔR_{ij} is the distance between hopping sites, γ is the inverse localisation length and $\Delta\varepsilon_{ij}$ is the energy difference between sites. Bässler also describes the disorder in the position of hopping sites using a second Gaussian distribution, this time with variance Σ^2 ; this he named the off-diagonal disorder. Through Monte-Carlo simulation Bässler created **Equation 7** to describe the behaviour of carrier mobility.

Equation 7.

$$\mu = \mu_0 \exp\left[-\left(\frac{2\sigma}{3kT}\right)^2\right] \exp\left[C\left\{\left(\frac{\sigma}{kT}\right)^2 - \Sigma^2\right\} \sqrt{E}\right]$$

where C is an empirical constant, μ_0 is the “disorder-free” mobility at the limit of infinite temperature and zero-field^[23] and $\Sigma^2 = 2.25$ for all $\Sigma \geq 1.5$.

The important results of the Bässler model are that μ scales as $\ln(\mu) \propto T^{-2}$ and $\ln(\mu) \propto E^{0.5}$. The $\ln(\mu) \propto E^{0.5}$ dependence shown by the Bässler model is supported by data such as that from Redecker *et al.*^[24]

The final model discussed here is a modification of the Bässler model proposed by Pasveer *et al.*^[25] The Pasveer model was formulated when it was noticed that the same semiconductor could show vastly different mobilities when used in diode and field-effect transistor architectures, suggesting that some parameter beyond the E-field and temperature Bässler included in his model has a significant effect on carrier mobility. This new parameter was the charge carrier density (p). The model proposed by Pasveer can be summarised by **Equation 8**, where there is a temperature and carrier density dependent term multiplied by a dimensionless, carrier density independent term that depends on both temperature and E-field.

Equation 8.

$$\mu(T, p, E) \approx \mu(T, p) f(T, E)$$

where T is the temperature, p is the charge carrier density, E is the electric field strength and μ and f are mobilities dependent on different factors.

This model approaches the Bässler model at low carrier density but fails at densities approaching $a^3/2$ (where a is the lattice constant of the system). It also states that μ scales with p as: $\mu \propto \exp(Ap^B)$, where A and B are constants that depend heavily on σ (the diagonal disorder seen previously). The p dependency of μ increases as σ increases and T decreases, μ showing little to no increase as p increases at low σ and high T .^[25]

1.1.2.2 Current Density

If the injection barriers are small within a given system (i.e. injection is Ohmic) then the maximum current will be limited by the transport of carriers across the semiconductor bulk,

so called bulk-limited transport, as opposed to the injection-limited transport seen in systems with high injection barriers.

Under bulk-limited transport there are two possible transport regimes, the Ohmic conduction regime and space charge limited current (SCLC) regime. It should be noted that both types of current are always present but one type will generally be dominant. Ohmic conduction is described by **Equation 9**, and it is only observed in systems which have a majority of charge carriers coming from dopants in the semiconductor rather than being injected from an electrode; this can be achieved by either having a highly doped semiconductor, or a small electric field across the bulk; a small E-field can arise from a long inter-electrode separation or only applying a low voltage across the electrodes.

Equation 9. $J_{ohm} = qn\mu E$

where J_{ohm} is the current density, q is the charge on the carriers and n is the carrier density.

In a system dominated by injected charge carriers SCLC behaviour will be observed. Unlike dopant induced carriers, the charge of injected carriers is not balanced by a counter-ion; this leads to a build-up of charge and therefore E-field shielding effects in the semiconductor bulk when a large build-up of injected carriers is achieved, eventually causing the E-field to drop to zero at the injecting electrode. SCLC behaviour is observed in systems with high injected charge carrier density with respect to dopant induced carrier density, this is usually caused by large applied voltages, small inter-electrode spacing and low levels of semiconductor doping. SCLC is described by **Equation 10**.

Equation 10.
$$J_{SCLC} = \frac{9}{8} \epsilon_r \epsilon_0 \mu \frac{V^2}{d^3} = \frac{9}{8} \epsilon_r \epsilon_0 \mu \frac{E^2}{d}$$

where d is the inter-electrode spacing.

It can be seen quite clearly from **Equation 10** that SCLC is very strongly dependent on electrode spacing and so Ohmic conduction will begin to dominate very quickly as electrode separation increases in all but the very purest semiconductors.

The transition between the injection-limited and SCLC regimes has been investigated by Wolf *et al*;^[26] they managed to find the transition was dependent on the carrier mobility,

the injection barrier height and the applied field. It was found that mobility at which the transition occurred for a fixed field was related to barrier height (Δ) as: $\log_{10}(\mu) \propto \Delta$. As field was increased the transition could occur for the same mobility at a larger barrier height.

1.2 **Organic Chemistry**

Here are described the basics of organic chemistry theory relevant to the field of organic field-effect transistors. At its core the entire area of organic chemistry is rooted in the study, synthesis and uses of materials composed primarily of carbon “back-bones” with attached, so called, functional groups and hydrogen atoms to “mop-up” any spare carbon valency. Carbon has the electronic configuration $1s^2 2s^2 2p^2$ in its ground state, meaning it must form four bonds to fill its valence shell orbitals. Compounds that contain the covalent carbon-hydrogen bond generally considered organic, whereas compounds such as carbonates and graphite are not considered organic.

1.2.1 **Organic Structure and Bonding**

When trying to predict the shape and electronic configuration of an organic molecule a variety of different models can be used. This section describes the most commonly used models. The basic shape of organic molecules is generally predicted through the valence shell electron pair repulsion theory (see section 1.2.1.1). The electronic configuration on the other hand involves two commonly used models, neither of which are exact; the first model is the valence bond approach, wherein the electronic structure within a molecule is built up by considering the localised bonding of each atom in turn, typified by the hybrid orbital description (see section 1.2.1.2); the second model treats the electrons as being delocalised over the entire molecule (see section 1.2.1.3)

1.2.1.1 **The Shapes of Organic Molecules**

One fundamental question often asked when considering an organic molecule is “what shape will this molecule be?”, the orientation of the constituent atoms of a molecule with respect to each other is of great importance when trying to form regular crystalline structures or trying to achieve a specific chemical reaction or interaction between molecules. The most common method to predict the shapes of molecules is through the

valence shell electron pair repulsion (VSEPR) theory;^[27] this theory makes the assumption that the geometry of a molecule depends solely on the interactions between electron pairs, be they bonding or lone pairs. The electron pairs repel each other forcing an arrangement of bonds (and lone pairs) that will create a minimum energy state. It should be noted that lone pairs have a greater repulsive effect than bonding pairs. The basic atomic arrangements depend, of course, on the number of bonds formed by an atom and the number of lone pairs remaining, **Figure 4** details the most common arrangements observed.

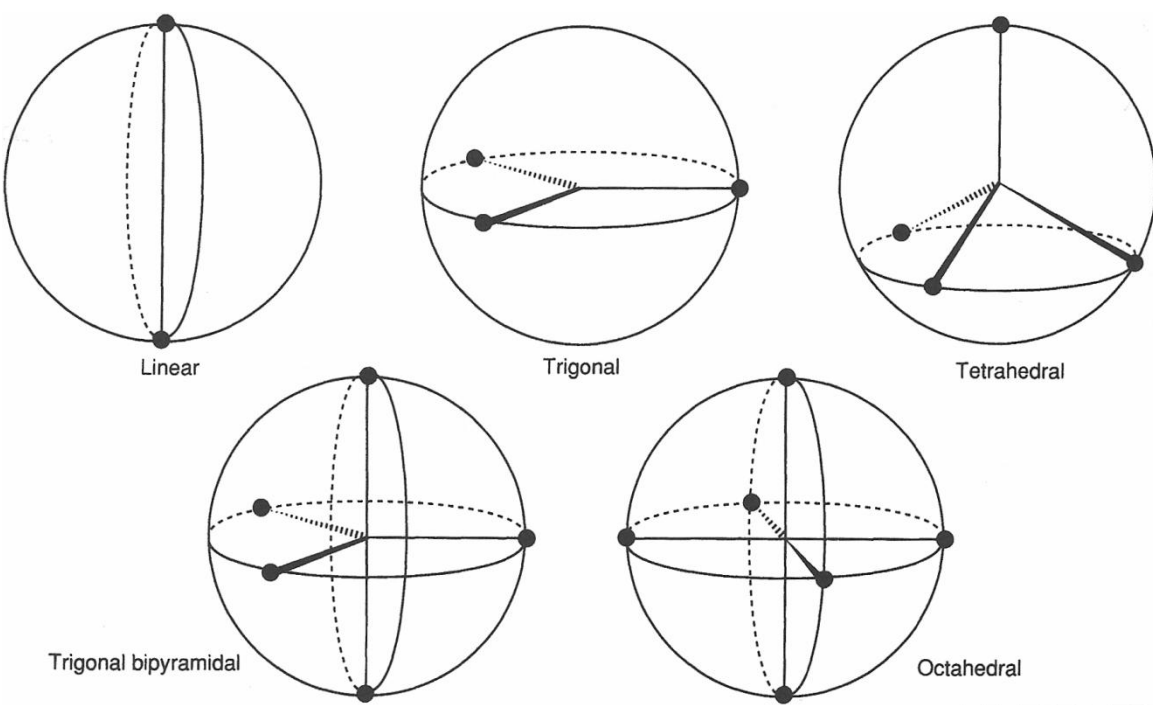


Figure 4. The common molecular structural geometries found for 2-6 electron pairs, predicted through VSEPR theory.^[27]

(Permission to reproduce this figure has been granted by Dr. Mark J. Winter)

The presence of lone pairs, however, complicates matters somewhat due to the greater repulsion they display (as mentioned above). For example ammonia (NH_3) has 3 bonding pairs of electrons and one lone pair. It can be seen from the **Figure 4** above that this should lead to a tetrahedral structure; the effect of the lone pair is to push the bonding pairs closer together creating a new bond angle of 106.6° from the original angle of 109.5° .

In a molecule such as ethane it is possible for the two halves of the molecule to rotate around the single carbon-carbon bond connecting them; however this rotation is not free. The cost of rotation is given by the rotational potential of the molecule, moving away from

the minimum potential requires the input of energy. The rotation of the molecule is quantified by the definition of a dihedral angle: the angle between two C-H bonds in two different planes of the molecule, measured in a plane perpendicular to that of the bond the rotation is taking place around. In the case of ethane minimum of rotational potential is when the dihedral angle is 60° , 180° or 300° (as in the right of **Figure 5**).

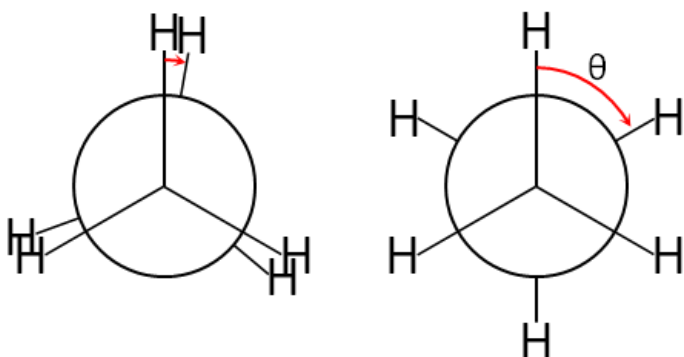


Figure 5. The view along the central C-C bond in ethane (Newman projection), showing the dihedral angle (left: $\theta = 10^\circ$, right: $\theta = 60^\circ$).

VSEPR theory is very useful when considering moderately small molecules. However, when we enter the realm of polymers the situation becomes more complex due to the possibility of rotation of molecules around single bonds. Although the monomer units of the polymers follow the general structural rules outlined above, the task of modelling the entire polymer chain is very difficult. A free chain in isolation can be modelled simply by a random walk, or more thoroughly by a self-avoiding walk taking into account entropic and enthalpic considerations.^[28] In a system involving multiple polymer chains and/or molecules of solvent the situation is further complicated by the inter- as well as intra-molecular interactions.

1.2.1.1.1 Polymers

A polymer is by definition a high molecular weight material, sometimes composed of thousands or hundreds of thousands of repeat units known as monomers, polymers made from more than one type of monomer unit are called copolymers. The length of a polymer chain is usually dependent on the synthesis pathway used to create it, the size of a polymer is generally expressed as a molecular weight; two different average molecular weights are

often quoted: the number average molecular weight (M_n) (see **Equation 11**) and the weight average molecular weight (M_w) (see **Equation 12**).

Equation 11.

$$M_n = \frac{\sum_i M_i N_i}{\sum_i N_i}$$

Equation 12.

$$M_w = \sum_i W_i M_i, \quad W_i = \frac{M_i N_i}{\sum_i M_i N_i}$$

where M_i is the molecular mass of a molecule and N_i is the number of molecules of each molecular mass.

The ratio of M_w to M_n is known as the polydispersity index and is a measure of the spread of chain lengths in a sample of a polymer; the closer the polydispersity index is to one, the more uniform the chain lengths of the polymer sample.

As mentioned in section 1.2.1.1 the polymer chains can be modelled by a self-avoiding random walk in isolation (in vacuum or in a good solvent) and by a regular random walk when in a polymer melt, but the stiffness of a chain is generally quantised through the persistence length parameter (L_p); the persistence length is the length over which the polymer is effectively rigid with all its monomer units aligned in the same direction, described by **Equation 13**.

Equation 13.

$$\langle \cos \theta \rangle = e^{-(L/L_p)}$$

where θ is the angle between a tangent to the polymer chain at any given point and a tangent to the chain a distance L away along the contour of the chain and L_p is the persistence length.

The polymers of interest to the field of organic semiconductors are those that are conjugated. As a conjugated molecule gets larger the electrons in the π -system of the molecule can delocalise over a larger area, this decreases the size of the bandgap; however, in conjugated polymers the bandgap energy remains constant after the polymer chain has exceeded a certain critical length. This can be explained by the idea of the molecule having a so-called “effectively conjugated segment” (ECS),^[29] the number of monomer units over which conjugation is maintained.

In a solid film the alignment of the polymer chains is affected primarily by the method and conditions of the deposition (as well as any annealing processes performed after deposition); while in solution the interactions of individual chains are affected by the type of solvent, the concentration of the solution and the temperature of the solution, poor solvents, high concentrations and low temperatures can cause the formation of aggregates.

It has been shown by Someya *et al* that crystal grain boundaries play a role in vapour sensing,^[30] it is therefore important to understand how polymeric materials can form crystalline structures. The most basic type of ordering found in polymer crystals is the chain-folded lamella, wherein the individual polymer chains fold themselves in such a way as to form regions of well-ordered parallel sections of polymer chain with disordered (amorphous) regions above and below the ordered (crystalline) region where the chains begin, end and fold (see **Figure 6**); it is possible for a single polymer chain to be part of several neighbouring lamellae. An alternative to the chain-folded lamella is the chain extended lamella, wherein the entirety of each polymer chain stacks as in the crystalline region of **Figure 6**, thus avoiding the amorphous regions above and below the ordered region; it is obvious that the chain extended lamella structure would be preferable to chain-folded, when an ordered structure is required, however, the chain extended structure is harder to form as most long polymer chains lack the mobility to form the structure unless extreme conditions are used for depositions (very high boiling point solvents, annealing processes etc.), it is much easier to form chain extended lamellae from shorter chain polymers.

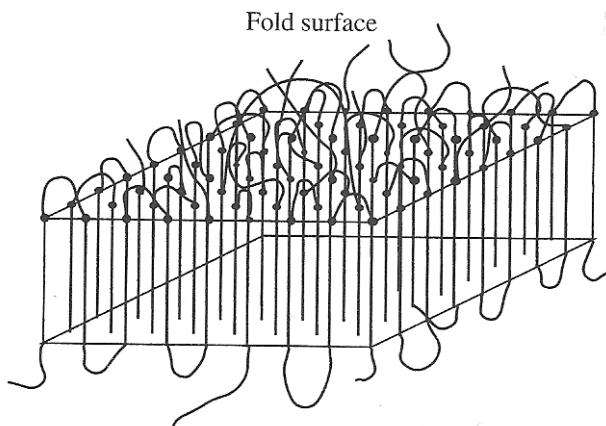


Figure 6. The structure of a chain folded lamella.^[31]

(Permission to reproduce this figure has been granted by Prof. Richard A. L. Jones)

The lamellae are also capable of organising themselves into a larger semi-crystalline structures known as spherulites (see **Figure 7**), wherein several sections of lamella begin to orientate themselves around a central nucleus, creating a micro-scale structure from the nano-scale lamellae. The space between the lamella branches and the space around individual spherulites is amorphous material.

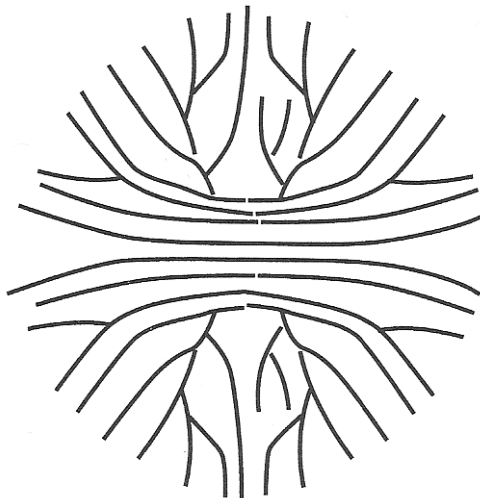


Figure 7. The structure of a spherulite.^[31]

(Permission to reproduce this figure has been granted by Prof. Richard A. L. Jones)

1.2.1.2 Carbon-Carbon Bonding (Orbital Hybridization)

When considering the bonding of one atom of carbon to the next, it is no longer prudent to consider the atomic orbitals of each of the carbon atoms in isolation, since this is an un-

realistic situation and provides no model for the bonding which occurs. Therefore the model of hybridisation was proposed, the theory states that through promotion of one of its electrons from the $2s$ orbital to the empty $2p_z$ orbital the carbon atom is then able to combine the $2s$, $2p_x$, $2p_y$ and $2p_z$ orbitals into new hybrid orbitals.

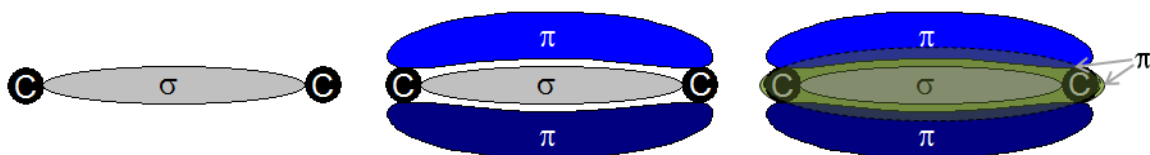


Figure 8. The orbital structure of single (left), double (middle) and triple (right) carbon-carbon bonds. The two blue areas form one π bond and the two green areas form a second.

The nature of the hybrid orbitals depend on the order of the carbon-carbon bonding required. In the case of a single bond being formed between adjacent carbon atoms, all three of the p-orbitals mix with the s-orbital to form four sp_3 hybrid orbitals; this allows carbon to potentially form four σ -bonds through the overlapping of one of its own sp_3 orbitals with one belonging to its bonding partner. If the carbon atom is to form a double-bond to its neighbour then it must undergo sp_2 hybridisation, wherein only two of the three p-orbitals will mix with the s-orbital to form three sp_2 orbitals in a common plane along with the remaining p-orbital perpendicular to the sp_2 plane. To form a double bond the sp_2 carbon must bond to another sp_2 carbon through orbital overlapping, creating a σ -bond and allowing its remaining p-orbital to mix with the p-orbital of its neighbour, delocalising the orbital both above and below the σ -bond to form a π -bond. Finally the creation of a triple bond requires the carbon atom to hybridise a single p-orbital with its s-orbital creating a pair of sp hybrid orbitals; to form the triple bond the carbon must overlap one of its sp orbitals with an sp orbital belonging to its bonding partner to create a σ -bond, the two remaining p-orbitals must again delocalise and merge with their counterparts on the bonding partner to create two π -bonds. **Figure 8** shows the shapes and orientations of the σ and π orbitals in single, double and triple carbon-carbon bonds. It should be noted that orbital hybridisation is not limited to carbon, or indeed to only s- and p-orbitals. Once hybridised the atomic orbitals of any given atom will form localised molecular orbitals when overlapped, this theory doesn't consider electrons delocalised over the whole molecule. The shapes of the hybrid orbitals are shown in **Figure 9**.

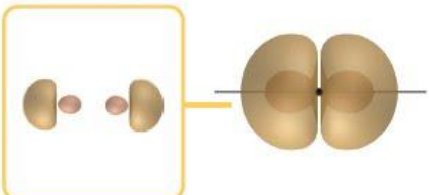
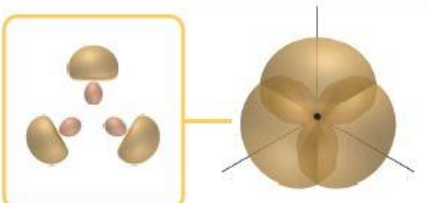
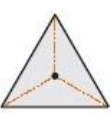
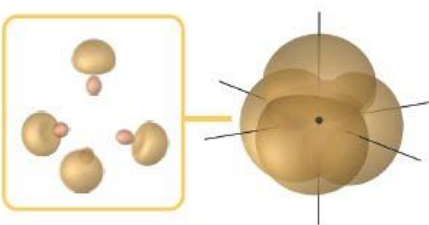
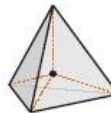
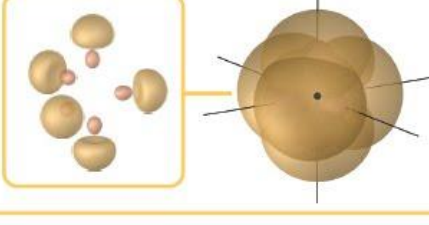
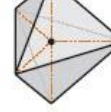
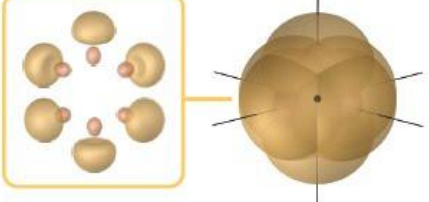
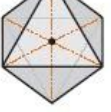
Arrangement of Hybrid Orbitals	Geometric figure	Example
Two electron pairs sp		 180° BeCl_2
Three electron pairs sp^2		 120° BF_3
Four electron pairs sp^3		 109.5° CH_4
Five electron pairs sp^3d		 90° 120° PF_5
Six electron pairs sp^3d^2		 90° 90° SF_6

Figure 9. The shapes of the hybrid orbitals for two to six electron pairs.^[32]

(From KOTZ/TREICHEL/TOWNSEND. *Chemistry and Chemical Reactivity*, International Edition, 8E. © 2012 Brooks/Cole, a part of Cengage Learning, Inc. Reproduced by permission. www.cengage.com/permissions)

1.2.1.3 Molecular Orbital Approach

An alternative method of modelling the orbital structure of a molecule is via the molecular orbital (MO) approach. Molecular orbitals are formed by the overlapping and mixing of atomic orbitals from different atoms through the linear combination of atomic orbitals (LCAO) method, unlike in hybridisation where only orbitals of the same atom are combined, this leads to the formation of delocalised molecular orbitals. The LCAO method involves the

addition of the wave functions of the atomic orbitals; the combination of the wavefunctions that describe the orbitals of two discrete atoms can occur with the wavefunctions in phase resulting in bonding molecular orbitals or can occur with the wavefunctions out-of-phase resulting in anti-bonding molecular orbitals (usually denoted with an *). The bonding molecular orbitals are of lower energy than the original atomic orbitals of the discrete atoms; the anti-bonding orbitals, however, are higher in energy than the original atomic orbitals, meaning that when filling the orbitals with electrons the bonding orbitals are filled first.

For the sake of illustration the case of a simple diatomic molecule (O_2) will now be discussed. Firstly the valence s-orbitals of the original atoms mix to create the σ_s and σ_s^* bonding and anti-bonding molecular orbitals; next the valence p-orbitals mix to form (in order of ascending energy) σ_p , $2 \times \pi_p$, $2 \times \pi_p^*$ and σ_p^* bonding and anti-bonding molecular orbitals. The p_z orbitals from each of the atoms are the ones taken to point along the atom-to-atom axis and so are the ones that mix to form the σ_p and σ_p^* orbitals, whereas the p_x and p_y orbitals that lie perpendicular to the p_z orbitals (and each other on both atoms) form the two π_p and two π_p^* orbitals with their counterparts. Finally the electrons from the original atoms are paired up into the new molecular orbitals according to the Pauli Exclusion Principle starting with the lowest energy and working upwards, filling degenerate orbitals with single occupants before pairing any up. A diagram of the orbitals for O_2 is shown in **Figure 10**.

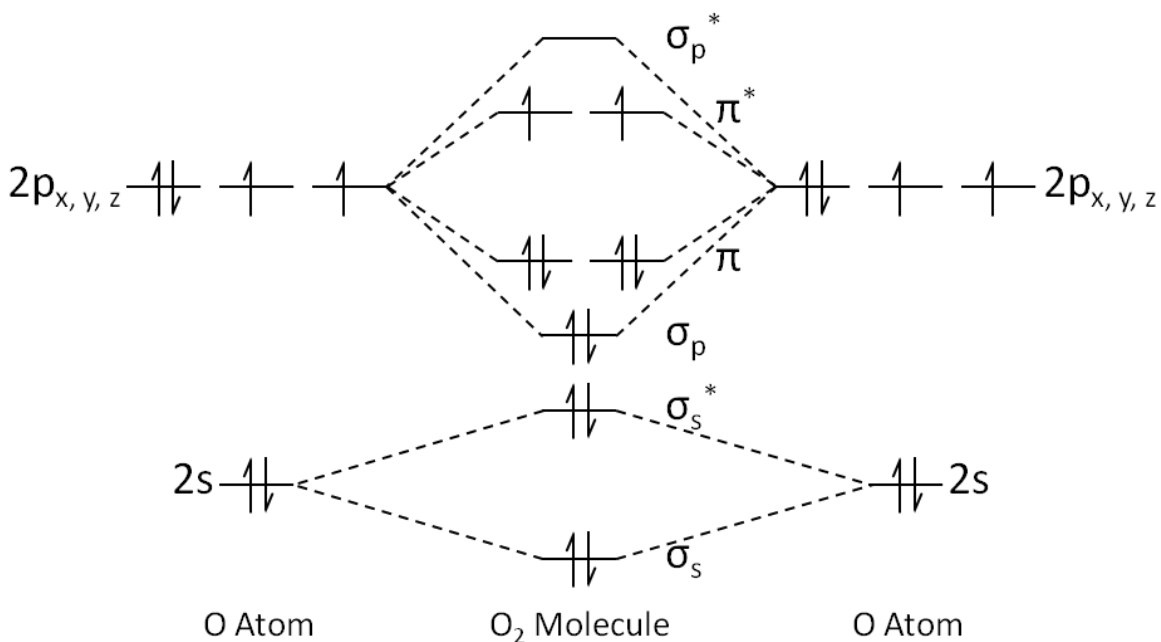


Figure 10. The molecular orbital structure in O_2 .

The case of O_2 has been chosen for the sake of simplicity as the interactions between the molecular orbitals are quite weak, but in other molecules the inter-orbital interactions are noticeably stronger, causing some molecular orbital energies to rise and some to fall. Also in molecules with non-identical atoms some orbitals are unable to mix due to symmetry considerations so become non-bonding orbitals.

The MO approach first uses the principles of VSEPR (see section 1.2.1.1) to position the atoms and then uses group theory analysis to predict the combination of atomic orbitals that will form bonding, non-bonding and anti-bonding molecular orbitals. Group theory analysis is a systematic discussion of symmetry that uses simple rules to arrive at a final structure. The energies of the orbitals can only be found through experimental methods or theoretical modelling.

1.2.1.4 Basic Organic Molecules and Functional Groups

Most organic materials are more than just long chains of carbon atoms with hydrogen atoms attached to fill their orbitals (known as **alkanes**); most materials are complex, incorporating many different types of atoms in a variety of bonding configurations. Carbon chains alone are not very chemically reactive (but can undergo combustion). However when the carbon-carbon bond order (number of bonds between carbon atoms) is increased (see

section 1.2.1.2) or other groups are added to the chain we are faced with a very different situation; these new parts of the molecule are known as functional groups which are responsible for all the interesting chemistry and physics. What follows is a short description of the functional groups regularly encountered in organic semiconductor and vapour sensing work.

First is the **alkene** group, this is a carbon-carbon double bond (i.e. one σ - and one π -bond, sp_2 hybridised carbon atoms, as discussed in section 1.2.1.2) and this is vital to the creation of organic semiconductors as discussed in section 1.1; next is the **alkyne** group, a carbon-carbon triple bond (one σ - and two π -bonds, both carbon atoms being sp hybridised). Molecules containing alkene and/or alkyne groups are said to be unsaturated as the additional bonds can be “opened” to allow new groups to attach to the double and triple bonded carbons, whereas molecules containing only single bonded carbons are said to be saturated as there is no opportunity to form additional bonds without breaking the carbon-carbon bond. Examples of alkanes, alkenes and alkynes are shown in **Figure 11**.

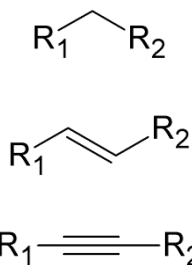


Figure 11. The chemical structures of a generic alkane (top), alkene (middle) and alkyne (bottom).

Alcohols contain a hydroxyl group (-OH) and the number of carbons attached to the carbon bonded to the hydroxyl group determines the type of alcohol. One carbon means it is a primary alcohol, two carbons correspond to a secondary alcohol and three to a tertiary alcohol (see **Figure 12**). The three types of alcohol have different degrees of reactivity due to the inductive effects (displacement of electron density on a molecule due to differences in electronegativity) of the neighbouring carbons, in that the electron clouds on the neighbouring carbons are shifted towards the electronegative oxygen atom (see section 1.2.4.2). The electronegativity of an atom is a measure of its tendency to pull local electron

density towards itself: the greater the electron density shift towards the atom, the higher the electronegativity of the atom.

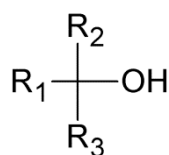
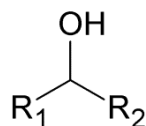
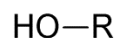


Figure 12. The chemical structures of a generic primary (top), secondary (middle) and tertiary alcohol (bottom).

Aldehydes and ketones are the functional groups with a double bonded oxygen attached to a carbon; if this carbon is only bonded to one more carbon then this is an aldehyde, more than one and it is a ketone. A very different group is created if the carbon already double bonded to an oxygen is also single bonded to a hydroxyl group; this is the **carboxylic acid** group. The structures of the aldehyde, ketone and carboxylic acid groups are shown in **Figure 13**. Aldehydes and ketones often have pleasant smells and make up part of the aroma of many fruits and flowers. Carboxylic acids are “weak acids”, in that they do not react with bases as readily as inorganic “strong acids” do.

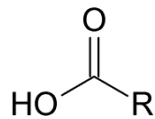
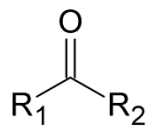
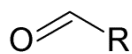


Figure 13. The chemical structures of a generic aldehyde (top), ketone (middle) and carboxylic acid (bottom).

The **amines** and the **nitriles** are nitrogen containing groups; the amine group is a single bonded nitrogen attached to at least one carbon atom, the nitrile group is a nitrogen atom triple bonded to a carbon atom (see **Figure 14**). A primary amine has one carbon bonded to the nitrogen atom, a secondary amine has two carbon atoms bonded to the nitrogen and a tertiary amine has three carbons, the remaining valency is taken up by hydrogen atoms. Amines are produced in the breakdown of proteins, meaning all meat and fish produce amines as they begin to spoil.

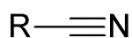
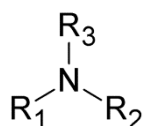
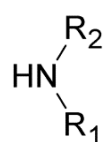


Figure 14. The chemical structures of a generic primary (top), secondary (2nd from top) and tertiary amine (2nd from bottom) and nitrile (bottom).

There are two main types of acids and bases these are Bronsted-Lowry (or protic) and Lewis acids and bases. Protic acids donate H^+ ions and protic bases accept H^+ ions, whereas Lewis acids accept a pair of electrons and Lewis bases donate electron pairs. The lone pair on the nitrogen atom of an amine group allows it to act as a Lewis base.

The **amide** and **ester** groups both contain a carbon atom double bonded to an oxygen atom. The amide, however, has an amine group (either primary, secondary or tertiary) also bonded to the carbon, while the ester has the carbon bonded to an oxygen atom that is also bonded to a carbon chain or single CH_3 group (see **Figure 15**). Amide groups are one of the main building blocks of proteins, so are very important in biological systems, they are also found in drugs such as penicillin and LSD (lysergic acid diethylamide). Some esters, like aldehydes and ketones, have pleasant aromas and are found commonly in nature.

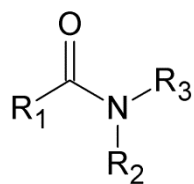
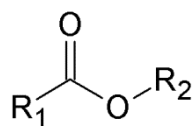


Figure 15. The chemical structure of a generic ester and amide.

The **halide** group could be in the form of the chloro, fluoro, bromo or iodo group (see **Figure 16**). The halide group therefore consists of a halogen atom joined to a carbon chain. A great many of the solvents used in organic chemistry contain halide groups, which are quite electronegative, so most of the halogenated solvents have a polar nature.

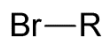
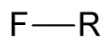
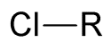


Figure 16. The chemical structures of a generic chloro- (top), fluoro- (2nd from top), bromo- (2nd from bottom) and iodo-group (bottom).

The **benzene ring** is a closed ring of six sp_2 hybridised carbon atoms (see **Figure 17**), wherein the π -bond electrons from the double bonds are delocalised around the whole ring (the electrons are no longer associated with a particular double bond). This is a conjugated ring structure, in that the molecule contains alternating single and double bonds, this is an important feature for organic semiconductors (see section 1.1). The presence of the delocalised π -system makes the double bonds found in benzene more stable than those found in regular alkenes, meaning it is more likely to substitute its hydrogen atoms than break its double bonds when it undergoes chemical reactions; this behaviour has led to benzene and other molecules that behave in this way to be classified as aromatic compounds.



Figure 17. The chemical structure of a benzene ring.

In the structure of the **pyridine ring**, one of the benzene ring's carbon atoms has been replaced with a nitrogen atom (see **Figure 18**), due to the nitrogen atom having a p-orbital available for bonding the aromaticity of the ring has been preserved, leading to reduced reactivity. In this molecule the nitrogen also retains its lone pair of electrons. Along with benzene, pyridine is found in many medicines.

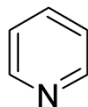


Figure 18. The chemical structure of a pyridine ring.

The **pyrrole ring** is another example of an aromatic compound (see **Figure 19**), the lone pair of electrons from nitrogen being put into a p-orbital and included in the delocalised π -system of the ring; however, the pyrrole ring is slightly more reactive than benzene and pyridine because of this. The pyrrole ring is an integral part of the structure of the porphyrins and phthalocyanines discussed later (section 1.2.3).

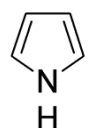


Figure 19. The chemical structure of a pyrrole ring.

The final aromatic “heterocycle” discussed here is the **thiophene ring** (see **Figure 20**), the sulphur atom provides its lone pair to the delocalised π -system as the nitrogen does in the pyrrole ring to maintain its aromaticity. Thiophene forms part of some notable organic semiconductors (see section 1.2.2.2.1)



Figure 20. The chemical structure of a thiophene ring.

1.2.2 Functional Organic Materials

1.2.2.1 Low Molecular Weight Organic Semiconductors

Low molecular weight organic semiconductors, as the name suggests, are relatively small molecules in comparison to high molecular weight conducting polymers (discussed later in section 1.2.2.2), meaning that inter-molecular conduction of charge carrier between molecules is a very important process due to the limited conduction length provided by each individual molecule. As a consequence a high degree of crystalline order is desirable in thin films of these materials to maximise semiconductor performance.

1.2.2.1.1 Pentacene

Pentacene is probably the best known and one of the most widely used organic semiconductors in the field of OFETs.^[33, 34, 35] Pentacene has been shown to be capable of mobilities up to $8.85\text{cm}^2\text{V}^{-1}\text{s}^{-1}$ given the appropriate processing conditions and device architecture^[36] making it among the best materials for high performance OFETs. However pentacene is very insoluble and is therefore generally deposited by thermal evaporation under vacuum and is incompatible with many of the newer solution based deposition processes such as ink-jet printing. Pentacene is a p-type (hole transport) material and so generally is used with gold electrodes. The structure of pentacene is shown in **Figure 21**.

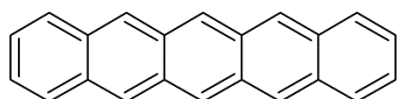


Figure 21. The chemical structure of pentacene.

1.2.2.1.2 *N,N'-bis (n-octyl)- dicyanoperylene-3,4:9,10-bis(dicarboximide)* (PDI8-CN₂)

N,N'-bis (n-octyl)- dicyanoperylene-3,4:9,10-bis(dicarboximide) (PDI8-CN₂) is a fairly modern synthetic development and one of the few high-performance n-type semiconductors used in OFETs. It is capable of producing devices with mobilities in the $0.1\text{cm}^2\text{V}^{-1}\text{s}^{-1}$ range and the crystal structure has been investigated by Rivnay *et al.*^[37] PDI8-CN₂ is soluble in a few

organic solvents so it can be solution processed to create thin films for use in OFETs. PDI8-CN₂ is unusual for an n-type in that its LUMO level is positioned at an energy low enough (4.3eV) to allow charge carries to be injected efficiently from gold electrodes. The structure of PDI8-CN₂ is shown in **Figure 22**.

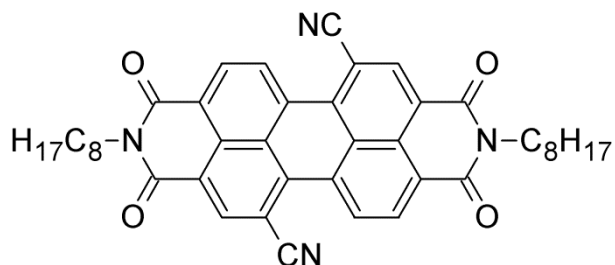


Figure 22. The chemical structure of PDI8-CN₂ (*N,N'*-bis (*n*-octyl)- dicyanoperylene-3,4:9,10-bis(dicarboximide)).

1.2.2.1.3 5,6,11,12-Tetraphenylnaphthacene (Rubrene)

5,6,11,12-Tetraphenylnaphthacene (Rubrene) is a p-type organic semiconductor, it is generally used in the form of a single crystal when in an OFET device as it is capable of reaching mobilities of 20-40cm²V⁻¹s⁻¹.^[38] The problem with using rubrene in the form of a single crystal is in the difficulty of growing the crystal on the device substrate in the position where it is needed or manipulating it into the afore mentioned position without causing damage to the crystal. The structure of rubrene is shown in **Figure 23**.

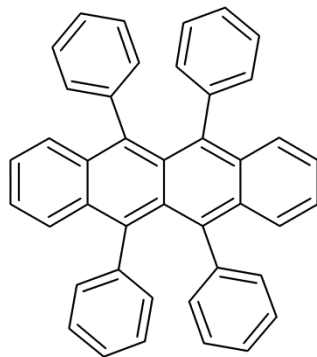


Figure 23. The chemical structure of Rubrene (5,6,11,12-Tetraphenylnaphthacene).

1.2.2.1.4 Buckminsterfullerene (C₆₀)

Buckminsterfullerene (C₆₀) is a material composed entirely of carbon in a spherical arrangement made up of hexagonal and pentagonal rings, with sp₂ hybridised carbon

throughout; first reported in 1985.^[39] C₆₀ is an n-type organic semiconductor and has been used in many OFET and organic photovoltaic (OPV) devices alongside a p-type organic semiconductor.^[40] The major problem with C₆₀ is its lack of air-stability, meaning devices need to be encapsulated to improve their lifetimes. The structure of C₆₀ is shown in **Figure 24**.

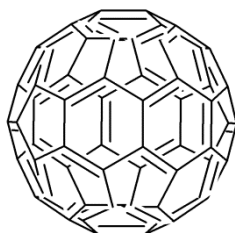


Figure 24. The chemical structure of C₆₀ (Buckminsterfullerene).

1.2.2.1.5 [6,6]-Phenyl-C₆₁-butyric acid methyl ester (C₆₀ PCBM)

[6,6]-Phenyl-C₆₁-butyric acid methyl ester (C₆₀ PCBM) is a C₆₀ derivative that is very widely used as the n-type organic semiconductor in OPV devices in conjunction with p-types such as P3HT.^[41] Again, like C₆₀, air stability is an issue with C₆₀ PCBM, so encapsulation is needed. The chemical structure of C₆₀ PCBM can be seen in **Figure 25** below.

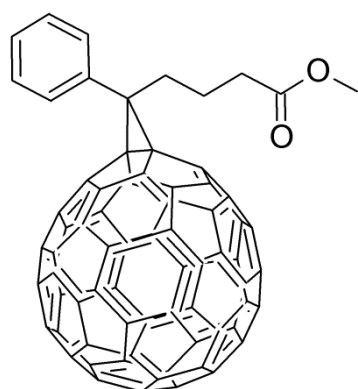


Figure 25. The chemical structure of C₆₀ PCBM ([6,6]-Phenyl-C₆₁-butyric acid methyl ester)

1.2.2.1.6 6,13-Bis(triisopropylsilylithynyl)pentacene (TIPS-pentacene)

6,13-Bis(triisopropylsilylithynyl)pentacene (TIPS-pentacene) is a solution to the problem of the insolubility of pentacene; by adding the two sidechains to the standard pentacene structure, the molecule has been made soluble. The consequence of the sidechains though is an increase in the difficulty of getting the molecules to stack into a highly ordered

structure, however, efforts have been made to discover methods to improve the stacking of TIPS-pentacene and therefore the mobility, achieving values of $4.6\text{cm}^2\text{V}^{-1}\text{s}^{-1}$.^[42] The structure of TIPS-pentacene is shown in **Figure 26**.

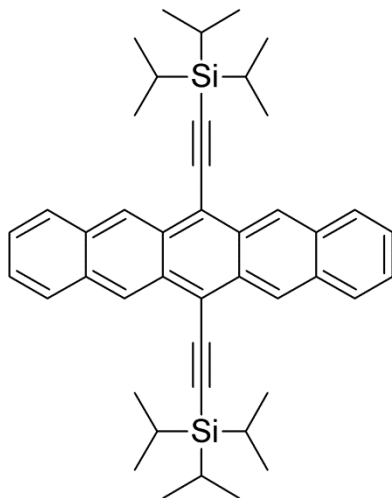


Figure 26. The chemical structure of TIPS-pentacene (6,13-Bis(triisopropylsilyl)pentacene).

1.2.2.2 Semiconducting Polymers and Oligomers

In addition to the low molecular weight materials mentioned above there are also certain polymeric materials that act as semiconductors. Unlike in the smaller molecules, polymers can possess a large conjugation length allowing charge carriers to travel relatively long distances along single molecules before needing to “hop” to the next molecule. Due to the low volatility of the high molecular weight polymers, evaporation is generally impossible without damage occurring to the polymer structure, so solution based deposition methods have to be used.

1.2.2.1 Poly(3-hexylthiophene-2,5-diyl) (P3HT)

P3HT is one of the most widely known and used semiconducting polymers.^[34, 43, 44] It has a backbone of conjugated thiophene molecules each with an attached hexyl side-chain (see **Figure 27**). The regioregular varieties of P3HT have a well defined arrangement of the hexane side groups, so can be made to stack together fairly efficiently. Through manipulation of the molecular orientation using different self-assembled monolayer (SAM) surfaces, Kim *et al* have achieved mobilities of up to $0.28\text{cm}^2\text{V}^{-1}\text{s}^{-1}$ in a bottom gate transistor architecture.^[45]

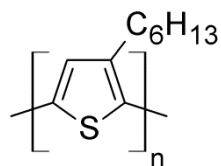


Figure 27. The chemical structure of P3HT (Poly(3-hexylthiophene-2,5-diyl)).

1.2.2.2.2 Poly(2,5-bis(3-hexadecylthiophen-2-yl)thieno[3,2-b]thiophene) (pBTTT)

Poly(2,5-bis(3-hexadecylthiophen-2-yl)thieno[3,2-b]thiophene) (pBTTT) is a p-type semiconducting polymer with a similar structure to that of P3HT but with some of the thiophene rings along its backbone fused together (see **Figure 28**). The addition of the fused thiophene rings into pBTTT has the effect of making it significantly more air-stable than P3HT, which makes it an attractive material for all manner of organic electronic devices, however, the loss of sidechains has made pBTTT less soluble than P3HT.^[46]

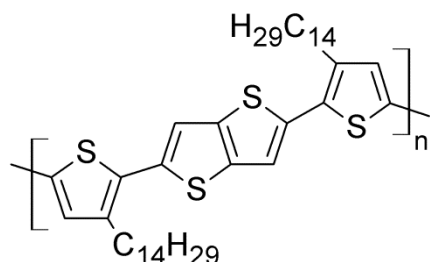


Figure 28. The chemical structure of pBTTT (Poly(2,5-bis(3-hexadecylthiophen-2-yl)thieno[3,2-b]thiophene))

1.2.2.2.3 Poly[[N,N9-bis(2-octyldodecyl)-naphthalene-1,4,5,8-bis(dicarboximide)-2,6-diyl]-alt-5,59-(2,29-bithiophene)] (P(NDI2OD-T2))

Like the PDI8-CN₂ discussed previously, poly[[N,N9-bis(2-octyldodecyl)-naphthalene-1,4,5,8-bis(dicarboximide)-2,6-diyl]-alt-5,59-(2,29-bithiophene)] (P(NDI2OD-T2)) is an n-type organic semiconductor with a LUMO level at an energy (4.0eV) that will allow electrons to be injected efficiently from gold electrodes. P(NDI2OD-T2) is highly soluble too and has been shown to produce electron mobilities up to 0.85cm²V⁻¹s⁻¹ in OFET devices.^[47] The structure of P(NDI2OD-T2) is shown in **Figure 29**.

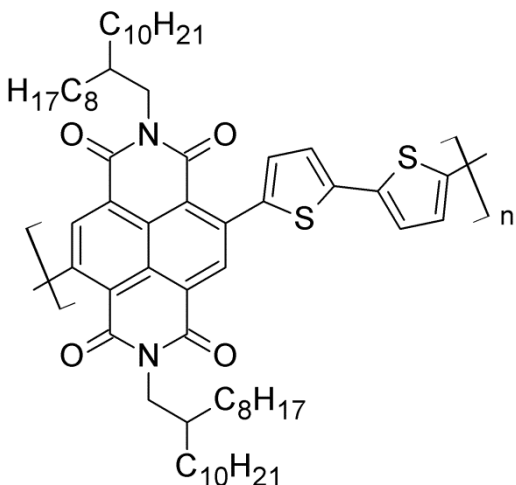


Figure 29. The chemical structure of P(NDI2OD-T2) (Poly[[N,N9-bis(2-octyldodecyl)-naphthalene-1,4,5,8-bis(dicarboximide)-2,6-diyl]-alt-5,59-(2,29-bithiophene)]].

1.2.2.3 Synthetic Metals

The synthetic metal group of materials are of great interest to flexible electronics as they generally start out as flexible polymers that are very highly doped in some way to give them metal-like conductivity, the best conductivities achieved are on-par with conventional metals. To be called a metal (synthetic or otherwise) a material should have a positive temperature coefficient, i.e. its resistance must increase as temperature increases, and it should still show some electrical conduction as its temperature approaches zero Kelvin. The polymers that still conduct as T tends to zero Kelvin have delocalised electronic states at the Fermi level and therefore do not need thermal activation energy to allow conduction to take place.^[48] Some highly doped polymers (conductive polymers) only show a metallic positive temperature coefficient at higher temperatures (i.e. above room temperature), switching to non-metallic behaviour at lower temperatures and so showing a negative temperature coefficient (increasing resistance with decreasing temperature).^[48]

A good example of a synthetic metal is PEDOT:PSS;^[49] PEDOT (poly(3,4-ethylenedioxythiophene)) alone is insoluble, but if it is created in aqueous solution in the presence of PSS (poly(styrene sulfonic acid)) the complex PEDOT:PSS is formed, which forms a dispersion in water and acts as a synthetic metal when deposited. Another example of a synthetic metal is polyaniline (PANI), the conductivity of this polymer material can be varied by changing the degree of oxidation of the polymer chains in solution prior to deposition; the degree of oxidation is generally controlled by the pH of the solution, so adding a strong

acid will highly oxidise PANI and make it very conductive, while adding a strong base will highly reduce it, turning it into a semiconductor.^[50]

1.2.2.4 Core Shell Nano-Particles

Core shell nano-particles have been used in a wide variety of applications in the fields of biomedical science as well as physical chemistry, such as targeted drug delivery and sensor applications.^[51] Core shell nano-particles are nano-scale clusters of a given element or compound (generally a metal) coated in an organic ligand (see **Figure 30**). The conduction properties of core shell nano-particles have been investigated by several groups in the past, as have their sensing properties.^[52] The electrical conduction in core shell nano-particle films is generally described via quantum mechanical tunnelling and thermally activated hopping transport,^[6] the conductance scales as in **Equation 14**. The dominant process is dependent on the inter-core separation.^[6, 53]

Equation 14. $\sigma \propto e^{-2\delta\beta} e^{-E_c/kT}$

where δ is the separation of adjacent cores, β is the quantum mechanical tunnelling factor and E_c is an activation energy.

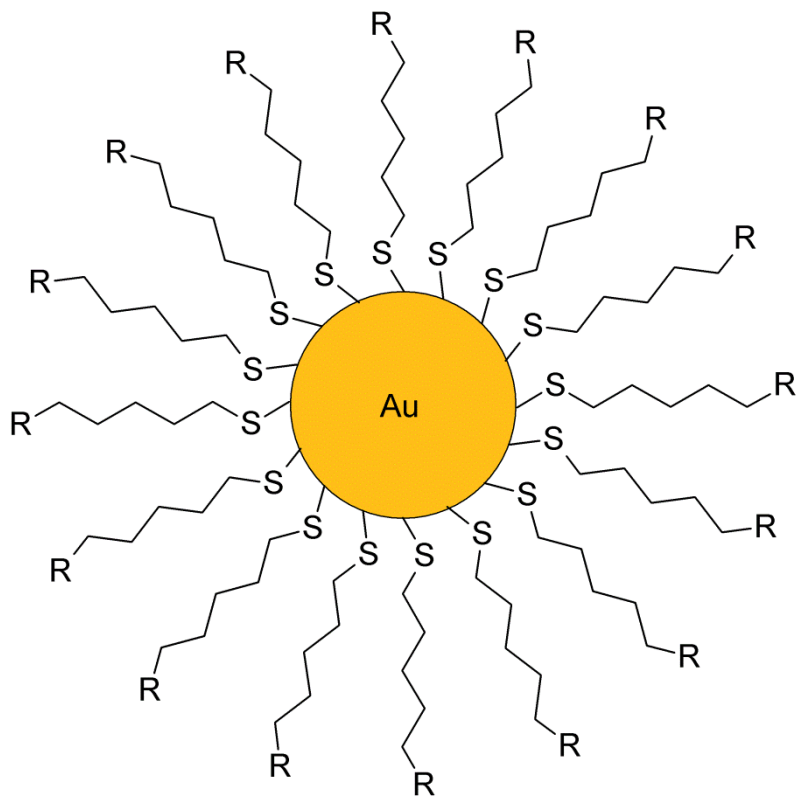


Figure 30. The chemical structure of a thiol coated Au core-shell nano-particle.

1.2.3 Macrocycles

1.2.3.1 Porphyrins

The basic structure of the porphyrin group is shown in **Figure 31**. It can be seen that it is in essence two pyridine and two pyrrole rings alternately positioned in a cyclic structure and bound together by a single carbon atom single bonded to one ring and double bonded to the other. Beyond the basic porphyrin ring, the structure of porphyrin molecules can be diverse due to the huge number of possible side groups that can be attached to the porphine ring and the possibility of complexing a metallic atom in the centre of the ring. The two hydrogen atoms in the central cavity are substituted for the desired metal atom (the chemistry of the process will not be discussed here), any metal with an oxidation state greater than +1 can be used, however, the ones in an oxidation state higher than +2 will have ligands to “use up” their remaining charge and valency. The Porphyrins are a class of aromatic heterocyclic compounds that occur naturally in living organisms, the most notable example of which is the organometallic compound haem. Haem is an iron-porphyrin complex which plays a role in the transport of oxygen in the blood.

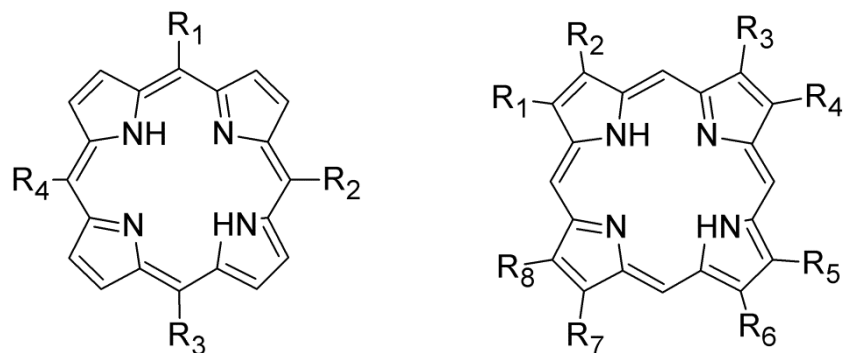


Figure 31. The chemical structure of the basic porphyrin ring, showing two possible R-group configurations.

The porphyrins, due to the versatile nature of their structure, have been used extensively as sensing materials, particularly in optical sensing systems due to their absorption within the visible spectrum, caused by the high degree of π -electron conjugation.^[8, 54] Some research groups have even reported success in using porphyrins as the organic semiconductor in organic field effect transistors, due in no small part to the high degree of conjugation in their structure (see section 1.1).^[55]

1.2.3.2 Phthalocyanines

Another group of materials with similar structures to the porphyrins are the phthalocyanines. The basic phthalocyanine has 4 more nitrogen atoms than the porphyrin, used in the place of the carbon atom to join together the rings, and it has a benzene ring bonded to each of pyrrole rings at the side opposite to the nitrogen atom. The structure of the phthalocyanine molecule is shown in **Figure 32**.

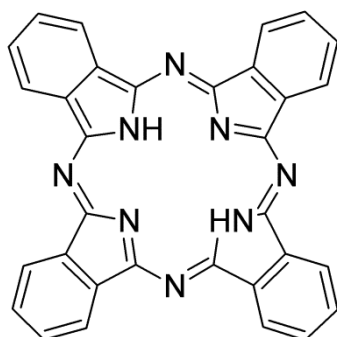
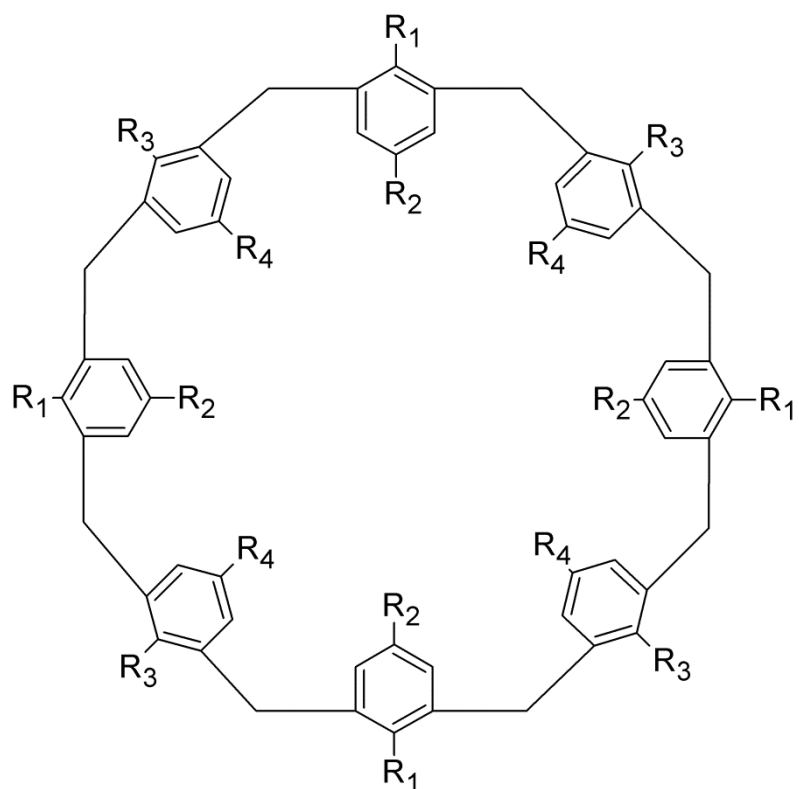


Figure 32. The chemical structure of phthalocyanine.

Like porphyrins the phthalocyanines can be substituted with a metallic atom at their central ring position to create an organometallic compound. They can also be modified by attaching side groups to the basic molecule. Phthalocyanines have been used successfully as organic semiconductors^[56] and have also been used as the active materials in optical sensors.^[57]

1.2.3.3 Calixarenes

The calixarenes are a group of materials that are bowl-shaped with a central cavity as indicated by the Latin meaning of the word *calix* being chalice or cup. Calixarenes are macrocyclic compounds consisting of a number of units bound together in a ring with a -CH₂ between each unit. Each unit is made up of benzene ring with an oxygen atom and an R-group that will form the “lower rim” of the molecule and an R-group opposite this which will form the “upper rim”. The number of units in a calixarene molecule can vary from 4 to commonly 8 or 10, but can be even larger depending on the application. The generic structure of calixarenes is shown in **Figure 33**.



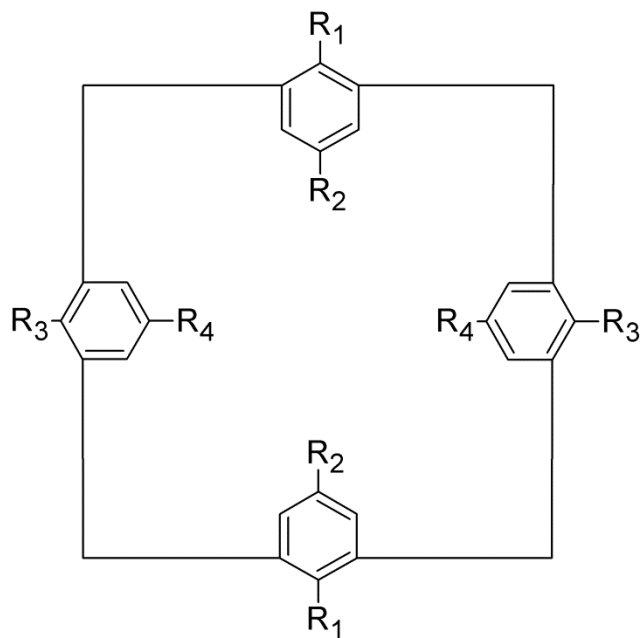


Figure 33. The chemical structures of a generic 8- (top) and a 4-member ring calixarene (bottom).

As with porphyrins and phthalocyanines (see sections 1.2.3.1 and 1.2.3.2), it is possible to complex a metal core into the cavity of a calixarene, however, the situation is more complex than that of complexing a porphyrin or phthalocyanine due to the differences in structure between calixarene molecules. Firstly the calixarene cavity must be large enough to accommodate the cation and the groups attached to the benzene rings of the calixarene's backbone must be long and flexible enough to reach the cation and bind to it in positions dictated by the VSEPR theory discussed in section 1.2.1.1. There must also be enough electron donating groups present to balance the charge and coordination requirements of the cation.^[58]

1.2.4 Organic Reactions and Interactions

1.2.4.1 A Basic Primer on Chemical Reaction Conditions and Mechanisms

From the simplest acid-base reaction to the most complex synthesis step, chemical reactions all have common requirements that allow them to take place. Firstly for two molecules to react with each other they must collide with each other, but they must collide with the correct orientation and sufficient energy for the reaction to take place. Chemical reactions are often only able to occur between two very specific parts of the molecules

involved. This means that these groups must collide directly with each other; the probability of this collision occurring is often increased by charges or dipoles within molecules which will be discussed later. The energy required for a chemical reaction to take place is usually referred to as the activation energy. Chemical bonds require the input of energy to break and allow new bonds to be formed. The stronger the bond, the more energy it will take to break it; this means that the directional σ -bonds require more energy to break than the de-localised π -bonds. Extra energy can be introduced into the system kinetically (through mixing) or thermally (through heating); the molecules in the reaction vessel will have a Boltzmann distribution of energies. Sometimes desirable reactions are very energetically unfavourable. This is where catalysis comes in – the introduction of a catalyst into a chemical reaction allows an alternate, lower activation energy reaction pathway to be taken, the new pathway generally involving the bonding of one or both of the reactants first to a catalyst then to each other. A catalyst is never “used up” in a chemical reaction and should be completely separated from the reaction product when the reaction is complete.

Purely under the influence of thermally induced motion, molecules will move randomly when in a fluid state. This is not an ideal situation when collisions between reactants are required to occur between specific sites on the reactant molecules. In reality the motion of molecules is influenced by electrostatic attraction and repulsion. When considering the distribution of charge within a molecule one must consider the electronegativity of the atoms within the molecule. Electronegativity is a measure of the ability of an atom to attract the electrons in a bond towards itself, skewing the probability distribution of electron positions in its favour. The effect of having varying electronegativities within a molecule is that dipoles are induced, thus giving some atoms a slight positive charge and some a slight negative charge. Along with true charges and lone electron pairs the dipoles help to attract potential reactants with a greater force (therefore greater kinetic energy) to the correct reactive sites.

It should be noted at this point that *all* chemical reactions are at their simplest level a flow of electrons. Most organic reactions are polar in nature and so involve both an electrophile (electron acceptor) and a nucleophile (electron donor). Now will be discussed some of the types of bonding relevant to this work.

Firstly when a bond is formed, charge can be transferred from one molecule or atom to another creating two oppositely charged species; this is ionic bonding. Ionic bonding is sometimes described as an extreme case of covalent bonding, wherein a pair of electrons (one coming from each of the bonding atoms or molecules) is shared between atoms or molecules. Another extreme of covalent bonding occurs when both of the electrons in the bond come from one of the bonding atoms or molecules; this is a dative (or coordinate) bond. Compounds that donate electron pairs are known as Lewis bases and compounds that accept electron pairs are called Lewis acids (discussed earlier in section 1.2.1.4). In some cases when a reaction takes place the reactants may be mutually oxidised and reduced; this is known as a redox reaction. Oxidation is the act of loosing electrons and increasing the oxidation state of an atom or molecule (this could be through, but not limited to, gaining an oxygen atom or losing a hydrogen), while reduction is the act of gaining electrons (which can be by losing oxygen or gaining hydrogen) thus decreasing the oxidation state.

1.2.4.2 Van der Waals Interactions

The term Van der Waals interaction is a blanket term encompassing a variety of different permanent and induced dipole interactions that occur at the molecular level. Three main types of dipole interactions can be observed, these are dipole – dipole interactions, dipole – induced-dipole interactions and induced-dipole – induced-dipole interactions. The dipole – dipole (or Keesom) interactions occur between molecules that have permanent dipoles built in to their structures, generally through the presence of electronegative or electropositive (electron withdrawing or electron donating) groups or atoms that create an anisotropic distribution of the “electron cloud” of the molecule. Through the physics of electromagnetism fixed parallel dipoles in a solid have an interaction potential energy that falls away as r^{-3} , while completely freely rotating dipoles in a fluid have zero net interaction potential energy. However in real liquids and gases molecular dipoles do not experience completely free rotation as mutual orientations that minimise energy are favoured giving the dipoles a net average interaction potential energy. The average potential of the interaction between two dipoles is described by **Equation 15**.

Equation 15.

$$\langle V \rangle = \frac{-2\mu_1^2 \mu_2^2}{3(4\pi\epsilon_0)^2 kT} \cdot \frac{1}{r^6}$$

where μ_n is the dipole moment of each of the interacting dipoles ($\mu = q \cdot d$) and r is the molecular separation.

It can be seen from **Equation 15** that the average interaction potential energy falls off as r^{-6} rather than the r^{-3} observed in interactions between a fixed dipole and a point charge.

The dipole – induced-dipole (or Debye) interaction occurs when the permanent dipole of one molecule causes a redistribution of the electron cloud on a neighbouring polarisable molecule. Once induced, the new dipole will then interact with the permanent dipole in a similar way to a second permanent dipole; the interaction is described by **Equation 16**.

Equation 16.

$$\langle V \rangle = \frac{-\mu_1^2 \alpha'_2}{4\pi\epsilon_0} \cdot \frac{1}{r^6}$$

where μ is the dipole moment of the permanent dipole and α' is the polarisability volume of the molecule with the induced dipole.

Finally the induced-dipole – induced-dipole (or London/dispersion) interaction allows two non-polar polarisable molecules to interact with each-other. Instantaneous dipoles arise in molecules due to the natural fluctuations in the electron clouds of the molecules. The net dipole moment created by these fluctuations in one molecule can induce a dipole on a neighbouring molecule. Two induced dipoles can then interact with each other, an approximation of the interaction potential energy being given by **Equation 17**.

Equation 17.

$$V = \frac{-3\alpha'_1 \alpha'_2 I_1 I_2}{2(I_1 + I_2)} \cdot \frac{1}{r^6}$$

where I_n are the ionisation energies of the two interacting molecules and α'_n are the polarisability volumes of the molecules.

It can be seen from **Equation 17** that the interaction potential energy is very dependent on the polarisability of both of the molecules, as the creation of large dipole moments requires loosely bound movable electrons.

1.2.4.3 Hydrogen Bonding Interactions

Hydrogen bonding is a very specialised type of bonding in that it can only occur if a specific set of conditions are met. For hydrogen bonding to occur between two molecules then one molecule must have a hydrogen atom bonded to a highly electronegative atom, the other molecule must also have a highly electronegative atom with a lone pair. Hydrogen bonding can be thought of in two ways; firstly, the attraction between the partial positive and negative charges of the hydrogen atom and lone-pair-possessing electronegative atom respectively; alternately the bonding can be considered by the formation of delocalised molecular orbitals over the three atoms involved, each supplying one atomic orbital to create the molecular ones: one bonding, one anti-bonding and one non-bonding. Hydrogen bonding is stronger than the Van der Waals interactions but is weaker than true atomic covalent bonds. An example of this is the O-H covalent bond in water, which has a strength of $\sim 492.21\text{ kJ}\cdot\text{mol}^{-1}$ ($\sim 5.12\text{ eV}$ per bond),^[59] while the O-H->O hydrogen bond has a strength of $\sim 23\text{ kJ}\cdot\text{mol}^{-1}$ ($\sim 0.24\text{ eV}$ per bond).^[60] The ability to form hydrogen bonds with a solute can also help a solvent to become more effective at dissolving the solute.

1.3 Organic Field-Effect Transistors

When discussing transistors in an inorganic context, there are two main categories of device: bipolar junction transistors (BJTs) and field-effect transistors (FETs); while in an organic context there is only the organic field-effect transistor (OFET), also known as the organic thin film transistor (OTFT).

The BJT is made up of alternately n-p-n doped or p-n-p doped semiconductor, the three connections (base, collector and emitter) are attached to the semiconductor as in **Figure 34**.

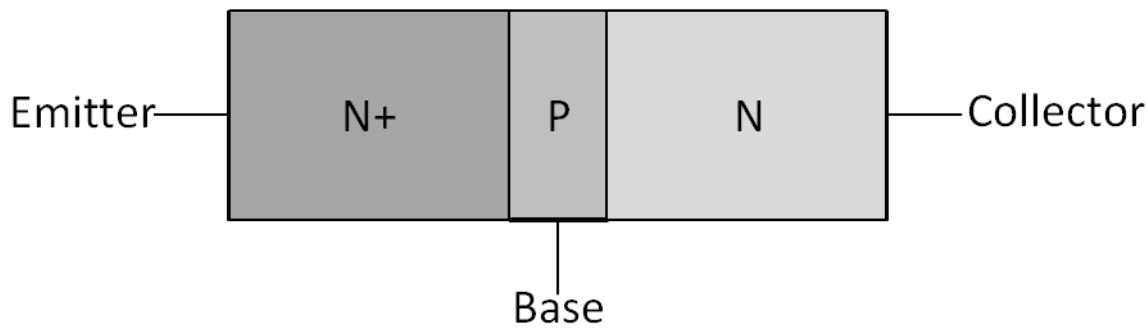


Figure 34. A schematic diagram of an n-p-n type bipolar junction transistor

In the case of an n-p-n device, the emitter (connected to heavily n-doped semiconductor) is biased to a higher potential than the base (connected to the p-doped semiconductor), which in turn is biased to a higher potential than the collector (connected to n-doped semiconductor); this causes a net flow of charge carriers from the high concentration in the heavily doped material to the lower concentration at the collector, as the application of the potential to the base region allows thermally activated diffusion of carriers through the p-doped region through which net transit would usually be discouraged by the in-built potential of the junction.

The OFET device is a unipolar (only transports one type of carrier) device made from undoped organic semiconductor and has three electrical connections known as the source, drain and gate (see **Figure 35** and **Figure 36**).

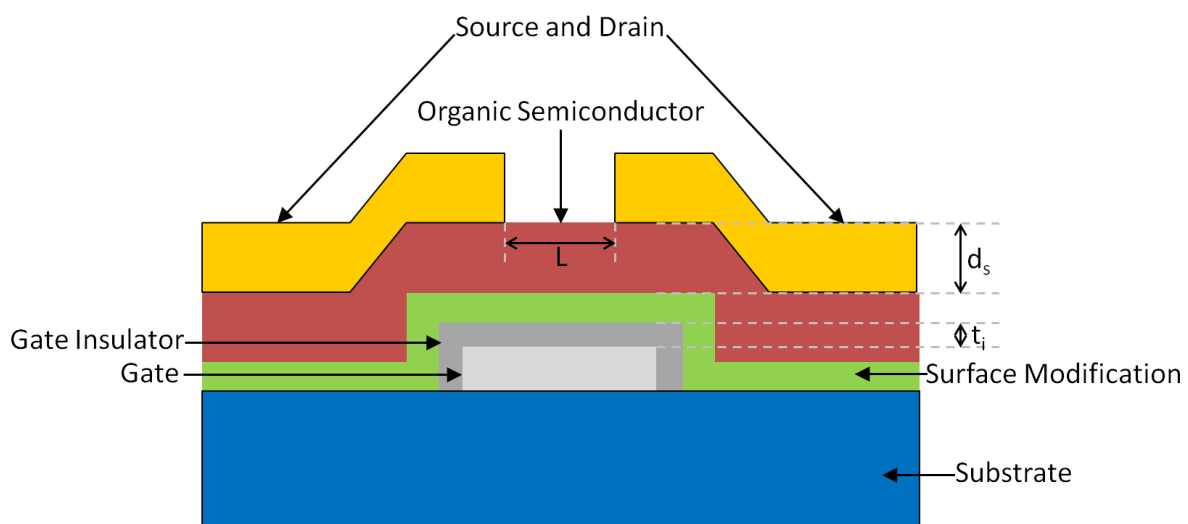


Figure 35. A cross-sectional diagram of an organic field-effect transistor.

When charge carriers are injected from the source and begin to travel across the “channel” of the device to the drain, where they exit the device, the device is said to be ‘on’. The gate is used to moderate the conductivity of the OFET through the creation of a highly conductive region of high carrier density known as the accumulation layer (this is discussed further in section 1.3.2), the charge accumulated in the channel can be calculated from the equation $Q=C\cdot V$, where Q is the charge, C is the capacitance of the gate dielectric and V is the potential difference between the source and gate electrodes. The gate (ideally) interacts with the device purely through the E-field it generates due to the applied “gate voltage” and does not allow current to pass in or out of the gate electrode. To achieve this, the gate electrode must be insulated from the organic semiconductor bulk. The OFET has many parameters which effect its current-voltage characteristics, the most important being the charge carrier mobility (μ) (discussed in section 1.1.2.1) and the threshold voltage (V_T). Threshold voltage will be discussed in detail in section 1.3.2, here it will just be said that the threshold voltage is the minimum gate voltage required to “switch on” an OFET. It should be noted at this point that the OFETs described here are the so-called “enhancement type” where the transistors are normally off and need to be switched on; another type of OFET is the “depletion type” which is normally on and the action of the gate is to switch it off – this type will not be discussed.

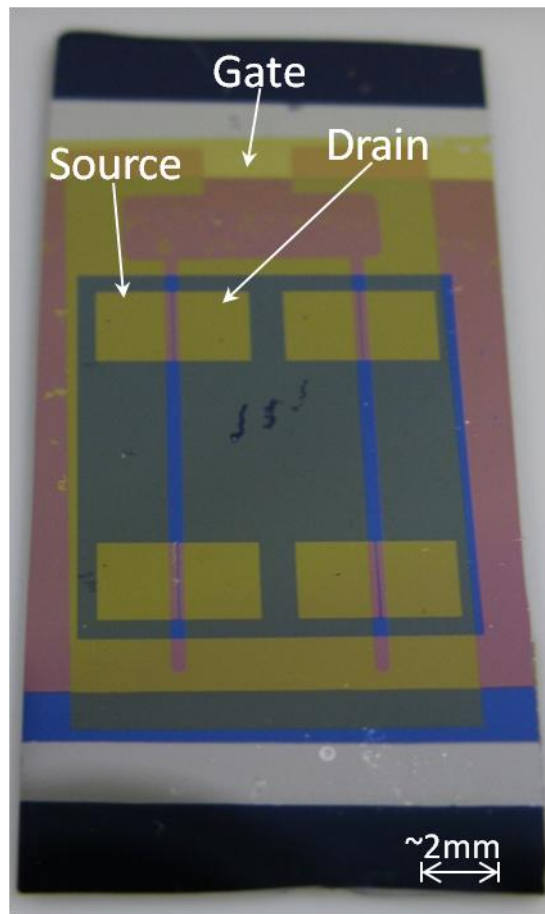


Figure 36. A photograph of a real pentacene OFET.

All of the organic transistors tend to be field-effect rather than bipolar junction for a variety of reasons; the first being the selective doping of small regions of semiconductor needed for BJTs, while fairly simple to do when working with inorganic semiconductors (introducing the dopant impurities whilst depositing the semiconductor by a method such as molecular beam epitaxy), this is very difficult in organic semiconductors, which are commonly processed from solution. Perhaps the most important reason, however, is that the vast majority of organic semiconductors (as mentioned previously in section 1.1.1) tend to be incapable of transporting more than one type of charge carrier, making them unsuitable as BJT materials.

1.3.1 Structure and Construction of an Organic Field-Effect Transistor

When creating OFETs the device design is very important to consider, small differences in device architecture and processing conditions can lead to huge differences in device performance. Here will be outlined many of the design considerations associated with OFETs and some of the solutions adopted by many research groups.

1.3.1.1 Standard Electrode Structures

The first major design consideration is the positioning of the three electrodes of the OFET, in every transistor the source and drain electrodes lie in the same plane and the gate must be positioned to cover *all* of the semiconductor channel. There are four main architectures used in OFET devices (see **Figure 37**); two of the architectures are “co-planar electrode” structures with the source, drain and gate electrodes on the same side of the semiconductor; two of the architectures are “staggered electrode” structures with the gate on the opposite side of the semiconductor to the source and drain.

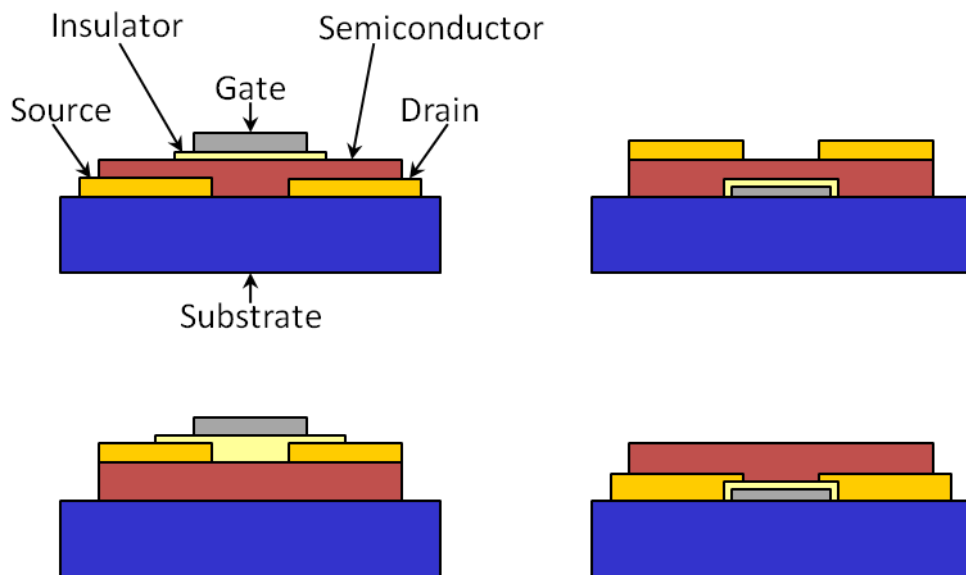


Figure 37. Cross-sectional diagrams of the four possible OFET electrode structures (top: staggered electrode structures, bottom: coplanar electrode structures).

Studies have been carried out previously into the effect of having top or bottom contacts,^[61] but ultimately it is the materials used in the construction of the device and the application of the device that will be the deciding factors in the architecture. Factors as simple as solution processed organic semiconductors not wetting certain electrode metals or gate insulators can influence the structure, as can the deposition or growth methods for the

various layers of the OFET e.g. if the gate insulator is grown through the anodisation technique (see section 2.3) then only a bottom gate architecture is possible.

1.3.1.2 Substrate Material and Electrode Adhesion Promotion

When choosing a substrate material for the OFET the intended OFET application must first be considered, for flexible electronics a plastic substrate (such as polyethylene terephthalate (PET) or polyethylene napthalate (PEN)^[62]) can be used, while other applications may call for a more rigid substrate such as glass or silicon oxide (SiO_2).

In cases where the electrode material has poor adhesion on the substrate, some surface preparation may be required beyond a standard chemical cleaning procedure (see section 2.1.1) to enhance adhesion, this can be done through a variety of methods, the most commonly used being oxygen plasma or UV-Ozone treatments (see section 2.1.2).

Electrode adhesion layers are sometimes required for devices where the electrode material has poor adhesion on the substrate (despite surface preparation), gate insulator or semiconductor material to prevent electrode de-lamination during use. A commonly quoted example is that of chromium as an adhesion layer for gold electrodes on SiO_2 surfaces; however, some environments and some applications require more robust, inert materials as adhesion layers.^[63]

1.3.1.3 Gate Contact and Gate Insulation

The main requirement of a gate contact material is to be conductive and the flat-band voltage (see section 1.3.2) does depend on its work function, but beyond that the choice of material depends on the desired deposition method and if it is capable of being anodised (see section 2.3), if an oxide insulator is to be grown on the surface via this method.

The choice of the gate insulator (dielectric) material in an OFET device is very important as it has an effect on many of the OFETs main conduction parameters; from **Equation 21** it can be seen that the saturated drain current is proportional to the capacitance per unit area of the gate insulator (C_i). From **Equation 22** and **Figure 42** it can be seen that as the capacitance of the gate insulator increases the range of gate voltages over which the device changes from off to on decreases, i.e. the switch between off and on becomes more definite

and less gradual; the magnitude of the threshold voltage also tends to decrease as C_i increases due to a greater charge density being accumulated at the semiconductor insulator interface for any given gate voltage at higher C_i . It is therefore obvious that the highest possible value of C_i is desirable in a gate insulator. From the classical description of the capacitance of a dielectric (**Equation 18**) it can be seen that for high capacitance, thin gate insulator layers made from materials with high dielectric constants (ϵ_r) are needed.

$$C = \epsilon_r \epsilon_0 \frac{A}{d}$$

Equation 18.

$$\Rightarrow C_i = \frac{\epsilon_r \epsilon_0}{t_i}$$

where t_i is the insulator thickness.

To minimise gate leakage current the gate insulator layer, whilst being required to be thin, must be free of pinholes (small holes through which current can leak).

There have been numerous research projects dedicated to finding new and improved gate insulator materials that meet the requirements outlined above in both the organic and inorganic FET areas. The materials with the highest ϵ_r values tend to be inorganic oxides, most notably those of aluminium, titanium and tantalum; the disadvantages of such materials in OFETs is that they are not flexible, limiting the choice of substrate, and tend to have high charge carrier trap density on their surfaces. The high trap density is thought to be due to the localised dipoles generated by the surface -OH (hydroxyl) groups present on metal oxides;^[16] it is usual, therefore, to have a self-assembled monolayer (SAM) as a buffer layer between the gate insulator and the organic semiconductor (see section 1.3.1.4).

Towards the creation of flexible electronics, polymeric dielectrics have been discovered. Polymers such as polyvinyl alcohol (PVA), polymethylmethacrylate (PMMA) and polyvinylphenol (PVP) are commonly used.^[64] However, flexible and solution-processable polymer dielectrics tend to have much smaller ϵ_r values and form much thicker layers than metal oxides, leading to much smaller capacitances.

There has recently been success in improving the performance of PVP by cross-linking it with dianhydrides^[65] and improving the performance of PMMA by cross-linking it with a molecule containing two trichloro-silane groups^[66]. The cross-linked polymers, while having

approximately the same ϵ_r values as before cross-linking, can be spun much thinner than their non-cross-linked counterparts (10s of nm rather than 100s) and still not contain pin-holes in the resulting films, leading to much higher capacitances (by **Equation 18**). **Table 1** gives the ϵ_r and typical C_i values for some common gate insulators.

Insulator	ϵ_r	Typical Thickness (nm)	C_i (nF·cm ⁻²)
SiO ₂	3.9	300	11.5
TiO ₂	80.0	8	8850
Al ₂ O ₃	9.0	4.8	1660
Ta ₂ O ₅	26.0	5	4600
PVA	10.0	500	17.7
PMMA	3.5	160	19.4
PVP	6.4	450	12.6
C-PMMA	3.5	30	103.3
C-PVP	6.4	22	165

Table 1. Properties of some Common Gate Insulators, C_i values have been measured for the thicknesses indicated.^[64-66]

It should be noted at this point that as the oxide insulator materials become very thin films, ϵ_r changes,^[67] therefore the values of ϵ_r given in the table are bulk values and the values of both ϵ_r and C_i may deviate from the stated values at low thicknesses.

1.3.1.3.1 Water-Gated Organic Field-Effect Transistors and the Electric Double Layer

As an alternative to using gate insulators such as oxides and polymers, an OFET can also be electrolyte-gated;^[68, 69] here will be discussed the case of OFETs using water as a gate medium. Water has been shown by others to work as a very effective gate medium;^[70] it is thought to be the action of the ultra-thin electric double layer (EDL) that allows very low threshold OFETs to be made when water is used as the gate medium, as the EDL has very high capacitance. An EDL is formed when a charged surface comes into contact with a liquid containing mobile ions, the mobile ions with a charge opposite to that of the surface are attracted to the surface and form a layer next to the surface.

The idea for electrolyte gating came from capacitors that use ionic liquids instead of a conventional dielectric material and as a result have very high capacitance (hundreds of Farads).^[71] In the field of OFET technology solid state electrolytes came first^[5], but were

superseded by liquid electrolytes in the form of ionic liquids.^[69] The problem with ionic liquids is the fact that many organic semiconductors are soluble in them.

There have been a few models proposed to describe the behaviour of EDLs and make predictions as to the structure of the double layers formed. The EDL was first described by Helmholtz in his model,^[72] which has a linearly varying potential between the charged surface and the layer of ions in solution; the ions in this model are held away from the charged surface by the water molecules which surround them, this layer of ions is known as the outer Helmholtz plane. The Helmholtz model was later modified to incorporate the effects of thermal motion on the formation of the layers of ions; this new model was called the Gouy-Chapman diffuse double layer model.^[73] In the diffuse double layer model the potential decreases exponentially away from the charged surface; but this model, like Helmholtz's, falls short of a complete description of the EDL. A better model, known as the Stern model, combines both the Helmholtz and diffuse double layer models;^[74] the Stern model proposes that the outer Helmholtz layer is formed but a further diffuse layer exists beyond it (see **Figure 38**), causing an initial linear drop in potential followed by an exponential one. More complex models than Stern have also been suggested incorporating multiple Helmholtz layers.

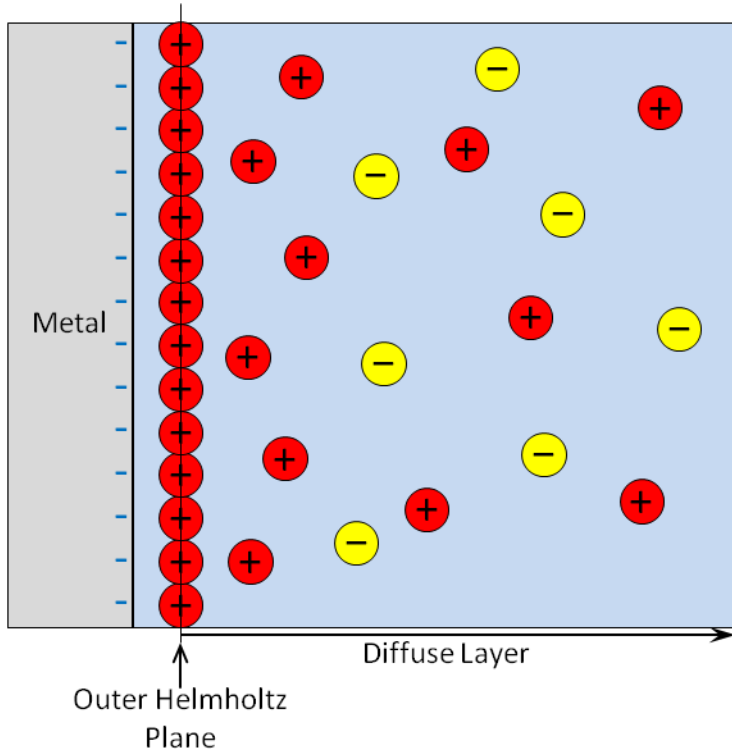


Figure 38. A graphical representation of the Stern model of the electric double layer.

The main property of interest when discussing a gate insulator for an OFET is generally the capacitance, however, the capacitance of water varies depending on its ion content. Work carried out by other research groups to measure the capacitance of low concentration NaF solutions (an additive sometimes found in tap water), has shown that the capacitance of the EDL formed in these low concentration solutions is in the range of $\mu\text{F}\cdot\text{cm}^{-2}$,^[75] comparable to the best oxide insulators at the limit of their performance (see **Table 1**). It can be seen, therefore, that even at low ion concentrations a high value of capacitance is achieved with water as the gate medium (the EDL capacitance is only weakly ion concentration dependent), this leads to devices with very low thresholds (see section 1.3.2). The behaviour at higher NaF concentrations has also been investigated.^[76] It should be noted however that the dependence of capacitance on voltage is not symmetric for positive and negative voltages.

The main problem when using water as the gate medium in an OFET is the frequency dependence of the capacitance, as demonstrated in the paper by Kergoat *et al*,^[70] the capacitance begins to rapidly decrease when varying the gate voltage at frequencies faster than tens of Hz, this suggests that the EDL cannot properly establish itself in less than a few

hundredths of a second in water. Below tens of Hz the capacitance still shows a degree of frequency dependence, albeit much less than at higher frequencies. Ionic liquids, while still showing frequency dependence, do not suffer capacitance loss as severely as water does at higher frequencies.^[69]

In the OFET architecture two EDLs would be observed one at the gate contact electrode and one at the water-semiconductor interface, an example of this is shown in **Figure 39**.

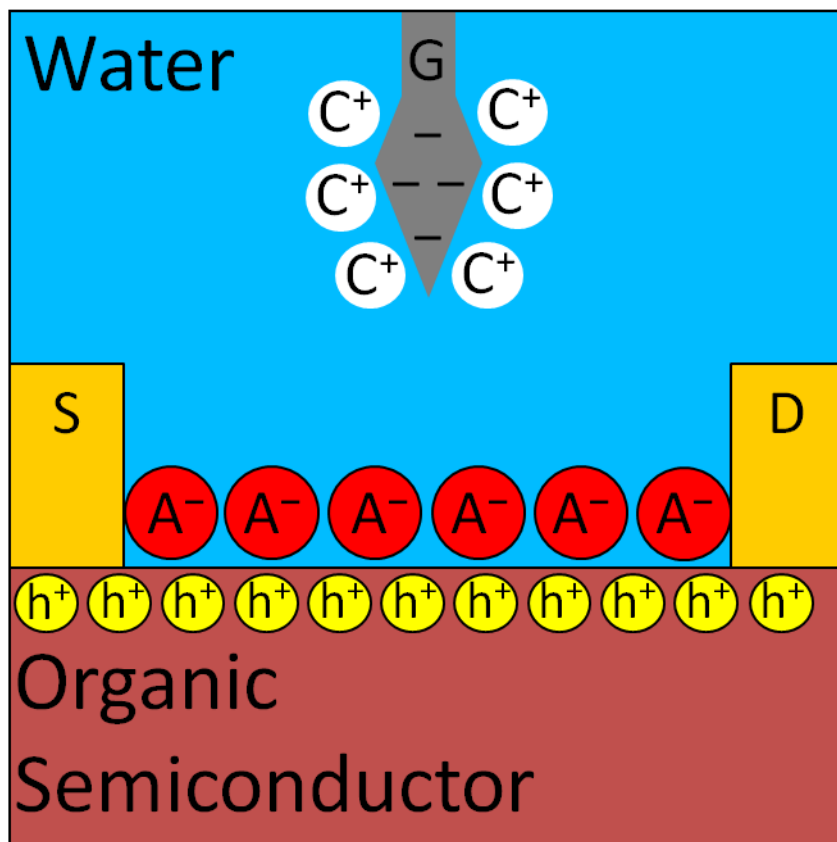


Figure 39. A schematic of the EDL formation in a water gated OFET.

1.3.1.4 Surface Modification

As mentioned previously in section 1.1.2 the surfaces of many commonly used gate insulators contain a high concentration of charge carrier trap states; it is therefore sometimes necessary to create a buffering layer. As we want the buffer layer to be thin to minimise the effect on gate capacitance, it is usual to use a self-assembled monolayer (SAM) as the buffer. SAMs are also believed to smooth the insulator surface and improve the growth of grains in crystalline semiconductors such as pentacene.^[64] When self-assembling

a monolayer a chemical reaction takes place to bond the molecules of the SAM to the insulator surface (see section 2.2.5). One of the most commonly used chemicals is octadecyltrichlorosilane (OTS) as its long, non-polar alkyl chain serves as a good buffer to the polar insulator surface. Chemicals used by researchers as buffer layers also include organophosphates^[77] and other silanes.^[78] The type of surface modification depends on the insulator surface (including which surface atoms are free for bonding) and the deposition method of surface modification depends on the hydrophobicity and surface topography required by the device; vapour phase or liquid phase self-assembly can be performed over 10s of minutes to several hours, or some materials can be spin-coated in under a minute.

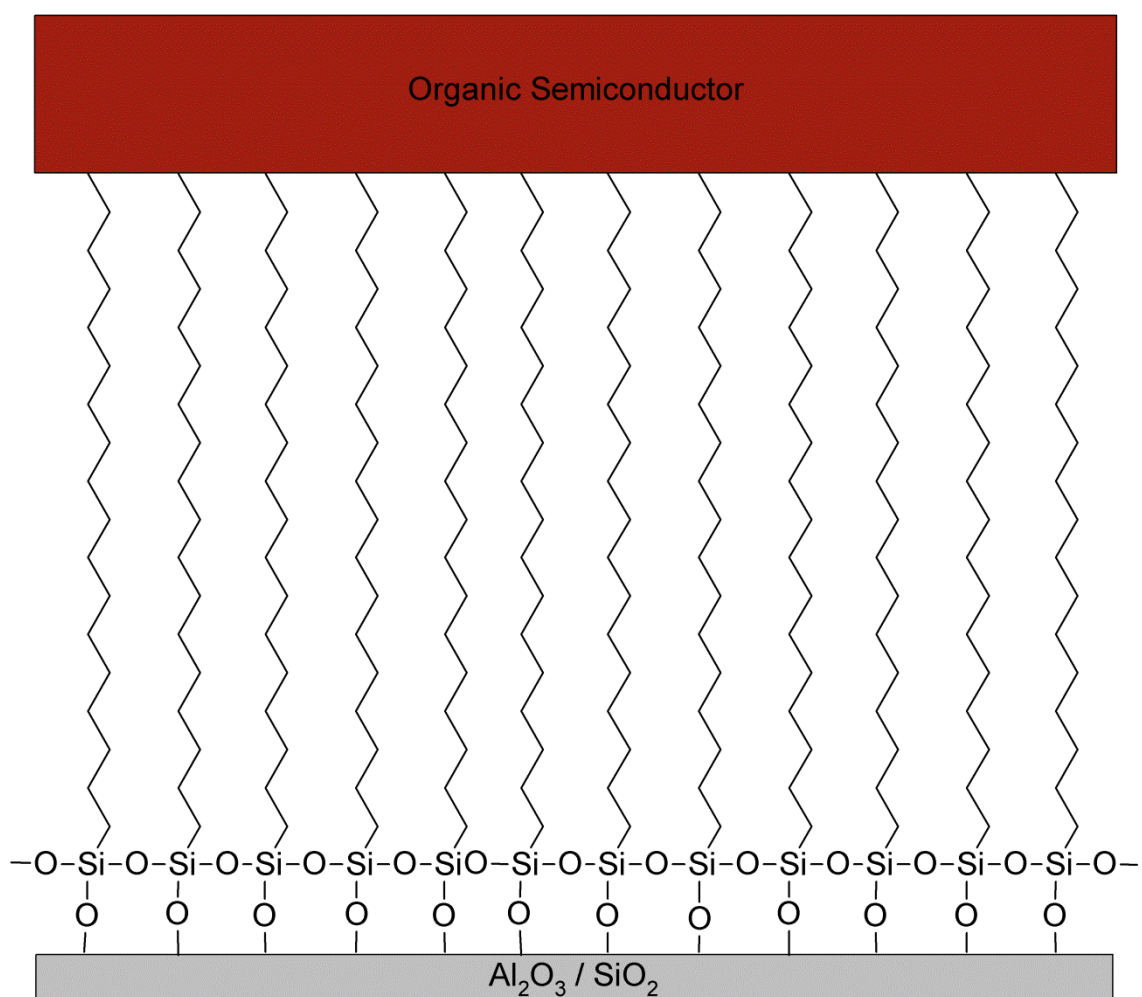


Figure 40. Diagram of a SAM of OTS on $\text{Al}_2\text{O}_3/\text{SiO}_2$ with a generic semiconductor.

1.3.1.5 Choice of Organic Semiconductor and Source/Drain Contact Material

Probably the most important decision when creating an OFET is the choice of organic semiconductor material and the source/drain electrode material to match. Firstly a semiconductor type must be chosen (either p- or n-type) and whether to use a low molecular weight material or a polymer. The deposition method of the semiconductor is of critical importance and has a huge bearing on device performance; for example, in the case of a spin-coated polymer, the choice of solvent and spin-speed determine the thickness and degree of order within the semiconductor film and thus affect the performance of the device. If the OFET is to be used as a sensor without a sensitiser layer (see section 1.3.1.6), then the semiconductor should be selected according to the presence of functional groups or regions likely to interact with the chemical that needs to be detected (analyte). Generally a semiconductor is required to be stable under ambient atmosphere (depending on its intended use) and should be vacuum safe if contacts need to be vacuum sublimated on top. A further requirement, if a solution processed semiconductor is used as well as a polymeric gate dielectric, is that the solvents of the semiconductor and the dielectric must be orthogonal, i.e. neither must dissolve any layer already deposited.

With regard to the source and drain electrode material, the main consideration is the work function of the material and how it matches the HOMO or LUMO level of the semiconductor (see section 1.1.1), as efficient injection is generally desirable. Next the material must be suitable for the environment that the device is required to work in and it must be possible to deposit the contacts on the semiconductor (in the case of top contact) without damaging the semiconductor. If a synthetic metal is used (see section 1.2.2.3) then not only must it be energy-level-matched to the semiconductor, but it must have an orthogonal solvent to all other layers of the OFET.

1.3.1.6 Sensitiser Layers

When creating an OFET for use in an analyte sensing application, it is possible to enhance the sensitivity of the OFET to specific analytes and decrease sensitivity to others through the application of a sensitiser layer. A sensitiser layer is a thin film (sometimes as thin as a

single monolayer) of an organic material deposited on top of a conventional OFET. Only OFET architectures with the semiconductor above the gate are suitable for use with a sensitiser layer (see the top and bottom right diagrams of **Figure 37**)

Calixarenes have already been reported as successful sensitiser materials for both OFETs and quartz crystal micro-balance (QCM) sensors.^[79, 80] The success of calixarenes as sensitiser materials is thought to be a consequence of their basket-like structure. The size and shape of the cavity within each calixarene molecule will determine which analytes it will accept and bind to strongly. Molecules too large to fit in the cavity will suffer from steric hindrance when trying to get close to the OFET surface, while molecules significantly smaller than the cavity will suffer from a weak binding once inside.^[79] To further increase selectivity shown by the calixarene molecule, functional groups which interact favourably with the desired analyte may be introduced into its structure e.g. hydrogen bonding groups. Other types of molecules (such as porphyrins) can also potentially be used as sensitisers as long as they interact with the desired analyte vapours; ideally a sensitiser would be very selective and only interact with one particular analyte to the exclusion of all others, however, finding such a material is very challenging. Some molecules display ‘lock-and-key’ type molecular recognition (similar to that shown by enzymes) and would, therefore, be very selective sensitisers. It is believed by Sokolov *et al* that the sensitiser layer traps the analyte molecules close to the semiconductor surface and influences the OFET performance through surface-dipole interactions .^[79]

1.3.2 Electrical Behaviour of Organic Field-Effect Transistors

The basic operating principle of an organic field-effect transistor (OFET) is to use a voltage, applied to the insulated gate (V_G), to control the current flow across the semiconductor channel between the source and drain (I_D) through moderation of the channel resistance; making the OFET, in effect, an electronic switch. In most systems the source electrode is kept on ground and a voltage (V_D) is applied to the drain. The channel resistance is reduced by the formation of a highly conductive region of high charge carrier density at the gate-insulator / semiconductor interface, known as the accumulation layer. The OFET requires voltages of the same polarity (with respect to ground) to be applied to both the drain and gate: this will be positive for n-type semiconductors and negative for p-types. The gate will

then pull carriers towards itself from the source to create an accumulation layer and the drain will draw charge carriers across the channel. The voltage that needs to be applied to the gate to form the accumulation layer is the threshold voltage (V_T). The value of threshold voltage is affected by a number of different factors, the foremost among these being: the injection barrier (contact resistance), the capacitance per unit area of the gate dielectric (C_i), the temperature, gate-bias stress effects, the flat-band voltage of the device (V_{FB}) and the thickness of the semiconductor layer (d_s) (for staggered electrode devices, see section 1.3.1.1).^[81] The flat-band voltage of a device is defined as “the gate bias at which charge first appears in the channel” (equivalent to the onset voltage, V_0 , shown in **Figure 42**), this will happen before the formation of the accumulation layer, therefore before V_T . Threshold is thought to have two main contributions the first is the flat-band voltage and the second is the residual conductivity of the organic semiconductor film, as shown in **Equation 19**.^[21] Horowitz *et al* allege that only devices with a gate-bias-dependent mobility actually display a threshold voltage in their paper “The Concept of “Threshold Voltage” in Organic Field-Effect Transistors”.^[82]

Equation 19.
$$V_T = V_{FB} + \frac{qp_0d_s}{C_i}$$

where V_{FB} is the flat-band voltage, q is the charge on each carrier, p_0 is the residual hole density, d_s is the thickness of the semiconductor film and C_i is the capacitance per unit area of the gate insulator. For an n-type device replace p_0 with $-n_0$.

When the gate voltage exceeds threshold, the OFET will switch on and enter the linear regime of conduction (as long as the drain voltage is lower than $|V_G - V_T|$, see **Figure 41**), drain current (I_D) is described by approximately by **Equation 20**. The device behaves as a resistor in this regime as $I_D \propto V_D$ at constant V_G .

Equation 20.
$$I_D \approx \frac{WC_i\mu}{L}V_D(V_G - V_T)$$

where V_D is the drain voltage (assuming source is at ground), V_G is the gate voltage, W is the channel width, L is the channel length, C_i is the capacitance per unit area of the gate insulator and μ is the carrier mobility.

As $|V_D|$ increases with respect to $|V_G|$, carrier density of the accumulation layer will decrease near to the drain contact as the potential difference of the drain and gate contacts is lower than that of the source and gate. Once the condition $V_D = V_G - V_T$ is met, I_D begins to saturate (see **Figure 41**). Saturation occurs as the accumulation layer begins to recede back towards the source, leaving an area of “non-field-effect doped” semiconductor in the conduction path, therefore raising the effective resistance; this effect is known as pinch-off. In this saturation regime the drain current no longer scales with drain voltage and instead starts to scale with the square of gate voltage, as in **Equation 21**.

Equation 21.

$$I_D = I_{D,sat} = \frac{WC_i\mu}{2L}(V_G - V_T)^2$$

where the parameters are as defined in **Equation 20**.

A quantity typically quoted in papers concerned with OFET performance is the on/off ratio; this is the ratio of the peak saturated drain current and the current just before the onset voltage (V_o), extracted from a plot of I_D vs. V_G at a fixed V_D . The onset voltage is the gate voltage at which I_D first begins to rise with V_G , V_o is always lower than V_T (see **Figure 42**).

As OFETs all show gate voltage dependent sub-threshold behaviour it is, therefore, sometimes useful to look at the sub-threshold regime (where $|V_G| < |V_T|$).

A useful quantity that can be extracted from a plot of $I_{D,Sat}$ (on a logarithmic axis) vs. V_G (see **Figure 42**) in the sub-threshold regime is the inverse sub-threshold slope (S^{-1}) otherwise known as the sub-threshold swing; S^{-1} is a measure of how well defined the switch between off and on is; a low value means that the transistor switches between the off and on states over a very narrow range of gate voltages, while a high value would result in a more gradual transition from the off to on state over a wider range of gate voltages. The inverse of S^{-1} is shown in **Figure 42**, S^{-1} is described by **Equation 22** in the region $|V_o| < |V_G| < |V_T|$ and typically quoted in units of V or mV per decade. It can be seen from **Equation 22** that it is desirable to have low trap density, to minimise C_s , and high gate insulator capacitance to minimise the value of S^{-1} .

Equation 22.

$$S^{-1} = \frac{\partial V_G}{\partial \log_{10}(I_D)} = \ln(10) \frac{kT}{q} \left(1 + \frac{C_s}{C_i} \right)$$

where q is the elementary charge, C_s is the capacitance per unit area of the traps at the semiconductor-insulator interface and C_i is the capacitance per unit area of the gate insulator. The pre-factor $\ln(10)kT/q$, gives the maximum possible value of S^{-1} , typically 57-59mV/decade.

The current and voltage profiles of OFETs can be presented in two ways: firstly as an output characteristic (**Figure 41**), a plot of the drain current response to changing drain voltage at a variety of gate voltages; and as a transfer characteristic (**Figure 42**), a plot of the drain current response to changing gate voltage at a fixed drain voltage. There are two types of transfer characteristic: a linear transfer characteristic and a saturated transfer characteristic; the linear characteristic is a plot where the value of the fixed drain voltage is given by $|V_D| < |V_G - V_T|$, while the saturated transfer characteristic is a plot where the value of the fixed drain voltage is given by $|V_D| \geq |V_G - V_T|$. When the transfer characteristic is discussed it is generally assumed to be the saturated transfer characteristic, the saturated transfer characteristic is regularly plotted as the square root of the saturated drain current ($\sqrt{I_{D, Sat}}$) against gate voltage. Both μ and V_T can be extracted from the saturated transfer characteristic, as explained in section 1.3.2.2; a plot of $I_{D, Sat}$ on a logarithmic axis is sometimes included in the saturated transfer characteristic to allow easier determination of the on/off ratio, V_o and S^{-1} parameters (as in **Figure 42**).

1.3.2.1 The Output Characteristic

As mentioned above the output characteristic is a plot of the drain current (I_D) response to changing drain voltage (V_D) at a variety of gate voltages (V_G). It can be realised through the use of computer controlled source-measure units and temporary contacts. Each curve of the characteristic is obtained by measuring I_D while sweeping V_D from 0 to a maximum voltage ($V_{D, Max}$) and back again to 0, under a fixed gate voltage. The gate voltage is then incremented to the next value and the measurement is repeated, this process is performed for the entire range of gate voltages from a minimum gate voltage ($V_{G, Min}$) to a maximum gate voltage ($V_{G, Max}$). Often $V_{G, Min} = 0$, unless the device is ‘normally on’ (i.e. ‘on’ for positive V_G in the case of p-type, or ‘on’ for negative V_G in the case of n-type) a limit to the highest possible gate voltage is given by the dielectric breakdown of the gate insulator material. The output characteristic is the collection of I_D verses V_D curves for the range of

gate voltages plotted in a single graph; an example of an output characteristic is shown in **Figure 41**. In this work quantitative analysis will only be carried out on the transfer characteristics, while qualitative conclusions will be made from the output characteristics. The output characteristic can be used to identify a variety of problems an OFET device can suffer from; in the initial (ideally linear, as predicted by **Equation 20**) region of the output characteristic, deviation from Ohmic behaviour (i.e. curvature) indicates source and/or drain contact problems and therefore non-ideal injection of charges (see section 1.1.1). In the last region of the graph, if I_D fails to saturate (as predicted by **Equation 21**) and continues to increase linearly, this indicates that the semiconductor film is doped, the degree of the non-saturated behaviour is indicative of the degree of doping. Leakage current to the gate can be seen in the output characteristic as a current at the opposite side of the x-axis to the main body of the graph at low V_D for all the V_G curves. Finally the difference shown between the traces of increasing V_D and decreasing V_D , the hysteresis of the graph, indicates the amount of charge carrier traps present in the semiconductor bulk or at the semiconductor-insulator interface, as well as any mobile ion impurities present.

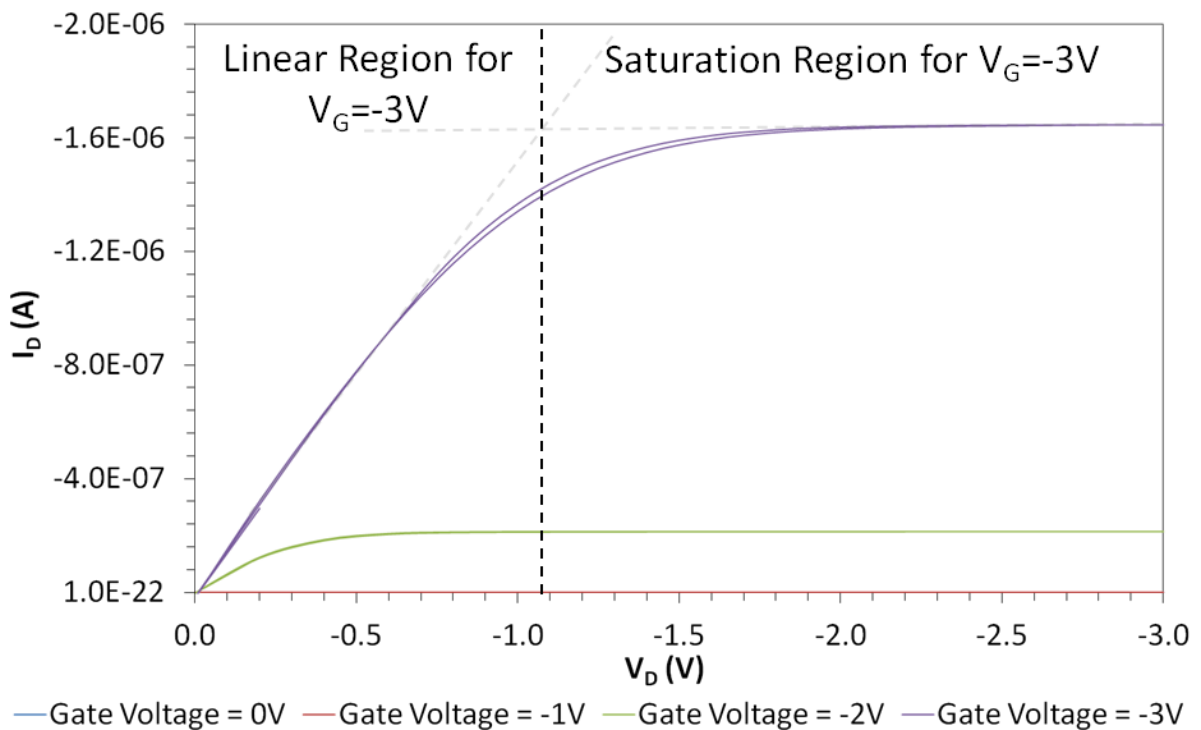


Figure 41. An output characteristic showing the linear region and saturation region labelled for the -3V curve.

1.3.2.2 The Saturated Transfer Characteristic

As mentioned above the saturated transfer characteristic is a plot of the drain current response to changing gate voltage at a fixed drain voltage and can be measured using an identical set-up to the output characteristic, albeit with a different drive scheme. The drain current response is monitored while V_G is swept from $V_{G, Min}$ to $V_{G, Max}$ (the same values used in the output characteristic) while V_D is held at $V_{D, Sat}$, generally $V_{D, Sat} = V_{G, Max}$. An example of a transfer characteristic is shown in **Figure 42**. The parameters carrier mobility (μ) and threshold voltage (V_T) can be extracted from the transfer characteristic by extrapolating a line back from the linear region of the transfer characteristic to the V_G axis (x-axis) and extrapolating a line forwards from the flat “off” current at the beginning of the plot; the x-axis value at the intercept of the two extrapolations will give the value of V_T and using **Equation 21** along with the gradient of the extrapolated line, μ can be calculated.

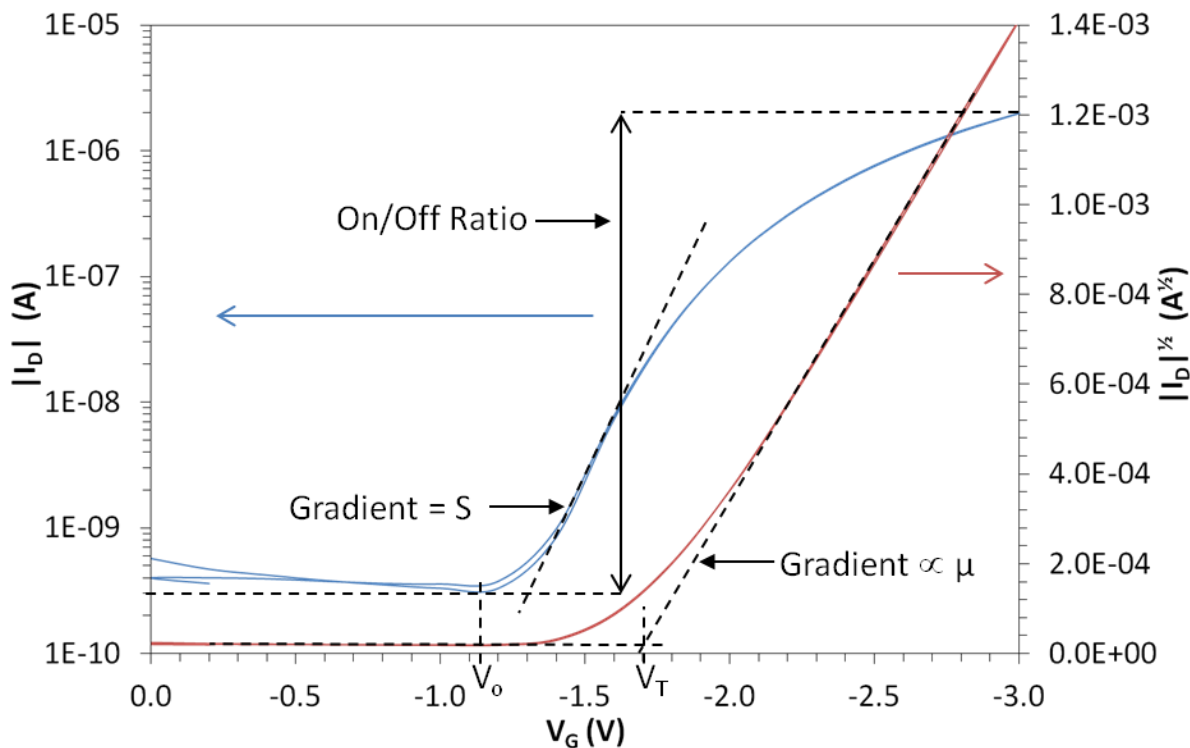


Figure 42. A saturated transfer characteristic with μ , V_T , V_o , S and the on/off ratio labelled.

1.3.2.3 Dynamic Properties of Organic Field-Effect Transistors

The maximum switching speed of an OFET is limited by the time it takes charge carriers to fill or empty the accumulation layer. This in turn depends on both the mobility of the semiconductor and the channel length, **Equation 23** describes the maximum theoretical operational switching frequency of a device: the cut-off frequency (f_c).^[83]

Equation 23.

$$f_c = \frac{\mu V_D}{2\pi L^2}$$

where μ is the carrier mobility, V_D is the drain voltage and L is the channel length.

The cut-off frequency is usually only of concern when fabricating OFETs for logic circuit or display addressing purposes, however, it should be kept in mind when devising vapour sensing systems with oscillating drive voltages. The cut-off frequency is the theoretical maximum switching frequency; the actual maximum can be lowered by large parasitic capacitances that need to be charged / discharged within devices.

As well as extracting the carrier mobility from the transfer characteristic of an OFET, it may also be calculated using the time-of-flight (TOF) method; the mobility extracted via this method will be different to the one extracted from the transfer characteristic as the TOF method is a low carrier density technique and, as stated in section 1.1.2.1, mobility is carrier density dependent. The calculation of the TOF mobility requires the measurement of the transit time (t_{tr}) of charge carriers across the channel, using a method such as Dost *et al*;^[84] in-effect applying pulses of voltage to the source/drain and gate connections sufficient to turn the device on and observing the delays in current beginning to flow at the start of a pulse and ceasing to flow at the end of the pulse. If performed for a range of channel lengths the general expression for transit time^[85] (see **Equation 24**) can be used to extract the mobility from a plot of t_{tr} vs. L^2 .

Equation 24.

$$t_{tr} \approx \frac{L^2}{\mu V_D}$$

where L is the channel length, μ is the time-of-flight mobility and V_D (in this case) is the effective voltage that drives carriers across the channel.

1.4 Thermodynamics

1.4.1 Vapour Pressure and Liquid-Vapour Equilibrium

The concept of vapour pressure and a sound understanding of how to apply this concept are very important in the field of vapour sensing. The vapour pressure is the parameter that determines how volatile a material is and thus dictates the amount of vapour that can be extracted from a material and how fast the vapour is replenished. The vapour pressure is defined as the pressure at which the liquid and vapour forms of a material are in dynamic equilibrium, i.e. the vapour is condensing at the same rate as the liquid is evaporating. When in an environment containing other gases the liquid will undergo net evaporation until its partial pressure within the gas mixture is equal to its vapour pressure (after which dynamic equilibrium will again be reached). Partial pressure is defined in **Equation 25**.

Equation 25. $p_y = x_y P$

where p_y is the partial pressure of the material y , x_y is the mole fraction of the material y (n_y/n_{total}) and P is the total pressure of the system (a linear sum of all the partial pressures).

From the above discussion of vapour pressure, it is therefore obvious that when a volume of the liquid form of a material is placed in a sealed vessel net evaporation will occur until the partial pressure of the material is equal to its vapour pressure; this is the basic working principle behind vapour generation for use in vapour sensing experiments.

The vapour pressure of a material is heavily dependent on the temperature of the material. The temperature dependence of vapour pressure is described by the Clausius-Clapeyron equation, see **Equation 26**.

Equation 26.
$$p = p^* \exp\left[-\frac{\Delta_{vap}H}{R}\left(\frac{1}{T} - \frac{1}{T^*}\right)\right]$$

where p^* is the vapour pressure at temperature T^* , $\Delta_{vap}H$ is the latent heat (or enthalpy) of vaporisation per mole and R is the gas constant.

It can be seen from **Equation 26** that higher temperatures lead to higher vapour pressures, therefore by the heating and cooling of liquid analytes the concentration of vapour can be modified for use in vapour sensing.

The vapour pressure of a material can also be modified through the application of pressure to the liquid phase of the material. Subjecting additional pressure to the liquid phase of a material can be done in a multitude of ways including mechanically or through the use of an inert gas. The increase in vapour pressure due to the application of pressure is given by **Equation 27**.

Equation 27.

$$p = p^* \exp\left[\frac{V_m(l)\Delta P}{RT}\right]$$

where p^* is the original vapour pressure, $V_m(l)$ is the molar volume of the liquid phase and ΔP is the applied pressure.

1.4.2 Reaction and Recovery of Organic Materials under Vapour Exposure

When describing the behaviour of vapour sensing systems, three possible scenarios can occur when a sensor material (be it the organic semiconductor or sensitiser layer) is exposed to an analyte; firstly, there could be no measurable interaction i.e. no response. Although this is an undesirable response towards a target analyte, it could be useful against other non-targeted analytes to increase device selectivity. Secondly, the sensor could undergo a reversible interaction with the analyte; this means it will respond whilst under analyte exposure but once the analyte atmosphere is removed the sensor will recover, ideally, to its original pre-exposure state. A reversible interaction is the ideal response for sensor applications as it means that the sensor is re-useable and does not need to be replaced after each use. Thirdly the sensor material could undergo an irreversible interaction with the analyte; in this situation the sensor will show a response to the analyte but once the analyte atmosphere is removed the sensor will not recover. Although a response is observed, this is not ideal sensor behaviour as the actual sensing medium would need to be replaced after each exposure, limiting it to use as a disposable “1-shot” sensor.

A reversible interaction indicates that the binding of the analyte molecules to the sensor material is such that the thermal energy present in the system is sufficient to overcome the binding energy holding the analyte and the sensor molecules together; the low binding strength present in this situation tends to suggest that the binding is achieved through Van der Waals forces (or even hydrogen bonding) rather than through true covalent bonding. This process is known as physisorption or physical adsorption and has a binding energy of the order 10^{-2} - 10^{-1} eV. Under the reversible regime the binding and desorption of analyte molecules will be a dynamic process while analyte exposure occurs; for surface physisorption, the desorption rate at any given temperature can be given by the Arrhenius-like **Equation 28**, for which there is a strong temperature dependence. It should be noted at this point that a sensor response is also generally considered reversible if the sensor will recover under heating rather than naturally at room temperature.

Equation 28.

$$\frac{dN}{dt} = vNe^{-E_d/kT}$$

where N is the surface density of adsorbed molecules, v is a rate constant unique to any given desorption and E_d is the activation energy required for a molecule to undergo desorption.

In the case of an irreversible interaction taking place, a much stronger binding between analyte and sensor molecule occurs, most likely accompanied by the formation of a true chemical bond which is much harder to overcome than a Van der Waals interaction or a hydrogen bond. This process is known as chemisorption or chemical adsorption and has a binding energy of the order 1-10eV, between 10 and 1000 times stronger than physisorption. Release of the analyte in this case would require the input of large amounts of energy which would be likely to modify the analyte or sensor molecule structure before breaking the desired bond.

It is possible for analytes to either bind (adsorb) to the surface of the sensing medium or they can penetrate (diffuse) into the sensing medium and bind (absorb) to the molecules deeper in the sensing medium.

The extent of the interaction/reaction between analyte and sensing material (receptor) is controlled by the Gibbs free energy of the system (G), defined as in **Equation 29**; if the Gibbs

energy was to be plotted against the extent of reaction then equilibrium would be reached at the point where the Gibbs energy was at a minimum, i.e. $\Delta_r G = 0$.

Equation 29.
$$G = H - TS$$

where H is the enthalpy, T is the temperature and S is the entropy of the system.

To describe the equilibrium position of the analyte-receptor interaction, firstly the standard reaction Gibbs energy ($\Delta_r G^\ominus$) and the reaction quotient / equilibrium constant (Q / K) must be defined. The standard reaction Gibbs energy is the difference between the standard molar Gibbs energies of the reactants and products. The reaction quotient is the ratio of the ‘amount’ of reacted material to un-reacted material at any non-equilibrium point, while the equilibrium constant is the same value at the point of equilibrium. These values are related as in **Equation 30** in any non-equilibrium state and as in **Equation 31** at equilibrium.

Equation 30.
$$\Delta_r G = \Delta_r G^\ominus + RT \ln Q$$

Equation 31.
$$\Delta_r G^\ominus = -RT \ln K$$

where $\Delta_r G$, $\Delta_r G^\ominus$, Q and K are as defined above, R is the gas constant and T is the temperature.

1.5 Vapour Response Mechanisms in Organic Field-Effect Transistors

The response to analyte vapours shown by organic semiconductor based field-effect transistors can be due to a variety of different interactions at different places within the OFET. Firstly the work by Someya *et al*,^[30] Torsi *et al*^[86] and Zan *et al*,^[35] has shown that grain boundaries play a very important role in sensing; vapours can penetrate organic semiconductors down to the region where most of the conduction is taking place (the accumulation layer) much more quickly and easily through the grain boundaries than through the semiconductor material, especially in semiconductors that form highly ordered, close-packed structures. At the grain boundaries, analyte molecules can either impede the conduction of charge carriers across the boundaries, essentially creating traps at the grain boundaries that reduce the overall mobility of the charge carriers; or analyte molecules can

dope the grain boundaries, in effect creating Schottky junctions at the boundaries, aiding the conduction of charge carriers across the boundaries and therefore increasing the overall mobility, as well as increasing the off-current of the devices. As long as these processes do not take the form of true chemical reactions, the effects will be reversible.

If analyte vapours are capable of changing the bulk morphology of the organic semiconductor (solvent annealing), the change seen in the mobility would be permanent and recovery would not be possible.^[87] The absorption spectrum of the semiconductor would also remain unchanged in the case of solvent annealing, but would be changed in the case of bonding or a non-permanent interaction.

The threshold voltage of devices can only be changed through the formation of the accumulation layer being hampered or assisted. The most likely mechanism to effect accumulation layer formation is the addition of dipoles that are close enough to affect the accumulation layer. Dipoles can be formed by the interaction or chemical bonding of any analyte with the semiconductor, however, the size of the dipole moment is dependent on the relative electronegativities of the bonding groups/atoms. Dipoles can also affect the carrier mobility as the E-field they generate can hamper or enhance the transit of charge carriers across the device.

The application of a sensitiser layer is meant to provide a layer for analytes to bind to, creating dipoles which then affect the conduction properties of the semiconductor film beneath. Analytes which do not bind to the sensitiser layer will find it harder to penetrate into the semiconductor film due to the need to diffuse through the sensitiser layer first; the nature of the packing, size of any cavities in the sensitiser molecules, the thickness of the sensitiser layer and the size of the analyte molecules will all effect the rate of diffusion of the analyte through the sensitiser layer.

1.6 Conventional Vapour Sensing Systems

In the field of vapour sensing, there are a wide range of different techniques available that take advantage of a variety of different material properties to produce a signal in response to the presence of a certain vapour. The different techniques all have pros and cons in terms of performance, so are generally suited to a particular application; be it sensing a

particular vapour or type of vapour (i.e. hydrocarbons or alcohols) or working in a specific environment.

Here will be discussed a selection of the techniques commonly used in research and in more commercial/industrial environments.

1.6.1 Mass Spectroscopy

In mass spectroscopy the sample of analyte material is first required to be vaporised, before being ionised and accelerated into the main body of the mass spectrometer in the form of an ion-beam. The paths of the individual ions are bent using a static magnetic field; the magnitude of the bending is determined by the mass-to-charge ratio. Using an array of detectors that record the charge of the ions passing into them, the mass-to-charge ratio of each ion is calculated. While being able to identify the individual molecules that make up a sample of vapour,^[88] the mass spectrometer is impractical for use as a vapour sensor in the field as it is quite a large, heavy device that requires large amounts of electrical power to run and the internal environment must be kept under high vacuum to allow the ions a large mean free path.

1.6.2 Metal Oxide based Resistor Sensors

One of the main methods of sensing using inorganic films is through the use of metal oxide films and the monitoring of their resistance. There are many proposed mechanisms as to why the resistance changes in response to certain vapours; these include the reduction of the oxide surface when sensing hydrocarbons,^[89, 90] bulk diffusion of oxygen into the oxide and surface chemisorption (see section 1.4.2) when sensing environmental gases.^[91] Carotta *et al* showed sensitivity to light alkanes at concentrations of 100ppm and methane at a concentration of 500ppm.^[90] This type of device tends to have a fast response time (in the order of seconds) and shows very good recovery.^[89] The main disadvantage of this method of sensing is the high temperatures (100s of °C) needed by the majority of the devices to operate as sensors.

1.7 Vapour Sensing Systems using Organic Materials

1.7.1 Optical Spectroscopy

Optical spectroscopy involves the use of a light source and a spectrophotometer. The sample under test has light (sometimes just visible or with wavelengths from ultraviolet through to infrared included as well) shone upon it from an optical fibre and a second optical fibre collects either the reflected or transmitted light from the sample and feeds it into a spectrophotometer. The spectrophotometer then samples the spectrum of light received using a combination of diffraction grating and an array of photo detectors (such as photodiodes); by comparing the spectrum received from the sample to a baseline of the light source an absorbance spectrum can be produced. The test sample can be in the form of a gas, liquid/suspension/solution or a solid; optical spectroscopy has been used successfully as a gas sensing technique in a number of ways, most notably for organic sensors, by monitoring the changes in the absorbance spectra of an organic material in solution or in the form of a film as the organic material interacts with the analyte vapour.^[7, 8, 92] Many research groups have used optical spectroscopy based systems to perform vapour sensing, Dunbar *et al* managed to sense a wide variety of vapours using this method and some porphyrin compounds both in solution and as thin films, the lowest concentration of analyte detected was 3ppm in the case of octanol.^[7] Previous work by the group has indicated that these porphyrin materials can be recovered back to their pre-exposed state under gentle heating ($\sim 48^\circ\text{C}$) over several minutes and that the response is relatively fast (50% of the device's saturated response is observed in less than 10 seconds).^[8] The major disadvantage of optical spectroscopy is the need for expensive light sources and spectrophotometers.

1.7.2 Quartz Crystal Microbalance (QCM) Sensors

Quartz crystal microbalance (QCM) sensors work on the principle of detecting changes in mass and therefore resonant frequency of the QCM (see **Equation 34**). Most QCM sensors are created by coating the gold electrodes of a QCM with an organic material that will interact with the target analyte vapour and cause a change in mass of the organic material deposited on the QCM this, as mentioned above, will lead to a resonant frequency shift in the QCM which can be interpreted as a sensing response.^[80, 93] QCM sensors built by Xhou *et al* have shown sensitivity to acetic acid and propyl amine down to concentrations of

50ppb, with response times in the tens of seconds range and recovery times up to 7 minutes.^[93]

1.7.3 Core-Shell Nano-Particle Swelling Based Sensors

The working principle of core-shell nano-particle based sensors is that their conductance is dependent on the spacing of the metal nano-particle cores as the conduction mechanism is quantum tunnelling based (see **Equation 14**); as the molecules of an analyte vapour penetrate the nano-particle film and begin to interact with the organic ligands surrounding the core, this will swell the film and so increase the core to core separation and therefore lower the conductance of the film.^[6, 53, 94, 95] Hanwell *et al* show devices sensitive to 0.5ppm NO₂ vapours, with a response time in the order of several seconds but very limited recovery even over timescales of hundreds of seconds;^[6] Al Qahtani *et al*, however, report devices with sensitivity to decane vapour down to a concentration of 15ppm and recovery back to their pre-exposure state taking less than 90 seconds.

1.7.4 Organic Field-Effect Transistor and Organic Chemi-resistor Based Sensors

Along-side the organic sensors that produce an optically observable change in response to vapour exposure, the other main type of organic sensor is the type that undergoes a change in electrical conduction properties in response to vapour exposure; the most common of these devices are the organic field-effect transistors (OFETs) and organic chemi-resistors. In the case of OFETs the actual sensing response can be characterised as a change in the channel on-resistance of a device as the organic semiconductor of the device starts to interact with an analyte vapour, alternately a sensitiser layer can be applied to the device to interact with the analyte vapour and in turn induce a change in the conduction properties of the OFET device.^[79] If the correct monitoring system is used to drive and measure the OFET, multi-parameter sensing is possible as the change in channel on-resistance can be broken down into changes in the device's charge carrier mobility and threshold voltage (see sections 1.1.2.1 and 1.3.2), the main parameters upon which the OFET's conduction properties depend. In a chemi-resistor device the interaction with the analyte vapour again happens in the organic semiconductor layer but only parameter generally monitored is the

resistance of the device. The currents obtained from chemi-resistor devices tend to be smaller than those produced by OFETs as the OFETs benefit from field-effect doping when in the on regime (see section 1.3).

1.7.5 Organic Sensing Devices: State of the Art

In this section the current state of the art will be discussed with respect to using organic devices to sense some of the analyte groups discussed in the results chapters of this thesis.

1.7.5.1 State of the Art: Amine Sensing

Many papers have been published on the sensing of amine vapours due to their importance to food freshness (as mentioned in section 1.2.1.4). Dunbar *et al* used an optical sensor based on a zinc porphyrin and observed the shift in the absorbance spectrum of the porphyrin to quantify a sensing response, they managed to sense octylamine vapour successfully with this device at a concentration of ~354ppm, with the response taking tens of seconds to saturate and total recovery of the sensor achieved upon heating to 48°C.^[96] Brittle *et al* used a calixarene-porphyrin hybrid molecule with a zinc core to perform an experiment using the same set-up as Dunbar *et al*; they managed to sense 90ppm dibutylamine vapour with the device showing half-saturated response after 8.8 seconds and total recovery under 80°C heating.^[97] Liu *et al* again used the shift in the absorbance spectrum to sense amine vapour, using zinc phthalocyanine as the sensor; the sensor takes tens of seconds to reach saturation under vapours with concentrations of 100s of ppm but at its limit of 5ppm (butylamine) takes around 2000 seconds to saturate and shows complete recovery under 45°C heating.^[98] Pacquit *et al* took a different approach than those mentioned previously, in that they made a sensor from a pH sensitive dye that changed colour in the presence of amine vapour (amine being basic in nature); the sensor response was read out using a reflectance colorimeter (two LEDs and a photodetector); a response was seen down to a concentration of 6.25ppm ammonia, with a saturated response to 14.29ppm seen in <20 seconds, the response was also reversible at room temperature.^[92] Liao *et al* used an array of polythiophene based thin film transistors (TFTs) to sense amine vapour, the saturated drain current of the devices was monitored throughout exposure to isolate a sensing response; sensing is shown at 10ppm for

butylamine and heptylamine, response time and recovery to this concentration is not discussed.^[99]

1.7.5.2 State of the Art: Aldehyde and Ketone Sensing

While the ability to sense aldehydes is quite important due to dangerous substances such as formaldehyde, ketones are less vital to sense so there have been fewer papers published on ketone sensing; described here are some of the successful methods and materials used to sense both aldehydes and ketones. Lin *et al* use a system similar to the QCM system mentioned previously (which measures a shift in the resonant vibrational frequency of the quartz), but instead of the bulk of the quartz crystal carrying the vibrational wave, only the surface of the crystal carries the wave in Lin *et al*'s device; this is known as a surface acoustic wave (SAW) quartz crystal. The SAW crystal was coated with a fullerene to act as the sensing medium. Lin *et al* managed to sense concentrations of acetone and propanal around 1900ppm but calculated a detection limit of ~1000ppm for acetone and ~325ppm for propanal; the response for propanal starts in 10s of seconds but doesn't saturate even after ~2500 seconds, but shows total recovery within ~2000 seconds. response/recovery data for acetone are not given.^[100] Li *et al* have reported a sensor that can detect aldehydes in solution using a rhodamine compound that will react with aldehydes to create a new compound that is highly coloured and highly fluorescent from the weakly coloured and non-fluorescent rhodamine starting compound; by monitoring the absorption and fluorescence emission spectra of the rhodamine compound in a dimethylformamide solution before and after the addition of methanal (formaldehyde), Li *et al* managed to detect methanal down to a concentration of ~270ppm no detail was given of the possibility of recovery or the speed of detection.^[101] To detect formaldehyde vapour Carquigny *et al* used a novel chemi-resistor sensor; the chemi-resistor had a thin film of a blend of a conducting polymer (polyaniline) and non-conducting polymer (fluoral-p) deposited onto some electrodes, the non-conducting polymer reacts with formaldehyde to produce an ammonia by-product which the conducting polymer is sensitive to; through monitoring the resistance change of the chemi-resistor Carquigny *et al* found a detection limit of 3.7ppm for formaldehyde, with a response time of the order of tens of seconds.^[102]

1.7.5.3 State of the Art: Ester Sensing

Like ketone sensing mentioned above, ester sensing is rarely reported in the literature, here will be discussed the ester sensing experiment most relevant to the work discussed in this thesis. Sokolov *et al* use a thiophene-based organic field-effect transistor with a calixarene sensitiser layer as the sensor for the ester ethylethanoate. Sokolov *et al* report sensing behaviour down to concentrations of 200ppm ethylethanoate vapour, the device shows no recovery after exposure and shows a sensing response within 10 seconds of exposure; devices made without the calixarene sensitiser layer show a greatly reduced response to the ester vapour.^[79]

1.7.5.4 State of the Art: Ethylene Sensing

While being a very important compound to sense due to its use as a ripening hormone in agriculture, most of the sensing systems reported in the literature are based on inorganic technologies, with relatively few organic devices used. Discussed here are two examples of organic sensing systems. Cabanillas-Galan *et al* report on a sensor based on visual colour changes of a palladium compound; a response was shown to 10ppm ethylene vapour, however, this response was very slow, taking several hours.^[103] Esser *et al* used a chemi-resistor based on carbon nano-tubes modified with organo-metallic copper compounds; Esser *et al* report responses down to ethylene concentrations of 0.5ppm, the rate of response appears to be in the order of seconds, but is not explicitly stated, and the devices show almost total recovery after exposure.^[104]

2 Experimental Methods

2.1 Cleaning Methods for Silicon Oxide Wafers

When creating an OFET, preparation of the substrate is of crucial importance. All contamination, be it particulate or residue, must be removed. Any impurities left behind can hamper adhesion of subsequent layers and effect organic film formation through non-homogeneous wetting and nucleation (when spin-coating the film). Evaporated organic films can also be adversely affected by an unclean surface, which may mimic a very rough surface and prevent the formation of a good crystalline film structure.

2.1.1 Chemical Cleaning

The first step used to prepare substrates for the work described here was the chemical cleaning step. Firstly the substrates were cleaned using the ketone acetone and a woven fibre clean-room wipe, acetone is commonly used as a de-greasing agent and will dissolve and wash away any biological residue (e.g. grease from fingers or saliva). Once the substrates were dry, through time spent on a hot-plate or through the use of a dry-nitrogen gun, a dilute aqueous solution of the strongly alkaline detergent Hellmanex^[105] was prepared. The substrates were submerged in the detergent and placed in a sonic bath for five minutes; this step should remove any remaining particulate dirt and residues not soluble in acetone, as well as any remaining acetone. After five minutes in the sonic bath the substrates were removed from the detergent and rinsed thoroughly, first in low-grade de-ionised water to remove any detergent, then in high-grade de-ionised water to ensure the lowest possible concentration of detergent and water-borne ions remain on the substrate to prevent any residue being left upon drying. Finally the substrates were submerged in the secondary alcohol propan-2-ol (iso-propanol, IPA) and placed again in the sonic bath for five minutes. Once removed the substrates were rinsed with fresh IPA before being dried. The substrates were then free of particulate dirt and residues.

2.1.2 Ultra-Violet Generated Ozone Cleaning

Although chemical cleaning methods remove the visible organic dirt from a silicon oxide surface, thin films can still be left behind. The UV-Ozone cleaning method, when used in conjunction with chemical cleaning methods, will remove even the thin films of organic material that is invisible to the naked eye. All of the silicon oxide substrates in the work presented here were treated for 4.5 minutes in a UV-Ozone unit (Bioforce Nanosciences - UV TC 220) after chemical cleaning was completed. The UV-Ozone cleaning works through two mechanisms; firstly the UV light generates Ozone (O_3) from ambient atmosphere which then breaks up large organic molecules through oxidation, creating highly volatile materials; next the UV photons hit the organic molecules and break the bonds which hold them to the oxide surface, allowing them to disperse into the atmosphere.^[106]

Cleaning substrates through this method has also been shown to increase the adhesion of aluminium, for a subsequent anodisation process in our work.

2.2 Deposition Methods

2.2.1 Thermal Evaporation

Thermal evaporation (also known as vacuum evaporation) is a very widely used deposition technique for metals, inorganic materials and low molecular weight organic materials in situations where accurate film thicknesses are required. The devices created for use in the work described here have all been fabricated using thermally evaporated electrodes and in some cases the semiconductor has also been thermally evaporated. The basic principles of thermal evaporation are fairly simple. It is performed under high vacuum firstly to prevent reaction of the evaporant with elements in the ambient atmosphere and secondly, to increase the mean free path of evaporant atoms/molecules to increase the fraction of atoms/molecules released that actually make it all the way to the substrates being deposited upon (see **Equation 32**). It is usual for vacuum pressures in the range 10^{-6} - 10^{-8} Torr to be used for thermal evaporation, achieved through the use of a rotary and high vacuum pump (such as an oil diffusion or molecular pump) in tandem.

Equation 32.

$$\lambda = \frac{kT}{P\pi d^2 \sqrt{2}}$$

where λ is the mean free path of atoms/molecules, T is the material temperature, P is the vacuum pressure and d is the diameter of the atoms/molecules.

The evaporant will be loaded into some form of heater, be it a tungsten/molybdenum boat, coil or basket, or even ceramic/quartz crucible mounted in a heating coil. The temperature of the heater will then be increased through resistive heating until the vapour pressure (see section 1.4.1) of the evaporant is sufficiently high (generally $>10^{-2}$ Torr),^[107] at which point evaporation will be observed as evaporant atoms/molecules will be released as a vapour and will condense on any cooler surfaces inside the evaporation chamber. The evaporation rate (as derived by Langmuir)^[108, 109] is given by **Equation 33**.

Equation 33.

$$\Gamma = P \left(\frac{M}{2\pi RT} \right)^{\frac{1}{2}}$$

where Γ is the evaporation rate, P is the vapour pressure of the evaporant at the temperature T , M is molecular weight and R is the gas constant.

The rate of deposition and total thickness are generally monitored through the use of a quartz crystal microbalance, in which a controller is programmed to extract the thickness of the layer deposited from the density of the material evaporated and the mass deposited, obtained from the change in resonant frequency of the quartz crystal. **Equation 34** describes the change of resonant frequency as a function of mass deposited upon the crystal.

Equation 34.

$$\Delta f = -\frac{2f_0^2}{A\sqrt{\rho_q\mu_q}} \Delta M$$

where Δf is the change in frequency, f_0 is the initial resonant frequency, ρ_q is the density of quartz, μ_q is the shear modulus of the quartz, ΔM is the change in mass and A is the exposed area of the quartz crystal.

Several factors can affect the quality (crystallinity, uniformity etc.) of the film obtained from evaporation, among the most important are: the evaporation rate, the temperature of the substrate, the relative positioning of the evaporation source and the substrates, the surface cleanliness/roughness of the substrates and the ambient gas present in the evaporator before vacuum was established.

To define certain areas of the substrate where deposition is desired a shadow mask can be placed in front of the substrates to block the evaporant from depositing where it is not required.

2.2.2 Spin Coating

For materials such as soluble polymers spin coating (or spin casting) is a very commonly used deposition method, mostly due to the speed, ease and repeatability of the process for batch production within a laboratory environment. The basic principles behind spin coating are as such: a solution of the desired organic material is made (generally in the region of $10\text{mg}\cdot\text{mL}^{-1}$ for most materials), the substrate is placed into the spin-coater and held in place by a vacuum, then the substrate is covered in the solution prepared previously and the substrate is accelerated to the desired spin speed. As the substrate is spinning several processes are taking place at its surface; firstly, a portion of the solution is thrown off the surface, meanwhile the rest of the solution is forced to spread across the substrate by the balance of forces both acting to throw it off the surface and causing it to adhere to the surface. As the substrate continues to spin the solution begins to dry as the solvent is evaporated at an accelerated rate, thus building up a thin film. The thickness of the film obtained is dependent on a variety of different parameters present in the process, see **Equation 35.**^[109]

$$\text{Equation 35. } d \approx \left(\frac{\eta}{4\pi\rho\omega^2} \right)^{\frac{1}{2}} t^{-\frac{1}{2}}$$

where d is the film thickness, η is the viscosity coefficient of the solution (a function of concentration), ρ is the solution density (also a function of concentration), ω is the angular velocity of spinning and t is the spinning time (up until the point the film is dry).

The choice of solvent is very important when creating spin coated films as the solvent must first be compatible with the surface and “wet” the surface well to enable good adhesion and secondly the volatility of the solvent will determine the thickness and level of order of the film; a highly volatile solvent will evaporate quickly creating a thick film and will “lock” disorder into the film as the molecules dissolved in the solvent will not have a great deal of time to re-arrange themselves while in solution; a low volatility solvent, while giving the

molecules more time to orient themselves, will cause lots of the solvent to be lost during spinning thus creating a much thinner film. It is generally believed that, despite the choice of solvent, films deposited through spin coating contain a large degree of disorder, but some materials have been found to create highly ordered films from spin coating.^[110]

2.2.3 Langmuir-Blodgett Deposition Technique

The Langmuir-Blodgett (L-B) technique was originally developed by Irving Langmuir and Katherine Blodgett as a way to investigate the physics of monolayer films. The technique endeavours to create a monolayer film of an organic material floating on a sub-phase (usually water) which can then be transferred to a solid substrate. The whole process of film creation and deposition takes place within a Langmuir trough; a Langmuir trough is a shallow PTFE coated receptacle with either one or two movable PTFE barriers (see **Figure 43**).

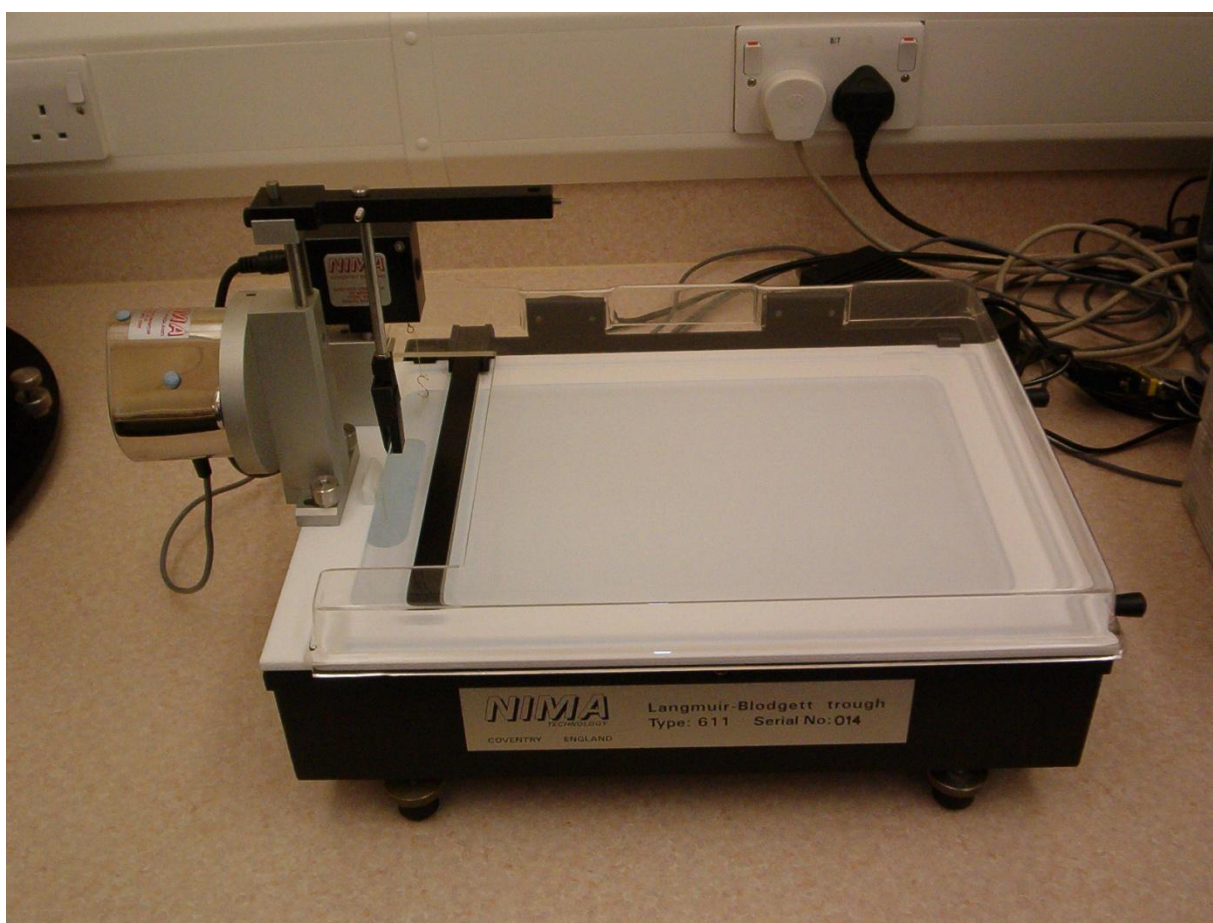


Figure 43. An example of a Langmuir trough.

First a solution of the desired material is created, usually of low concentration to prevent aggregation of the material in solution, using a solvent that has a high evaporation rate and is not readily miscible with the sub-phase material. The solution is then spread carefully over the sub-phase surface and the solvent is allowed to evaporate, leaving behind the solute floating on top of the sub-phase. If the sub-phase is water the organic material is required to be either hydrophobic or (ideally) amphiphilic, having both hydrophilic and hydrophobic sides. Once all solvent has evaporated the organic material is compressed to form an ordered monolayer; the compression is performed by the movable barrier(s) of the trough slowly sweeping the sub-phase surface. The transition from a disordered arrangement of material to the desired ordered monolayer is monitored through measurement of the two-dimensional surface pressure using a sensor based on the Wilhelmy plate. The Wilhelmy plate (generally a rectangular piece of filter paper) is suspended from a sensitive balance into the sub-phase of the Langmuir trough; a number of forces will act on the plate, namely gravity, surface tension and buoyancy, the net force on the plate is given by **Equation 36**.^[111]

Equation 36.
$$F = \rho_w g l w t + 2\gamma(t + w)\cos\theta - \rho_L g t w h$$

where ρ_w and ρ_L are the density of the plate material and the density of the sub-phase liquid respectively, g is the gravitational constant, l , w and t are the length, width and thickness of the plate, γ is the surface tension of the sub-phase, ϑ is the contact angle of the sub-phase to the plate ($\vartheta = 0$ for filter paper in water) and h is the immersion depth of the plate into the sub-phase.

The change in the force on the plate indicates a lowering of the surface tension of the sub-phase caused by the addition of organic material to the sub-phase surface. The changes in the surface tension and changes in the net force on the plate are related by **Equation 37**.^[111]

Equation 37.
$$\Delta\gamma = \frac{\Delta F}{2(t + w)} \approx \frac{\Delta F}{2w} \text{ for } t \ll w$$

From data of the change in surface pressure (π) as a function of the sub-phase surface area a Langmuir isotherm can be generated. From this isotherm we can discern the values of surface pressure at which the various regimes of monolayer film formation can be observed (see **Figure 44**). Contrary to commonly held belief that the organic molecules in the initial

"disordered" region of the isotherm are all approximately isotropically arranged on the sub-phase surface, the molecules actually tend to form discrete regions of (ideally) monolayer material (domains) due to the intermolecular attractive forces between the individual molecules.^[112] During compression these domains are pushed together and start to interact with each other, this interaction manifesting itself by a more abrupt increase in surface pressure with respect to the ever-reducing surface area. A second increase in the isotherm gradient is observed when the regions have all come together into a single monolayer film. To force a greater degree of organisational order into the film it must be compressed further. Care must be taken once the last regime is entered as over compression will result in disruption of the monolayer, via collapse mechanisms such as buckling, bilayer formation or 3D crystallisation.

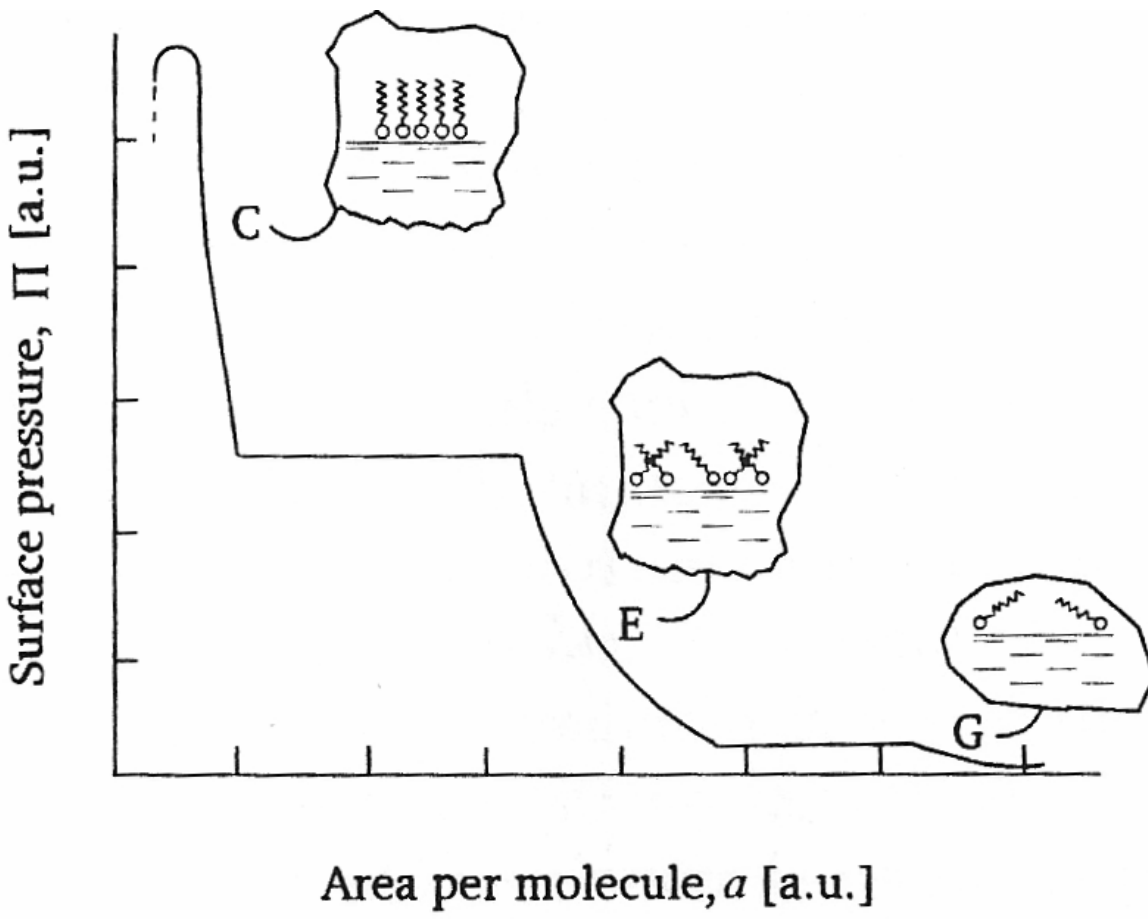


Figure 44. A typical Langmuir isotherm: c = condensed mono layer (solid), e = expanded mono layer (liquid), g = gaseous.

(Permission to reproduce this figure has been granted by Dr. M.C. Petty)

To transfer the film to a substrate the substrate is positioned with its face perpendicular to the trough surface and is then slowly dipped through the film into the sub-phase, then pulled slowly out of the sub-phase through the film. There are three types of deposition which can be observed when performing L-B deposition, depending on whether the molecules (i) adhere to the substrate surface from both the up and down sweeps of the substrate (Y-type deposition), (ii) stick as a result of the downwards dipping stage only (X-type deposition) or (iii) stick as a result of the upwards sweep only (Y-type deposition). See **Figure 45** for a graphical representation of each of these cases.

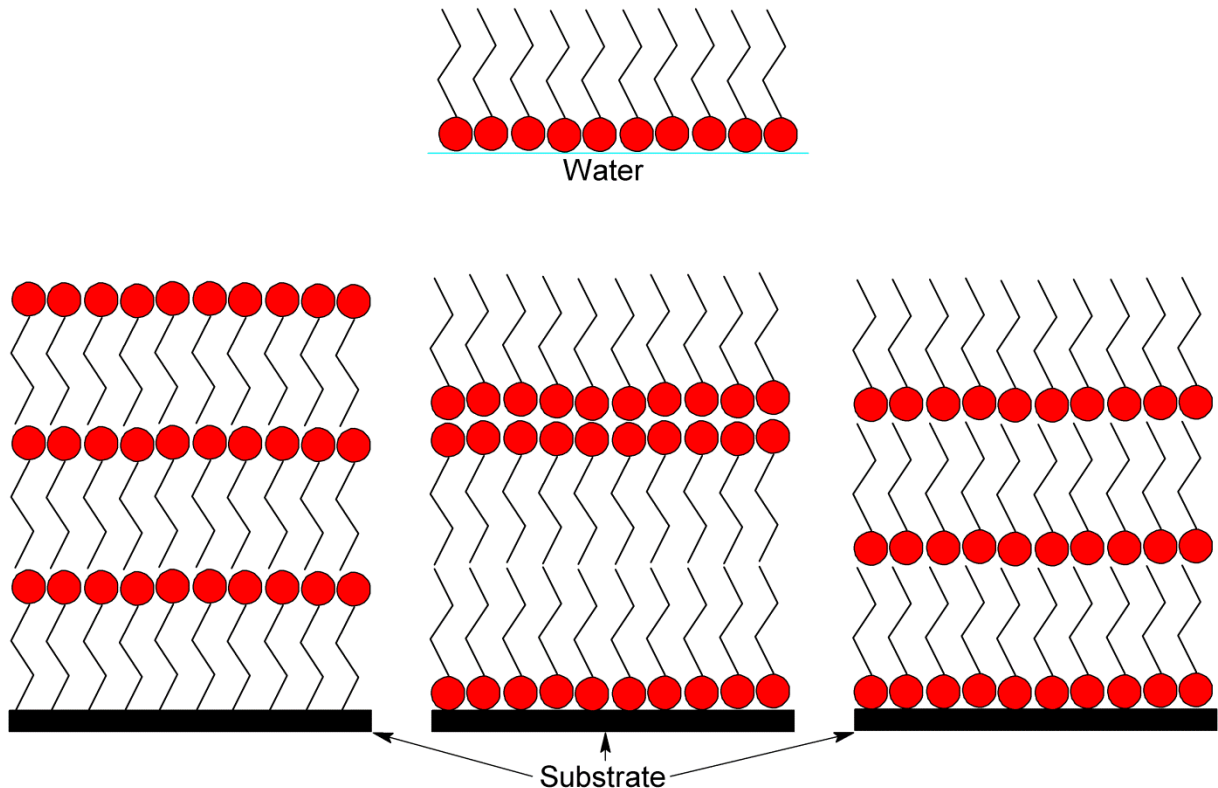


Figure 45. Diagrams of a monolayer film on water (top) and the X- (left), Y- (middle) and Z-type (right) deposition types.

The type and quality of deposition can be determined through constant monitoring of the deposition (or transfer) ratio, see **Equation 38**. Values outside the range 0.95-1.05 indicate poor film homogeneity.^[109]

$$\text{Equation 38.} \quad \tau = \frac{A_L}{A_S}$$

where τ is the deposition ratio, A_L is the decrease in film area on the sub-phase surface and A_S is the substrate surface area.

As expected the L-B technique of film deposition leads to highly ordered film formation, which is very desirable for some applications.

2.2.4 Langmuir-Schaefer Deposition

The Langmuir-Schaefer (L-S) technique is identical to the L-B technique except for the orientation of the substrate upon dipping. In L-B deposition, the substrate face is positioned perpendicular to the sub-phase, whereas in L-S the plane of the substrate is positioned parallel to the sub-phase (generally with one corner lower than the rest to allow any sub-phase material to drain off). The film achieved through L-S deposition should be of the X-type (see **Figure 45**) and the same considerations with regard to film quality and the deposition ratio are taken into account.

2.2.5 Self-Assembly from Solution

Among the simplest deposition methods to perform, self-assembly from solution involves the submergence of a substrate in a solution of the organic material of choice which will then grow a monolayer on the substrate surface. The process is in essence chemisorption (mentioned briefly in section 1.4.2) where the solute molecules form chemical bonds to the substrate surface, generally through an anchoring group. Self-assembly is generally a slow process, sometimes taking hours or days depending on the substrate, solute and temperature. Commonly observed examples of self-assembly are those of thiols on gold surfaces and silanes on oxide surfaces (see **Figure 40**). In the case of octadecyltrichlorosilane (OTS) on an Al_2O_3 surface, one of the chlorine atoms attached to the silicon of OTS leaves the molecule and bonds to the hydrogen atom of one of the OH groups at the surface of the Al_2O_3 creating a molecule of HCl while the silicon atom forms a bond to the oxygen atom remaining on the surface; this reaction occurs more efficiently in the presence of a very small amount of moisture, too much and mass polymerisation between OTS molecules occurs leading to the formation of large areas of a white solid of polymerised OTS.

2.3 Metal Anodisation

To create a layer of oxide upon a metal there are several approaches, but among the easiest, cheapest and fastest is anodisation.^[113-115] It should be noted at this point that only metals which naturally form a stable surface oxide layer (native oxide) when exposed to air (valve metals) can be anodised, metals such as aluminium, titanium and tungsten. In this process a bath is prepared with a fixed (usually platinum) electrode and a weak acid solution. The sample needing to be anodised is connected as the counter electrode to the fixed one, then a potential is applied across the two electrodes so that the sample is the most positive of the two. The acid solution will dissociate and the negative ions will flow to the sample (the anode) and oxidise it, while the positive ions will travel to the cathode. As the oxide layer grows, the resistance of the sample will increase until eventually little or no current will flow. The thickness of the oxide layer depends on the applied voltage and the thickness to voltage ratio (anodisation ratio) of the material being anodised. Schultze *et al* give a range of anodisation ratios (referred to as formation factors) for different materials in their paper on passive films.^[116] Dang *et al* show that the quality of the oxide layer in the case of aluminium is dependent on the applied voltage, the current density and the duration of anodisation; higher voltages and current densities lead to oxide layers with a greater percentage of porous material making up the total oxide thickness.^[113] The anodisation ratio of aluminium oxide in this work is taken to be $1.3\text{nm}\cdot\text{V}^{-1}$,^[115] meaning that a 5V anodisation yields a film approximately 6.5nm thick with a capacitance per unit area measured to be $640 \pm 30\text{nF}\cdot\text{cm}^{-2}$.^[117]

2.4 Contacting the Electrodes of a Organic Field-Effect Transistor

When an OFET device is complete and has been characterised using the standard methods (see section 2.6) with contact needle connections, it must then be contacted in such a way as to be compatible with any electronic equipment it is to be used in conjunction with.

2.4.1 Contacting with a Carbon-Black Paint

The main method used to wire-up the OFETs used in this work is through the use of carbon-black paint, more specifically the material Leit-C (Sigma-Aldrich). The paint contains conductive carbon and a binding agent suspended in a volatile solvent (xylene); when applied to two conductive surfaces the solvent will evaporate leaving behind the carbon particles bound together by the binding agent and will serve as a conductive bridge between the two surfaces. There are, however, problems with this method of contacting devices; firstly the OFET will be exposed to the solvent from the paint and may undergo an irreversible sensor response and secondly the solvent may dissolve the organic semiconductor and undercut the electrodes. **Figure 46** shows the contacting arrangement used in this work.

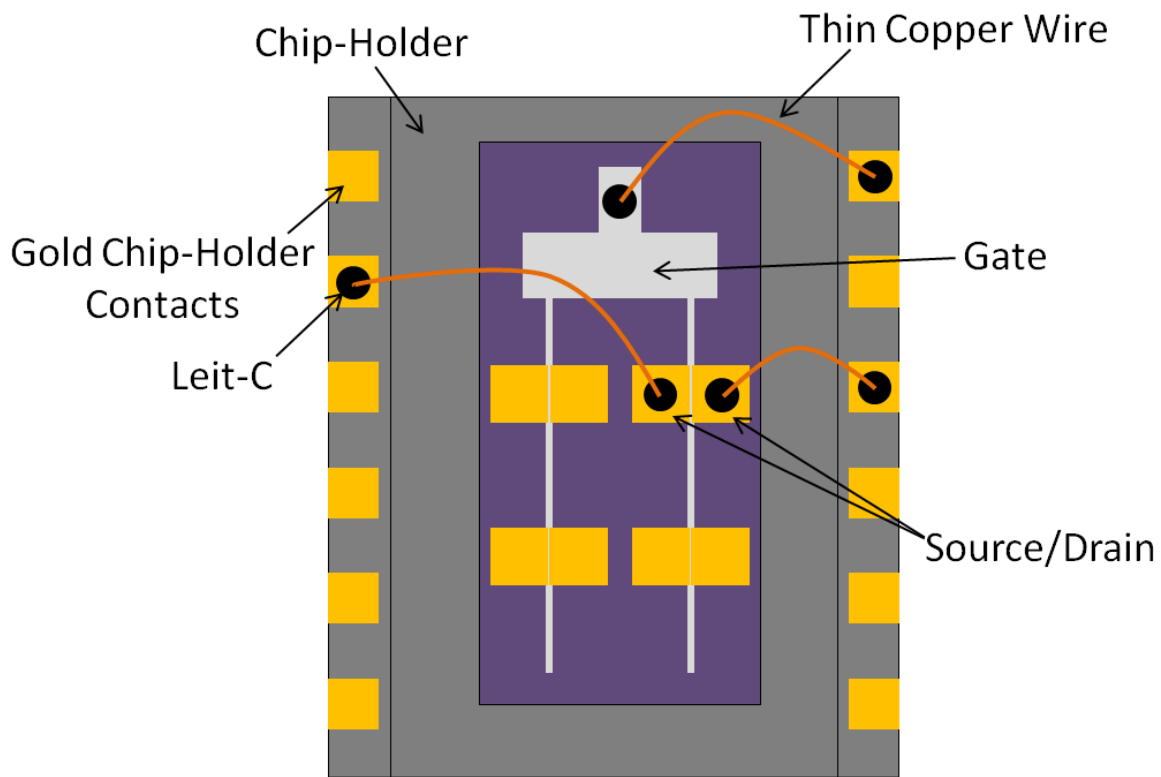


Figure 46. A diagram of the contacting arrangement used in this work.

2.4.2 Contacting with a Low-Melting Point Solder

In addition to more conventional contacting methods, OFETs can also be contacted through the use of a low melting point solder such as the alloy MCP58 (Mining & chemical products Ltd.) which has a melting point of 58°C. To use the solder the OFET must be heated to between 60 and 70°C on a hot bench then using a heated syringe the solder can be

dispensed onto the OFET and a wire can be attached. However, care should be taken when contacting devices with organic semiconductor layers that are damaged by being heated in ambient atmosphere.

2.5 Thermal Annealing Organic Semiconductors under Vacuum

A commonly used technique to improve device performance in many areas of organic electronics is the thermal annealing technique. Firstly newly grown organic thin films are placed in a vacuum vessel, once vacuum is established the samples are heated to relatively high temperatures (one to several hundreds of degrees Celsius); the heating will give the individual molecules kinetic energy and allow them to overcome any potential barriers that are holding them in a disordered configuration and rearrange themselves into a more energetically favourable (more ordered) state, as well as driving out any residual solvent (or even dopants) remaining within the organic film. Greater degrees of order in the film will improve the electric conduction properties (see section 1.1.2). It should be noted however that thermal annealing does not work for all materials, the electronic properties of some films actually get worse as a consequence of thermal annealing; thermal annealing is generally more effective when used to complement spin coating from a low boiling point solvent (as discussed in section 2.2.2). It should also be noted that some groups anneal under inert gas atmospheres rather than vacuum.

2.6 Organic Field-Effect Transistor Characterisation

When fabricating OFET devices for any application it is very important to thoroughly test them to find out how they perform and if they perform consistently or if they have some underlying faults in their construction that may affect results in later experiments. When using OFETs as sensor transducers, characterisation is effectively the sensor readout; the advantages of OFETs over conventional optical transducers are the inexpensive and simple readout circuits that can be implemented and the possibility of multi-parameter sensing readout exists for the OFETs.

2.6.1 Measuring Output Characteristics

The first stage of characterisation is to obtain an output characteristic; this is the family of drain current (I_D) verses drain voltage (V_D) plots at a fixed gate voltage (V_G) (described in detail in section 1.3.2.1), taken for a variety of gate voltages. In this work the set-up used to measure the output characteristics is a pair of Keithley 2400 source measure units connected to three tungsten needles through three Süss microtec PH100 probeheads via coaxial cables (see **Figure 47**), controlled by a computer program written in testpoint (see **Figure 48**) using a GPIB-PCI interface.

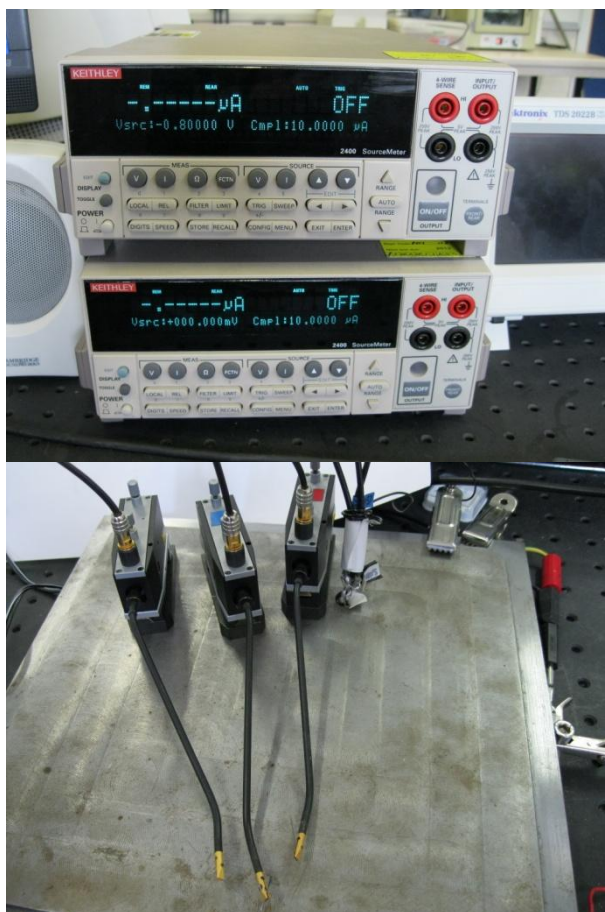


Figure 47. A picture of the Keithleys (top) and probeheads (bottom).

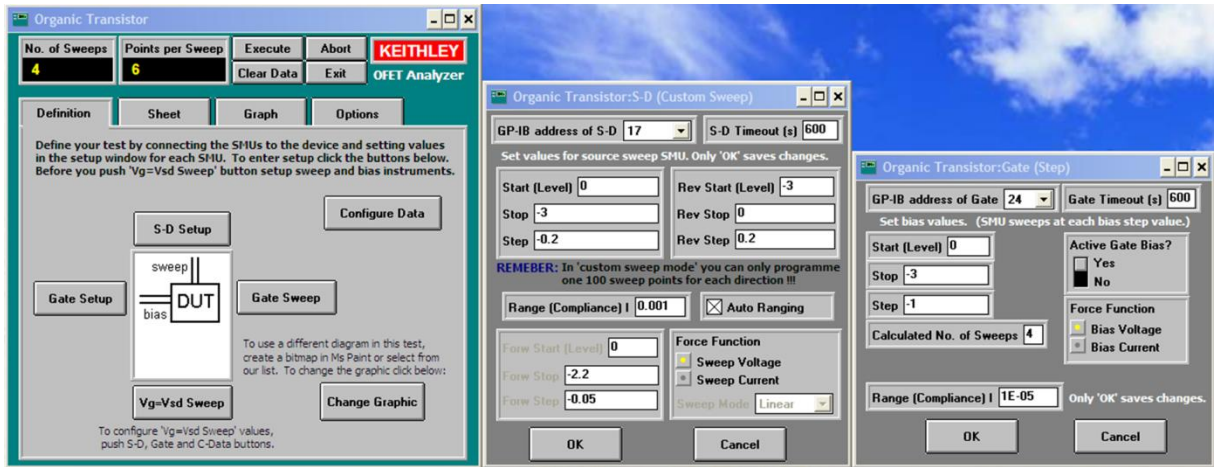


Figure 48. A screenshot of the output characteristic measurement program.

The output characteristics can be used to qualitatively analyse the OFETs for a range of common problems, as described in section 1.3.2.1.

2.6.2 Measuring Transfer Characteristics

The second stage of characterisation is to obtain a saturated transfer characteristic; this is a measurement of the saturated drain current ($I_{D,Sat}$) response to changing gate voltage (V_G) at a drain voltage in the saturation region ($V_{D,Sat} \geq V_G$), it can be realised using the same set-up as the output characterisation in section 2.6.1 (Figure 47), but using a measurement protocol provided by a different part of the testpoint program (see Figure 49).

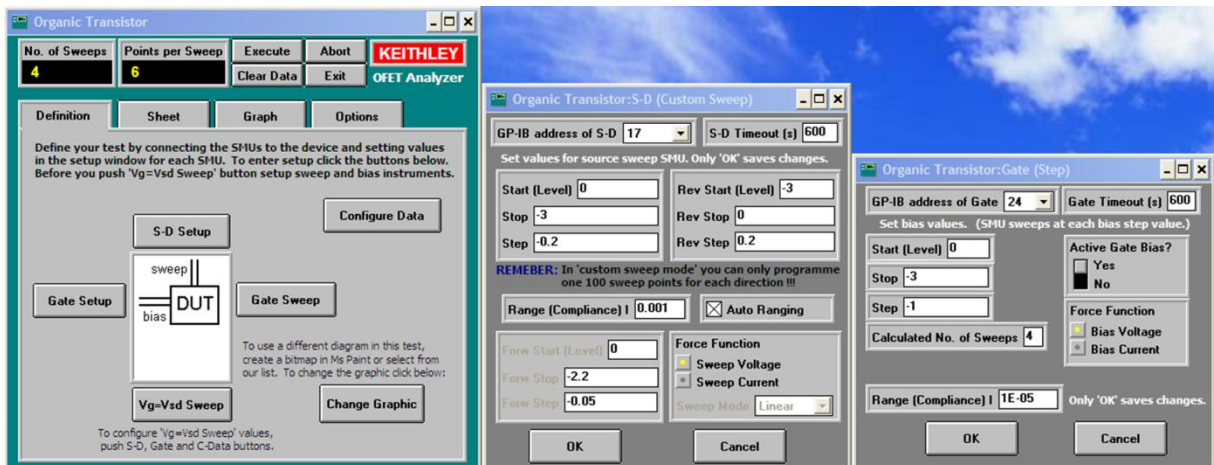


Figure 49. A screenshot of the transfer characteristic measurement program.

The transfer characteristics can be used to quantitatively analyse the OFETs to extract a number of important quantities such as carrier mobility and threshold voltage, as described in section 1.3.2.2.

2.6.3 Gain Method Characterisation

When using OFETs in a vapour sensing application, dynamic monitoring is required to track changes in the various parameters of the OFET. Thus, the gain method characterisation scheme was developed by Dost *et al.*^[117] The scheme consists of a circuit, pictured in **Figure 50**, and a computer interface. The method uses three resistors, a pull-down resistor in series with the OFET in a voltage divider arrangement (R_P) and a pair of resistors that control the gain of an operational amplifier (op-amp) (R_{fix} and R_{trim}); the source of the transistor is driven with a square wave voltage and the gain (given by **Equation 39**) is constantly adjusted (through the resistor R_{trim}) to match the drain voltage (V_D) to the source voltage (V_S) as $G \cdot V_D = V_S$.

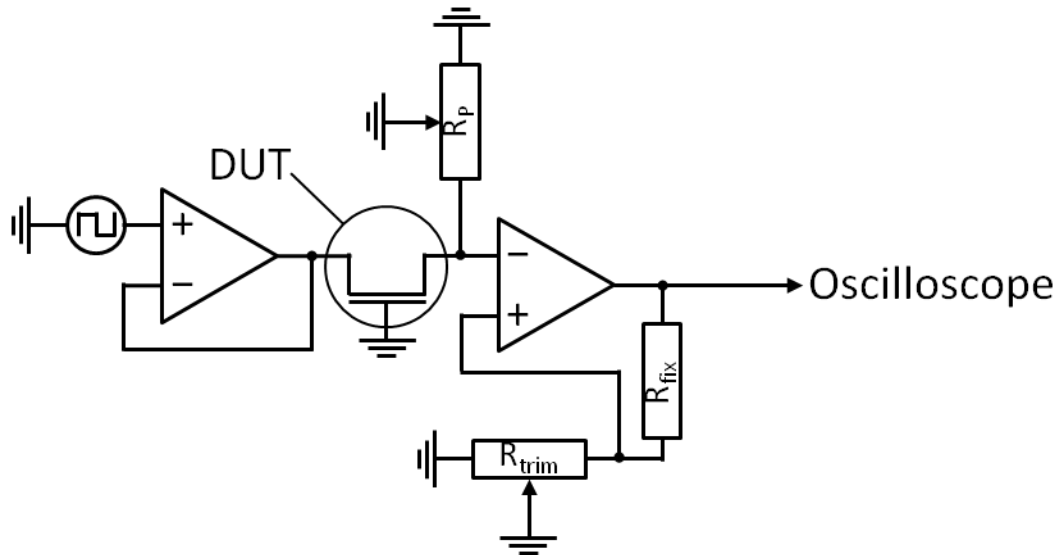


Figure 50. Circuit diagram of the gain method circuit.

$$\text{Equation 39.} \quad G = 1 + \frac{R_{fix}}{R_{trim}}$$

where G is the gain factor, R_{fix} is the value of the fixed resistor and R_{trim} is the value of the adjustable resistor.

Therefore through use of the gain values and the modification of **Equation 21** that pertains to this circuit (**Equation 40**) the mobility, threshold and even channel resistance values can be constantly monitored; this allows multi-parameter monitoring of OFETs under vapour exposure.

Equation 40.

$$\frac{V_s}{G} = \frac{W}{2L} R_p \mu C_i (V_s - V_T)^2$$

where G is the gain factor, V_s is the drive voltage, W is the channel width, L is the channel length, R_p is the value of the pull-down resistor, μ is the carrier mobility, C_i is the capacitance per unit area of the gate insulator and V_T is the threshold voltage.

To calculate the mobility and threshold the computer program monitoring the circuit effectively performs a linear fit to a plot of $(V_s/G)^{1/2}$ versus V_s for a range of V_s values, the gradient of the fit is proportional to mobility and the x-axis intercept of the fit is proportional to the threshold voltage.

2.6.4 Chemi-Resistor Characterisation

When using a chemi-resistor as a vapour sensor it is important to be able to reliably monitor the change in its resistance, towards this end the device can be used as part of a square-wave generator circuit (see **Figure 51**); this circuit provides a simple, low-cost, real-time method of resistance monitoring that will work for a wide range of resistances and would be simple to automate using a computer to monitor the frequency output.

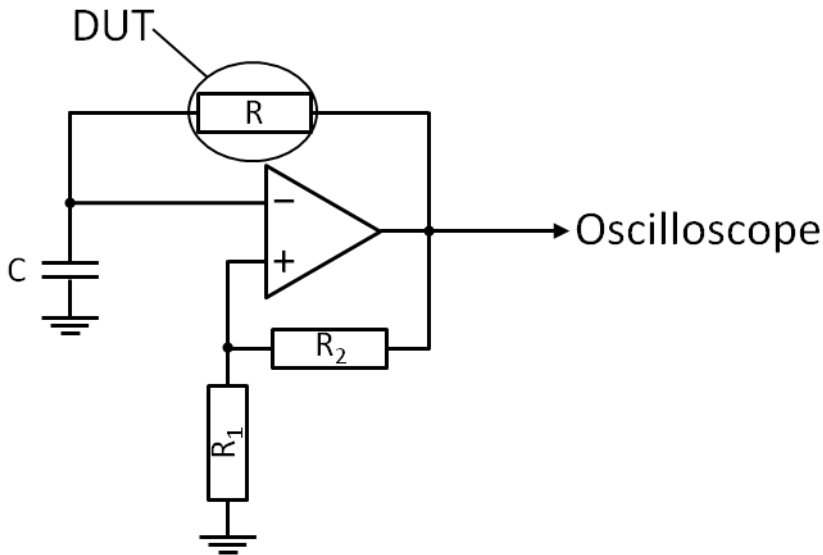


Figure 51. Square wave generator circuit diagram.

The equation for the frequency of the square wave output is given in **Equation 41**, it can be seen from this equation that the frequency of the square wave is inversely proportional to the resistance (R) of the chemi-resistor. Therefore by monitoring the change in frequency of the output wave, the change in device resistance is also monitored.

Equation 41.

$$\frac{1}{f} = 2RC \ln \left[\frac{1 + \left(\frac{R_1}{R_1 + R_2} \right)}{1 - \left(\frac{R_1}{R_1 + R_2} \right)} \right]$$

where f is the square wave frequency, R is the resistance of the chemi-resistor, C is the value of the capacitor and R_1 and R_2 are the values of the resistors in the potential divider.

2.7 Organic Materials Used in this Work

Many different organic materials have been used throughout the work reported within this doctoral thesis, this section will give a complete account of all of them. Firstly the conventional organic semiconductors have already been discussed in section 1.2.2, the ones actually used in within the work reported here are pentacene (section 1.2.2.1.1), PDI8-CN₂ (section 1.2.2.1.2) and P3HT (section 1.2.2.2.1). A total of 5 different porphyrin molecules have been used in the work presented here as sensitizers or organic semiconductors. Their structures are shown in **Figure 52**, **Figure 53** and **Figure 54**.

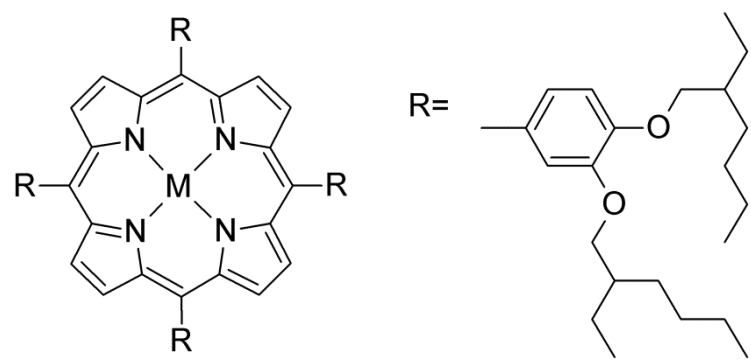


Figure 52. The chemical structure of metallated EHO (5, 10, 15, 20-Tetrakis (3, 4-bis (2-ethylhexyloxy) phenyl)-21H, 23H-porphine), M = Co or Au.

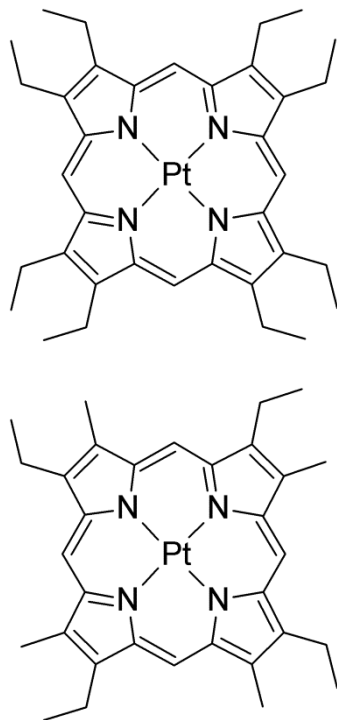


Figure 53. The chemical structures of PtOEP (Platinum (II) 2,3,7,8,12,13,17,18-Octaethyl-21H,23H-porphine) (top) and PtEP-I (2,7,12,17-Tetraethyl-3,8,13,18-tetramethyl-21H,23H-porphine) (bottom).

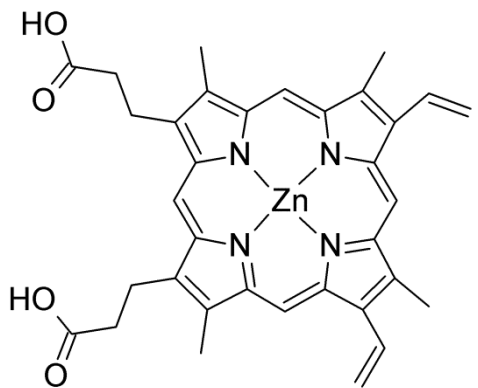


Figure 54. The chemical structure of PPIXZn(II) (Zinc (II) 3,7,12,17-Tetramethyl-8,13-divinyl-2,18-porphinedipropionic acid).

Only a single phthalocyanine has been used in the work reported here, the structure of this phthalocyanine is shown in **Figure 55**.

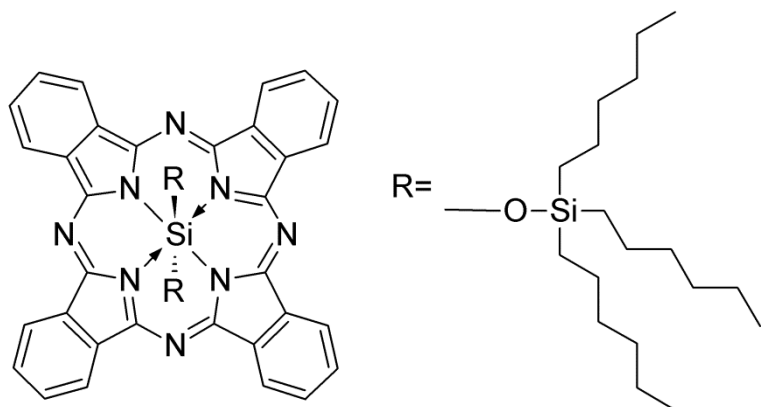


Figure 55. The chemical structure of Si(IV)PTSO (Silicon (IV) phthalocyanine bis (trihexylsilyl oxide)).

A pair of calixarenes have been used in this work as sensitizers and encapsulation; the structures of the calixarenes are shown in **Figure 56**.

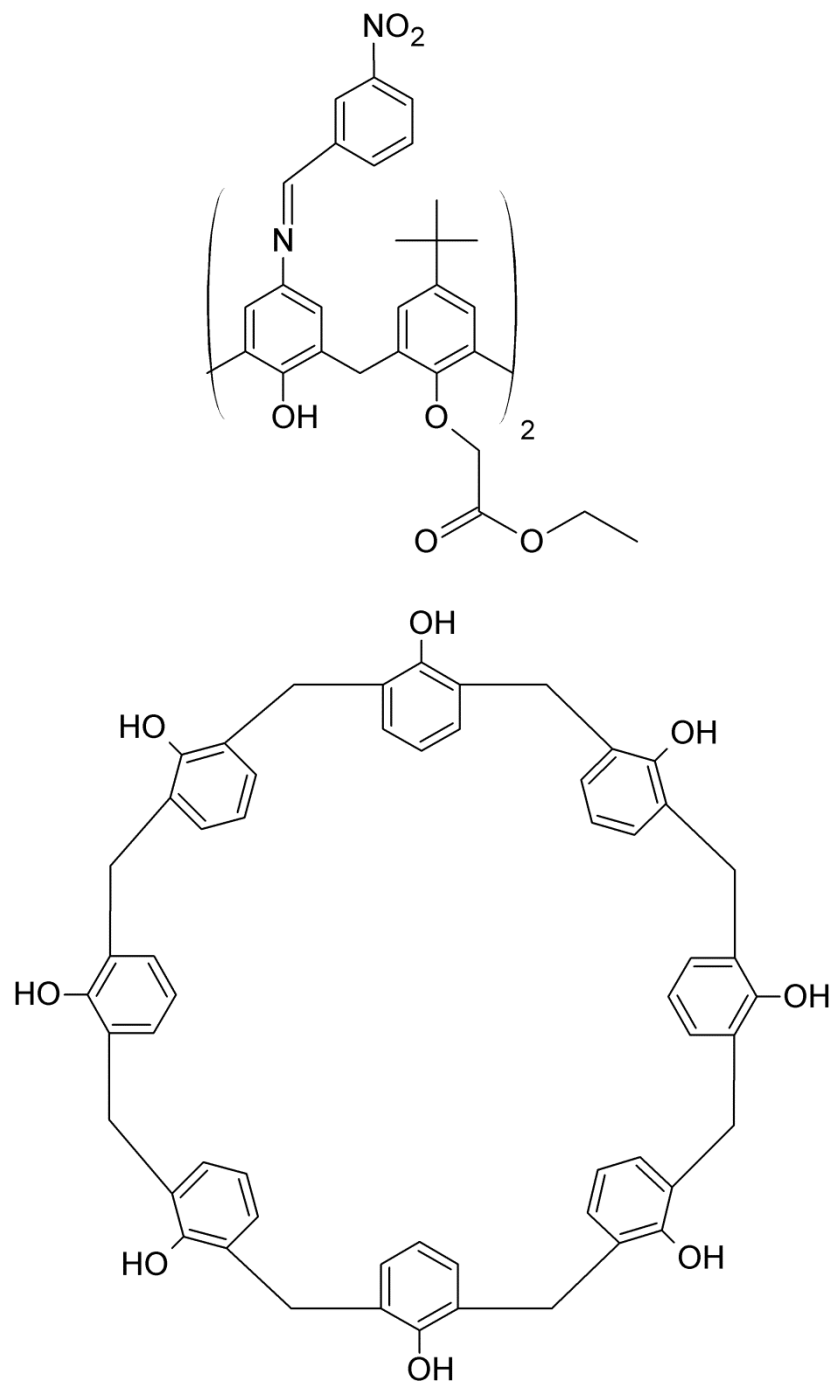


Figure 56. The chemical structures of calixarene 1 (5,17-(34-nitrobenzylideneamino)-11,23-di-*tert*-butyl-25,27-diethoxycarbonyl-methyleneoxy-26,28dihydroxycalix[4]arene) (top) and calixarene 2 (calix[8]arene) (bottom).

3 Instrumentation and Equipment Developed for this Work

To allow the characterisation of OFETs and the monitoring of their parameters under controlled vapour exposure, new measurement systems had to be developed and the existing vapour exposure rig had to be extensively modified. The new systems will be discussed here.

The current to voltage converter was taken from a standard electronics circuit and turned into the characterisation scheme by myself, the “555” based scheme was designed by Dr. Martin Grell and both were turned from circuit diagrams to physical working circuits by myself. Data was collected from the current to voltage converter by myself and the data from the “555” based system was collected in collaboration with Dr. Delia Puzzovio and Dr. Martin Grell.

The vapour exposure system was originally designed by Dr. Alan Dunbar but was extensively modified by me to the extent that only the mass-flow controllers and the program running them were left from the original exposure system.

3.1 Electronic OFET Characterisation Schemes

The ability to accurately monitor the electronic properties of an OFET dynamically during vapour exposure is a necessity for vapour sensing experiments. Towards this end the monitoring systems described here were developed.

3.1.1 Current to Voltage Converter Characterisation Scheme

The current to voltage converter scheme was designed to be the first step towards the development of a low-cost, portable real-time characterisation scheme. The core of the characterisation scheme is based around a simple operational-amplifier (op-amp) circuit, the op-amp at the centre of the circuit is an AD549L (Analogue devices), chosen for its ultralow bias current (current lost when feeding it into the op-amp) of 60fA.^[118] In the op-

amp circuit (see **Figure 57**) the OFET sample is positioned such that its source electrode is connected to a function generator (Blackstar Jupiter 2000), which outputs a sinusoidal voltage (V_{in}) that oscillates between $\pm V_{max}$ (determined by the OFET being tested) at 70Hz (the reasons for this type of drive are discussed in section 5.2.1.3.1); its drain electrode is connected to the inverting input of the op-amp and its gate is on ground. The op-amp itself has its non-inverting input at ground and its output linked to its inverting input through a feed-back resistor (R_f), realised through the use of a dial-up resistance box (Time electronics 1040). An oscilloscope is used to read the output of the op-amp (as well as the drive voltage).

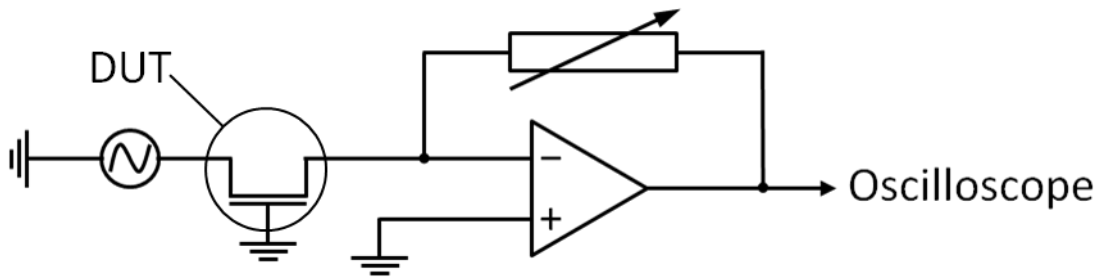


Figure 57. Current to voltage converter circuit diagram.

The operating principle of the circuit is that the op-amp will compare the inputs from both the inverting and non-inverting terminals and try to match them. Towards this end it will create a voltage that will drive a current through the feedback resistor equal in magnitude but opposite in sign to the current that is fed into the inverting input in order to create a virtual ground at the inverting input. The output voltage of the op-amp (V_{out}) is given by: $V_{out} = -R_f I_D$, where I_D is the drain current of the OFET. As the gate is on ground and the drain is on virtual ground the relationship: $V_{in} = -V_G = -V_D$ will give the gate voltage (V_G) and drain voltage (V_D) at all times, and as $V_G = V_D$ at all times the transistor will always be in the saturation regime (when the OFET is on, $V_{in} \geq V_T$). The frequency of 70Hz was chosen as it is low enough to take ‘quasi-static’ readings while being high enough to provide real-time characterisation data; it is also far enough from the mains-electricity frequency of 50Hz as not to pick up any significant noise.

The OFET under test will switch on once the V_{in} reaches threshold then switch off once V_{in} falls below threshold again, the threshold can therefore be deduced from a plot of the

oscilloscope traces of source voltage against time and V_{out} against time as the value of V_{in} where V_{out} begins to sharply rise (see **Figure 58**).

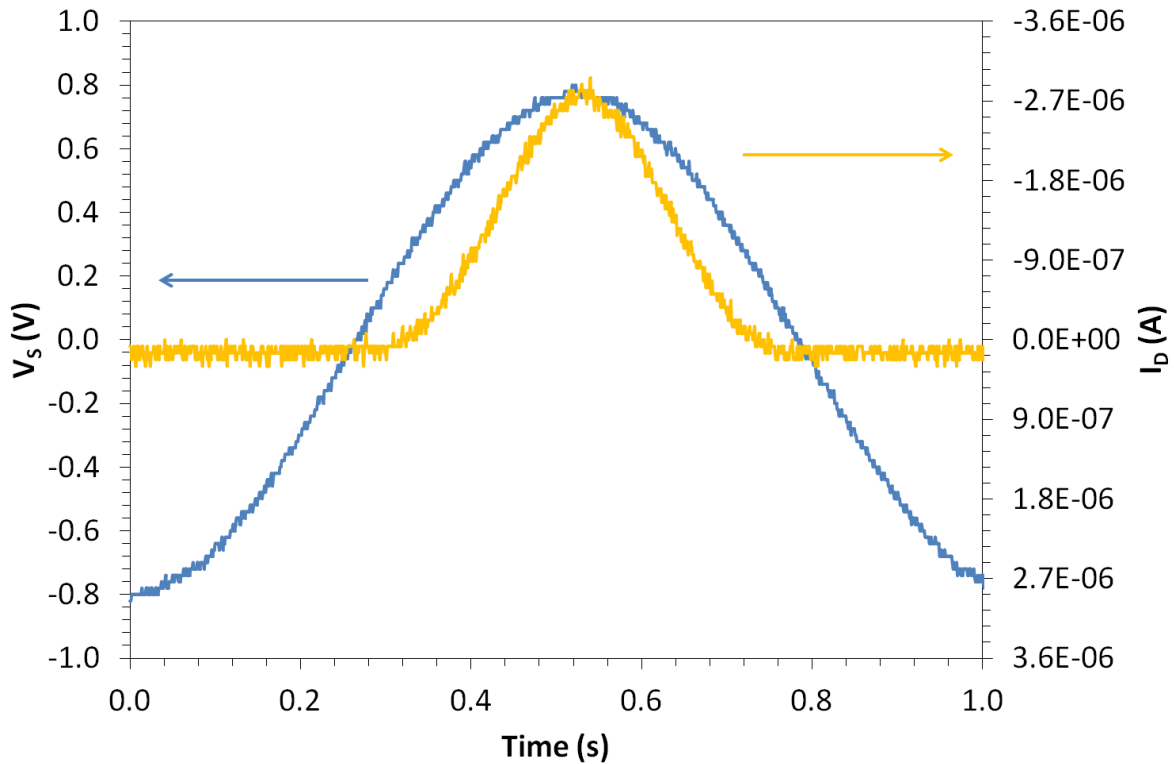


Figure 58. An example p-type current to voltage converter trace.

From a modification of **Equation 21** the mobility of the OFET can be extracted using the peak voltages of any on-cycle and the **Equation 42**.

$$\text{Equation 42.} \quad \mu = \frac{2L}{WR_f C_i} \frac{|V_{peak}|}{(|V_{max}| - |V_T|)^2}$$

where μ is the carrier mobility, L is the channel length, W is the channel width, R_f is the feedback resistance, C_i is the capacitance per unit area of the gate insulator, V_{peak} is the value of V_{out} at V_{max} , V_{max} is the maximum value of V_{in} in the on-cycle and V_T is the threshold voltage of the OFET.

During vapour sensing runs the peak of the V_{out} trace can be matched to the peak of the V_{in} trace on the screen of the oscilloscope through adjustment of the feedback resistor, this allows dynamic monitoring of the channel on-resistance of the OFET throughout vapour sensing experiments. Practically it is useful to set the V_{out} channel of the oscilloscope to 10

times less $V \cdot \text{div}^{-1}$ than the V_{in} channel, this means that the relationship $R_{on} = 10R_f$ is used to extract the OFET channel on-resistance (R_{on}) from the feedback resistance. The mobility and threshold can be extracted from ‘screen-shots’ of the traces from the oscilloscope by eliminating time as a parameter and plotting the square root of the output current against drive voltage and using **Equation 21** (see **Figure 59**).

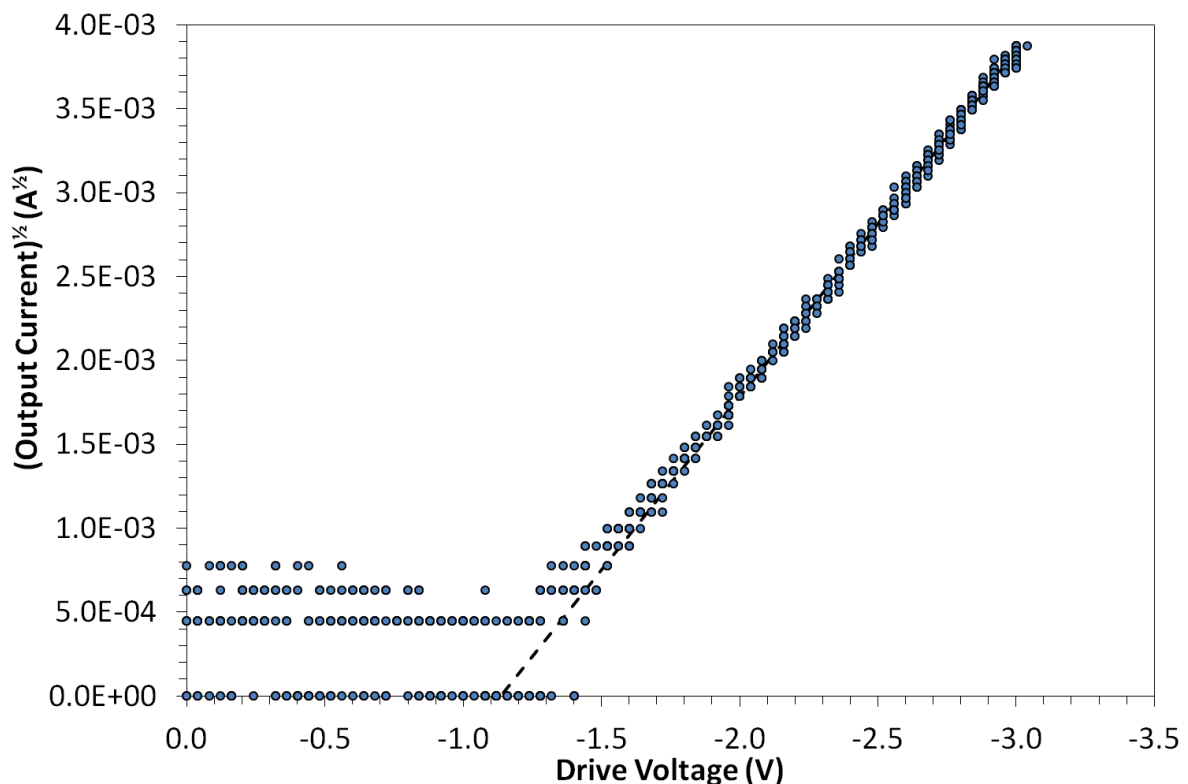


Figure 59. An example p-type saturated transfer characteristic from current to voltage converter data.

When used to monitor vapour sensing experiments in the work discussed here, the results will be expressed as a percentage response, calculated as in **Equation 43**.

$$\text{Equation 43.} \quad \% \text{Response} = \frac{R_{after} - R_{before}}{R_{before}} \cdot 100$$

where R_{before} is the resistance box value before a vapour exposure and R_{after} is the resistance box value after a vapour exposure.

3.1.2 555 Chip Based Characterisation Scheme

The 555 chip^[119] based characterisation scheme is the first step in the development of a wireless characterisation scheme;^[120] by necessity the scheme is low power (less than $200\mu\text{W}$) and can be powered by two AA batteries. The 555 chip itself was chosen as it only draws a low supply current ($\sim 80\mu\text{A}$), can work at low voltages (3-16V) and only requires low trigger, threshold and reset currents ($\sim 20\text{pA}$).

The 555 chip is wired-up in a configuration (shown in **Figure 60**) which will cause it to oscillate at a frequency determined by the OFET.

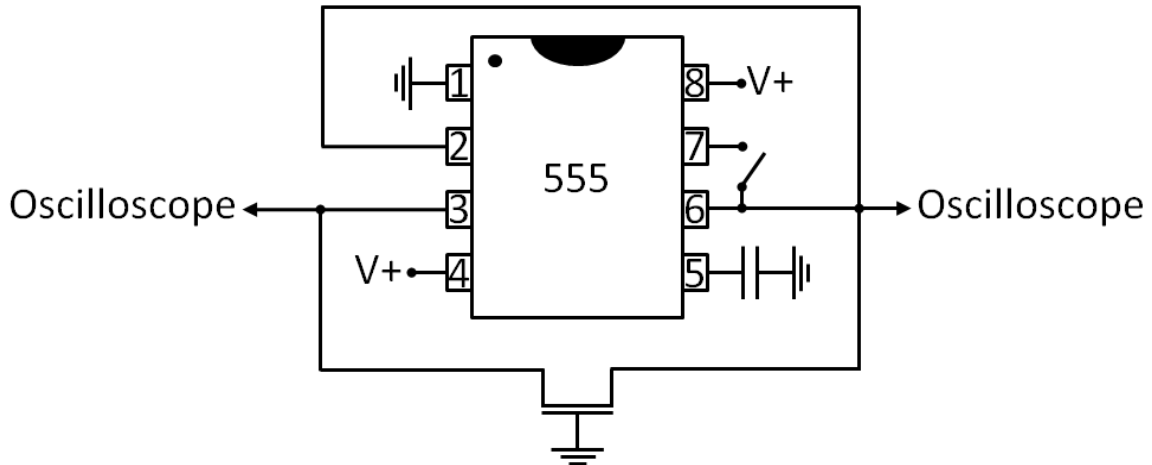
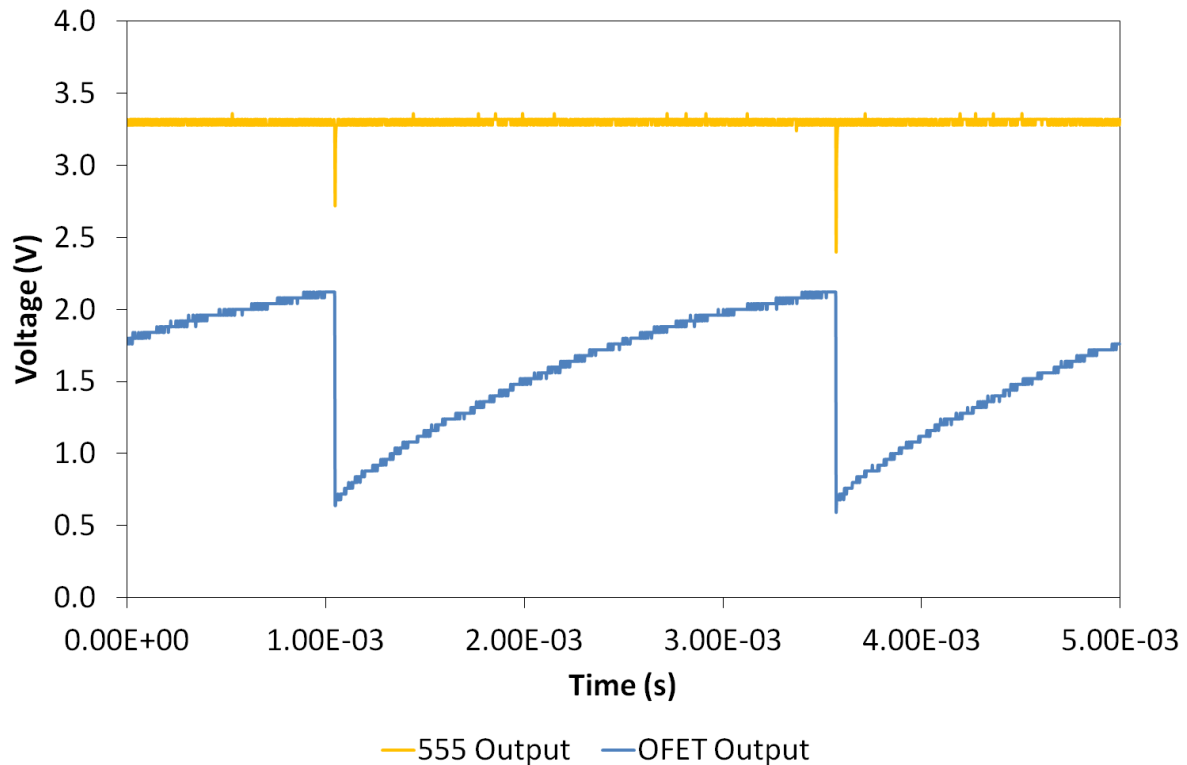


Figure 60. A circuit diagram of 555 circuit.

The drive voltage has a maximum that is determined by the supply voltage of the chip ($V+$). The circuit operates by firstly the OUTPUT (pin 3) of the 555 applying $V+$ to the source electrode of the OFET, switching on the OFET and causing the drain electrode's parasitic capacitance to charge, thus causing drain voltage (V_D) to rise; once drain voltage reaches $\frac{2}{3}V+$ the OUTPUT switches off (goes to 0V) and thus switches off the OFET causing the parasitic capacitance to discharge (the $\frac{2}{3}V+$ as the switching threshold is a hard-wired feature of the 555 chip). If the 555's DISCHARGE (pin 7) is connected to the drain, then the drain will be linked to ground as OUTPUT goes to 0V and thus causes the parasitic capacitance to discharge very quickly therefore causing the drain voltage to drop very quickly too. If the DISCHARGE pin is disconnected the parasitic capacitance must discharge across the OFET device through the OUTPUT, so the drain voltage will drop much more

slowly. As the drain voltage falls below $\frac{1}{3}V_+$ the TRIGGER (pin 2) will be activated and OUTPUT will be switched back to V_+ . Typical traces obtained from the 555 scheme in both DISCHARGE connected and disconnected configurations are shown in **Figure 61**.



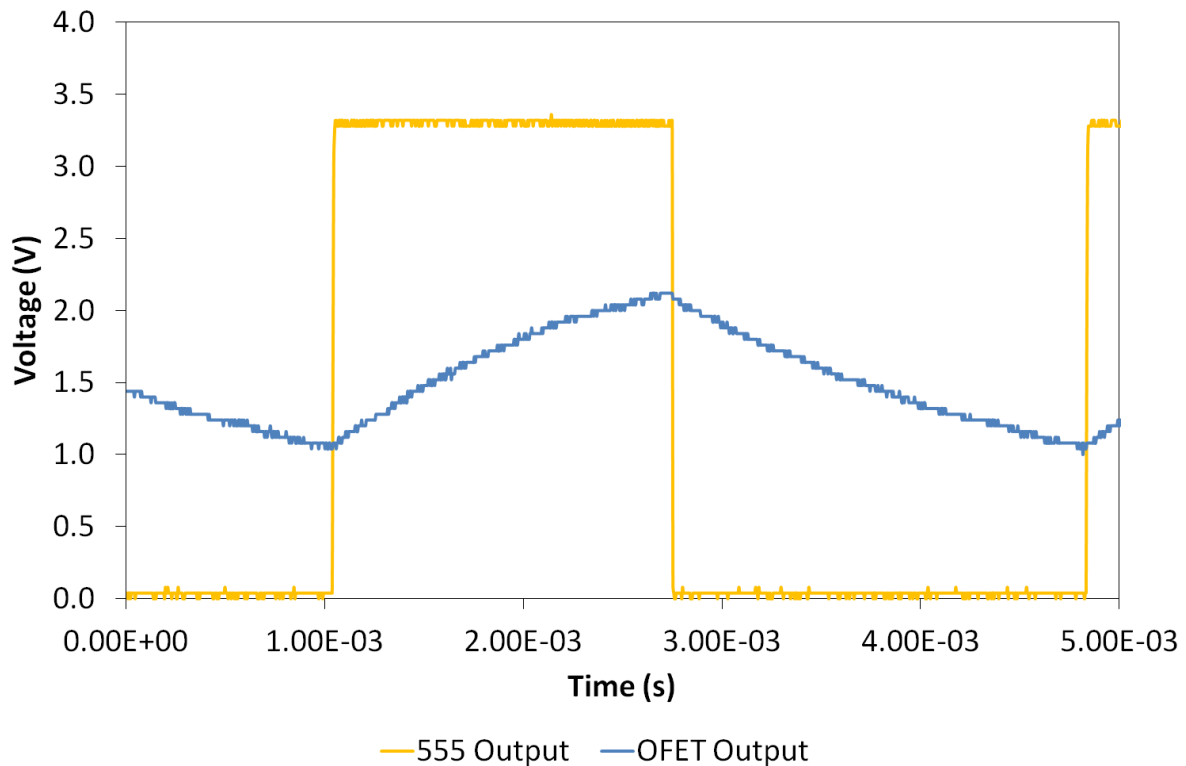


Figure 61. Oscilloscope traces of the DISCHARGE connected (top) and disconnected (bottom) cases.

This type of circuit is commonly known as a relaxation oscillator and the frequency (when a conventional resistor and capacitor pair is used in the place of an OFET) is given by **Equation 44**.

$$\text{Equation 44.} \quad f = \frac{1}{2 \ln(3) RC}$$

However in the case of the 555 and OFET implementation the situation becomes more complex as the OFET has both internal resistance and capacitance, so all that can be said without more extensive investigation is that as drain current (I_D) is proportional to the resistance of the OFET (see **Equation 21**), then the frequency should scale with I_D and in cases of constant threshold voltage the frequency should scale with mobility.^[120]

3.2 Vapour Exposure

Accurate and highly controllable vapour exposure is a very important requirement when performing vapour sensing experiments. Thus, existing exposure equipment had to be

modified and new equipment created; this section will describe the advances made during this work.

The boiling points and vapour pressures of the analytes used in this work are presented in **Table 5**.

3.2.1 Saturated Vapour Generation and Dilution

The creation of analyte vapour from a liquid analyte and the dilution of the analyte vapour are achieved through the use of controlled dry nitrogen gas flow (evolved from a liquid source), a “nitrogen-bubbler” vessel and the mixing of pure nitrogen with the evolved saturated vapour; a diagram of the entire gas flow system is shown in **Figure 62**. To generate saturated vapour from the liquid analyte it was decided that rather than passing a flow of nitrogen gas across the top of the liquid analyte, the nitrogen would be bubbled through the liquid analyte to agitate it and stimulate vapour release, to facilitate this a “nitrogen-bubbler” vessel was devised; the nitrogen bubbler is a cylindrical glass vessel with a fitted glass, stopper-like, lid containing both a nitrogen inlet and outlet pipe (see **Figure 63**). The seal between the lid and the main body of the vessel is assured by the use of ground-glass surfaces and a PTFE sleeve.

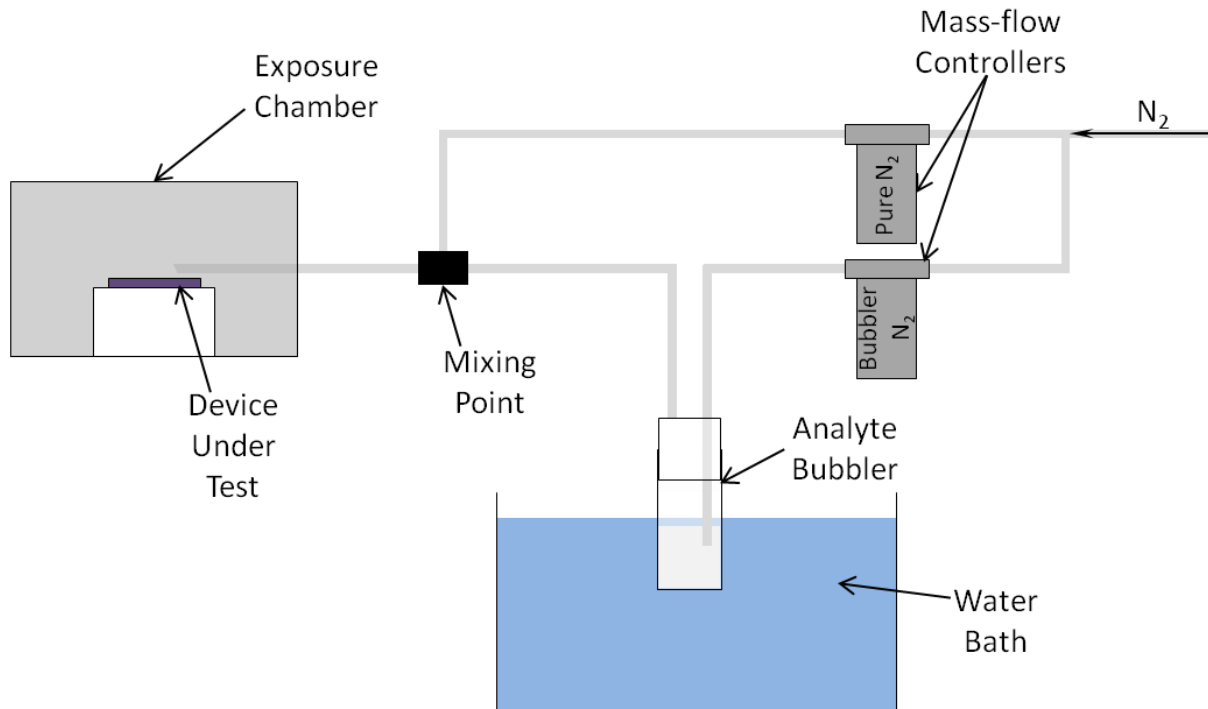


Figure 62. A diagram of the gas flow system.

The nitrogen inlet pipe is set to be well below the surface of the liquid analyte so that nitrogen passed through it will bubble through the analyte, picking up vapour and agitating the analyte surface when bubbles break it (a sparger can be used to make smaller bubbles with a greater surface area to volume ratio if required). The outlet pipe is set flush with the top of the lid of the vessel.



Figure 63. A picture of the bubbler vessel.

Control of the vapour concentration is achieved through two separate methods: control of the analyte temperature and the dilution ratio of saturated analyte vapour with pure nitrogen gas. The bubbler vessel is kept submerged in a temperature controlled water bath (Clifton NE4-D stirred) at all times to maintain a constant temperature, allowing calculation of the saturated vapour pressure (see section 1.4.1); a bath of ice-water can also be used to obtain smaller vapour pressures outside of the water bath's normal capacity. After the saturated vapour leaves the bubbler vessel it is taken to a mixing point where it is mixed with pure dry nitrogen in a pre-programmed ratio to obtain the desired concentration. The relative nitrogen flow of both the analyte and pure nitrogen gas-lines is controlled by a pair of mass-flow controllers (Tylan FC260) controlled by a LabVIEW program via a pair of USB controllers (U12 Labjack), see **Figure 64**.

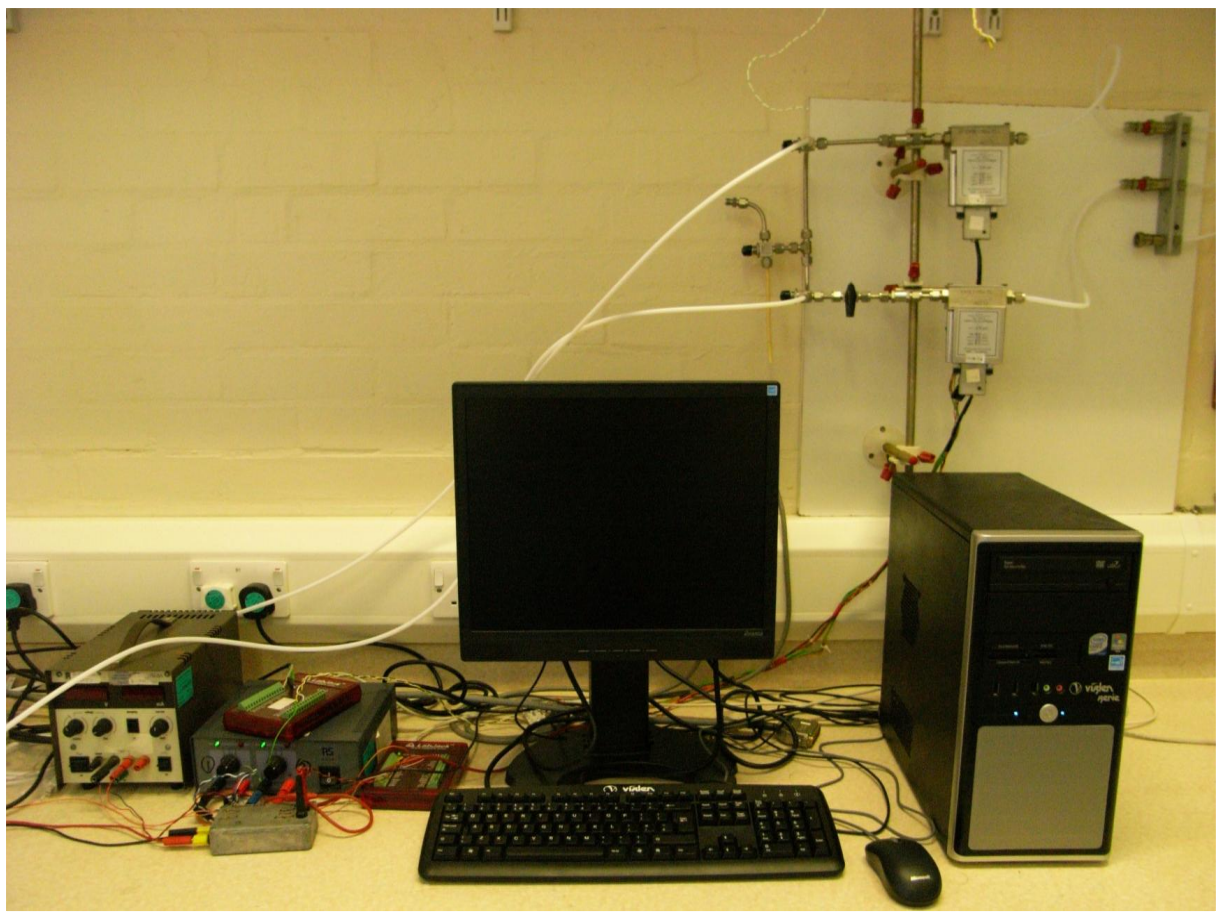


Figure 64. A picture of the mass-flow controller setup.

The gas-lines themselves are $\frac{1}{4}$ inch OD (outer-diameter) PFA (perfluoroalkoxy) piping with a wall thickness of 0.47inch (Swagelok) and standard Swagelok stainless steel fittings. Also in the gas lines are three one-way check-valves (Swagelok) to prevent the backflow of gas in the system, the valves have PTFE coated insides and a cracking pressure of 1psi; the three valves are positioned before and after the bubbler on the analyte line and before the mixing point on the pure nitrogen line. Once mixed the analyte dilution is fed into an exposure chamber and allowed to flow over device under test, in the case of an OFET the gas flow is directed over the channel of the device being tested.

3.2.2 Gas Flow, Heating and Electrical Monitoring within the Exposure Chamber

Exposure of OFET samples to analyte gasses was done in a specially designed exposure chamber (see **Figure 65**); the chamber is constructed mainly of aluminium and is lined in

PTFE to avoid adsorption of analyte to the metal during exposure cycles then desorption during recovery cycles. The analyte gas is delivered into the chamber through a PFA pipe shaped to direct the gas flow directly onto the OFET sample under test, the gas is allowed to leave the chamber through an outlet pipe into a fume-hood (Labcaire aura 750L) and the external atmosphere is kept out by a large, chemically resistant, o-ring between the lid and main body of the chamber; the chamber has a volume of 0.8m^3 and so it takes 1.6 minutes to completely cycle the chamber's atmosphere at the normal purging flow rate of $500\text{ml}\cdot\text{min}^{-1}$; vapour exposure is performed at a tenth the flow rate ($50\text{ml}\cdot\text{min}^{-1}$) to allow saturated analyte vapour to be evolved. Electrical connections can be made to the sample through electrical feed-throughs inserted around the circumference of the entire chamber. The chamber itself is kept at ground potential to create an effective Faraday cage when clips are applied between the body and lid of the chamber, thus protecting the devices tested within from RF interference. All external cabling between the chamber and any testing circuit is generally co-axial with its shielding to ground potential to continue the RF shielding effective in the chamber.

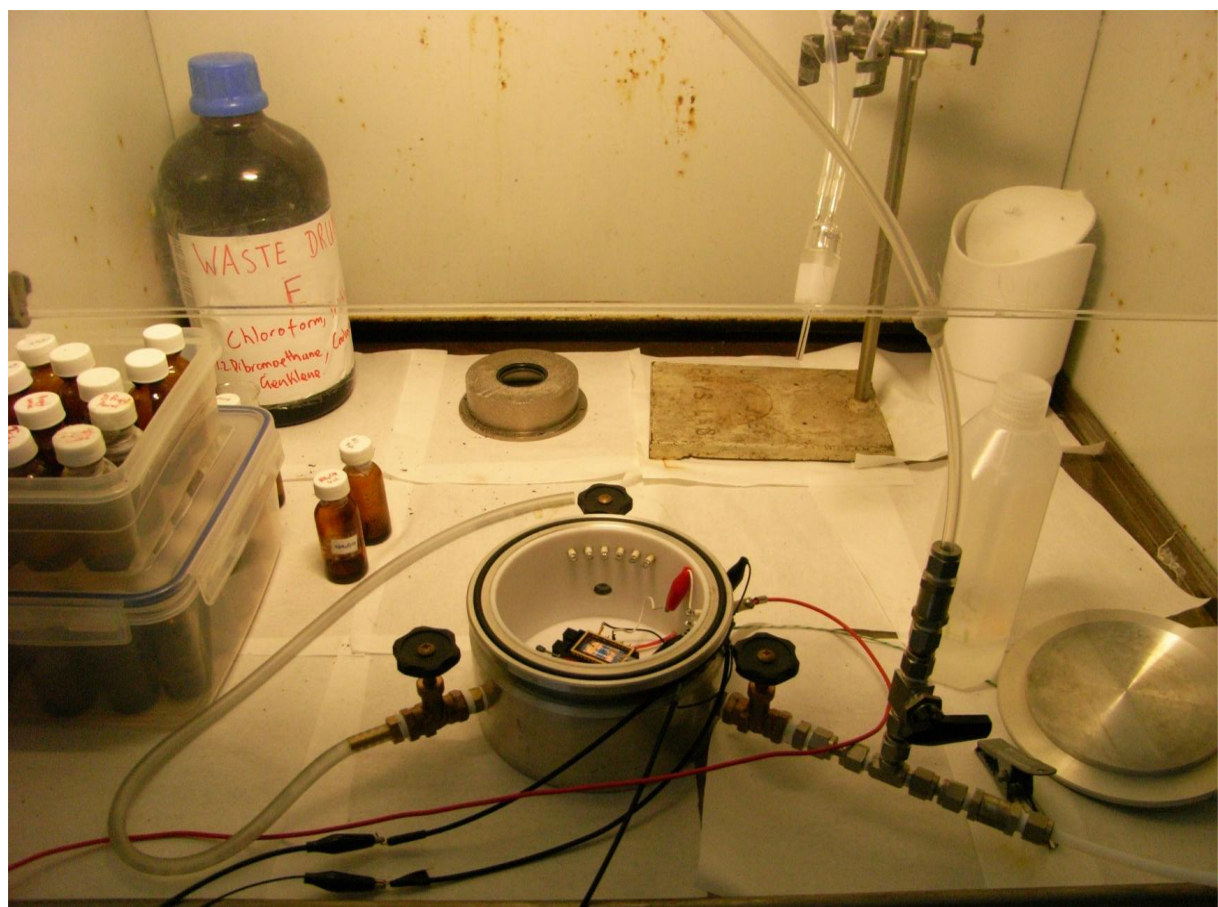


Figure 65. A picture of the exposure chamber.

4

Hydrophobic Surface Modification Studies

The data shown in this chapter was collected from OTS and OCS samples prepared completely by myself and HMDS samples prepared in collaboration with Mr. Adam Hobson. The contact angle date was collected in collaboration with Dr. Stuart Brittle.

To ascertain the self-assembly time required for the silane used in the work described here as OFET surface modification, an investigation was undertaken. The contact angle of water on the surface was used as an indicator of when self-assembly was complete, as the contact angle should saturate when a monolayer is achieved. The investigation was carried out using not only octadecyltrichlorosilane (OTS) assembled on Al_2O_3 surfaces (the combination used for OFETs), but also using two other silanes: the commonly used hexamethyldisilazane (HMDS)^[7, 8] and the monochloro version of OTS: chloro(dimethyl)octadecylsilane (OCS), as well as both Al_2O_3 and SiO_2 surfaces. The substrates were first cleaned as described in section 2.1, after which the substrates which would become the Al_2O_3 surfaces had 100nm of Al thermally evaporated onto them and were then anodised as described in section 2.3 to 5V to grow the oxide layer. The self-assembly of OTS and OCS was performed by submerging the substrates into a $2.58 \times 10^{-2}\text{M}$ ($10\text{mg}\cdot\text{mL}^{-1}$ in the case of OTS) solution of each silane in cyclohexane under a nitrogen atmosphere in a low quality glove box; upon extraction each sample was rinsed in fresh cyclohexane to remove any non-bonded material and then dried. For each surface modification chemical and surface combination six samples were prepared using different self-assembly durations, the durations were as follows: 10 minutes, 30 minutes, 60 minutes, 120 minutes, 240 minutes and 480 minutes. The HMDS self assembly was performed by placing the substrates into sealed Petri dishes with a small open vial containing enough liquid HMDS to establish a saturated environment.

After fabrication each sample then had its hydrophobicity tested as a measure of the completeness of the self-assembled monolayer, the hydrophobicity was tested by measuring the contact angle of a DI water droplet with the surface. The contact angle is related to the surface energies of the water droplet and substrate through Young's equation (**Equation 45**) an expression of the contact angle in terms of the interfacial tensions due to the interactions of the solid surface, liquid droplet and the gaseous surroundings.

Equation 45.

$$\theta_C = \cos^{-1} \left(\frac{\gamma_{SG} - \gamma_{SL}}{\gamma_{LG}} \right)$$

where γ_{SG} is the interfacial tension between the surface and the air, γ_{SL} is the interfacial tension between the surface and the droplet and γ_{LG} is the interfacial tension between the droplet and the air.

To measure the contact angles the KSV instruments “Attension Theta” was used, in effect this equipment is a high contrast camera connected to a computer with a curve fitting program. The results of the testing are shown in **Figure 66** and **Figure 67** for SiO_2 and Al_2O_3 surfaces respectively. Published data of the OTS, OCS and HMDS DI water contact angles on SiO_2 give values of 115° ^[65] ~ 100° ^[121] and 53.76° ^[122] respectively, while the DI water contact angles of OTS and HMDS on Al_2O_3 are reported as 115° ^[123] and 82.9° ^[124] respectively. Data for OCS on Al_2O_3 could not be found.

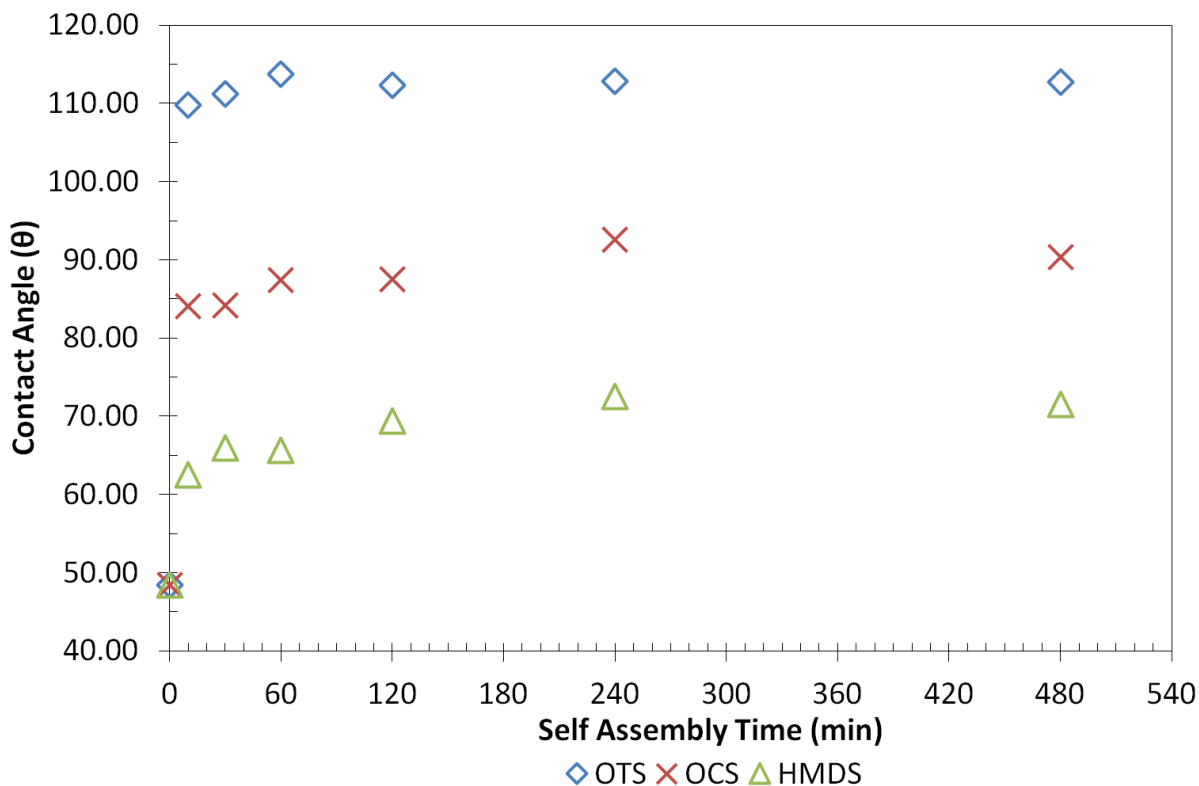


Figure 66. SiO_2 surface modification data.

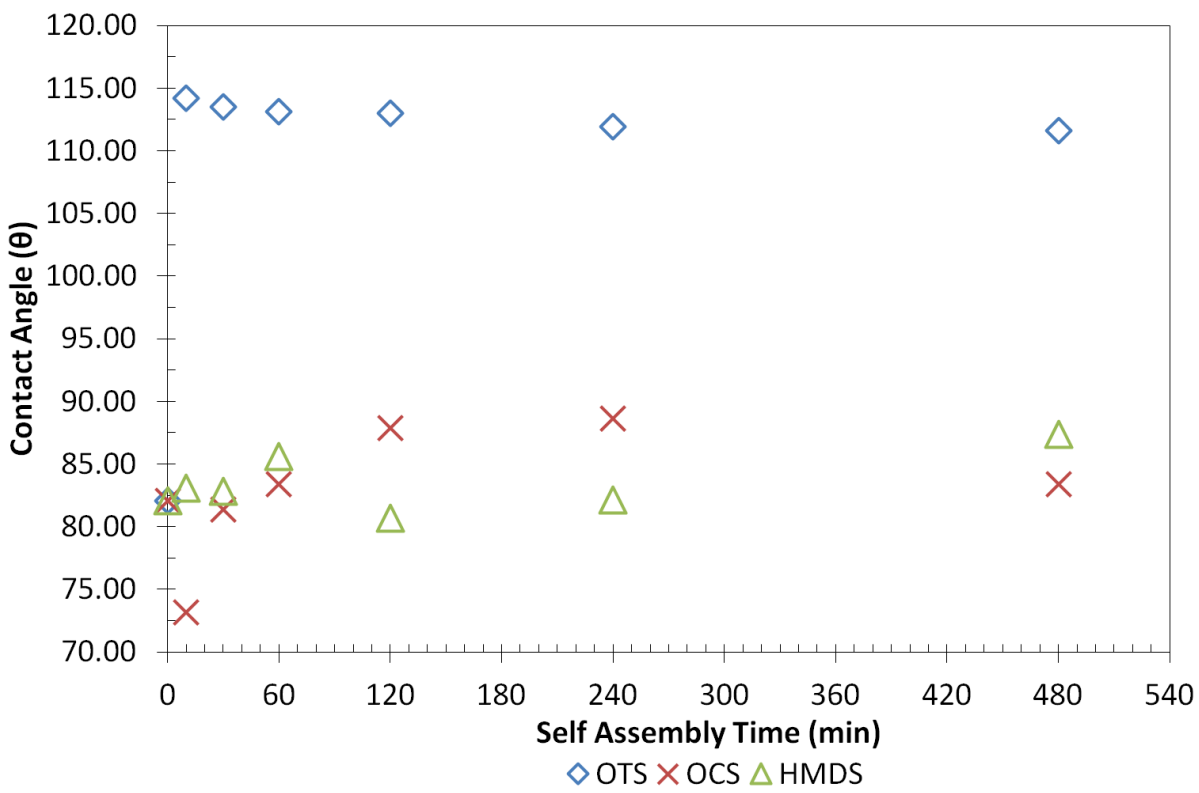


Figure 67. Al_2O_3 surface modification data.

Firstly dealing with the most important result, the OTS on Al_2O_3 , from the data collected the contact angle of the sample is maximised at 10 minutes of self-assembly and appears to get worse as self-assembly time progresses further, the contact angle steadily decreases. Comparing this to the OTS on SiO_2 it can be seen that to achieve the peak contact angle, a full 60 minutes of self-assembly is required; this shows, if nothing else, that the oxide surface of aluminium is much better surface on which to self-assemble OTS. The other two materials create a less hydrophobic surface than OTS on both Al_2O_3 and SiO_2 but may still be a better surface for some applications purely due to their morphology and chemical composition. Taking the case of OCS, the contact angle hits a maximum at 240 minutes for the Al_2O_3 surface and at 240 minutes for the SiO_2 ; to narrow down the exact time between 240 and 480 minutes at which the maximum actually occurs, more experimentation is required. HMDS seems to reach a maximum around 240 minutes for a SiO_2 surface and continues increasing until the final point at 480 minutes for the Al_2O_3 surface; however throughout the initial stages of the Al_2O_3 HMDS self-assembly the contact angle fluctuates, indicating perhaps that the results from HMDS on an Al_2O_3 are slightly unreliable and should be repeated including a larger range of times.

5 Sensing Results

All devices used in this chapter were prepared by myself, with the exception of the ones used in ethylene sensing and the nano-particle devices; the ethylene sensing devices were prepared in collaboration with Dr. Delia Puzzovio and the nano-particle devices were prepared by Mr. Hadi Al Qahtani. All of the sensing data was collected by myself, with the exception of the ethylene sensing data and the nano-particle sensing data; the ethylene sensing data was collected by Dr. Delia Puzzovio using an automated version of the current to voltage converter designed and built by Mr. Antonis Dragoneas; the nano-particle device sensing data was collected in collaboration with Mr. Hadi Al Qahtani.

5.1 Porphyrin and Phthalocyanine Based Organic Field-Effect Transistor Vapour Sensors

Building on the success of Dunbar *et al* using a UV-visible spectroscopy based optical vapour sensing method to test a variety of porphyrin materials against a wide selection of organic vapours,^[7] it was decided that a selection of these materials would be tested for their suitability as the active materials in OFET vapour sensing devices, firstly for organic semiconducting behaviour then for analyte sensitivity.

5.1.1 Material Screening Studies

The preliminary study involved the testing of various porphyrins and a phthalocyanine for measurable semiconducting behaviour in a bottom-gate, top-source/drain OFET architecture. The transistors described in this section were fabricated on silicon wafer substrates, which had 100nm of thermally grown oxide; the gate on each device was created from 100nm of thermally evaporated aluminium which was anodised to 5V to create a ~6.5nm thick aluminium oxide gate insulator, then each device had a monolayer of octadecyltrichlorosilane (OTS) surface modification self-assembled on top of the oxide to reduce the charge carrier trapping at the semiconductor-insulator interface. The porphyrin or phthalocyanine organic semiconductor layer was deposited via L-B or was thermally evaporated on top of the OTS; finally the 50nm gold source/drain electrodes were thermally

evaporated on top. The electrodes had a 10 μm channel and a width of 2mm. The aluminium was deposited with a slow initial rate onto the clean UV-ozone treated SiO₂ substrates to improve the adhesion to the surface and to prevent de-lamination of the aluminium during anodisation.

The first material tested was Co-EHO (5, 10, 15, 20-tetrakis (3, 4-bis (2-ethylhexyloxy) phenyl)-21H, 23H-porphyrinato cobalt (II)), a porphyrin-cobalt complex with large side groups (see **Figure 52**). This material was chosen as it showed a good optical response to the pesticide component TMP (trimethylphosphate) and the various amines (among other functional groups) by Dunbar *et al.*^[7] The Langmuir isotherm is shown in **Figure 68** for two volumes of a 0.2mg·mL⁻¹ chloroform solution spread on the trough. Although no monolayer collapse event is evident from the isotherm plots there was visual evidence in the actual film that collapse had occurred for the 1000 μL isotherm.

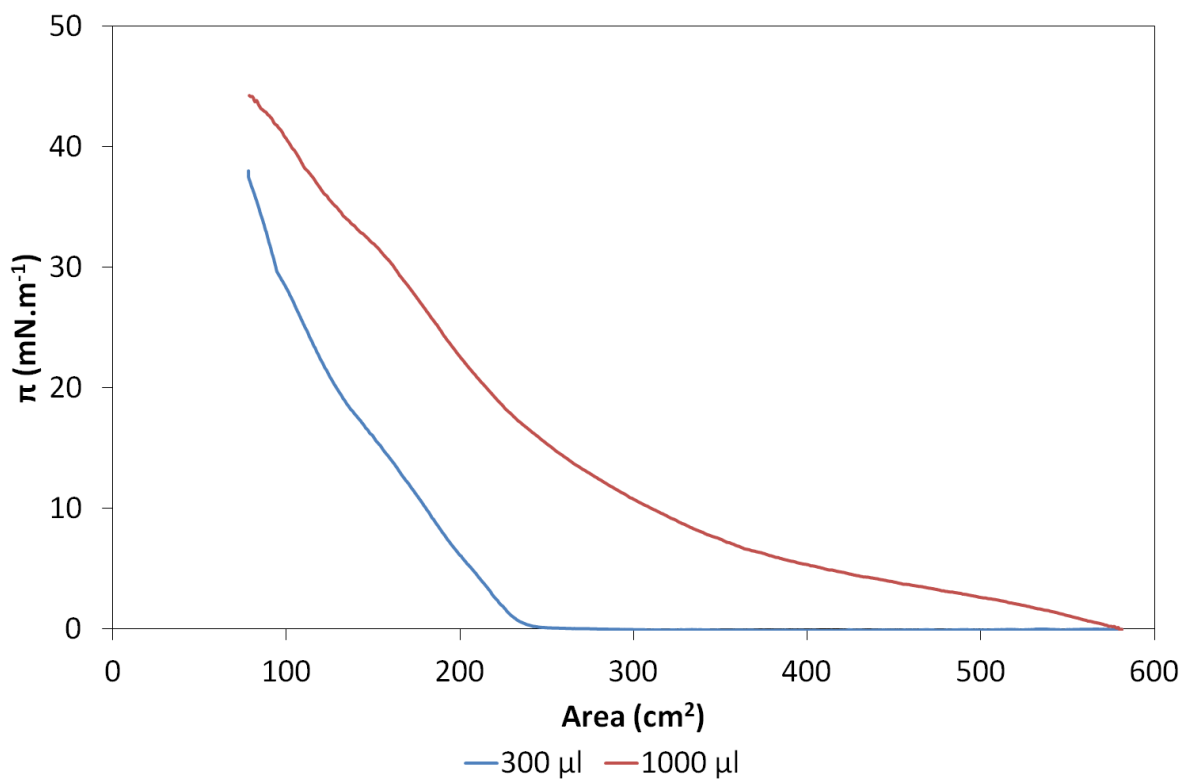


Figure 68. Isotherms of 300 μL and 1000 μL spreading volume for Co-EHO.

Six layers of the Co-EHO monolayer film was deposited onto the OFET devices as the organic semiconductor at a surface pressure of 15mN·m⁻¹ and the devices were characterised as described in sections 2.6.1 and 2.6.2; six layers were chosen as this should be approximately

2-3 times the thickness of OFET channel, and so allow the channel to properly form while not being so thick as to introduce lots of charge carrier traps; the devices did not show any transistor action and did not produce any measurable current. It can therefore be concluded that this material is unsuitable as an organic semiconductor for our device architecture (described above). This material has not been tested at higher gate voltages as the 5V anodised gate insulator used here cannot tolerate them.

The next material tested was Au-EHO (5, 10, 15, 20-tetrakis (3, 4-bis (2-ethylhexyloxy) phenyl)-21H, 23H-porphyrinato gold (III)), another porphyrin like Co-EHO but with very different sensing properties, that showed sensitivity to an aldehyde in the work by Dunbar *et al* (albeit in solution rather than as a film).^[7] The Langmuir isotherm for the Au-EHO is unusual (see **Figure 69**) having a plateau around $25\text{mN}\cdot\text{m}^{-1}$ for $300\mu\text{L}$ of the 10^{-4}M solution spread on the trough; it was therefore decided to deposit six layers of the film onto the OFET at $15\text{mN}\cdot\text{m}^{-1}$, below the plateau, as this could indicate a film collapse.

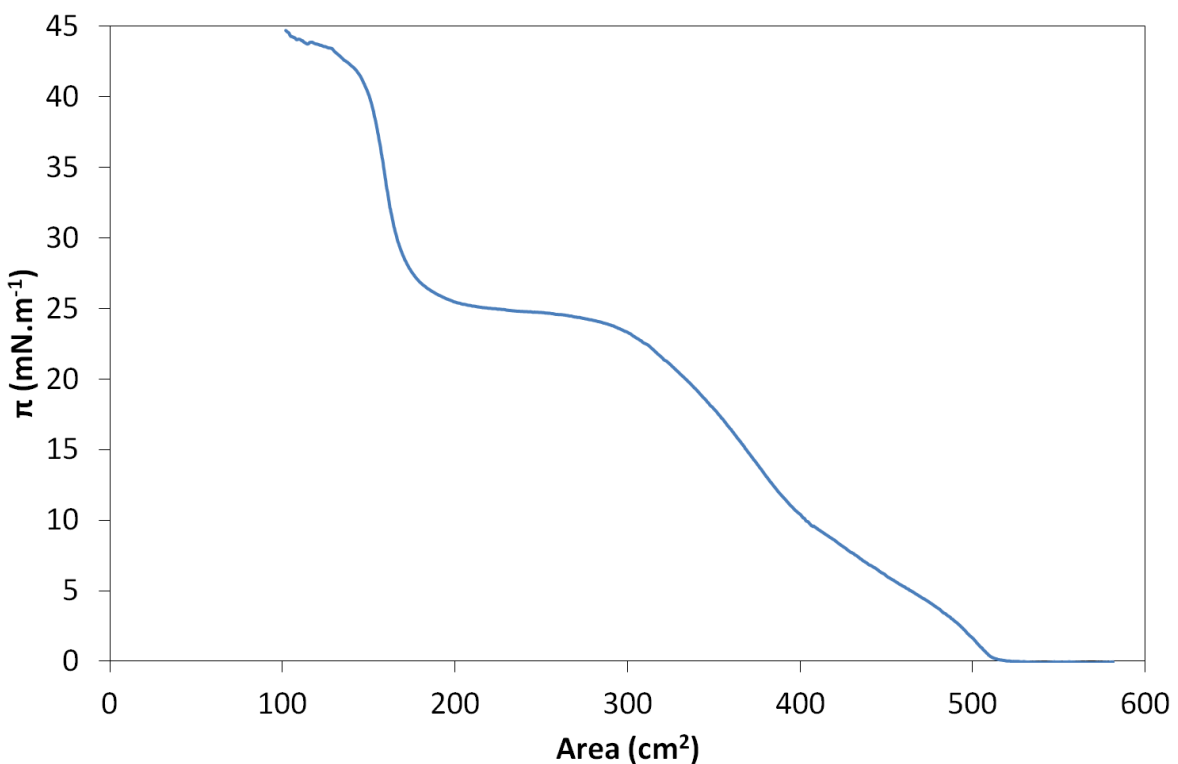


Figure 69. Isotherm of $300\mu\text{L}$ spreading volume for Au-EHO.

When tested electrically the OFET device showed no measurable current, as in the case of its cobalt counterpart, so it was decided to abandon the EHO derivatives. The lack of

conduction is thought to be a consequence of the large non-conjugated side groups insulating the highly conjugated central ring and preventing efficient stacking, therefore minimising orbital overlap and increasing charge carrier hopping distance.

After the EHO derivatives were abandoned, a phthalocyanine material was tested next as phthalocyanines have been successfully used as organic semiconductors in the past, obtaining mobilities in the region of $1 \times 10^{-3} \text{ cm}^2 \text{V}^{-1} \text{s}^{-1}$ in a OFET architecture.^[56] The phthalocyanine tested was Si(IV)PTSO (silicon (IV) phthalocyanine bis (trihexylsilyl oxide)), a phthalocyanine-silicon complex; again a 10^{-4} M solution with chloroform as the solvent was used and isotherms were recorded from spreading volumes of $300 \mu\text{L}$ and $1000 \mu\text{L}$. Unfortunately the isotherms were incomplete, i.e. didn't collapse, before the preset minimum trough area was reached. Therefore a solution of 10^{-3} M (1mM) concentration was used; an isotherm was obtained from the new solution with a $300 \mu\text{L}$ spreading volume, shown in **Figure 70**. OFET devices had six layers deposited onto them as the semiconductor at a surface pressure of $10 \text{ mN} \cdot \text{m}^{-1}$ after a re-compression of the film was performed; the re-compression was deemed necessary as the large "kink" observed in the isotherm of the first compression was noticeably smaller and occurred at a higher surface pressure in the re-compression. This "kink" could be a consequence of initial formation of domains during the first compression which do not re-spread upon expansion of the trough area.

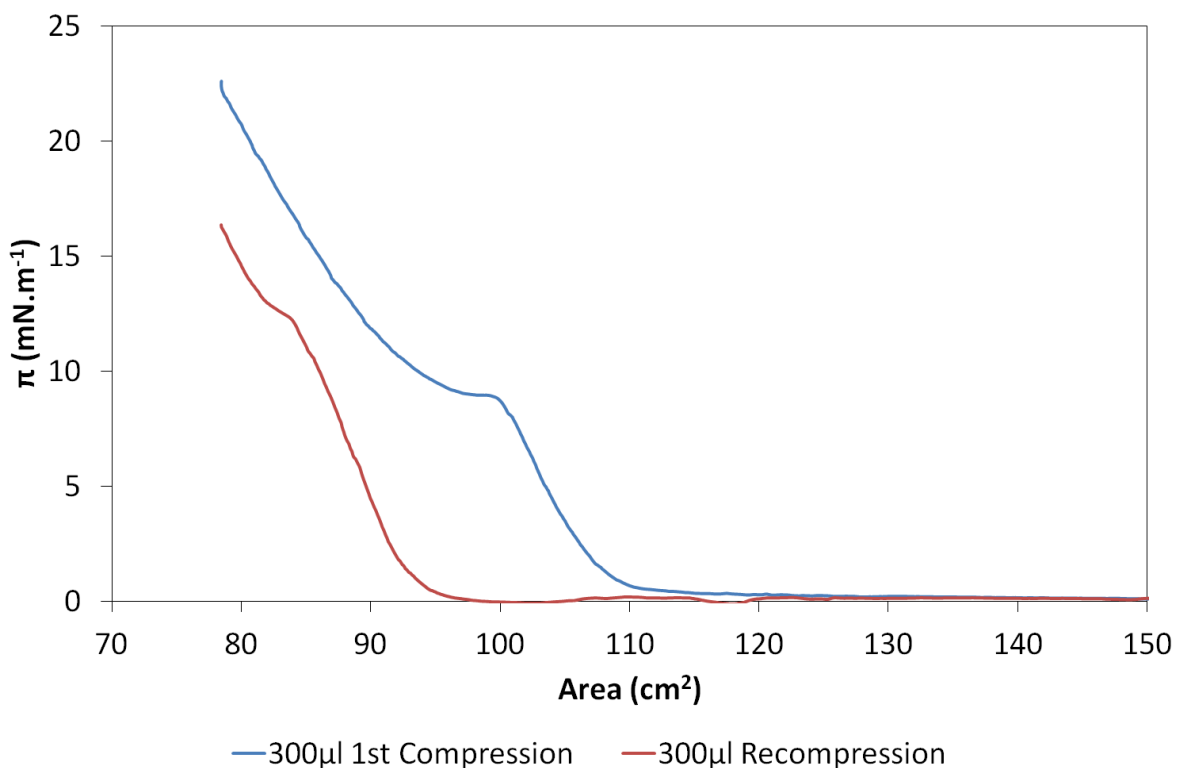


Figure 70. Si(IV)PTSO 300μL spreading volume initial isotherm and recompression.

Unfortunately as with the EHO derivatives there was no observed current when the OFETs were tested. Again the non-conductive behaviour of this material may be attributed to the long non-conjugated side groups; it was therefore decided to test some smaller molecules next, molecules with shorter or fewer un-conjugated side-groups.

PPIXZn(II) (Protoporphyrin IX zinc (II)) was tested next, since it was believed that the polar carboxylic acid side groups on one side of the molecule (see **Figure 54**) would cause the molecules to stand-up on the water (subphase) surface and improve molecule to molecule hopping in the OFET. Due to limited solubility in chloroform a 10^{-4} M solution was made using a solvent 95% chloroform and 5% DMSO (dimethyl sulfoxide) and a complete isotherm was obtained from 300μL of the solution spread on the L-B trough, see **Figure 71**.

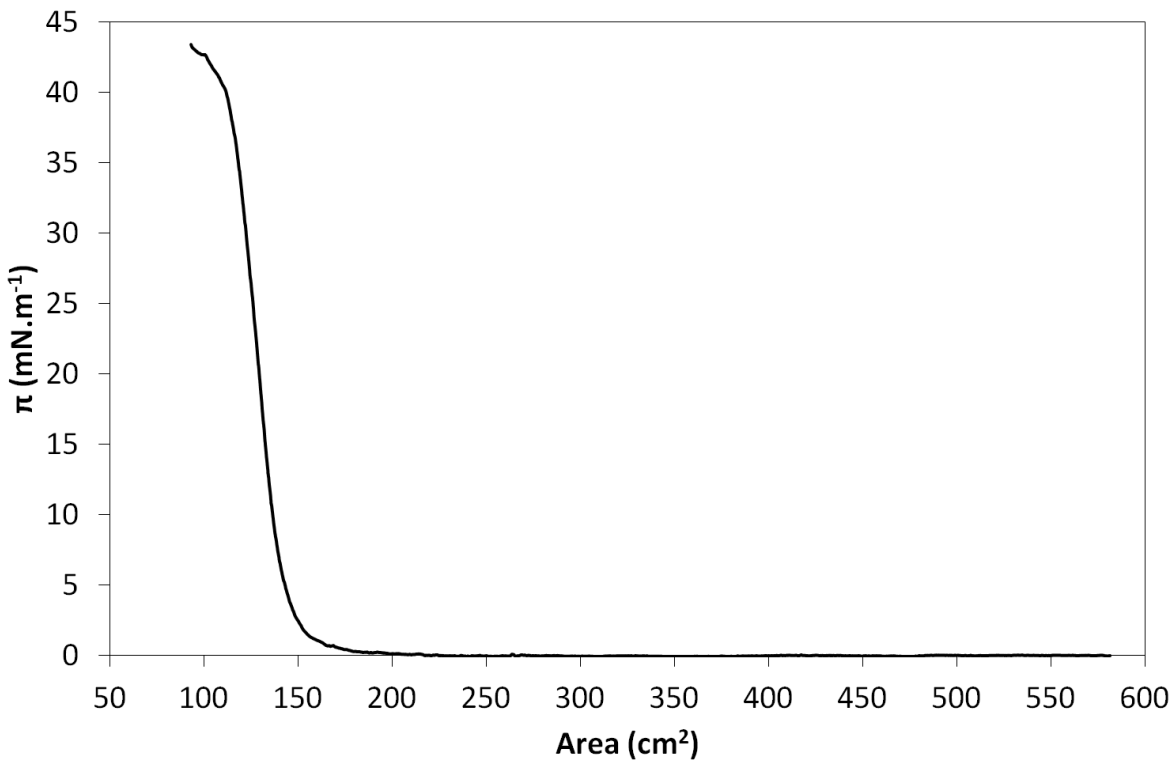


Figure 71. Isotherm of 300 μ L spreading volume for PPIXZn(II).

As the isotherm was so steep and collapse occurred very close to the minimum trough area it was decided to spread 500 μ L when depositing onto OFET devices. Devices were created from 20 layers of PPIXZn(II) deposited at a surface pressure of 30mN·m⁻¹. The devices created again showed no transistor action possibly due to a large number of charge carrier traps being present in the organic layer as a consequence of the highly polar carboxylic acid groups on each molecule.

To produce a saturated drain current above the detection threshold of the Keithley units using the device architecture described at the start of the section the organic semiconductor of the OFET must have a carrier mobility greater than $7.8 \times 10^{-7} \text{ cm}^2 \text{V}^{-1} \text{s}^{-1}$ (by **Equation 21**, assuming a threshold voltage of around -1V, at a gate voltage of -3V).

After the lack of semiconducting behaviour shown by sensing materials it was decided to try an organic compound that has already shown semiconducting behaviour but has not been used in a sensing application previously. With this in mind, PtOEP (platinum (II) octaethyl porphyrin) would be tested next as Noh *et al* had success using PtOEP as a p-type OFET material, achieving a hole mobility of $2.2 \times 10^{-4} \text{ cm}^2 \text{V}^{-1} \text{s}^{-1}$.^[125] A solution was created of

concentration $5 \times 10^{-4} \text{ M}$ and an isotherm was obtained from a spreading volume of $300 \mu\text{L}$, see **Figure 72**.

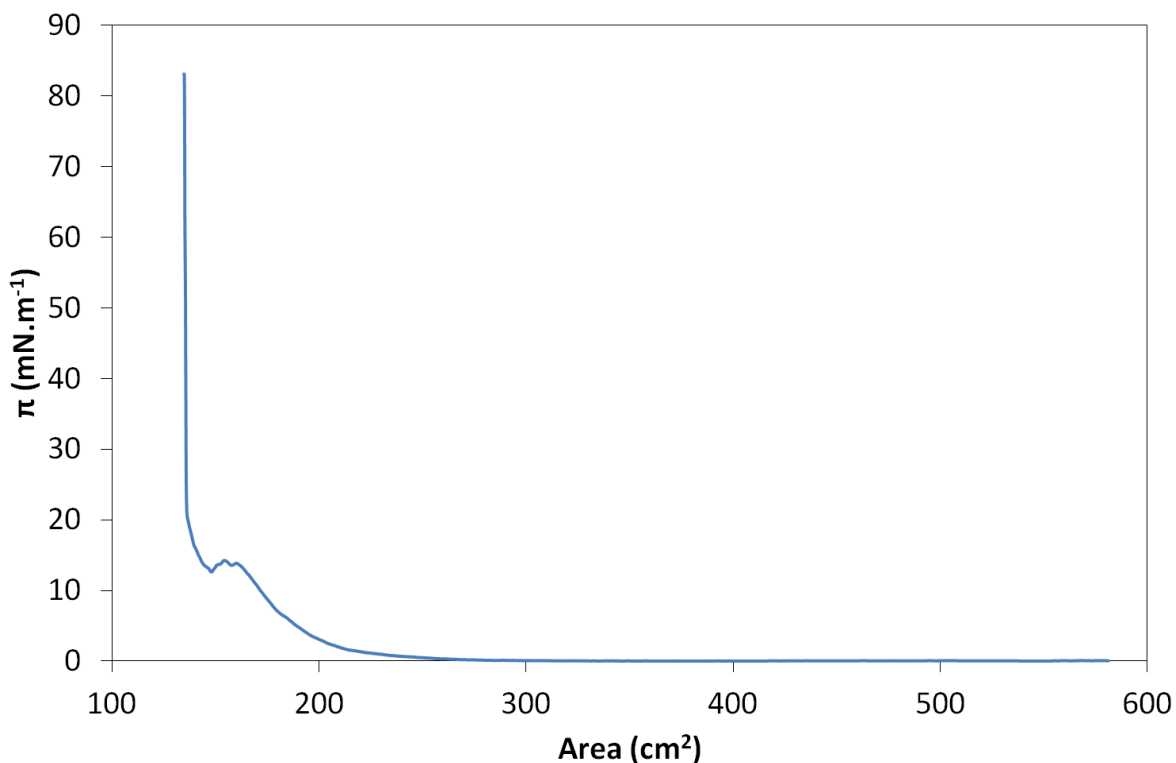


Figure 72. Isotherm of $300 \mu\text{L}$ spreading volume for PtOEP.

However upon depositing an OFET sample it was noticed that the porphyrin would not adhere to the OFET substrate, so another deposition method was required. Thermal evaporation was adopted as the new deposition method; a layer of PtOEP was successfully deposited with an approximate thickness of 60 nm , the initial deposition rate was $0.15 \text{ nm}\cdot\text{s}^{-1}$ for approximately 15 nm before the rate was increased to $1.7 \text{ nm}\cdot\text{s}^{-1}$. When electrically tested the OFET devices showed transistor action and will be discussed in more detail in section 5.1.2.

The final material to be screened was a porphyrin very similar in structure to PtOEP; this material was Etioporphyrin-I (PtEP-I) (see **Figure 53**). This material has been successfully used to create OFET devices by Che *et al* with a peak hole mobility of $3.2 \times 10^{-1} \text{ cm}^2\text{V}^{-1}\text{s}^{-1}$ quoted in their paper,^[55] a higher mobility than the PtOEP porphyrin used previously. It is thought that the higher mobilities observed were a consequence of the alternating ethyl and methyl groups allowing more efficient molecular packing. Due to the problems

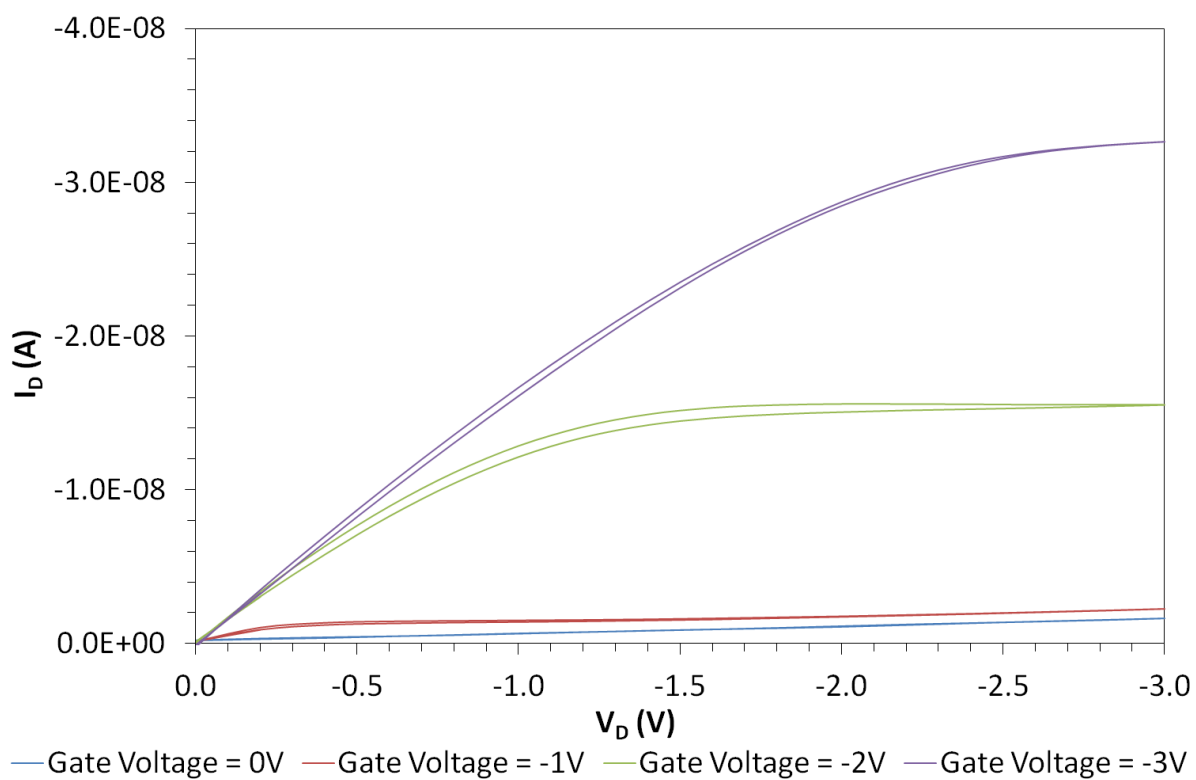
encountered when trying to deposit PtOEP via the L-B technique, thermal evaporation was used immediately for PtEP-I. The PtEP-I was deposited at $0.67\text{nm}\cdot\text{s}^{-1}$ until a thickness of $\sim 65\text{nm}$ was achieved. When electrically tested the OFET devices showed transistor action and this will be discussed in more detail in section 5.1.3.

5.1.2 Platinum Octaethylporphyrin

The transistors described in this section were fabricated as described in the previous section (section 5.1.1) with PtOEP thermally evaporated onto the devices to a thickness of $\sim 65\text{nm}$.

5.1.2.1 Transistor Characteristics

The PtOEP transistors were characterised as described in sections 2.6.1 and 2.6.2 using V_D , $_{Max} = V_{G, Max} = -3\text{V}$ and $V_{G, Min} = 0\text{V}$. The characteristics of two of the transistors, later used in vapour sensing, are shown in **Figure 73** and **Figure 74**.



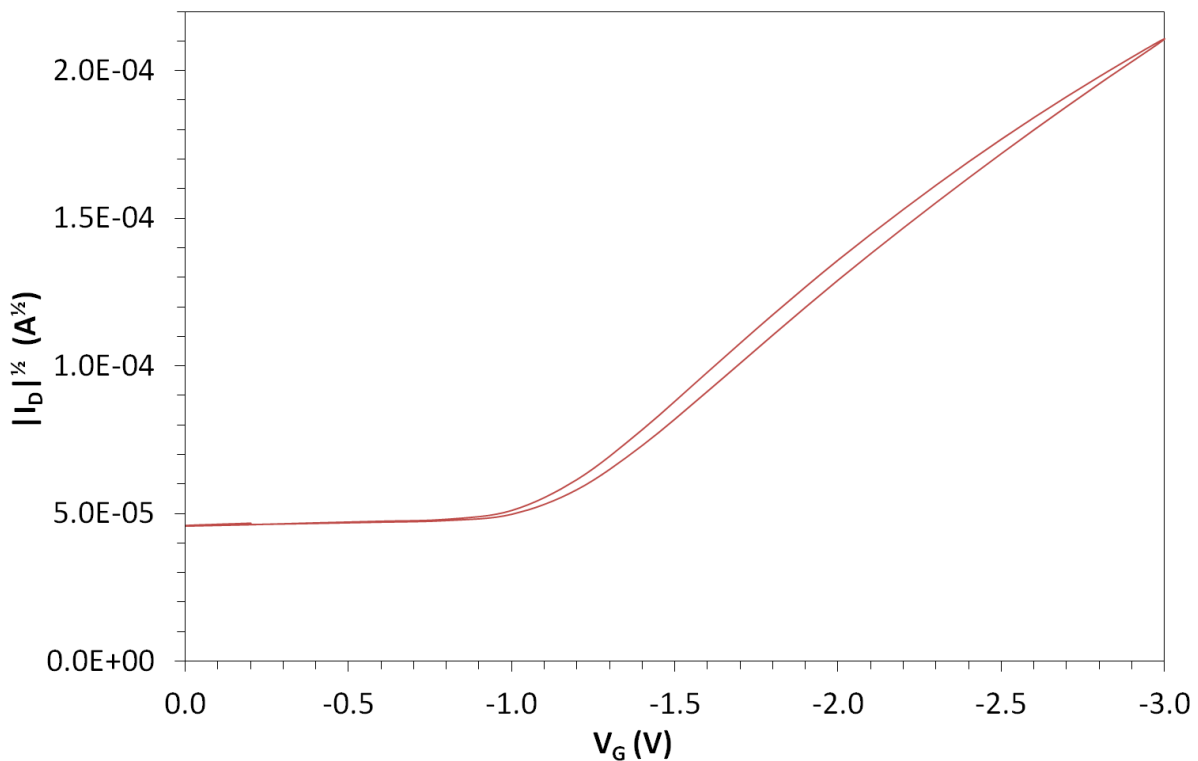


Figure 73. PtOEP 5 TR output and transfer characteristics.

It can be seen from the output and transfer characteristics in **Figure 73** that this particular transistor, PtOEP 5 TR, had a small amount of hysteresis but shows good saturation, therefore a negligible amount of doping, and Ohmic contacts evidenced by the lack of curvature in the linear region of the output characteristic. From the extrapolation of the transfer characteristic, the mobility and threshold extracted were $(1.37 \pm 0.01) \times 10^{-4} \text{ cm}^2 \text{V}^{-1} \text{s}^{-1}$ and $-1.13 \pm 0.01 \text{ V}$ respectively.

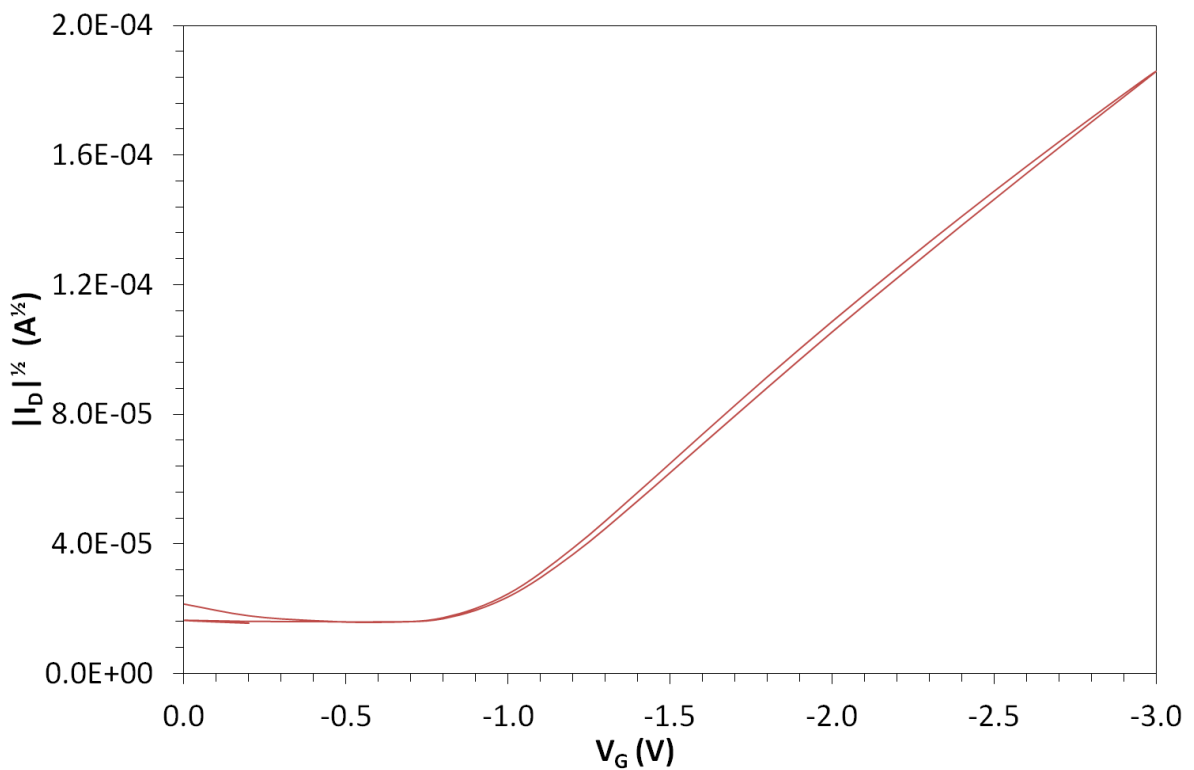
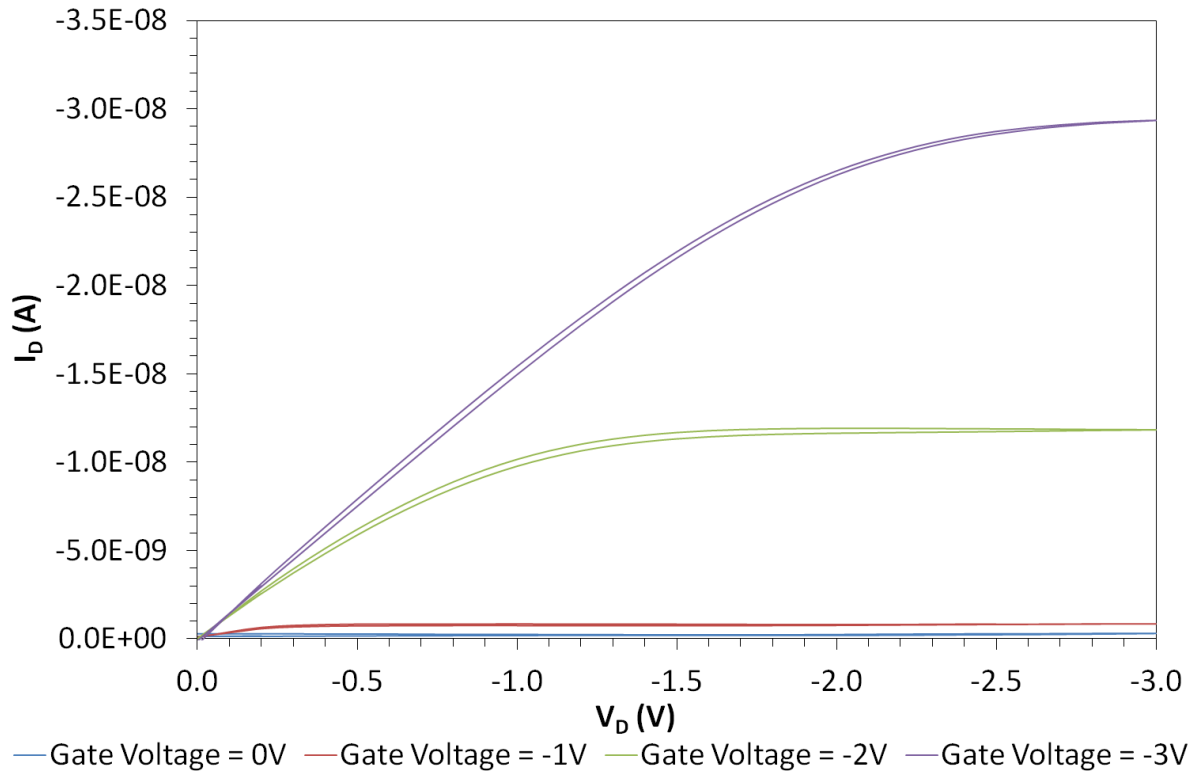


Figure 74. PtOEP 8 BL output and transfer characteristics.

The transistor PtOEP 8 BL, whose characteristics are shown in **Figure 74**, is very similar to PtOEP 5 TR in that it showed a little hysteresis, Ohmic contacts and negligible doping.

However its peak current was smaller than PtOEP 5 TR, as a consequence its mobility and threshold were slightly worse with values of $(1.13 \pm 0.04) \times 10^{-4} \text{ cm}^2 \text{V}^{-1} \text{s}^{-1}$ and $-0.96 \pm 0.03 \text{ V}$ respectively.

With peak drain current values around $-3 \times 10^{-8} \text{ A}$ these OFETs had channel on-resistances of the order $10^8 \Omega$. This is quite a high value and leaves little room for increase under vapour sensing. A material which produces a higher peak drain current would be preferable for vapour sensing applications.

5.1.2.2 Vapour Sensing Results

Vapour sensing experiments were carried out using the techniques and equipment described in section 3.2 and the transistors were monitored using the gain-method, as described in section 2.6.3. Sensing experiments were carried out using two common solvents as the analytes. Firstly the transistor PtOEP 5 TR was exposed to 50% saturated isopropanol (IPA) vapour (a mixture of 50% pure nitrogen to 50% nitrogen bubbled through the liquid analyte), the changes in mobility and threshold were monitored and recorded throughout the exposure and recovery stages of the vapour sensing experiment. IPA was chosen as the first analyte as it is a readily available and highly volatile example of an alcohol, which would generate high concentrations of vapour to sense; the theoretical concentration of the analyte at 100% saturation is $4.65 \times 10^4 \text{ ppm}$ at 22°C (the temperature of the room at the time of exposure). Plots of the threshold and mobility can be seen in **Figure 75**. Due to the noisy nature of the data obtained a five-point median was used to smooth the data, this can be seen at the bottom of **Figure 75**. The raw drain current data can be seen at the top of **Figure 75**.

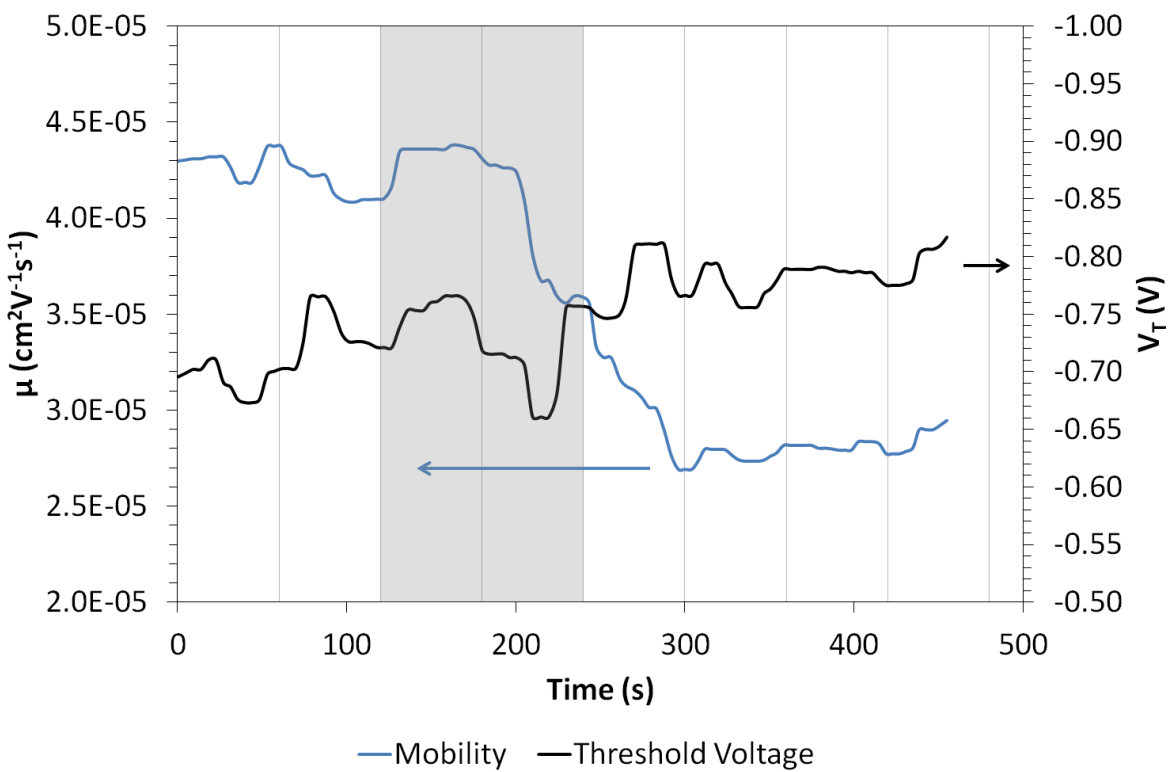
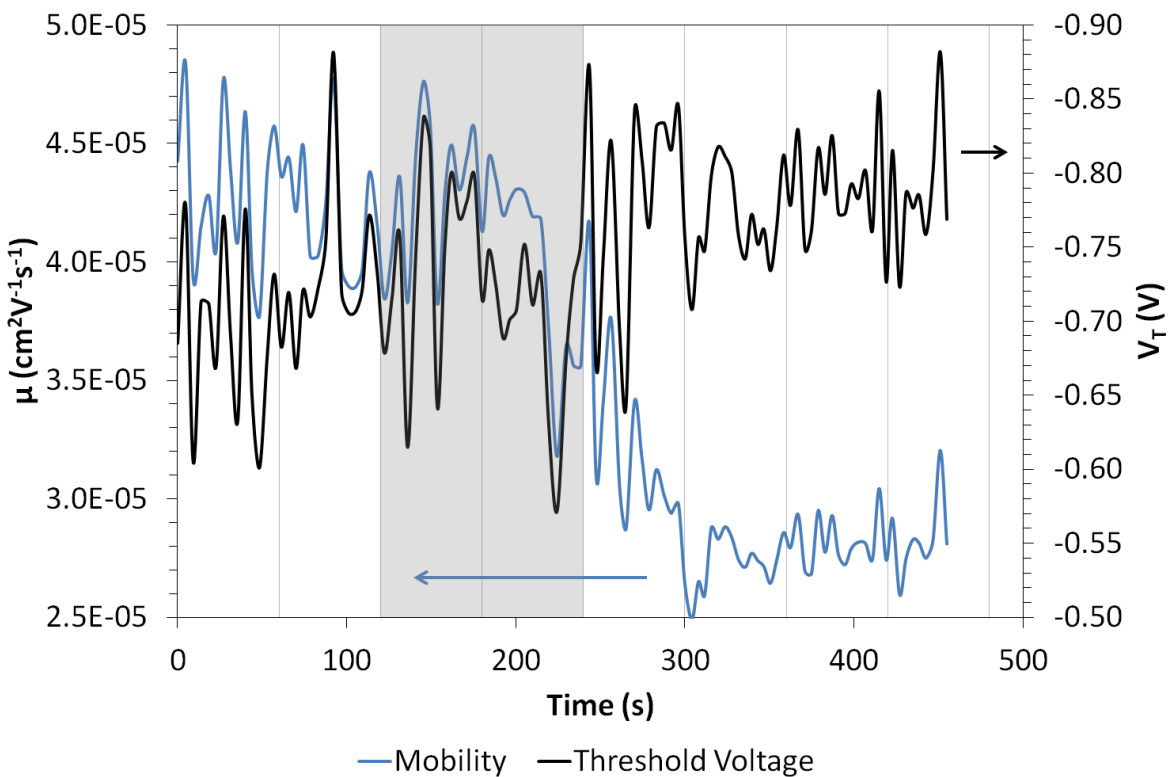


Figure 75. PtOEP 5 TR IPA raw sensing results (top) and five-point median (bottom). N.B. grey shaded areas indicate analyte exposure.

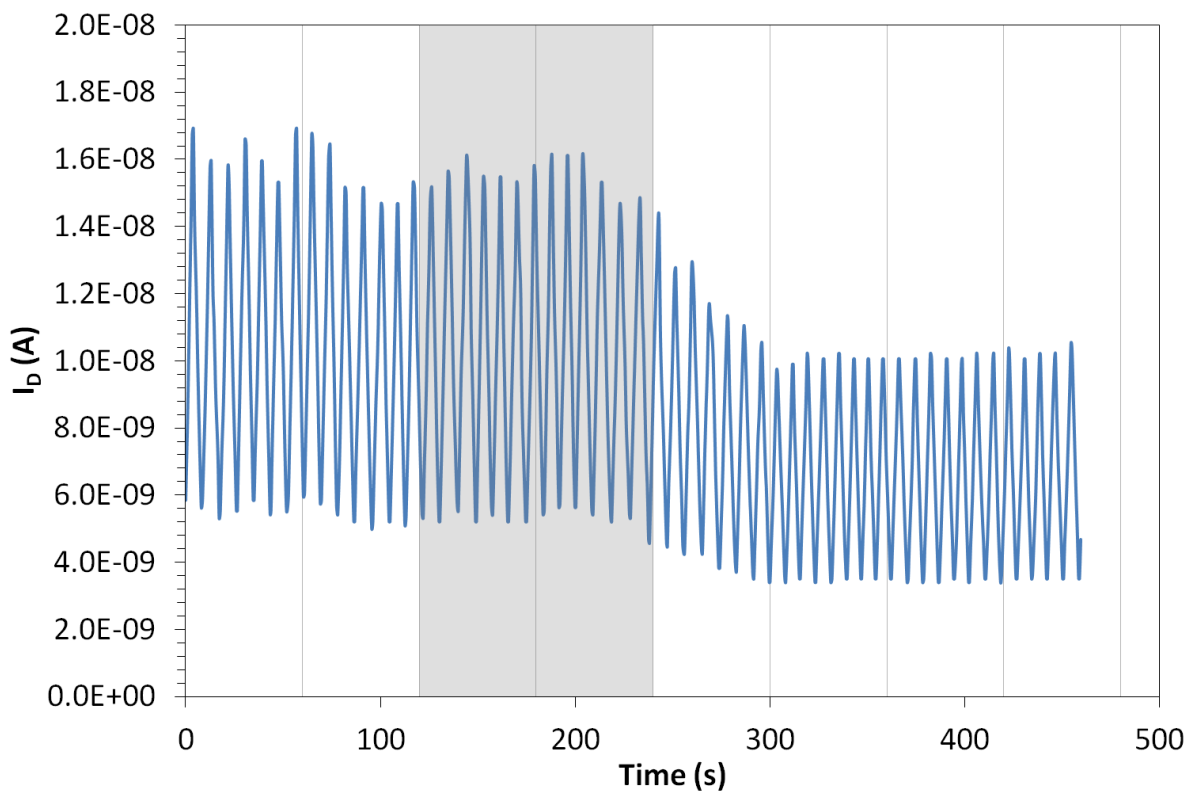


Figure 76. PtOEP 5 TR IPA sensing results (drain current). N.B. grey shaded area indicates analyte exposure.

Figure 75 shows an overall decrease in mobility and drain current is also seen to decrease (see **Figure 76**) after exposure to IPA; however, the decrease in mobility does not happen immediately upon exposure instead it takes around 80 seconds to begin and lasts for approximately 60 seconds after exposure has ended and recovery has begun. This could indicate that the IPA requires a certain amount of time to penetrate into the PtOEP and start effecting mobility then takes a finite time for un-reacted/un-interacted IPA to leave the PtOEP; the irreversible nature of the interaction may stem from some IPA solvent annealing effects, causing structural changes in the PtOEP film that hinder charge transport or IPA molecules penetrating down through grain boundaries and causing carrier trapping.

Next the transistor PtOEP 8 BL was exposed to 50% saturated acetone vapour (50% pure nitrogen to 50% nitrogen bubbled through the analyte), acetone being an example of a commonly used volatile ketone; the theoretical concentration of analyte at 100% saturation is 2.52×10^5 ppm at 22°C (the temperature of the room at the time of exposure). As before the mobility, threshold and drain current were monitored throughout exposure and

recovery cycles, the results can be seen in **Figure 77** and **Figure 78**; as before, the mobility and threshold data was very noisy so a five-point median was used to smooth it.

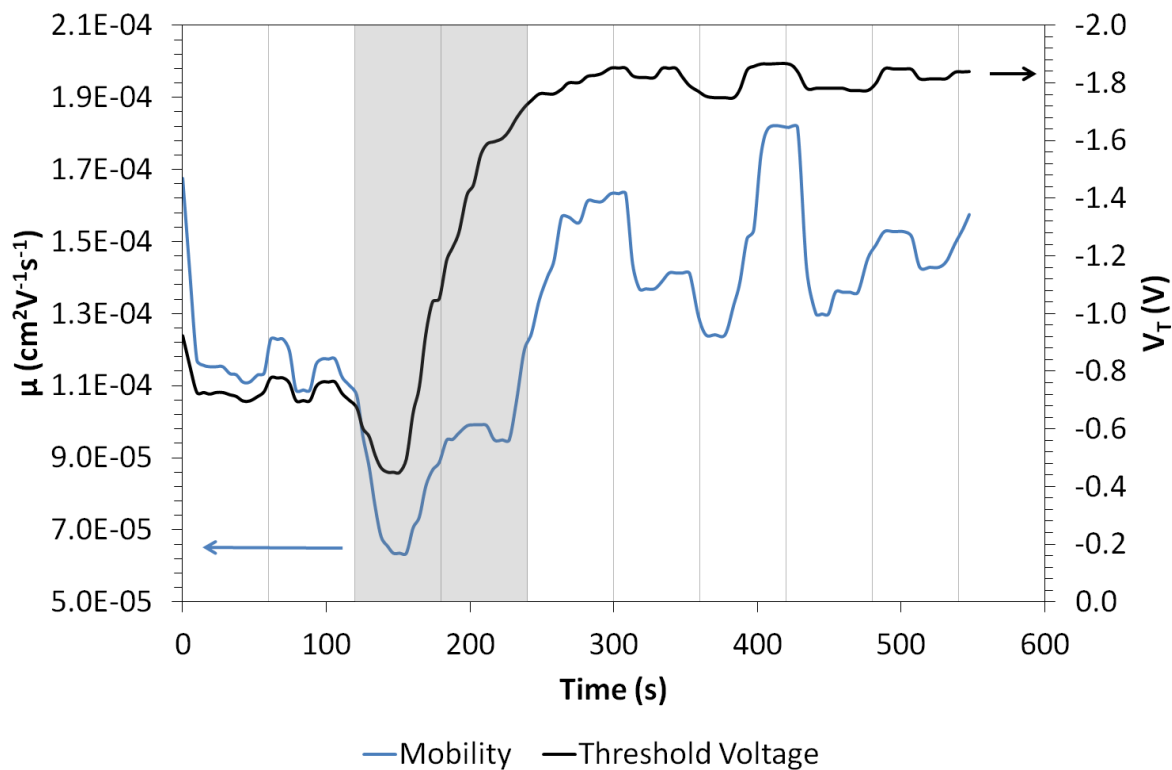


Figure 77. PtOEP 8 BL acetone sensing results five-point median. N.B. grey shaded area indicates analyte exposure.

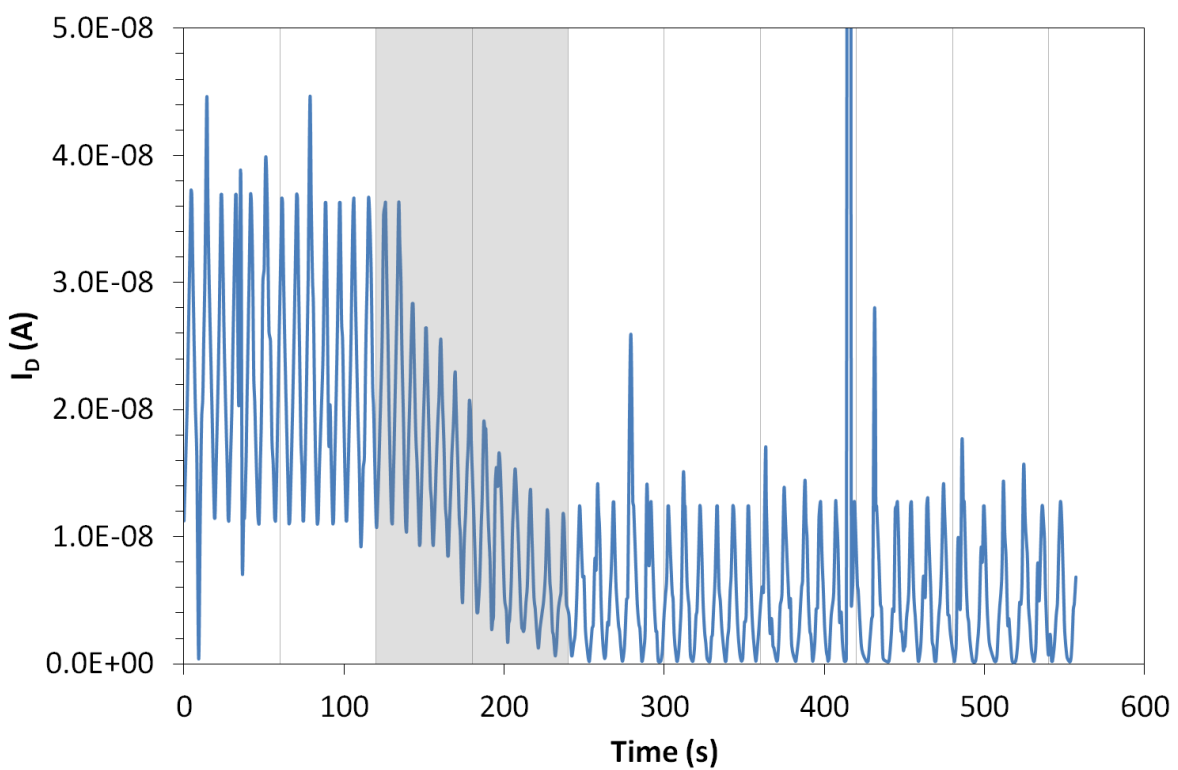


Figure 78. PtOEP 8 BL acetone sensing results (drain current). N.B. grey shaded area indicates analyte exposure.

It can be seen from **Figure 77** that, unlike under IPA exposure, the changes in mobility and threshold happen immediately under acetone exposure. Both the mobility and threshold suffer from initial drops then rise to final values higher than their initial ones, however, looking at the drain current (**Figure 78**) the initial drop in mobility and threshold has no noticeable effect, the current begins to drop at a steady rate with no significant deviations. These changes could again be the result of some kind of solvent annealing effect causing a permanent, irreversible change in the conformation of PtOEP molecules, this time increasing crystallinity but making the interface between the organic semiconductor and the gate insulator worse; the changes could also be attributed to doping effects of acetone at grain boundaries causing increased mobility and the dipoles formed as a result of the binding hindering accumulation layer formation and thus increasing threshold.

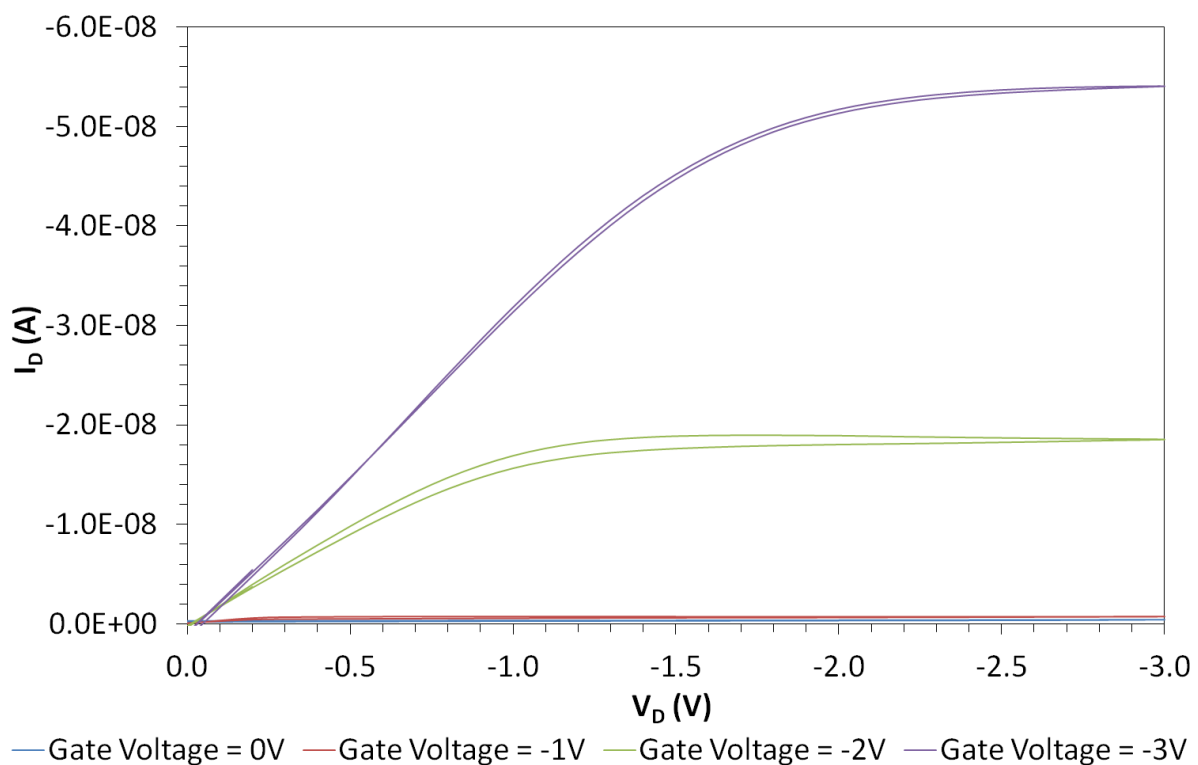
Neither of the interactions seem to be immediately reversible, meaning this material would be a poor sensing material for IPA and acetone as it would only make one-shot sensors.

5.1.3 Platinum Etioporphyrin-I

The transistor described in this section was fabricated on a silicon wafer substrate, which had 100nm of thermally grown oxide. The gate was created from 100nm of thermally evaporated aluminium which was anodised to 5V to create a \sim 6.5nm thick aluminium oxide gate insulator, then the device had a monolayer of octadecyltrichlorosilane (OTS) on top of the oxide to reduce the trapping at the semiconductor-insulator interface; PtEP-I was thermally evaporated onto the device to a thickness of \sim 65nm, then 50nm gold source/drain electrodes were thermally evaporated on top.

5.1.3.1 Transistor Characteristics

The PtEP-I transistors were characterised as described in sections 2.6.1 and 2.6.2 using V_D , $Max = V_G, Max = -3V$ and $V_G, Min = 0V$. The characteristics of the transistor later used in vapour sensing are shown in **Figure 79**.



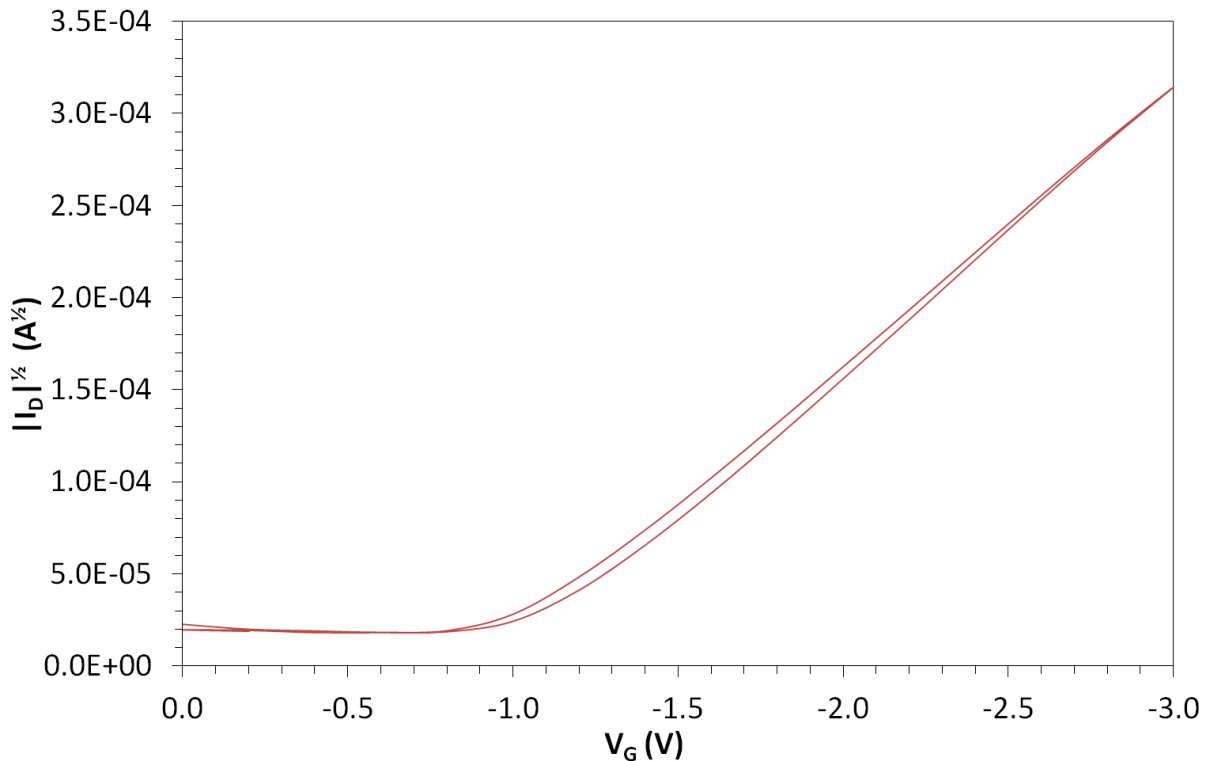


Figure 79. PtEP-I 15 TL output and transfer characteristics.

From **Figure 79** it can be seen that the transistor has almost no doping and very little hysteresis. There also appear to be no contact issues with the device. From the transfer characteristic, values of $(4.05 \pm 0.03) \times 10^{-4} \text{ cm}^2 \text{V}^{-1} \text{s}^{-1}$ and $-1.13 \pm 0.01 \text{ V}$ were extracted as the mobility and threshold of the device.

Again like the PtOEP transistors the peak drain current of the PtEP-I device is still quite low at around $-5.5 \times 10^{-8} \text{ A}$ meaning a channel on-resistance of approximately $5.5 \times 10^7 \Omega$, which is better than the PtOEP devices but still quite high.

5.1.3.2 Vapour Sensing Results

The vapour sensing experiment was carried out using the techniques and equipment described in section 3.2, the transistor was monitored using the gain-method (as described in section 2.6.3). It was decided to assess the response to a group of analytes that are of interest to the food industry, the amines, more specifically the lowest molecular weight primary amine that is still liquid at room temperature: propylamine; propylamine, being very volatile, could be used to generate high concentrations of analyte vapour. Platinum interacts with nitrogen compounds in its role as a catalyst in a catalytic converter and is also

complexed in a porphyrin structure by nitrogen atoms; so it was believed that an amine vapour may have a measurable interaction with the PtEP-I. It was also decided to test the detection limit (if PtEP-I did indeed respond to propylamine), so the mixing percentage between pure nitrogen and nitrogen that has been bubbled through the analyte, and thus the concentration of the analyte vapour was increased incrementally. Six concentrations were used: 1% saturated (1% N₂ to bubbler), 5% saturated (5% N₂ to bubbler), 10% saturated (10% N₂ to bubbler), 30% saturated (30% N₂ to bubbler), 50% saturated (50% N₂ to bubbler) and 100% saturated (100% N₂ to bubbler); the theoretical concentration of the vapour at 100% saturation is 1.21×10^5 ppm at 21°C (the temperature of the room at the time of exposure). Each run was carried out on the same transistor (PtOEP 15 TL) and the runs were carried out consecutively starting with the lowest concentration and working up to the highest. As previously observed, the mobility and threshold data from the gain-method circuit was noisy, so was smoothed using a five-point median; these data and the drain current data are shown in **Figure 80**, **Figure 81**, **Figure 82**, **Figure 83**, **Figure 84**, **Figure 85**, **Figure 86**, **Figure 87**, **Figure 88**, **Figure 89**, **Figure 90** and **Figure 91**. The current evolution plots are clipped to show the peak values as when the entire range of values are shown the peak evolution is not very noticeable.

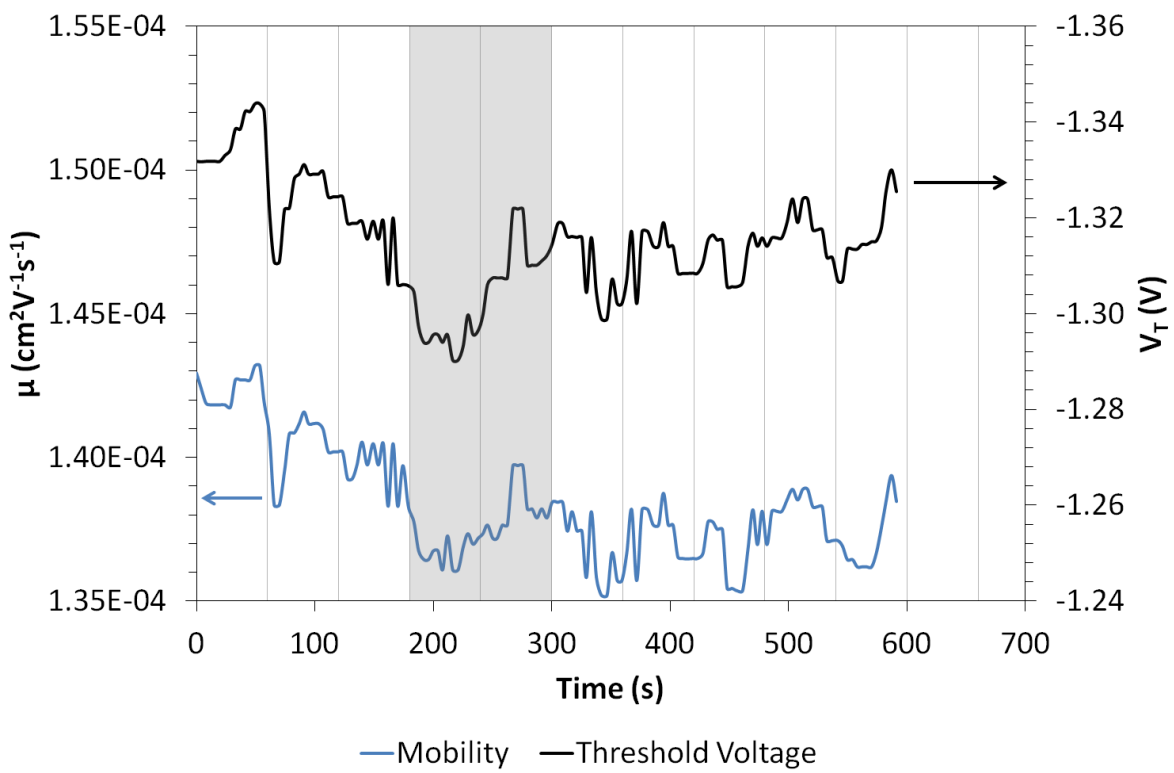


Figure 80. PtEP-I 15 TL 1% propylamine sensing results five-point median. N.B. grey shaded area indicates analyte exposure.

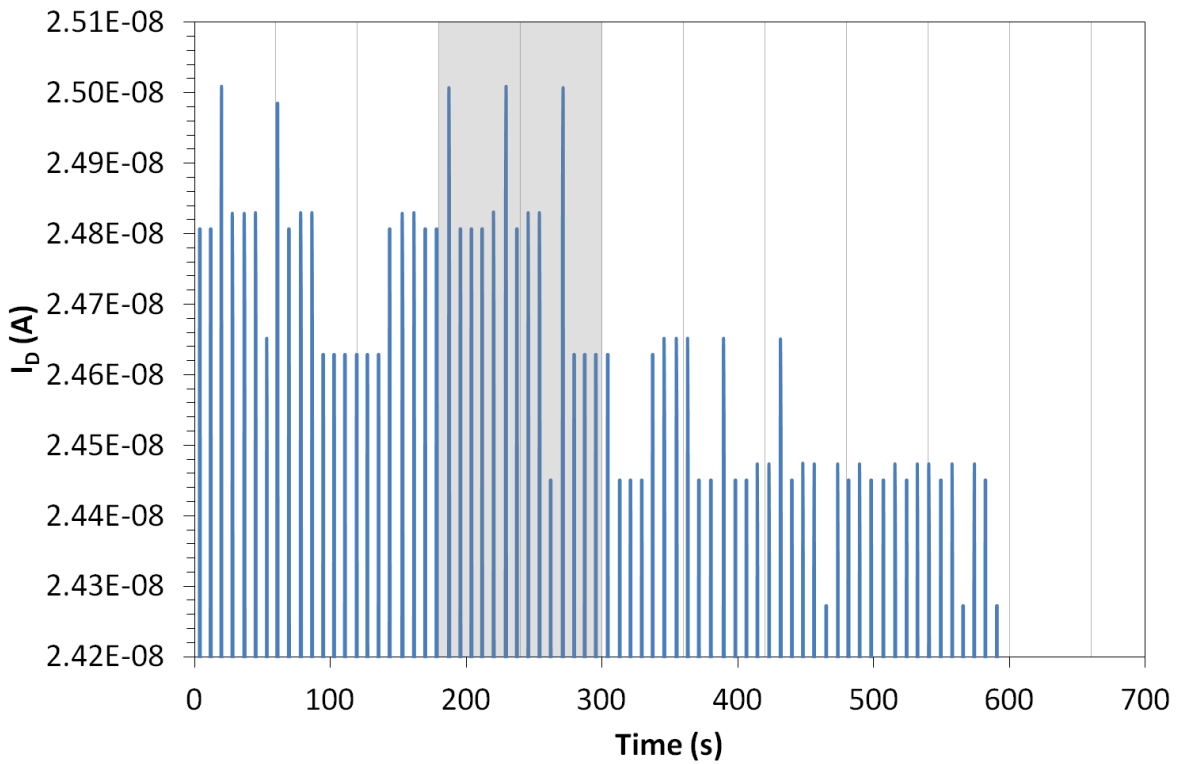


Figure 81. PtEP-I 15 TL 1% propylamine sensing results (peak drain current evolution). N.B. grey shaded area indicates analyte exposure.

Figure 80 shows a fall in both the mobility and the threshold in the nitrogen purge before the onset of vapour exposure. This could be due to some sensitivity of the device to oxygen or moisture present in the atmosphere outside the exposure chamber and the reduction of OFET parameters could be recovery. During the exposure phase a very small increase in both parameters is observed, although no recovery is detected after exposure. Looking at the evolution of the peak drain current during the experiment (**Figure 81**), a small overall drop is observed beginning during the second minute of exposure.

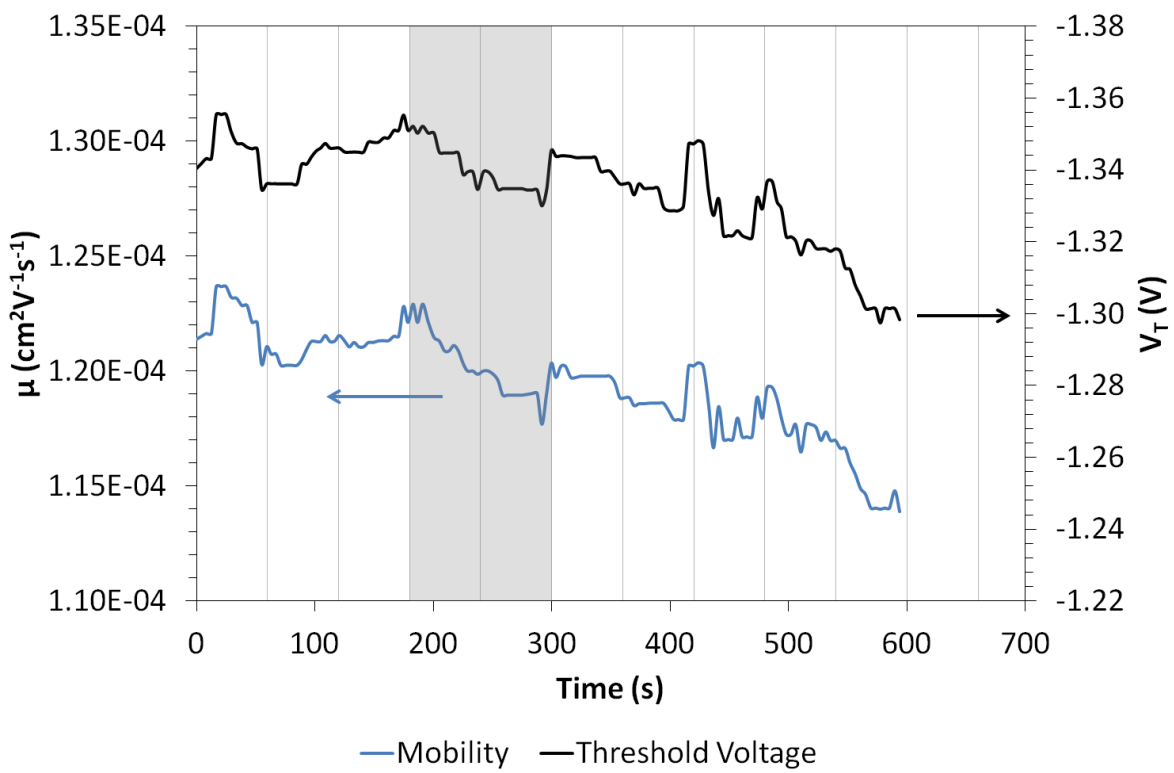


Figure 82. PtEP-I 15 TL 5% propylamine sensing results five-point median. N.B. grey shaded area indicates analyte exposure.

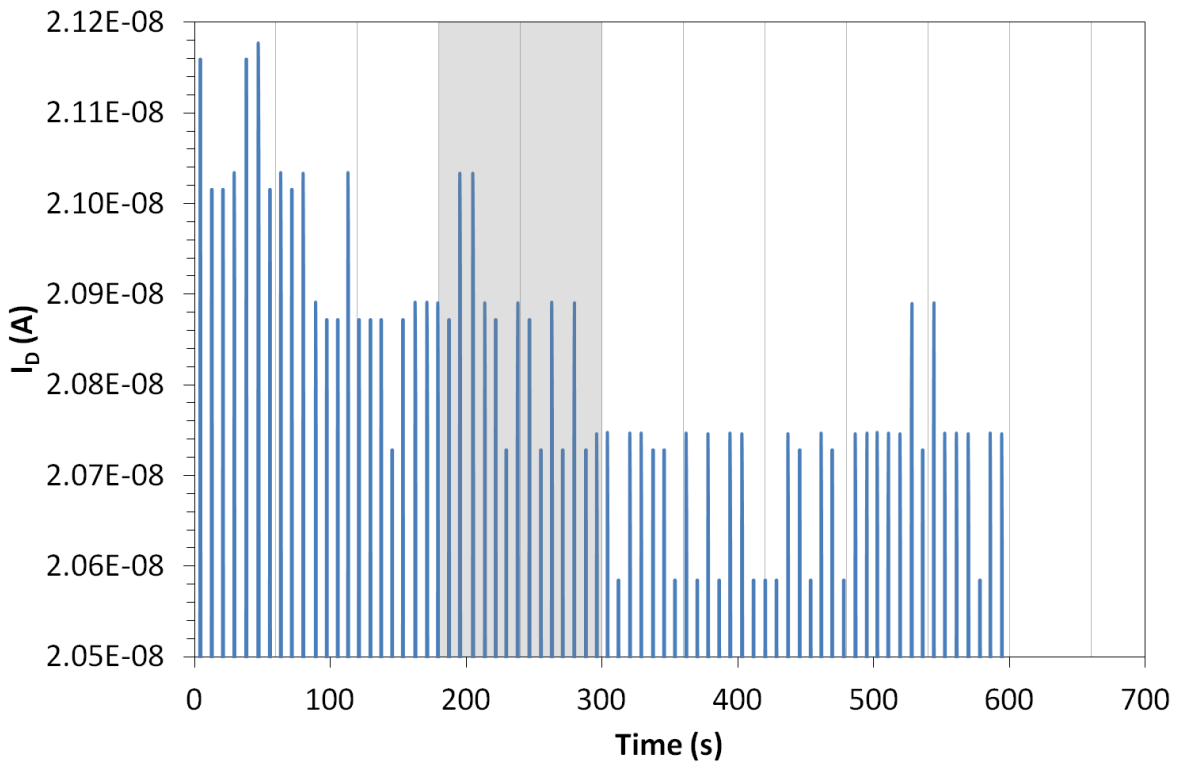


Figure 83. PtEP-I 15 TL 5% propylamine sensing results (peak drain current evolution). N.B. grey shaded area indicates analyte exposure.

During the 5% saturation exposure run (**Figure 82** and **Figure 83**) no significant response to the vapour is observed but a constant downward trend is present in all three parameters throughout the run, being more pronounced for mobility and threshold in the recovery stage after exposure.

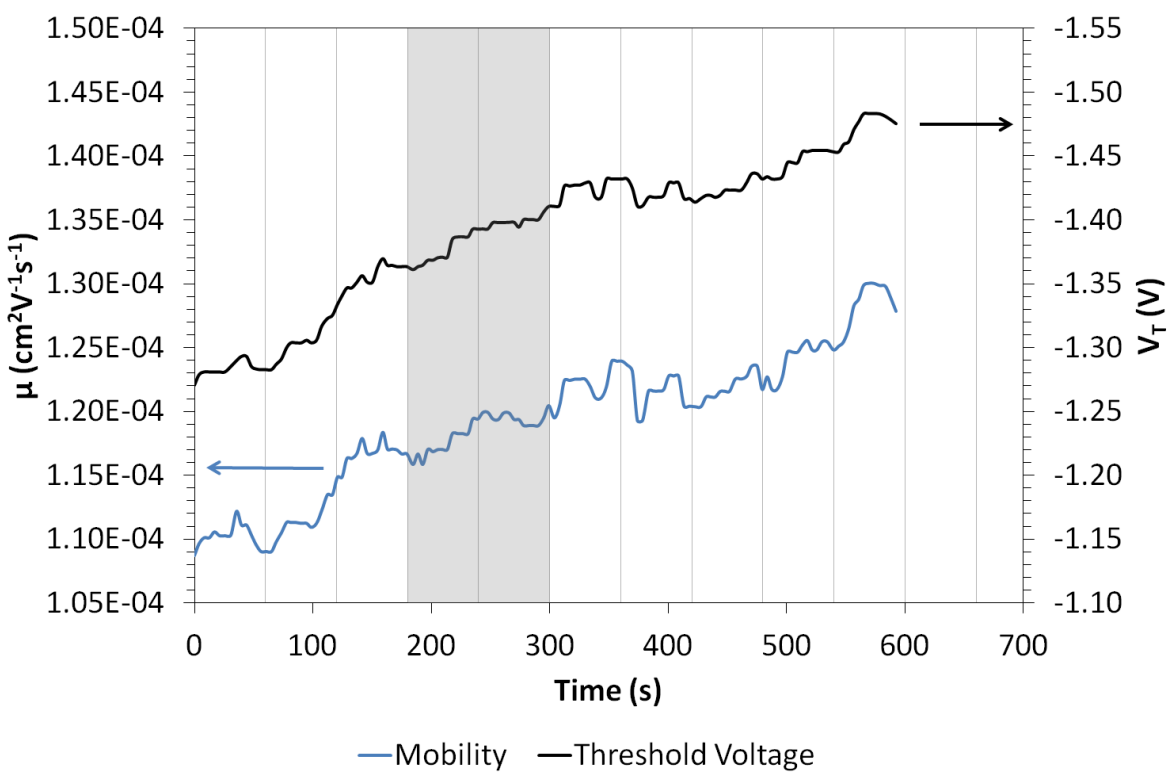


Figure 84. PtEP-I 15 TL 10% propylamine sensing results five-point median. N.B. grey shaded area indicates analyte exposure.

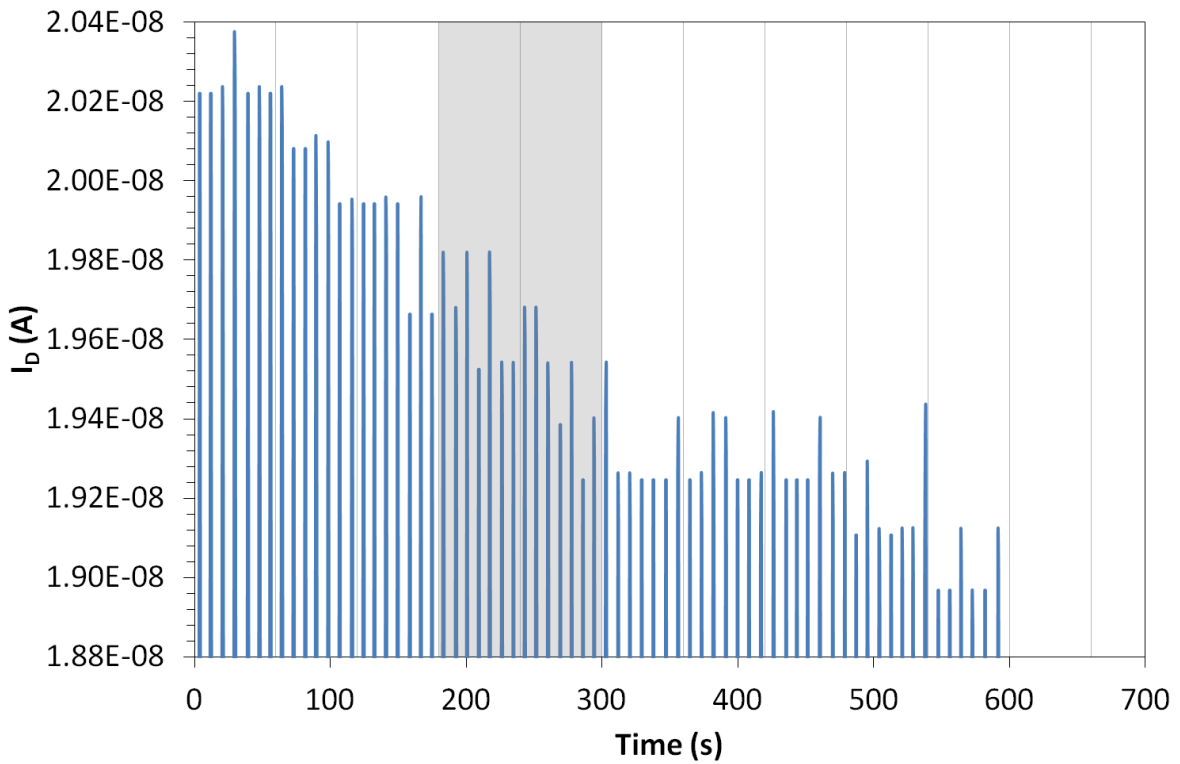


Figure 85. PtEP-I 15 TL 10% propylamine sensing results (peak drain current evolution).

N.B. grey shaded area indicates analyte exposure.

Again a “drift” is observed throughout the run in **Figure 84** and this time both the parameters are increasing. It is becoming obvious that the PtEP-I device is not very stable. This drift is also observed as a reduction in the peak drain current (**Figure 85**).

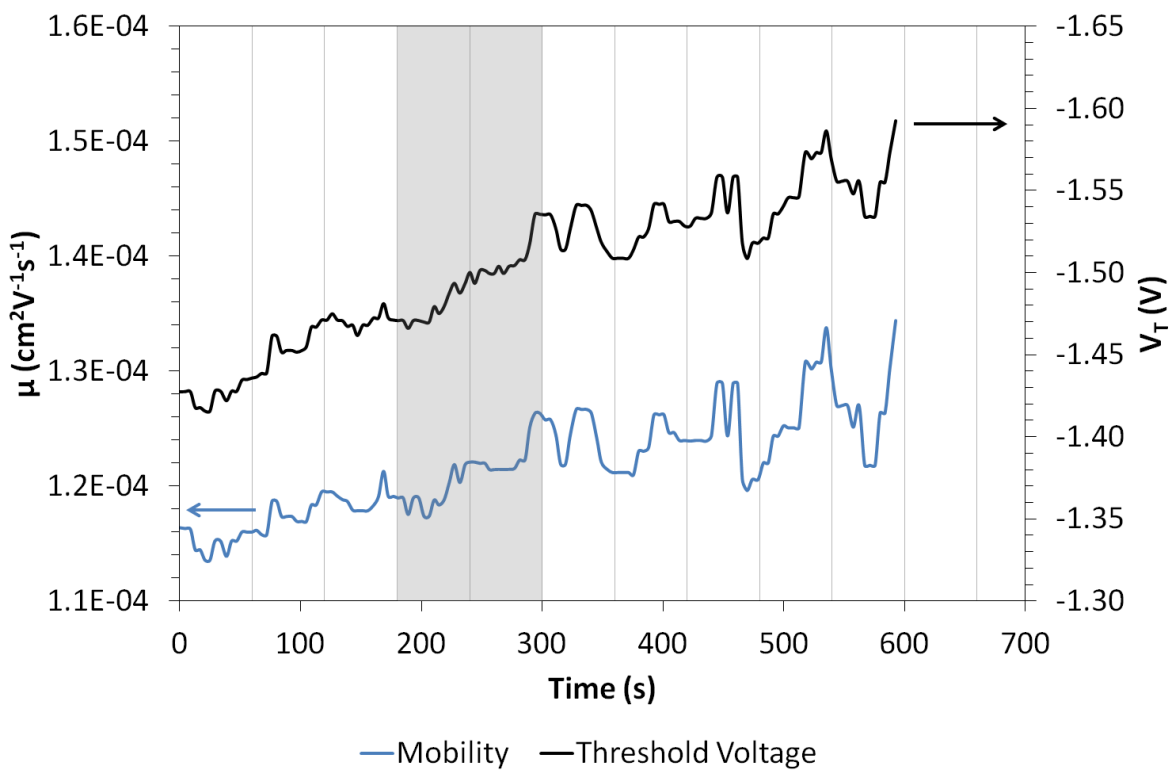


Figure 86. PtEP-I 15 TL 30% propylamine sensing results five-point median. N.B. grey shaded area indicates analyte exposure.

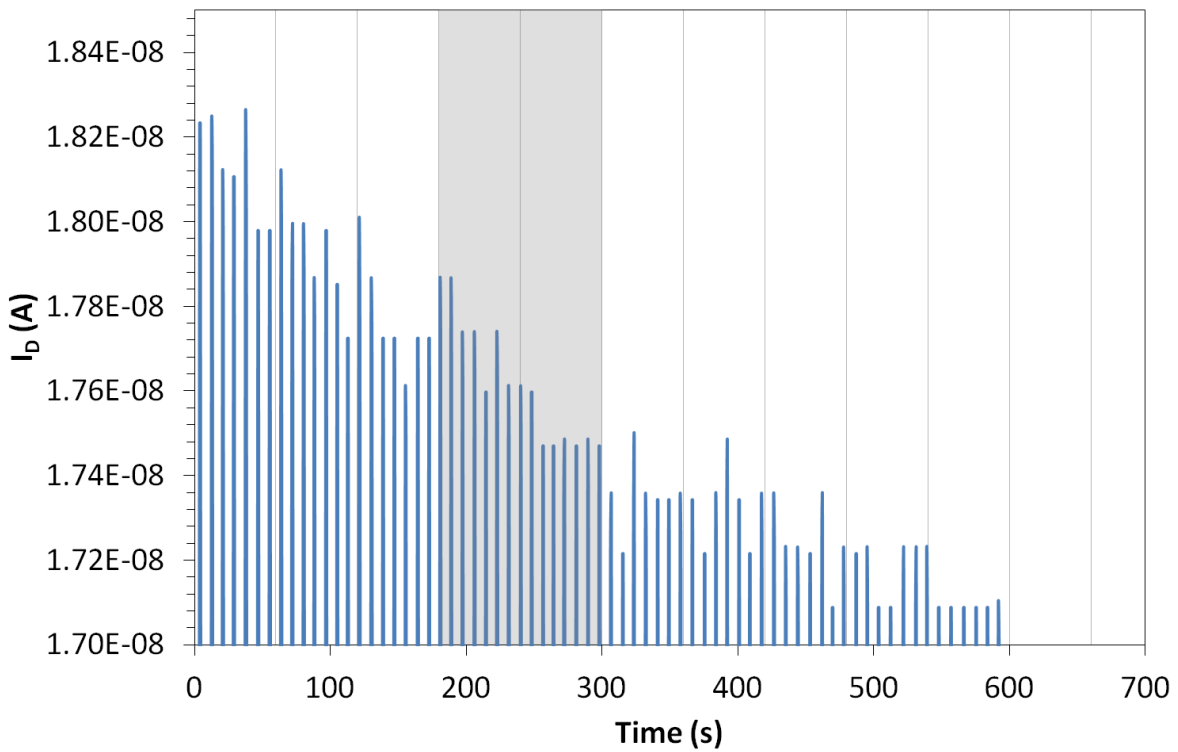


Figure 87. PtEP-I 15 TL 30% propylamine sensing results (peak drain current evolution).

N.B. grey shaded area indicates analyte exposure.

At 30% saturation (**Figure 86** and **Figure 87**) the story is the same as in **Figure 84**, a gradual upwards drift of mobility and threshold and a gradual downwards drift of peak drain current, showing no significant distinction between recovery and exposure phases.

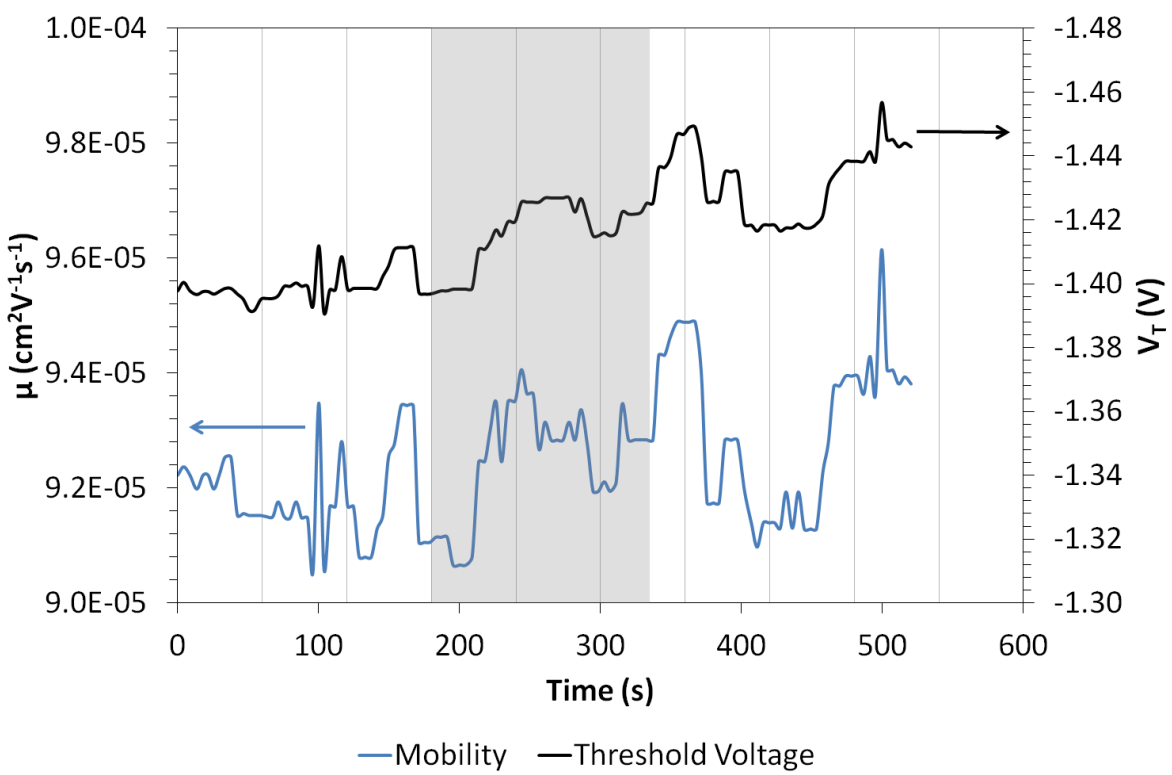


Figure 88. PtEP-I 15 TL 50% propylamine sensing results five-point median. N.B. grey shaded area indicates analyte exposure.

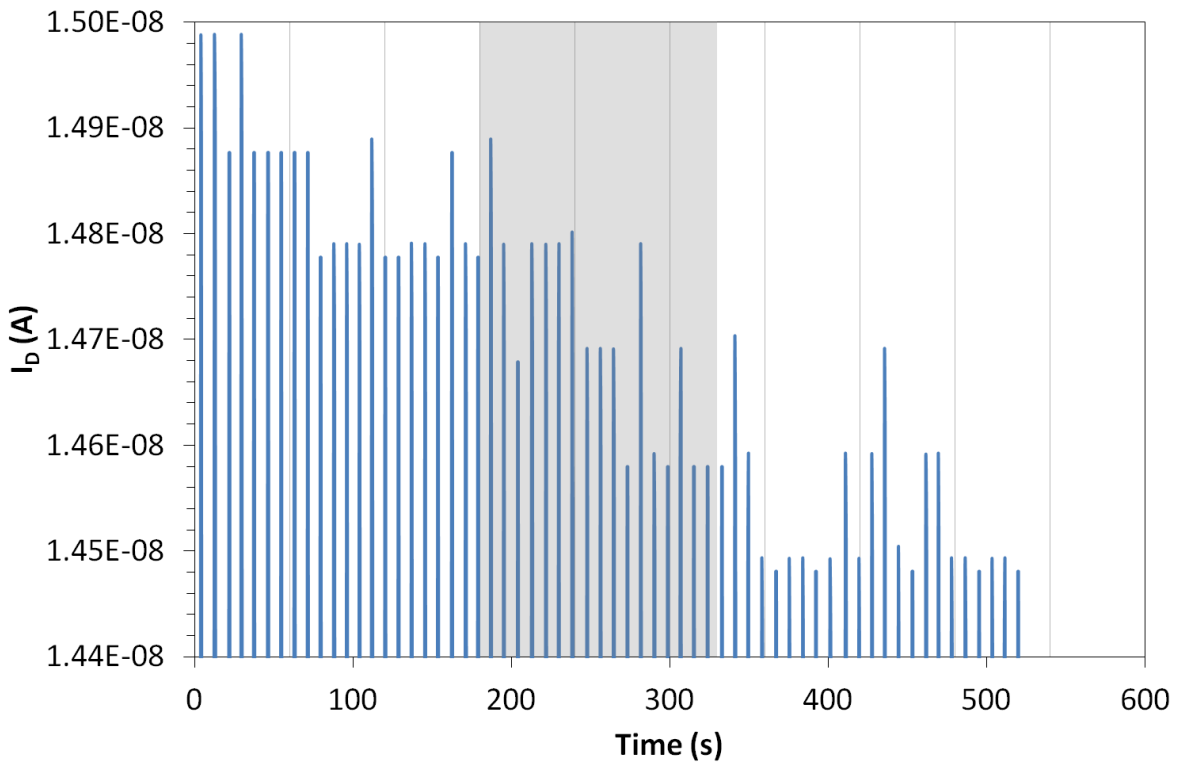


Figure 89. PtEP-I 15 TL 50% propylamine sensing results (peak drain current evolution).

N.B. grey shaded area indicates analyte exposure.

In **Figure 88** there appears to be a small increase in mobility and threshold upon exposure but the data becomes unstable afterwards, continuing the upwards trend before falling then rising again. The peak drain current (**Figure 89**) appears to fall more quickly during the exposure phase, hinting at some manner of interaction.

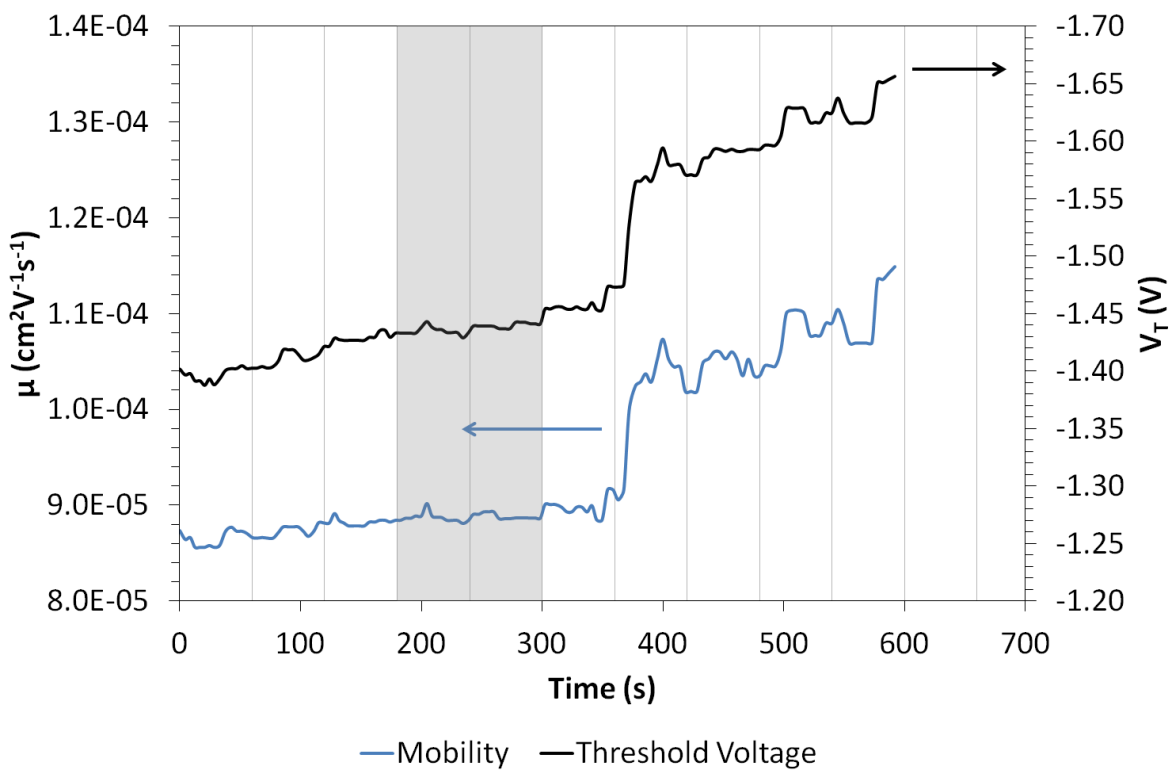


Figure 90. PtEP-I 15 TL 100% propylamine sensing results five-point median. N.B. grey shaded areas indicate analyte exposure.

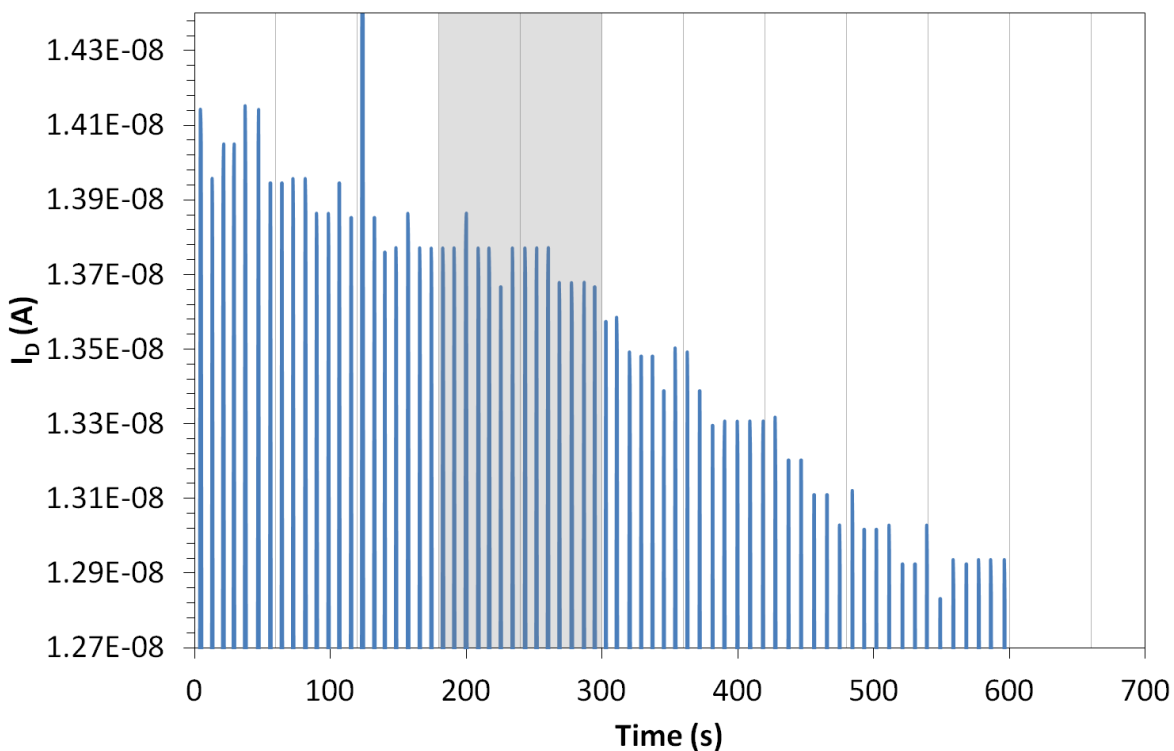


Figure 91. PtEP-I 15 TL 100% propylamine sensing results (peak drain current evolution).
N.B. grey shaded area indicates analyte exposure.

Finally in the 100% saturation exposure run (**Figure 90**), the parameters are stable throughout the initial nitrogen purge and the vapour exposure, then increase and become very noisy in the recovery phase. The peak drain current (**Figure 91**) is gradually decreasing from the start of monitoring, but the rate of decrease is increased during the second minute of exposure and continues beyond.

The PtEP-I device does not appear to show any significant sensitivity towards propylamine; however, due to the data for both mobility and threshold having identical peaks and troughs throughout most of the exposure runs, it is thought that the circuit is struggling to work with such a low current device, so a new material was needed with higher drain current.

5.2 Pentacene Based Organic Field-Effect Transistor Vapour Sensors

5.2.1 Non-Sensitised Pentacene Organic Field-Effect Transistors

All the transistors described in this section were fabricated on silicon wafer substrates, which had 100nm of thermally grown oxide. The gate on each device was created from 100nm of thermally evaporated aluminium which was anodised to 5V to create a ~6.5nm thick aluminium oxide gate insulator, then each device had a monolayer of octadecyltrichlorosilane (OTS) on top of the oxide to reduce the trapping at the semiconductor-insulator interface. Pentacene was thermally evaporated onto the devices to a thickness of ~60nm, then 50nm gold source/drain electrodes were thermally evaporated on top. The transistor Pentacene 17 TR had nickel source/drain contacts.

5.2.1.1 Transistor Characteristics

The pentacene transistors were characterised as described in sections 2.6.1 and 2.6.2 using $V_{D, Max} = V_{G, Max} = -3V$ and $V_{G, Min} = 0V$. The characteristics of the transistors, later used in vapour sensing, are shown in **Figure 92**, **Figure 93**, **Figure 94**, **Figure 95**, **Figure 96**, **Figure 97**, **Figure 98**, **Figure 99** and **Figure 100** (with the exception of the devices used in ethylene sensing, these are shown in section 5.2.1.8).

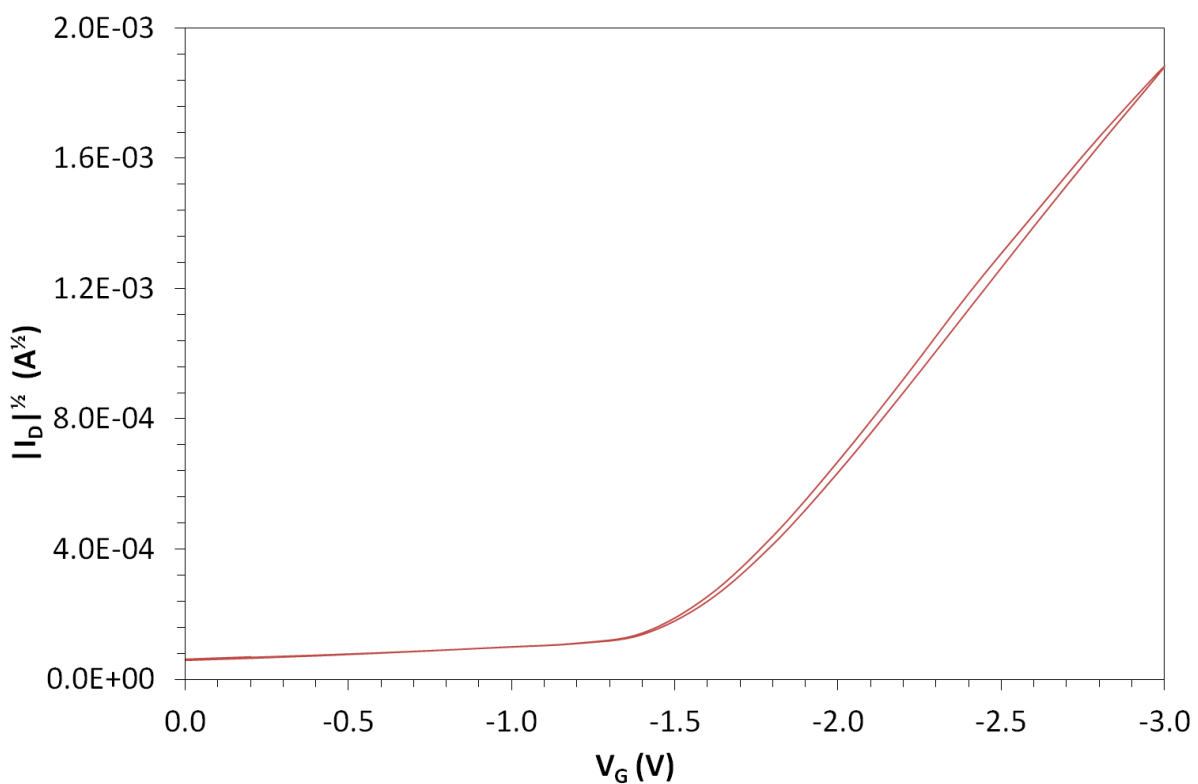
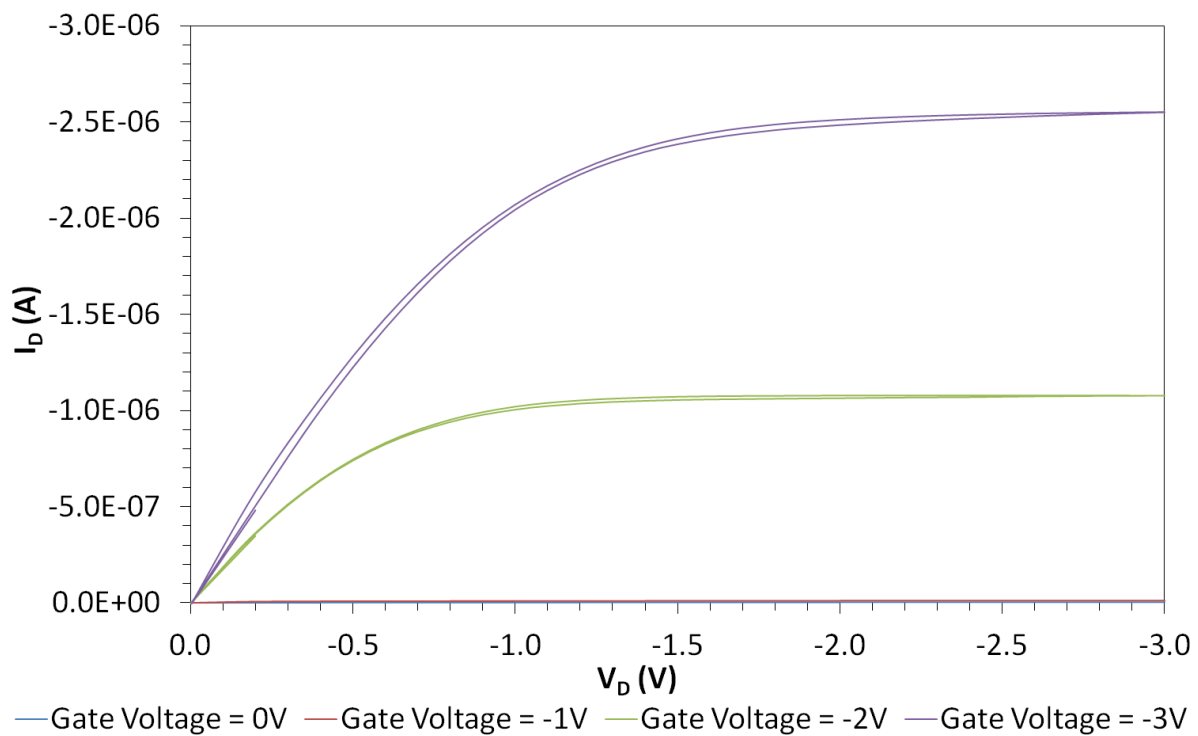


Figure 92. Pentacene 4 TL output and transfer characteristics.

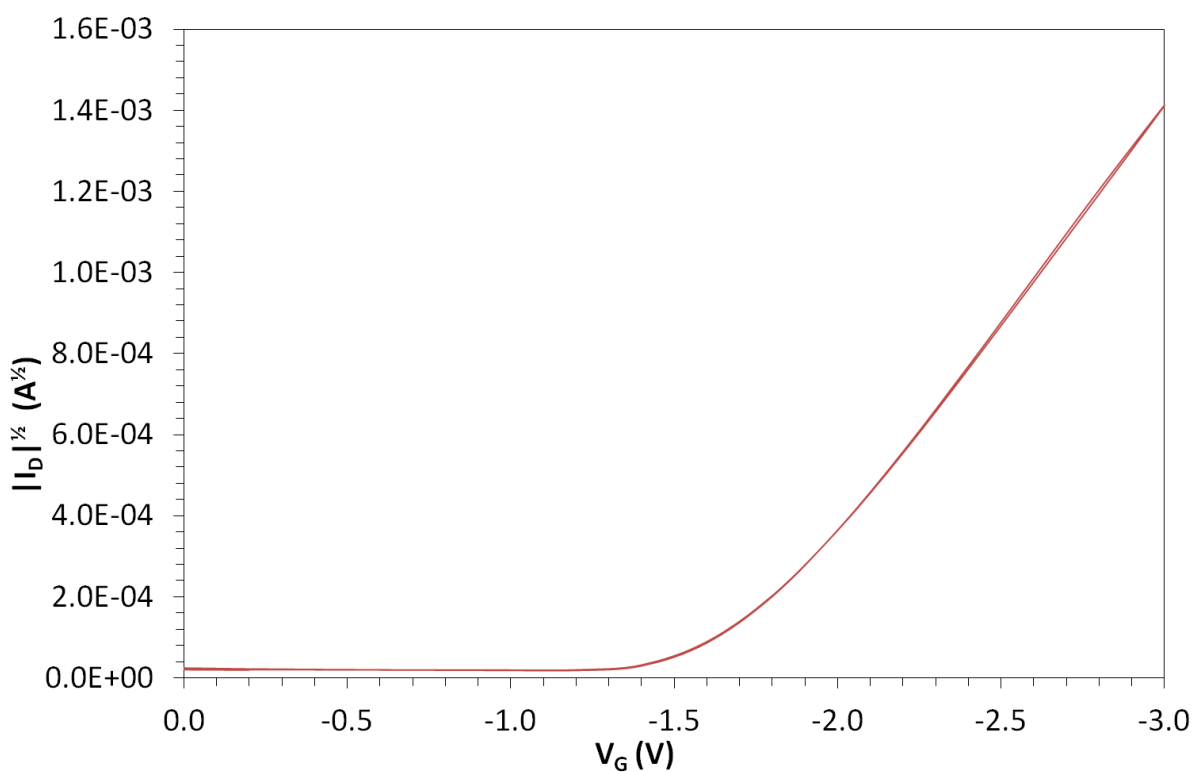
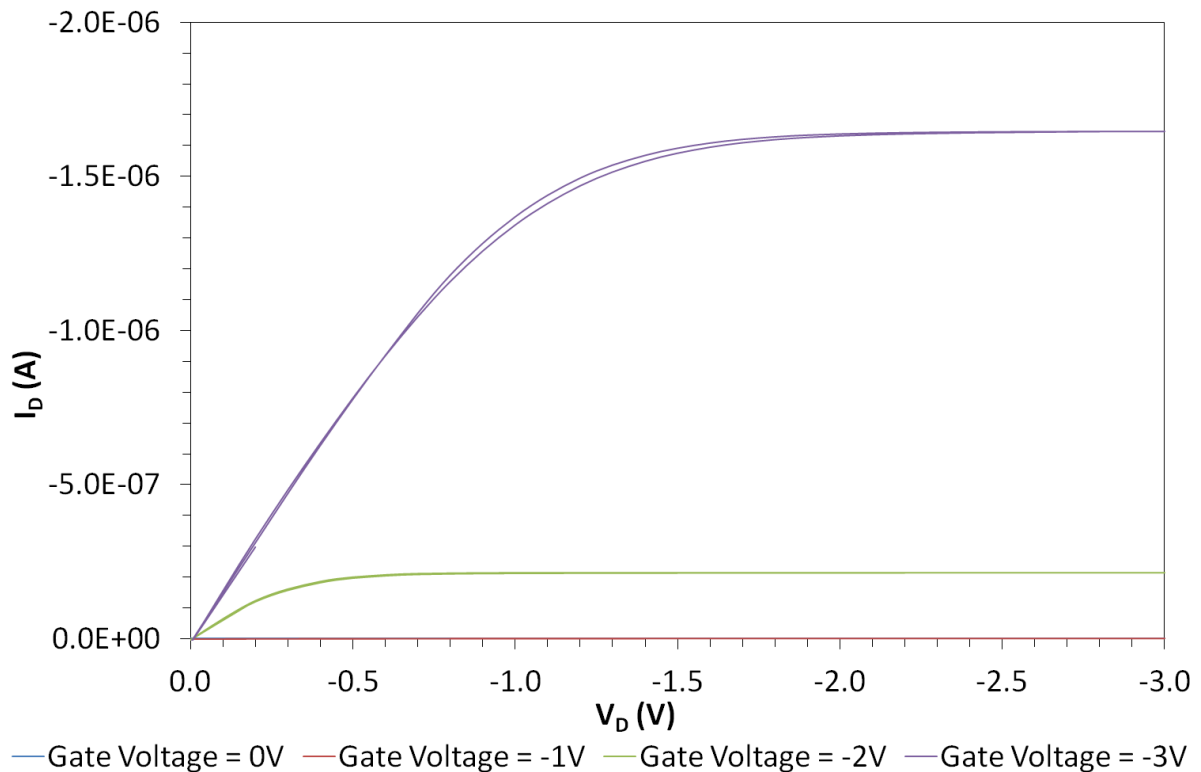


Figure 93. Pentacene 9 BL output and transfer characteristics.

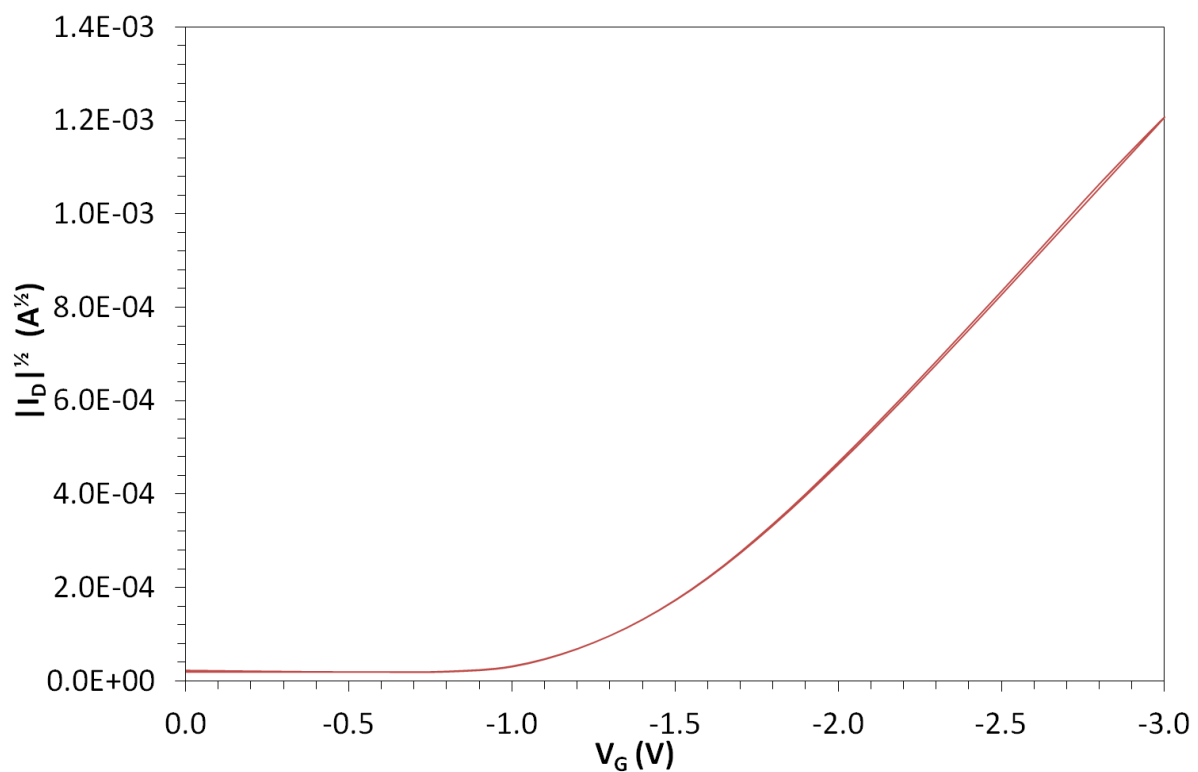
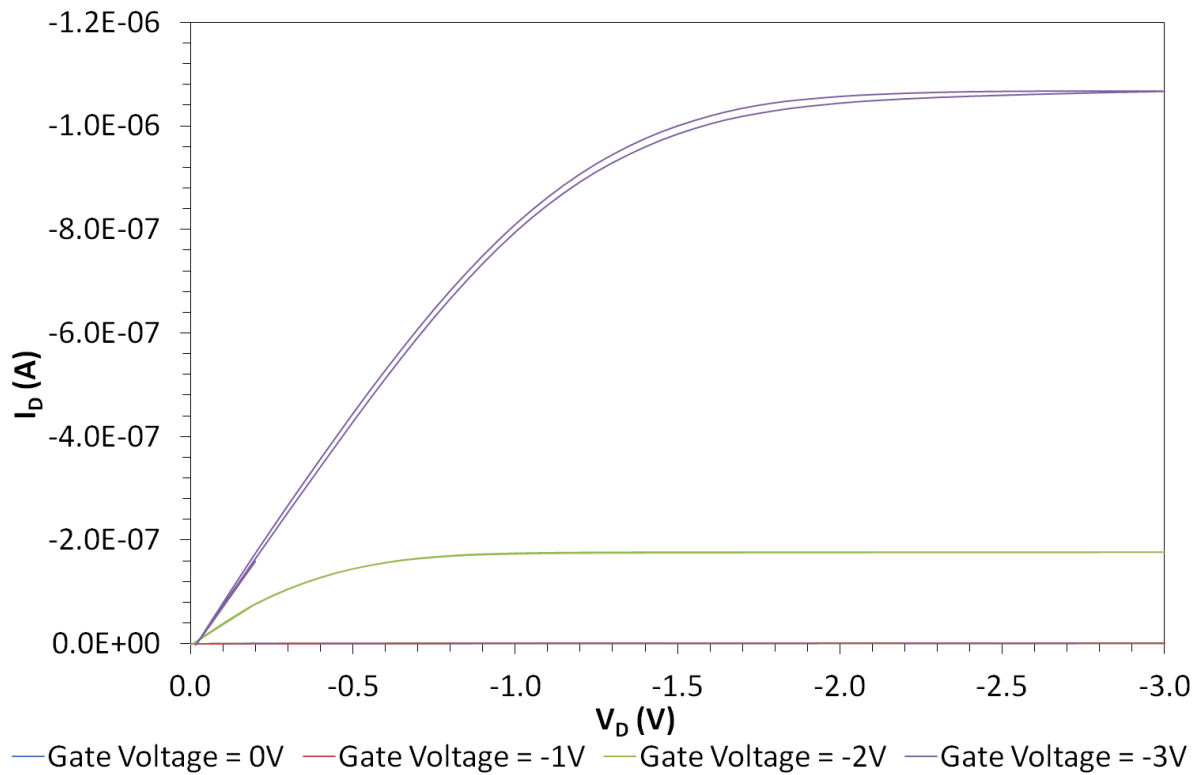


Figure 94. Pentacene 10 BL output and transfer characteristics.

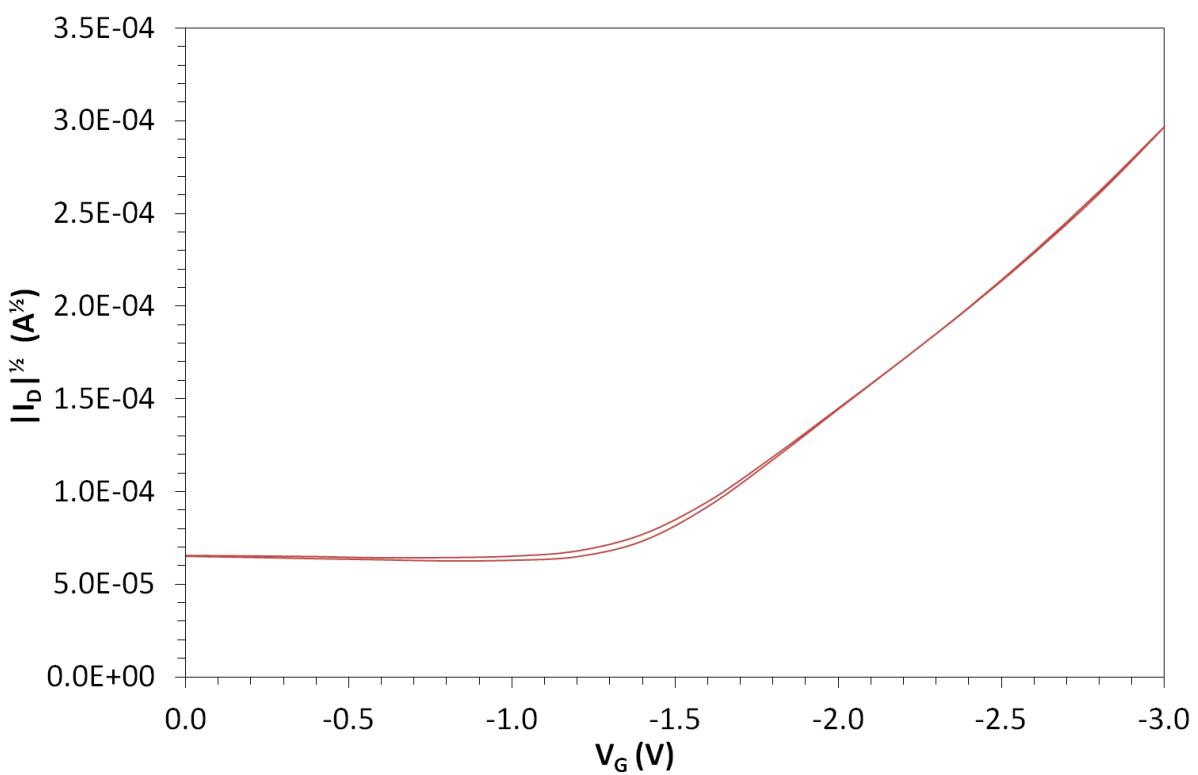
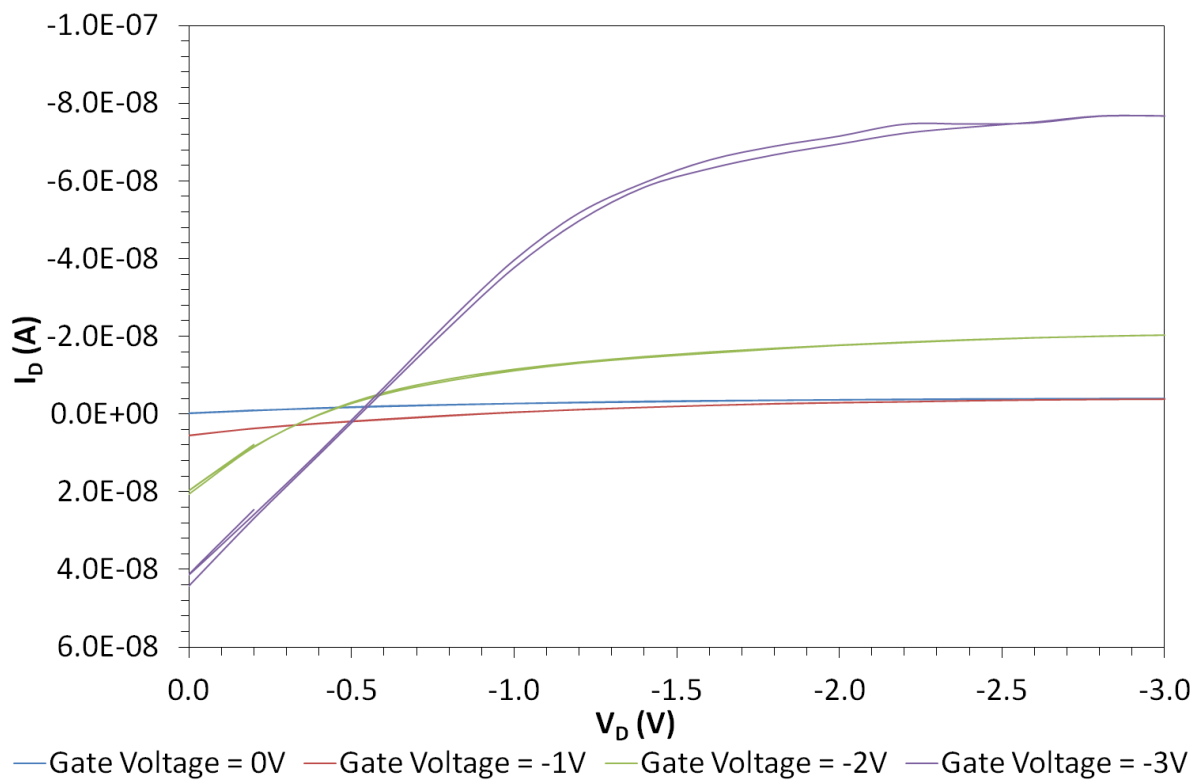


Figure 95. Pentacene 17 TR output and transfer characteristics.

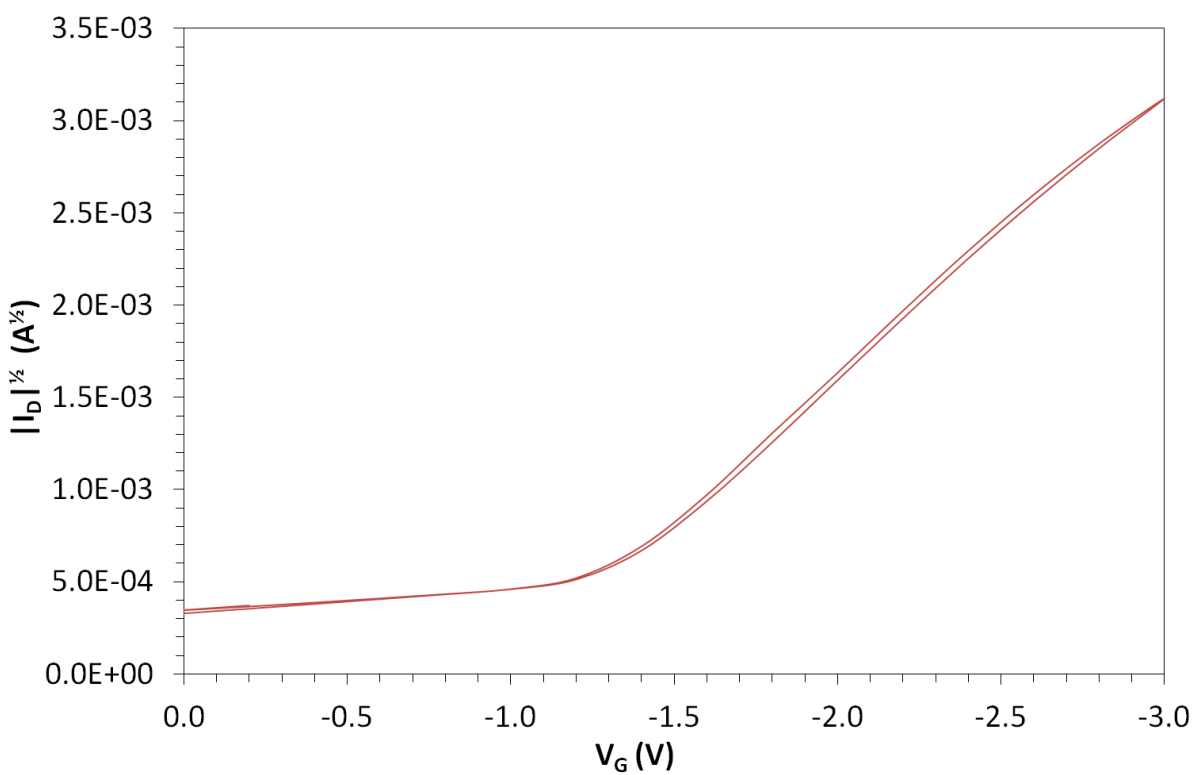
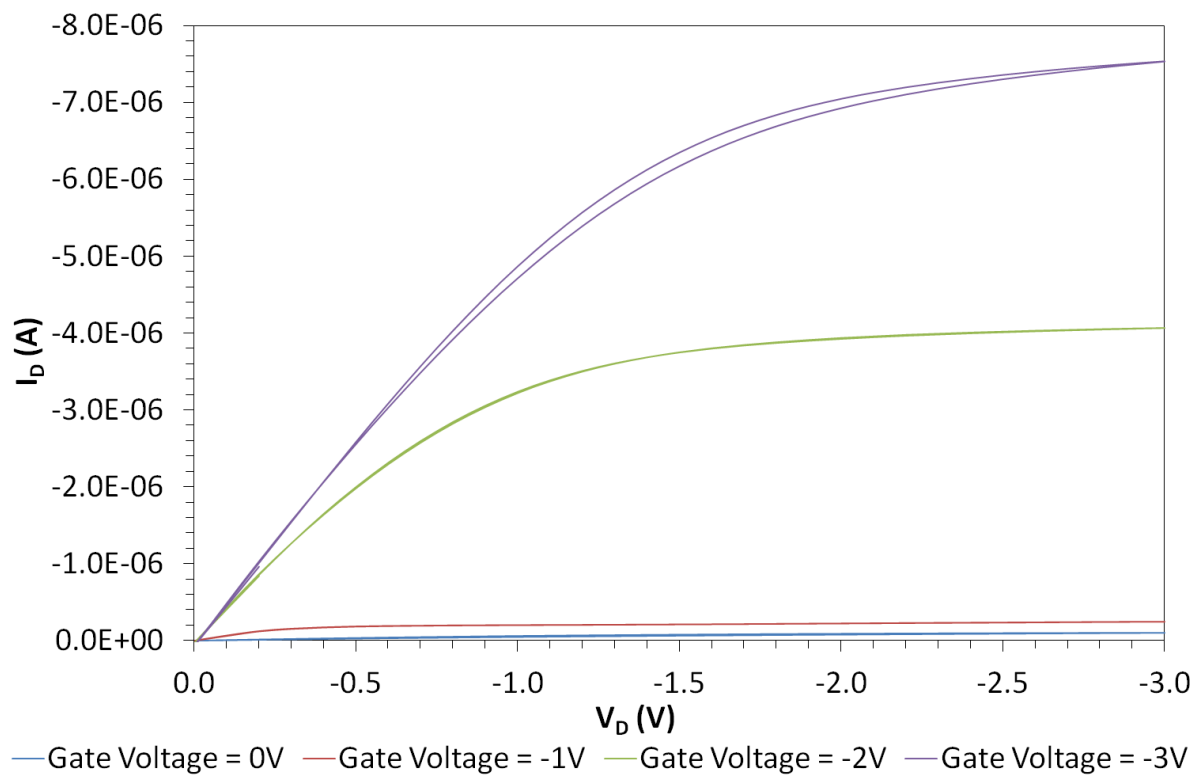


Figure 96. Pentacene 21 TL output and transfer characteristics.

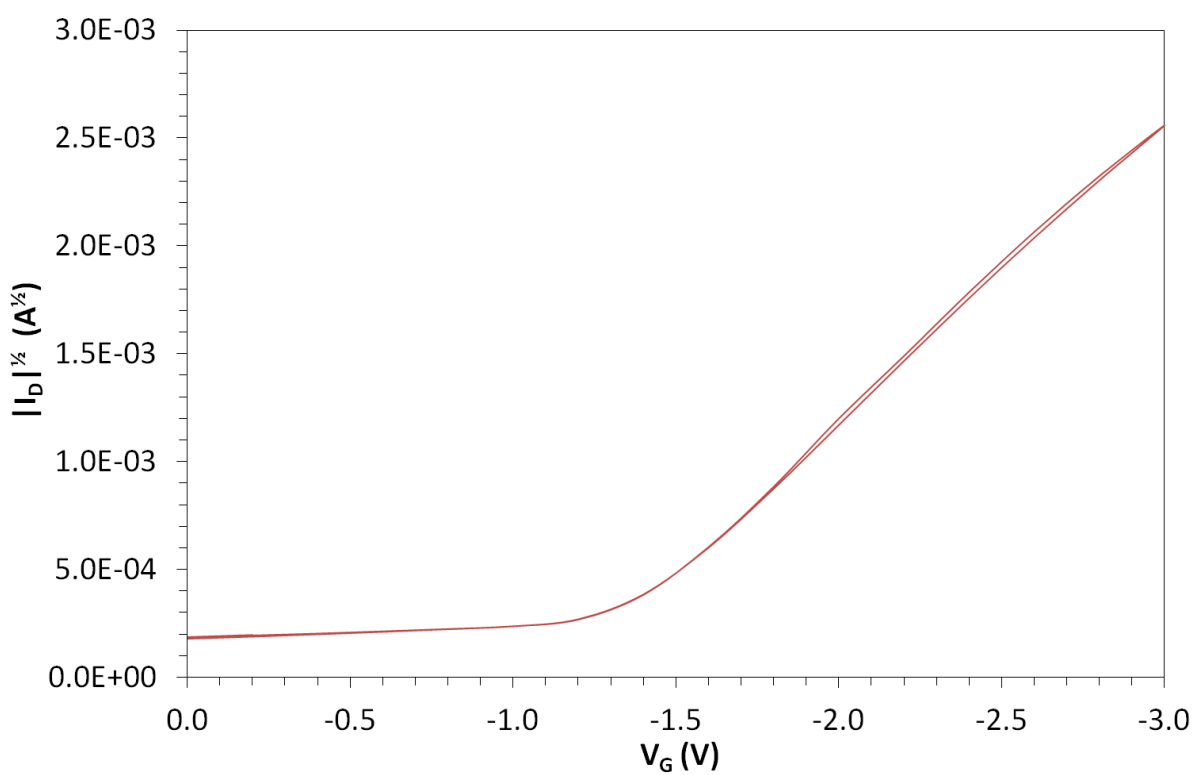
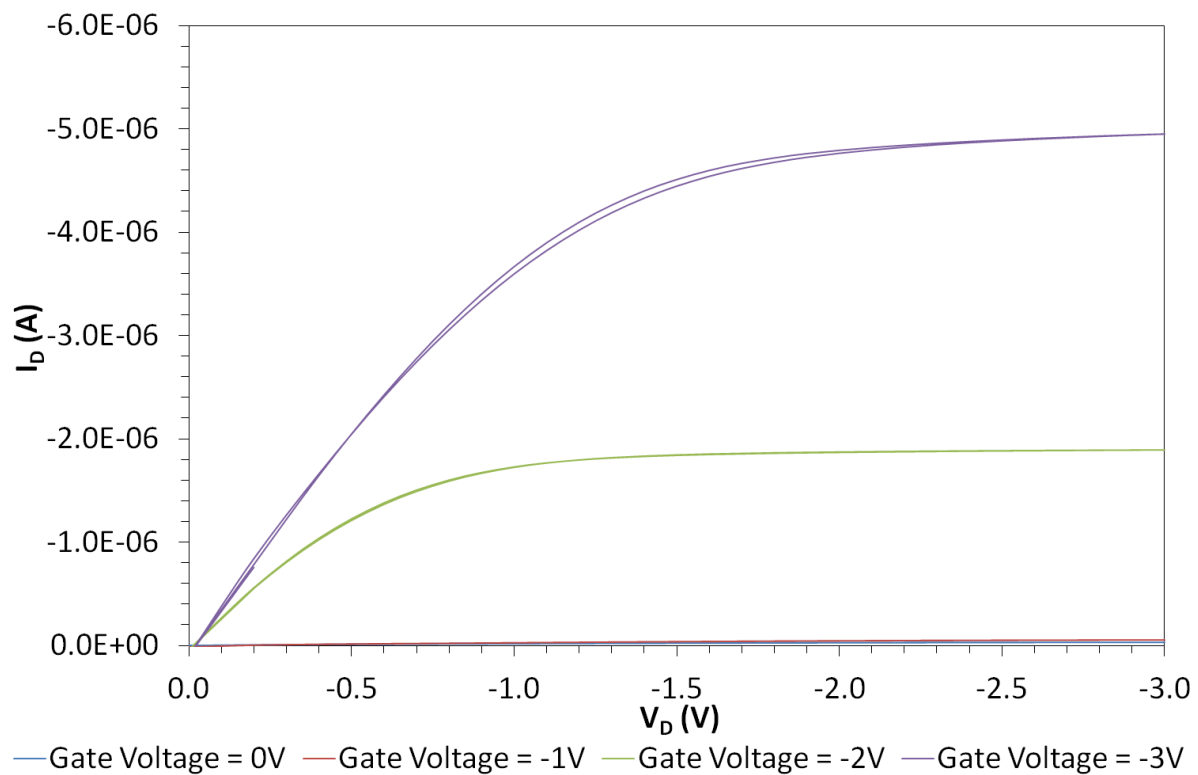


Figure 97. Pentacene 24 BR output and transfer characteristics.

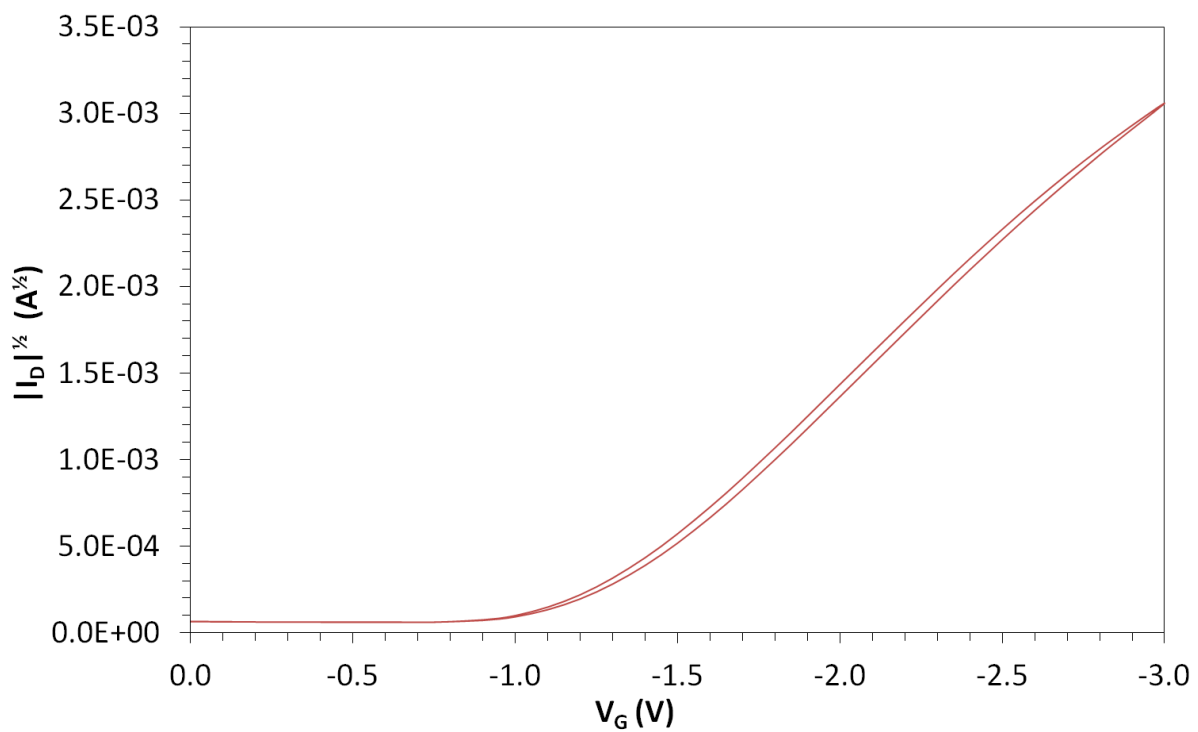
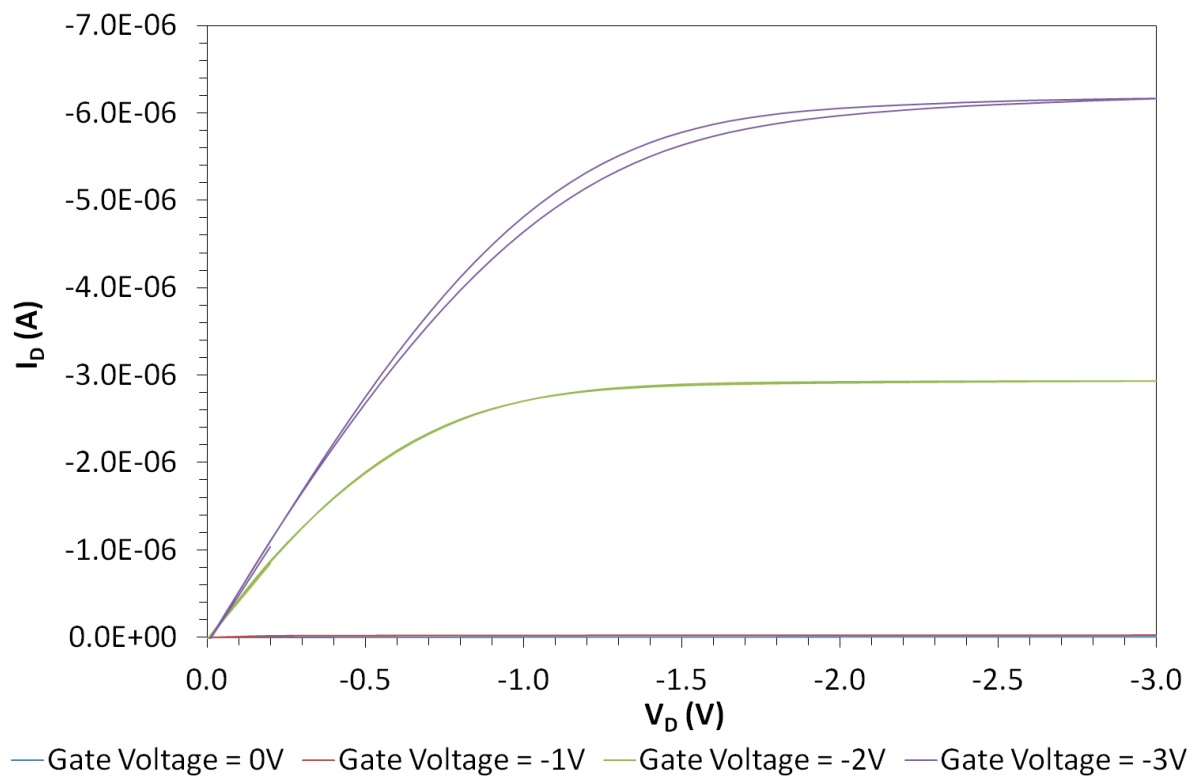


Figure 98. Pentacene 31 BR output and transfer characteristics.

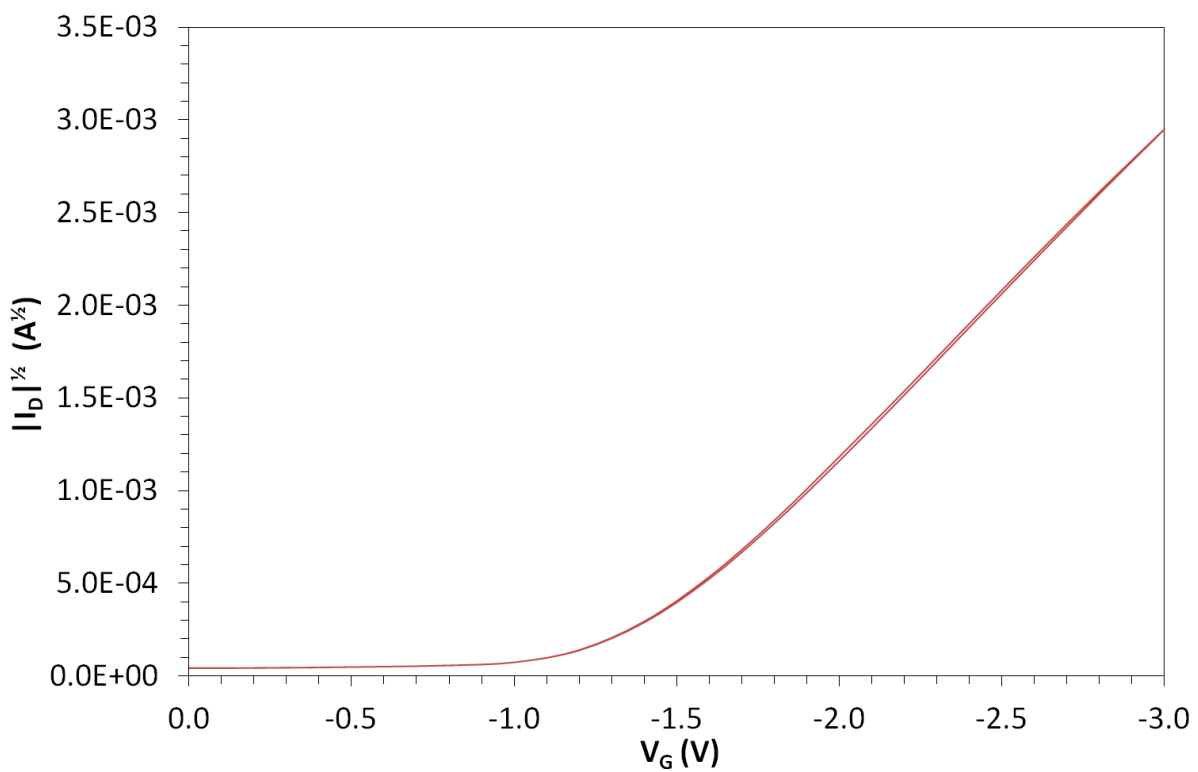
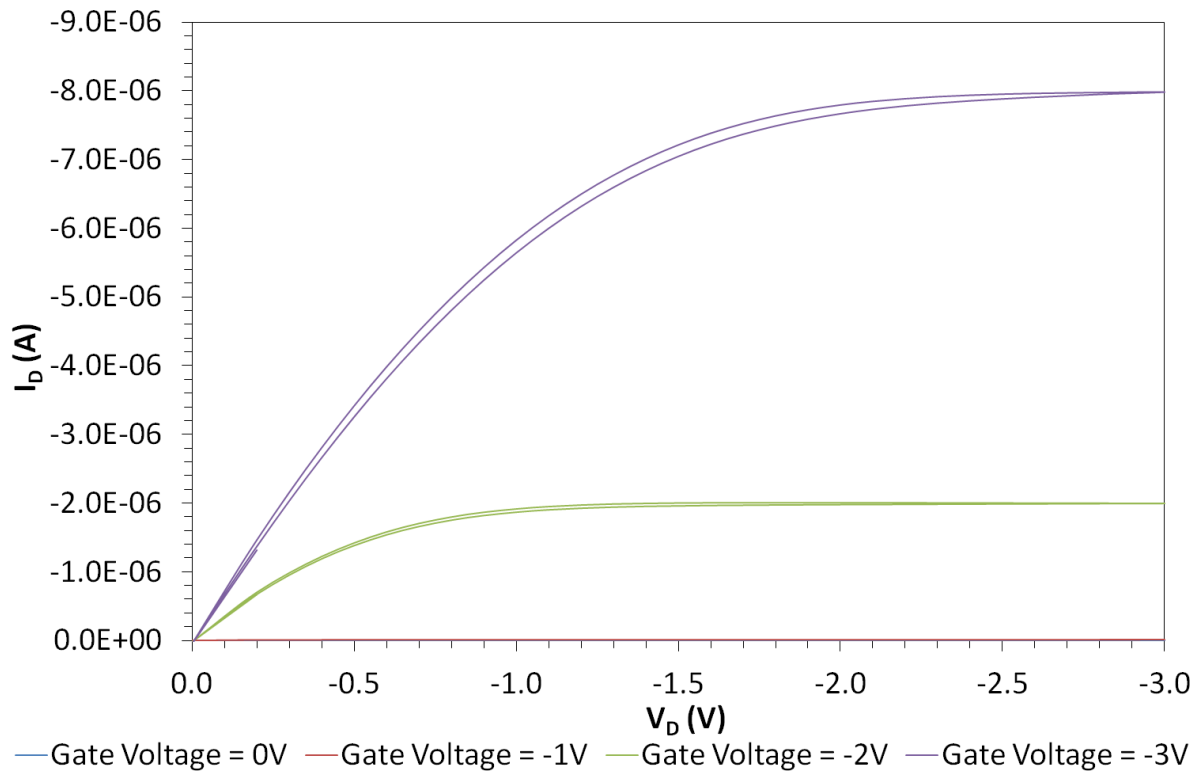


Figure 99. Pentacene 45 TL output and transfer characteristics.

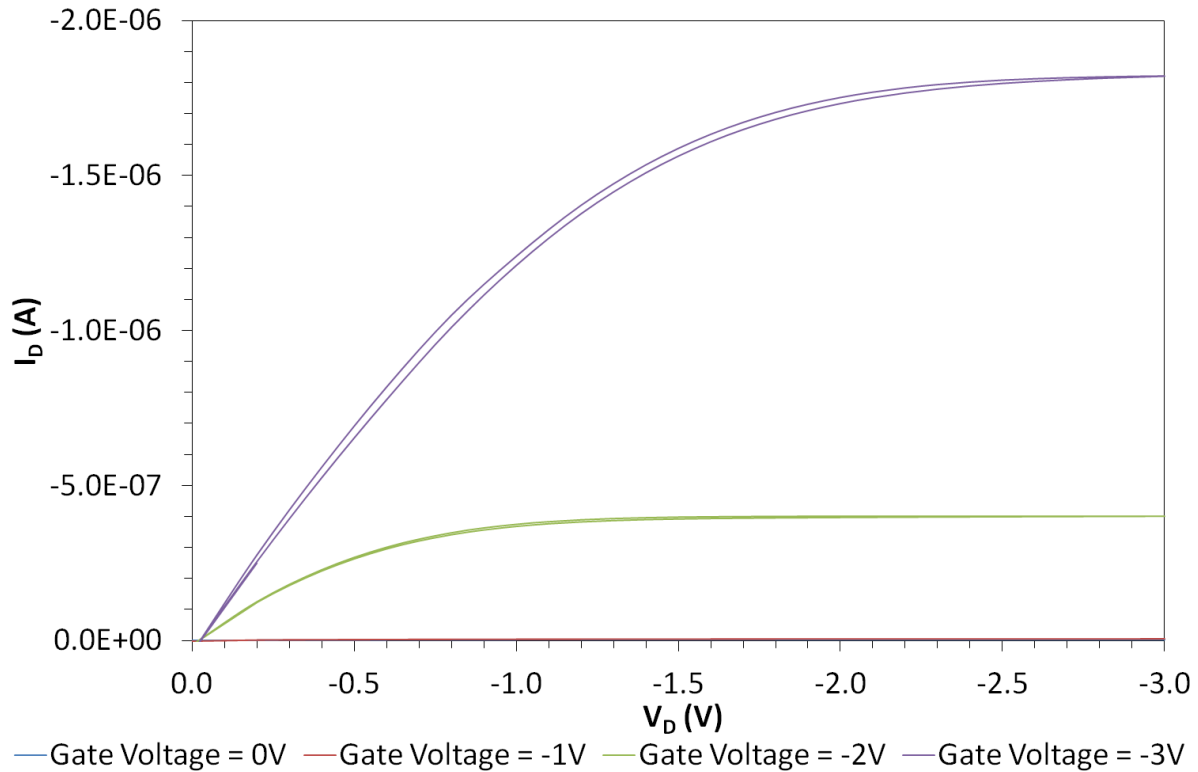


Figure 100. Pentacene 55 BR output and transfer characteristics.

From the output characteristics shown in **Figure 92**, **Figure 93**, **Figure 94**, **Figure 95**, **Figure 96**, **Figure 97**, **Figure 98**, **Figure 99** and **Figure 100** it can be seen that all the OFET devices

show a very low degree of hysteresis in their output characteristics and all have very little in their transfer characteristics. All devices appear to have good contacts, as indicated by the linear behaviour in the initial region of their output characteristics. However the device with nickel source/drain contacts (Pentacene 17 TR, **Figure 95**), although linear in the initial region of its output characteristic, shows considerable gate leakage in the form of the initial positive drain current; this leakage is probably a consequence of the much higher temperatures needed to evaporate nickel causing damage to the device and possibly allowing some nickel to tunnel through the semiconductor.

With regard to the transfer characteristics, they appear to show no obvious problems for any of the devices, aside from the hysteresis mentioned above and a slight curvature in the characteristic of the nickel contacted device. The carrier mobilities and threshold voltages of the devices can be seen in **Table 2**, the mobilities range from $(5.04 \pm 0.10) \times 10^{-2} \text{ cm}^2 \text{V}^{-1} \text{s}^{-1}$ (Pentacene 31 BR) to $(2.81 \pm 0.06) \times 10^{-4} \text{ cm}^2 \text{V}^{-1} \text{s}^{-1}$ (Pentacene 17 TR) and the threshold voltages range from $-1.27 \pm 0.02 \text{ V}$ (Pentacene 31 BR) to $-1.69 \pm 0.03 \text{ V}$ (Pentacene 9 BL). While the threshold voltages are all very good (sub -2V), the mobility values are nowhere near the best that can be achieved from pentacene;^[36] this is due to the fact that high mobility devices are not necessarily needed for this work, so the costly modifications to techniques and equipment needed to produce high mobility devices have not been made (e.g. performing the fabrication and testing in a nitrogen glovebox). Higher mobilities and lower threshold voltages result in larger maximum drain currents; in vapour sensing applications sufficient drain current is required for a low noise measurement to be possible and to allow the current to drop significantly under vapour exposure, but still be above the detection limit of the monitoring system used.

OFET	S/D Material	μ ($\text{cm}^2\text{V}^{-1}\text{s}^{-1}$)	V_T (V)	Peak I_D (A)	R_{on} (Ω)
Pentacene 4 TL	Au	$(2.49 \pm 0.03) \times 10^{-2}$	-1.60 ± 0.02	-3.55×10^{-6}	8.46×10^5
Pentacene 9 BL	Au	$(1.75 \pm 0.03) \times 10^{-2}$	-1.69 ± 0.03	-2.00×10^{-6}	1.50×10^6
Pentacene 10 BL	Au	$(7.16 \pm 0.30) \times 10^{-3}$	-1.34 ± 0.05	-1.46×10^{-6}	2.06×10^6
Pentacene 17 TR	Ni	$(2.81 \pm 0.06) \times 10^{-4}$	-1.39 ± 0.03	-8.82×10^{-8}	3.40×10^7
Pentacene 21 TL	Au	$(4.19 \pm 0.09) \times 10^{-2}$	-1.33 ± 0.03	-9.75×10^{-6}	3.08×10^5
Pentacene 24 BR	Au	$(3.38 \pm 0.03) \times 10^{-2}$	-1.38 ± 0.01	-6.56×10^{-6}	4.57×10^5
Pentacene 31 BR	Au	$(5.04 \pm 0.10) \times 10^{-2}$	-1.27 ± 0.02	-9.35×10^{-6}	3.21×10^5
Pentacene 45 TL	Au	$(4.52 \pm 0.20) \times 10^{-2}$	-1.35 ± 0.05	-8.69×10^{-6}	3.45×10^5
Pentacene 55 BR	Au	$(1.07 \pm 0.02) \times 10^{-2}$	-1.40 ± 0.03	-1.89×10^{-6}	1.58×10^6

Table 2. Mobility and threshold values for pentacene OFETs.

The peak drain currents in the transfer characteristics range from -8.82×10^{-8} A for Pentacene 17 TR to -9.75×10^{-6} A for Pentacene 21 TL, meaning a range of on-resistance values from $3.08 \times 10^5 \Omega$ to $3.4 \times 10^7 \Omega$ (see **Table 2**). The average mobility, threshold, and on-resistance of the gold source/drain OFETs presented here (17 TR excluded) are $2.89 \times 10^{-2} \text{ cm}^2\text{V}^{-1}\text{s}^{-1}$, -1.42 V and $4.60 \times 10^6 \Omega$ respectively.

5.2.1.2 Amine Sensing Results Using the Gain Method Characterisation Scheme

The vapour sensing experiment was carried out using the techniques and equipment described in section 3.2 and the transistor was monitored using the gain-method, as described in section 2.6.3. Continuing on with the amine sensing work that was begun in section 5.1.3.2, this time a less volatile amine (octylamine) was chosen to allow lower vapour concentrations to be created using the bubbler and gas mixing system. The transistor Pentacene 4 TL was used to sense two different concentrations of octylamine vapour: 1% saturated (1% of nitrogen to the bubbler, with the bubbler immersed in ice water) and 5% saturated (5% of nitrogen to the bubbler, with the bubbler immersed in ice water); the theoretical concentration for 100% saturated vapour is 354 ppm at 0°C. The mobility and threshold data was smoothed using a five-point median, the data is presented in **Figure 101** for 1% saturated vapour exposure and in **Figure 103** for 5% saturated exposure; while the raw drain current data is presented in **Figure 102** for 1% exposure and in **Figure 104** for 5% exposure.

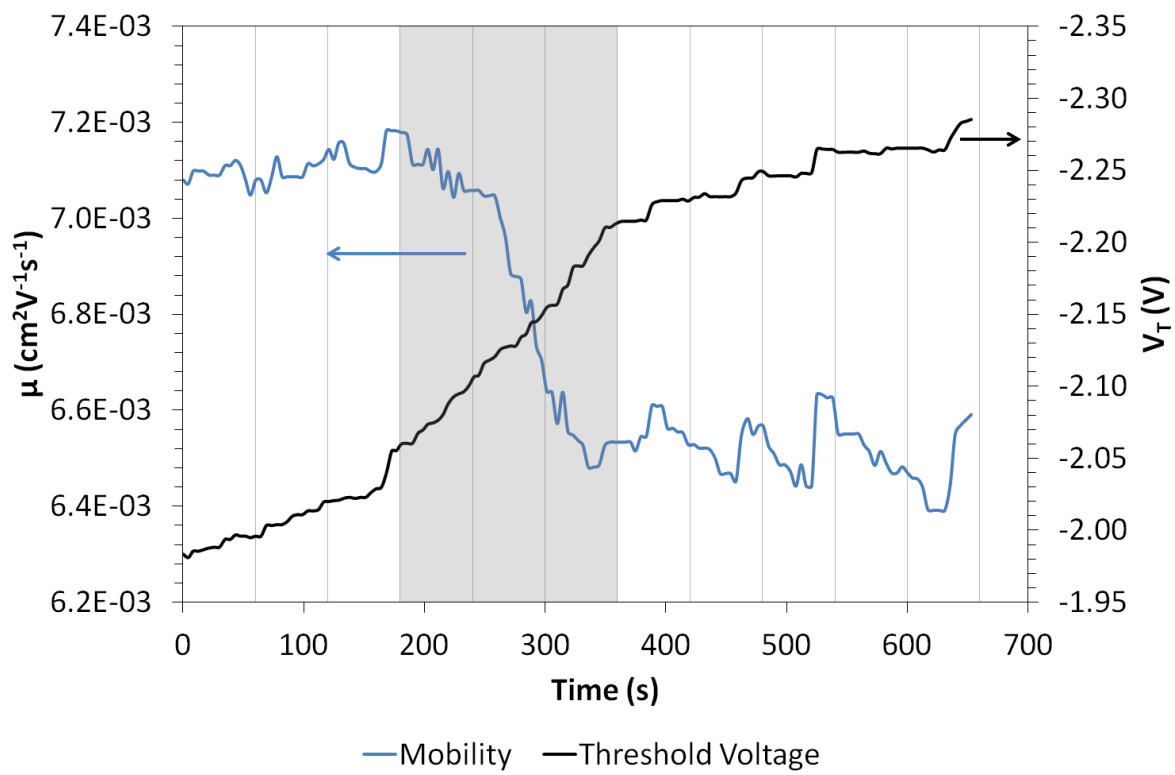


Figure 101. Pentacene 4 TL 1% octylamine sensing results five-point median. N.B. grey shaded area indicates analyte exposure.

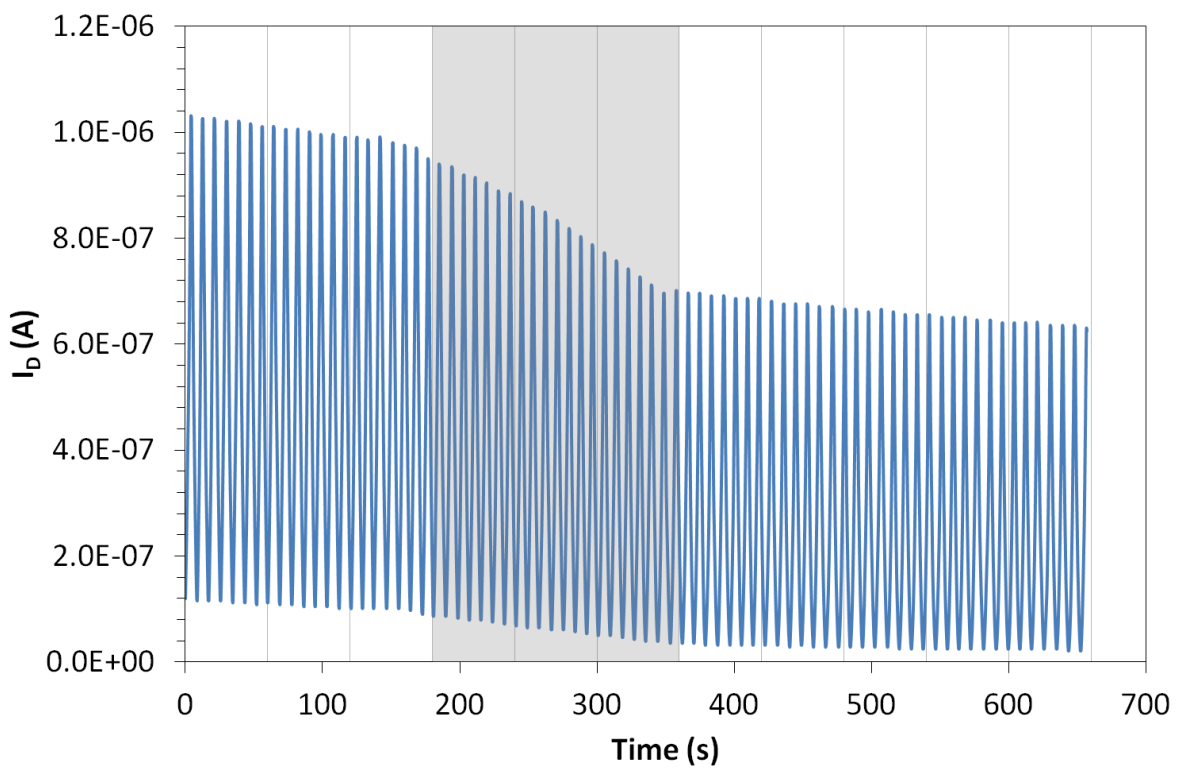


Figure 102. Pentacene 4 TL 1% octylamine sensing results (peak drain current evolution).

N.B. grey shaded area indicates analyte exposure.

From the 1% exposure run shown in **Figure 101**, it is obvious that the octylamine exposure evokes a response in the pentacene OFETs. The magnitude of this response is characterised by the $\sim 8\%$ ($\sim 0.6 \times 10^{-3} \text{ cm}^2 \text{V}^{-1} \text{s}^{-1}$) reduction in mobility and the $\sim 8\%$ ($\sim -0.17 \text{ V}$) increase in threshold voltage. From **Figure 102** it can be seen that the peak drain current is reduced by $\sim 27\%$ ($\sim 2.53 \times 10^{-7} \text{ A}$).

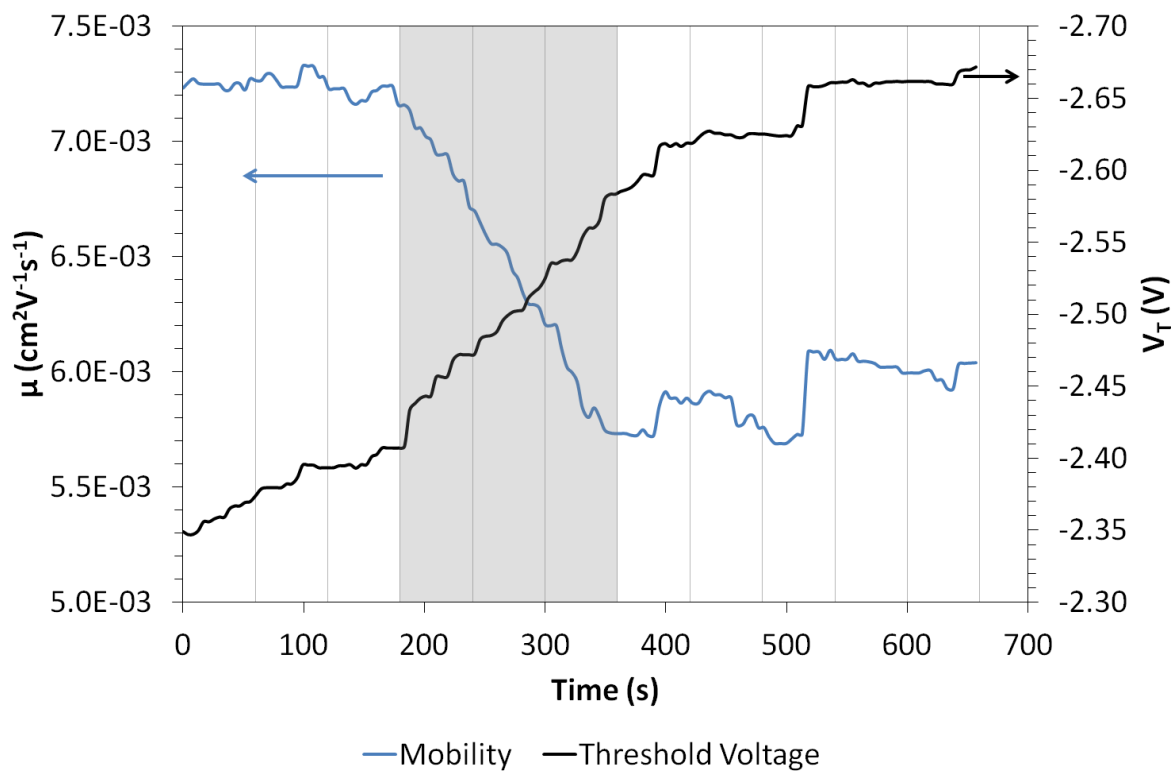


Figure 103. Pentacene 4 TL 5% octylamine sensing results five-point median. N.B. grey shaded area indicates analyte exposure.

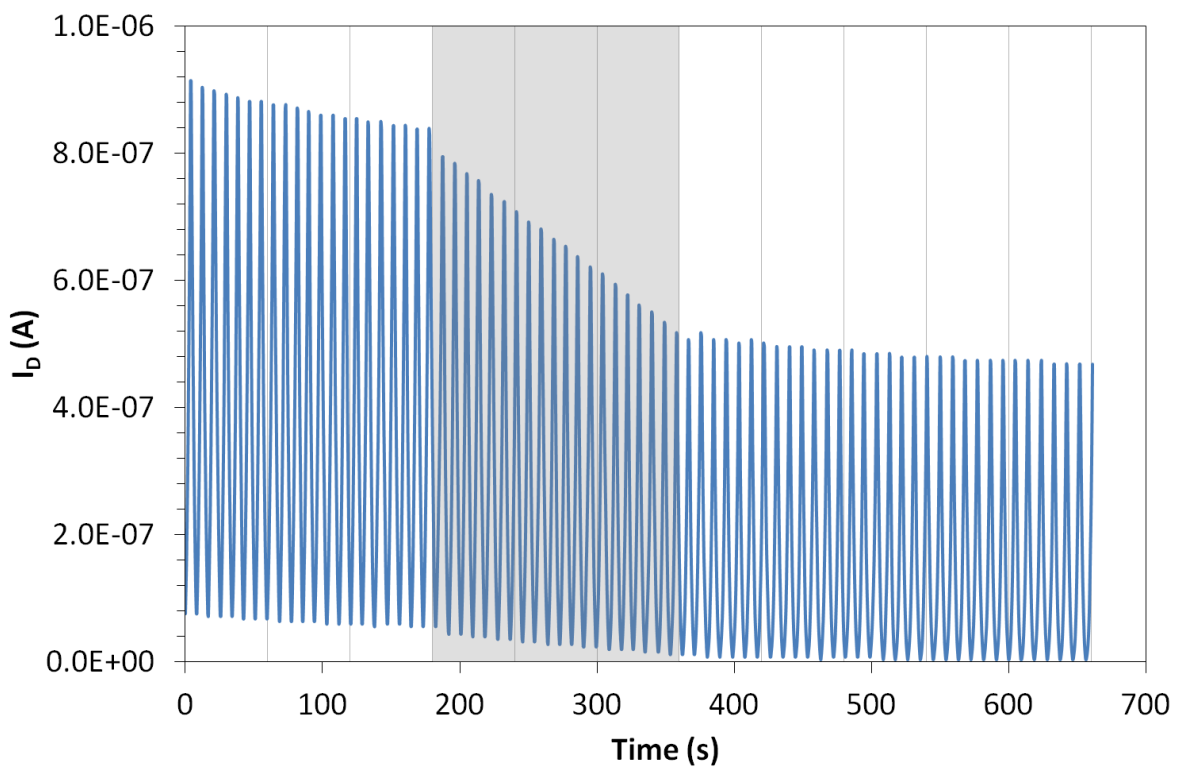


Figure 104. Pentacene 4 TL 5% octylamine sensing results (peak drain current evolution).

N.B. grey shaded area indicates analyte exposure.

In the 5% saturated vapour exposure run (**Figure 103** and **Figure 104**) the octylamine exposure induces a greater mobility change than the 1% exposure but a very similar change in the threshold; the changes were as follows: mobility decreased by $\sim 19\%$ ($\sim 1.3 \times 10^{-3} \text{ cm}^2 \text{V}^{-1} \text{s}^{-1}$), threshold voltage increased by $\sim 7\%$ ($\sim -0.17 \text{ V}$) and peak drain current decreased by $\sim 40\%$ ($\sim 3.32 \times 10^{-7} \text{ A}$). Therefore a 5-fold increase in amine concentration creates a mobility response that is just over twice as large as before. The absolute value of the threshold change is the same in both cases, but a smaller percentage change in the case of higher concentration. While the decrease in peak drain current is just over 1.3 times larger in the absolute sense and almost 1.5 times larger as a percentage of the pre-exposure value. However, as the tests were carried out consecutively on the same OFET it can be seen from **Figure 101** and **Figure 103** that mobility has managed to recover back to its pre-exposure value between tests, but threshold voltage has not recovered at all meaning we are seeing a cumulative effect on the threshold. **Figure 102** and **Figure 104** show that the peak drain current does not completely recover either between tests. The effect on the threshold and drain current and their subsequent refusal to recover may be explained by the characteristic

amine bonding preference for gold^[126] causing the amine to coat the source and drain electrodes to hamper injection and thus raise the threshold and therefore lower the peak drain current. It can also be seen from **Figure 101** and **Figure 103** that the threshold also suffers from an upwards drift in both exposure runs, possibly indicating some kind of gate bias stress effects or constant damage being done to the gate insulator by the drive voltage, causing a gradual increase in gate leakage and therefore threshold.

The mobility changes could be explained by the amine penetrating into the pentacene grain boundaries and hampering the conduction by creating traps between grains and therefore reducing the effective mobility, more testing with different grain-sizes or channel lengths would be required to confirm this (as in the work performed by Someya *et al*).^[30]

5.2.1.3 Amine Sensing Results Using the Current to Voltage Converter Characterisation Scheme

Although good results have been obtained from the gain-method circuit in previous sections, unfortunately the system had a “bug” in its control software that caused it to regularly “crash” and cease all data acquisition and voltage driving activities, also ruining many sensing runs performed on devices with irreversible responses. A new simpler data monitoring circuit for vapour sensing was created - the current to voltage converter circuit, see section 3.1.1 for more details.

5.2.1.3.1 Determination of the Best Drive Voltage Function

To perform initial testing on the new characterisation scheme it was necessary to use a sensor/odour combination that created an easily measurable response, so the pentacene OFET and octylamine vapour combination was chosen. Firstly a square-wave drive was used similar to that used by the gain-method with a voltage =±3V. The transistor chosen for this test was Pentacene 9 BL, the octylamine concentration used was 1% saturation (1% of nitrogen to the bubbler, with the bubbler immersed in ice water); as mentioned previously the theoretical concentration at 100% saturation is 354ppm at 0°C. The results of the exposure can be seen in **Figure 105**.

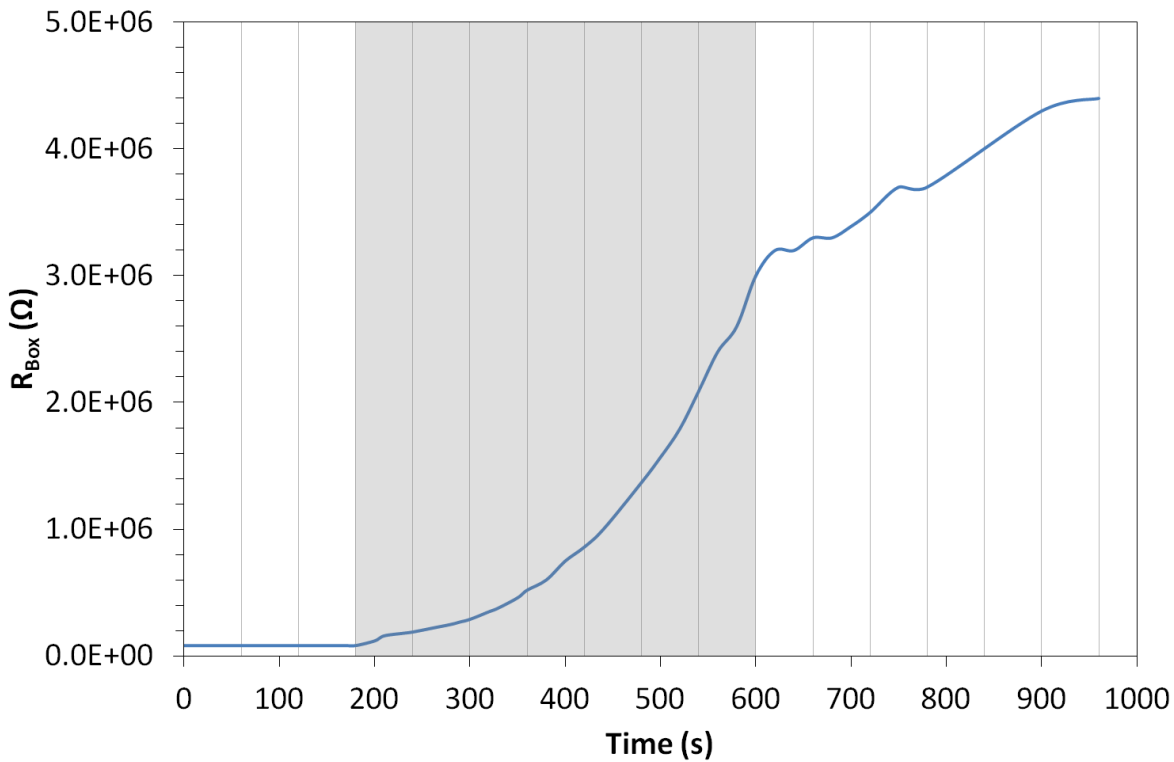


Figure 105. Pentacene 9 BL 1% octylamine sensing results. N.B. grey shaded area indicates analyte exposure.

Inspection of **Figure 105** shows an impressive response to amine exposure. However after exposure has finished and nitrogen flushing begins the channel resistance of the OFET continues to rise fairly rapidly indicating some kind of problem present in the system. Electrical testing of the OFET after exposure shows almost all of the current is now lost to gate leakage, meaning the gate insulator must have been damaged in some way during sensing. Upon inspection of the input “square wave” signal from the function generator it becomes apparent that voltage spikes are present when the function generator first increases or decreases voltage to a new value. These voltages can be quite large so it is thought that the spikes may be damaging the gate insulator, as the Al was only anodised to 5V, any voltages larger than this will cause dielectric breakdown (see section 2.3).

In light of this discovery it was decided that a function with a more gradual voltage rise should be used as the drive voltage, so a sine wave was chosen. Therefore the same concentration of octylamine was used again along with the OFET Pentacene 10 BL to perform an exposure run, the results can be seen in **Figure 106**.

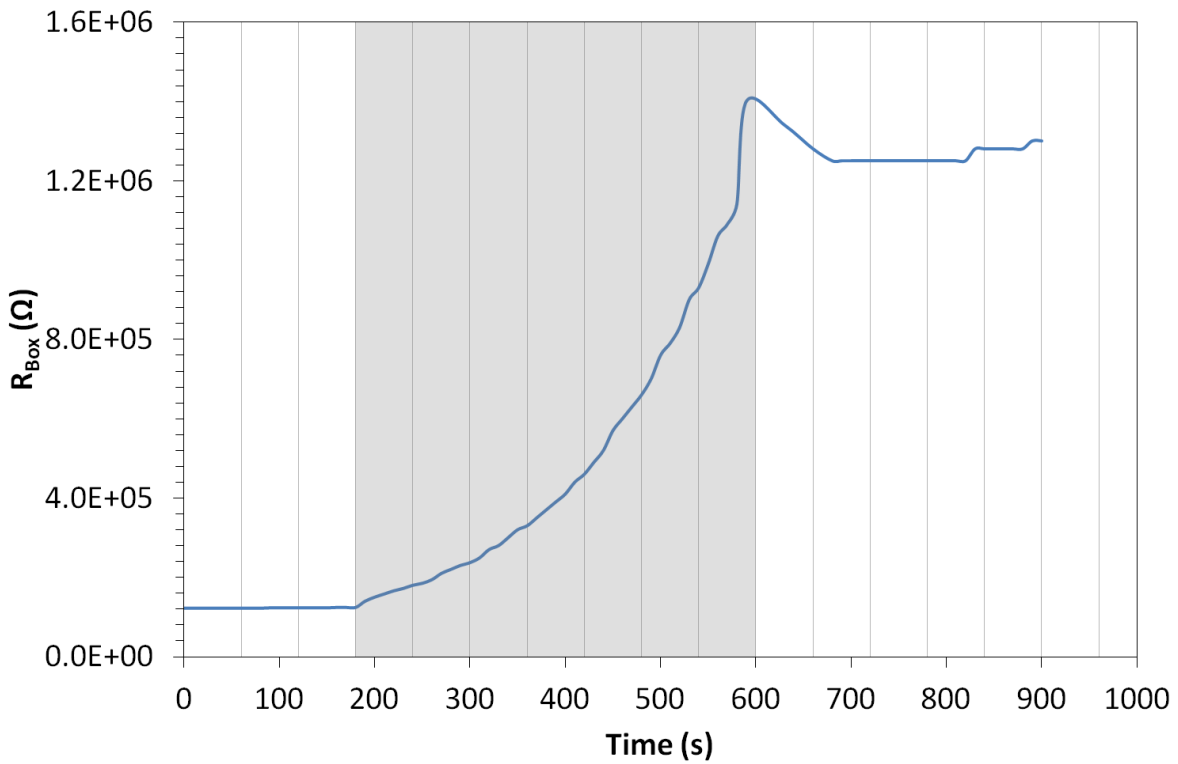


Figure 106. Pentacene 10 BL 1% octylamine sensing results. N.B. grey shaded area indicates analyte exposure.

In contrast to **Figure 105**, **Figure 106** still has the good response but abruptly stops rising when exposure ends and even undergoes a small recovery; it was therefore decided that a sine wave drive voltage would be used for future experiments.

5.2.1.3.2 The Influence of Contact Metal on Sensing Behaviour

As mentioned previously in section 5.2.1.2 it is believed that at least part of the sensing response of the pentacene transistors is due to the binding of amine molecules to the gold source and drain contacts of the device. To verify this theory, an attempt to sense amines using an OFET with source drain contacts that were fabricated from something other than gold was made; nickel was chosen as its work function (5.01eV) is very close to that of gold (5.1eV). The device used for sensing was Pentacene 17 TR, whose characteristics are shown in **Figure 95**. This shows much worse performance than the other pentacene OFETs made with gold contacts, which could be a consequence of either the lower work function or the larger temperature required for thermal evaporation of nickel causing damage to the OFET device. The device was exposed to 10% saturation octylamine (10% of nitrogen to the

bubbler, with the bubbler immersed in ice water) three times for periods of 2 minutes with 3 minute recovery periods in-between. The results of this exposure run can be seen in **Figure 107**.

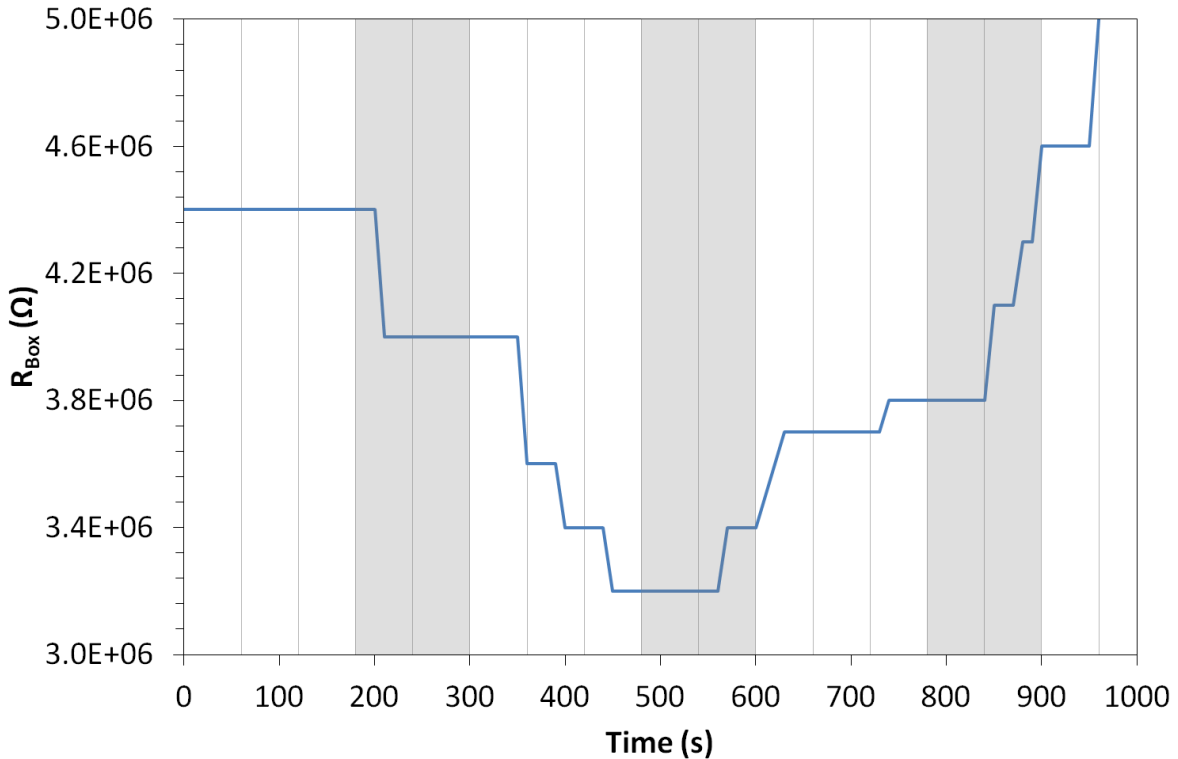


Figure 107. Pentacene 17 TR 10% octylamine sensing results. N.B. grey shaded areas indicate analyte exposure.

In the first exposure window shown in **Figure 107** the transistor reacted in an unexpected way, showing a decrease in channel resistance rather than the expected increase. The reduction in channel resistance continued in the recovery phase after the first exposure, upon the second exposure the expected behaviour was shown, albeit after more than a minute of exposure; the channel on-resistance continued to rise slowly in the recovery phase after the second exposure. However after one minute of exposure to octylamine in the third exposure cycle, the resistance begins to rise more rapidly. Although the initial behaviour is anomalous it can be concluded that the sensing response of pentacene OFETs to octylamine is, at least in part, due to an interaction of the pentacene with octylamine as a response is still observed in the absence of gold source and drain electrodes. The contribution of the gold contacts to the sensing response is still a question that needs to be answered.

5.2.1.3.3 Reusability Study on Pentacene Octylamine Sensors

It has been stated previously that the sensing response of pentacene OFETs to octylamine is non-reversible meaning that as sensors from a practical stand-point they are not that ideal. However if the sensors could still respond after already being exposed to amine several times, they may still be considered as viable sensors; towards this end the pentacene OFET was run for several exposure cycles separated by short recovery cycles. It was decided to use the transistor Pentacene 21 TL and an octylamine concentration of 1% saturation (1% of nitrogen to the bubbler, with the bubbler immersed in ice water), as mentioned previously the theoretical concentration at 100% saturation is 354ppm at 0°C; the exposure duration was 2 minutes and the recovery duration was 3 minutes. The results of the exposure run are shown in **Figure 108**.

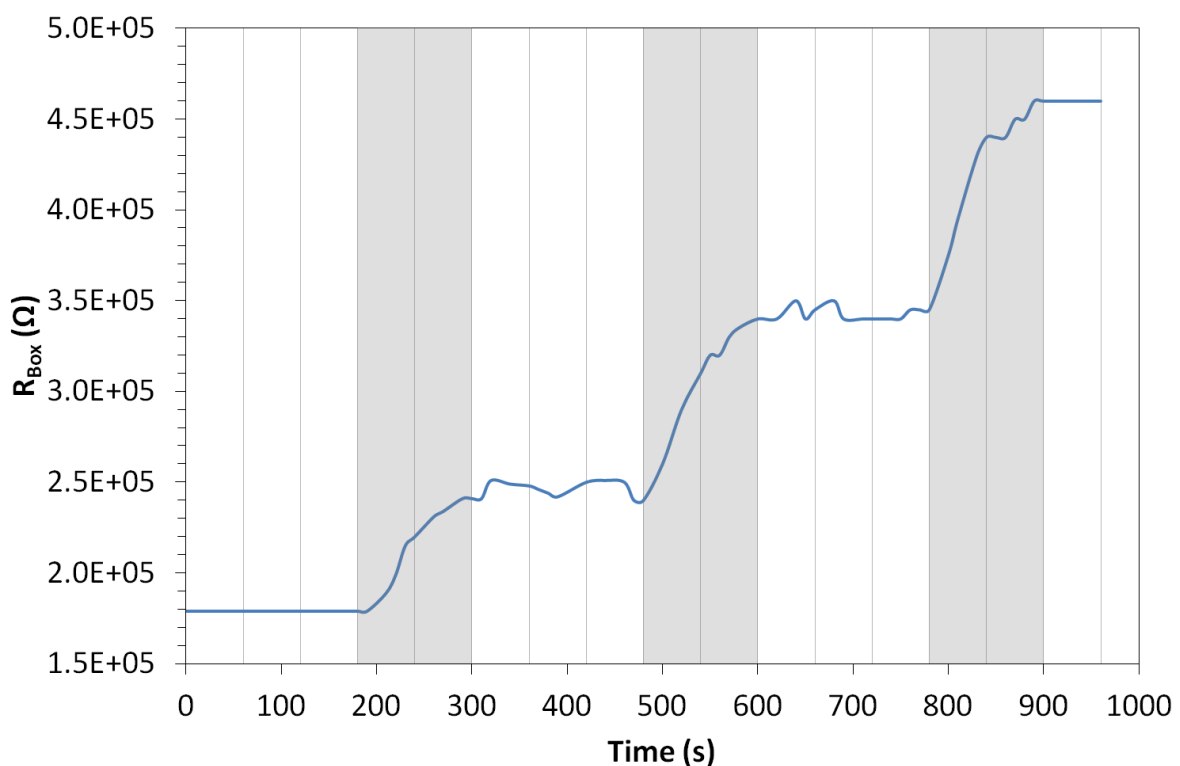


Figure 108. Pentacene 21 TL 1% octylamine cycles sensing results. N.B. grey shaded areas indicate analyte exposure.

The data presented in **Figure 108** is very encouraging as it clearly shows that a pentacene OFET can be used to sense multiple exposure events. In-fact, the device seemed to respond more strongly to each subsequent exposure. The channel resistance increase (10 times the

box resistance increase) was $620\text{k}\Omega$ for the first exposure, $1\text{M}\Omega$ for the second and $1.15\text{M}\Omega$ for the third. Taking the pre-exposure resistance as the base resistance for each exposure, the percentage responses ($[\Delta R/R] \times 100$) are 35%, 42% and 33% for the first second and third exposures respectively. This experiment proves that the pentacene OFETs, while having a non-reversible interaction with octylamine, can be used more than once as sensors for it.

5.2.1.3.4 Very Low Concentration Static-Environment Sensing

Finally it was decided to round off the octylamine sensing experiments on pentacene OFETs by testing the detection limit of the sensors. Towards this end a new method of vapour generation was required as the lower limit of the bubbler based delivery system had already been reached to produce the 3.54ppm (1% saturation) concentration used previously. A method was devised using a sealed exposure chamber and a dilute solution of octylamine in a carrier solvent that would not produce a significant sensing response from the OFET being tested. The carrier solvent chosen was cyclohexane due to its non-polar nature and lack of any functional groups, the OFET that was going to be used for all the testing (Pentacene 24 BR) first needed to be exposed to a neat cyclohexane atmosphere to measure its response (if any) before any amine sensing was performed. Firstly the OFET was sealed in the exposure chamber under a pure nitrogen atmosphere. Next solutions were created of octylamine in cyclohexane that would create atmospheres with 100ppb and 1ppm when carefully measured volumes were deposited in a small watch-glass and allowed to evaporate in a sealed exposure chamber. Lastly the OFET was exposed to each of the concentrations in turn starting with the smallest; the results of the cyclohexane control and the octylamine exposures are shown in **Figure 109**. To end the exposure, the chamber was flushed with pure dry nitrogen gas.

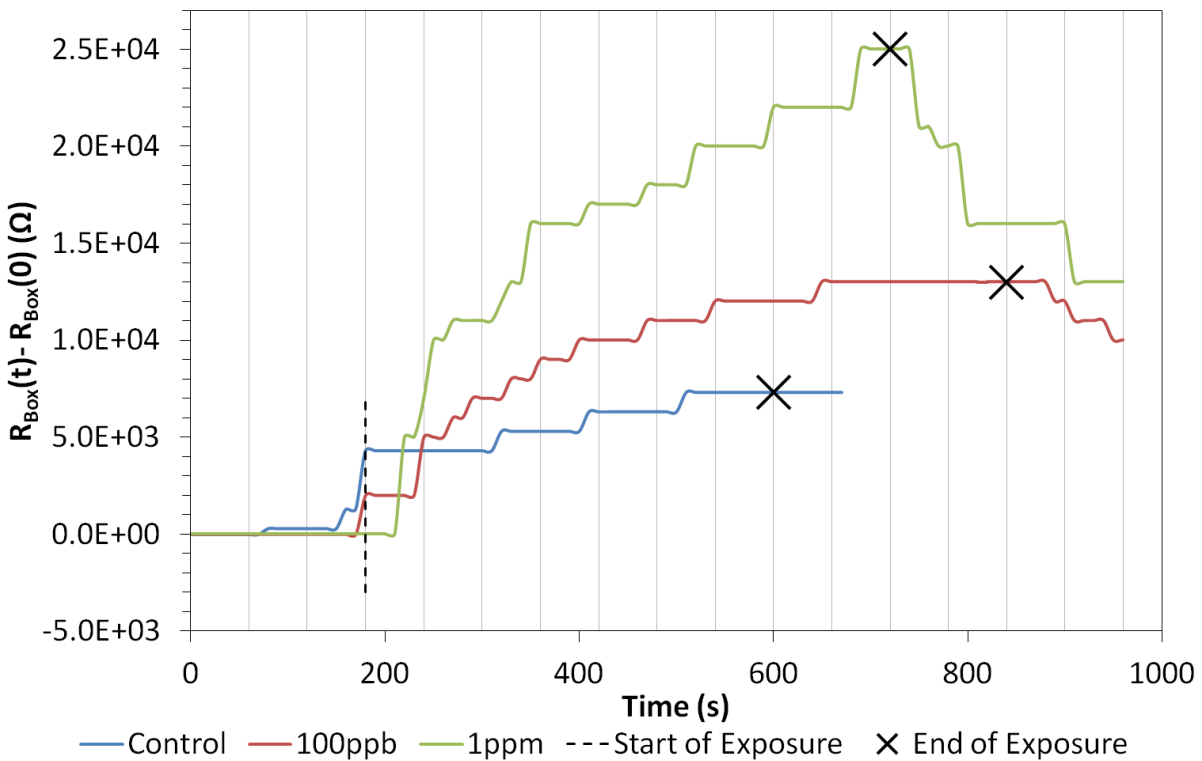


Figure 109. Pentacene 24 BR 100ppb / 1ppm octylamine and cyclohexane control sensing results.

The plots of the sensing data in **Figure 109** are plotted as $R_{Box}(t)-R_{Box}(0)$ to allow easier comparison between the three curves. The cyclohexane control curve shows a sudden initial jump upon exposure followed by a steady increase in resistance, upon nitrogen flushing the resistance does not immediately begin to reduce. Under 100ppb exposure, however, the initial spike was not as large as under the control but the rate of increase clearly is, leading to an apparent saturation point at around 650 seconds (470 seconds after the start of the exposure). This is perhaps an indication that the amine atmosphere takes time to establish itself; however upon nitrogen flushing the device began to recover, unlike any of the exposure runs seen previously. The 1ppm exposure did not elicit a change in the OFET's resistance for the first 30 seconds of exposure, presumably due to a combination of the effect of the previous exposures and the time taken to build up the octylamine atmosphere. After the initial 30 seconds the resistance of the OFET began to rise rapidly for around three minutes, before the rise proceeded at a slower rate. Upon nitrogen flushing the device again began to recover, but much more rapidly than in the 100ppb exposure. In the cases of the control, 100ppb and 1ppm exposures the percentage changes observed

were 5%, 6% and 10% respectively. It is clear from this investigation that the pentacene OFET is sensitive to concentrations of octylamine as low as 100ppb and perhaps even lower. However the response to the carrier solvent precludes investigations of smaller concentrations.

5.2.1.4 Ester Sensing Results

The main reason behind ester sensing with the pentacene OFET is to provide a control response to compare with the response after calixarene sensitising (see section 5.2.2.1.4). However it does provides an insight into the selectivity and different responses pentacene OFETs have to other groups of analytes.

The ester used for the sensing was ethylethanoate at a variety of concentrations: 1% saturation (1% of nitrogen to the bubbler, submerged in ice-water), 10% saturation (10% of nitrogen to the bubbler, submerged in ice-water) and 100% saturation (100% of nitrogen to the bubbler, submerged in ice-water); the theoretical concentration of ethylethanoate at 100% saturation is 2.96×10^4 ppm at 0°C. The OFET used for this investigation was Pentacene 31 BR (see **Figure 98**). The results of the sensing experiment are shown in **Figure 110**.

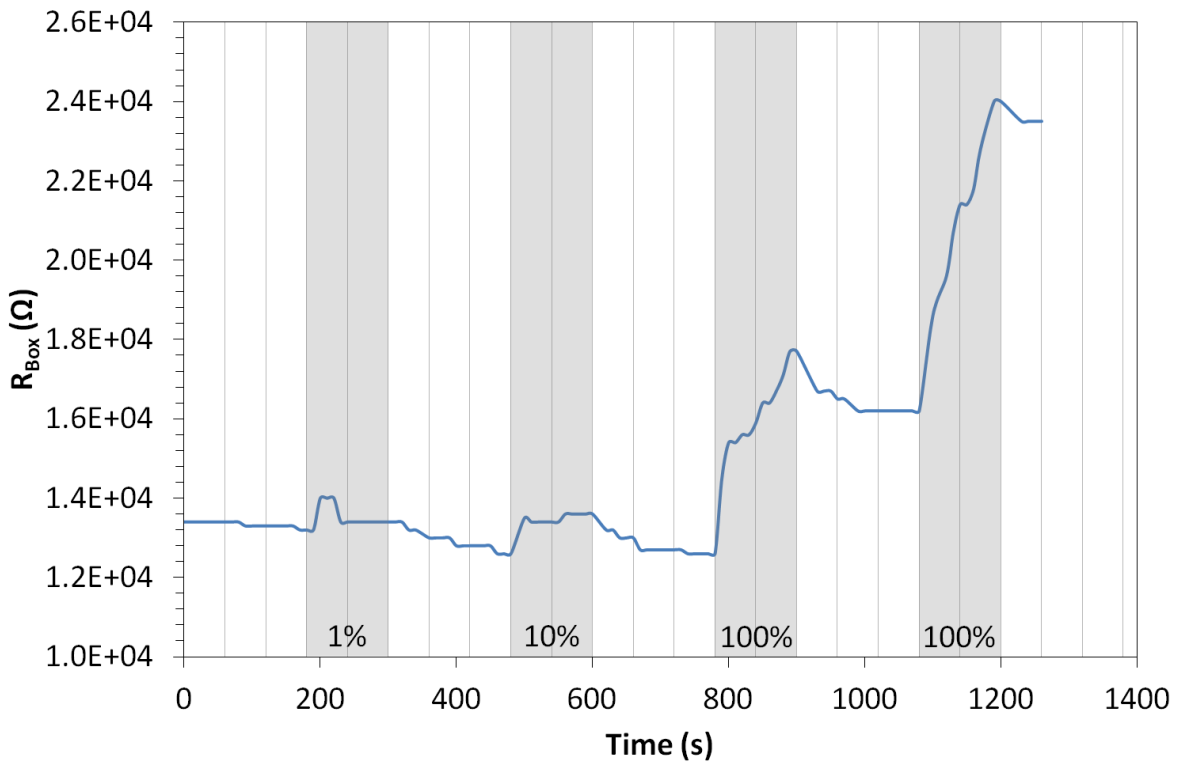


Figure 110. Pentacene 31 BR variable % ethylethanoate sensing results. N.B. grey shaded areas indicate analyte exposure.

It can be seen from **Figure 110** that firstly pentacene OFETs are sensitive to ethylethanoate and secondly the sensing response occurs down to the minimum concentration that can be produced from the bubbler system. At 1% saturated vapour the sensor response takes the form of an 8kΩ (6% of pre-exposure) channel resistance “spike” within the first minute of exposure. This spike did subside before the second minute of exposure, however, indicating that this concentration is probably right on the edge of the detection limit of the sensor. After some downwards drift in the resistance during the three minute recovery phase, the channel resistance rose by a total of 10kΩ (8%) during the next exposure stage, this time 10% saturated vapour, the majority of which happened in the first 20 seconds of exposure. After the second exposure phase, the OFET appeared to recover back to its pre-exposure resistance. Upon 100% saturated vapour exposure the OFET’s channel resistance increased rapidly for the first 20 seconds then more slowly up to a maximum channel on-resistance of 177kΩ, meaning a total change of 51kΩ (40%). After the exposure a small amount of recovery was observed before the next 100% saturation exposure. In the final exposure phase the channel resistance increased at a roughly constant rate throughout the two

minutes of exposure to produce a maximum increase of $78\text{k}\Omega$ (48%). It seems from this data that the response of the pentacene OFET does not scale linearly with vapour concentration either in terms of the absolute change or the percentage change in channel resistance. To find the actual relationship, more testing would be required. From the last two exposures it appears that the OFET responds more strongly once it has already been exposed to a significant amount of ethylethanoate, although more testing would be required to confirm this. The increase in channel on-resistance could be down to a reduction in mobility or an increase in threshold caused by the formation of traps or dipoles in the grain boundaries of the pentacene due to the interactions between the ester and the pentacene.

5.2.1.5 Amide Sensing Results

Again as in section 5.2.1.4 the purpose of this testing was to act as a control to the sensing response shown by a calixarene sensitised pentacene OFET discussed later (in section 5.2.2.1.5). The amide chosen was formamide and it was used in four different concentrations: 1% saturation (1% of nitrogen to the bubbler, submerged in ice-water), 10% saturation (10% of nitrogen to the bubbler, submerged in ice-water), 50% saturation (50% of nitrogen to the bubbler, submerged in ice-water) and 100% saturation (100% of nitrogen to the bubbler, submerged in ice-water); the theoretical concentration of formamide at 100% saturation is 3.53ppm at 0°C . The transistor used for the sensing work was Pentacene 45 TL, see Figure 89 for its pre-exposure electrical characteristics. The results of the exposure run are shown in **Figure 111** below.

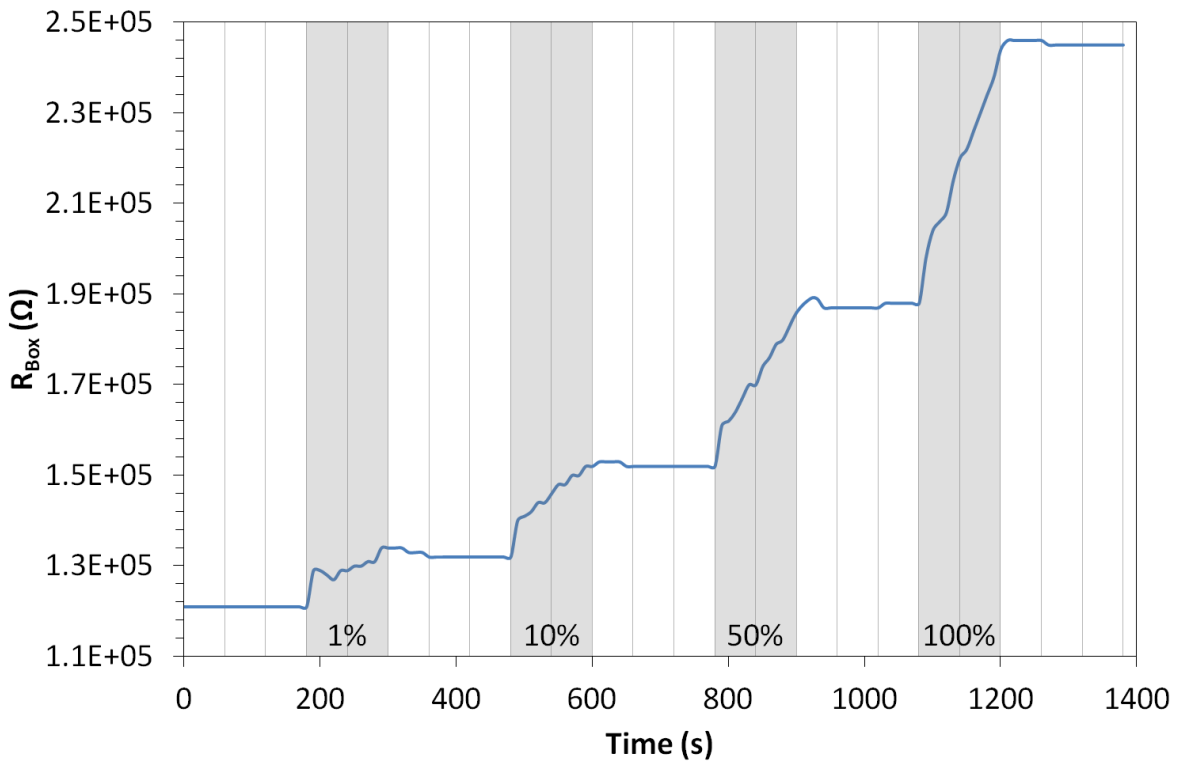


Figure 111. Pentacene 45 TL variable % formamide sensing results. N.B. grey shaded areas indicate analyte exposure.

It should first be noted that this transistor was very stable under nitrogen before and after the exposures. Recovery from formamide exposure was minimal in all cases. However the OFET dealt very well with the multiple exposures, showing good sensing behaviour each time. The first exposure was the lowest concentration of 1% saturated vapour, this triggered an unmistakeable response in the OFET causing the channel on-resistance to undergo an initial jump of $80\text{k}\Omega$ in the first 10 seconds of exposure before proceeding to rise a total of $130\text{k}\Omega$ in the whole two minute exposure window, corresponding to a rise of 11% of the pre-exposure value. Next the 10% saturated vapour exposure again caused an initial jump within the first 10 seconds again of magnitude $80\text{k}\Omega$, and the channel resistance continued to rise, albeit more slowly, to a final value $210\text{k}\Omega$ higher than the starting value. This final value was reached 10 seconds after the nitrogen flushing had begun (this corresponds to a 16% increase). During the subsequent 50% saturated vapour exposure the channel on-resistance rose by $370\text{k}\Omega$ (24%) again continuing to rise after the exposure had ended, this time for 30 seconds. The final 100% saturated vapour exposure produced an increase of $580\text{k}\Omega$ in the channel on-resistance of the device, corresponding to a 31%

increase, this time the rise only continuing for 10 seconds after exposure ended. The pentacene OFET shows very clear discrimination between different concentrations of analyte gas and while it shows little or no recovery, it does show the ability to keep sensing even after multiple exposures. Again the increase in channel on-resistance could be down to a reduction in mobility or an increase in threshold caused by the formation of traps or dipoles in the grain boundaries of the pentacene due to the interactions between the amide and the pentacene.

5.2.1.6 Ketone Sensing Results

This sensing experiment was performed as a control experiment to the calixarene : porphyrin blend sensitised pentacene OFET discussed later (see section 5.2.2.2.3). The ketone used was octan-2-one used at four different concentrations: 1% saturation (1% of nitrogen to the bubbler, submerged in ice-water), 10% saturation (10% of nitrogen to the bubbler, submerged in ice-water), 50% saturation (50% of nitrogen to the bubbler, submerged in ice-water) and 100% saturation (100% of nitrogen to the bubbler, submerged in ice-water); the theoretical concentration of octan-2-one at 100% saturation is 250ppm at 0°C. The exposure windows are two minutes in duration sandwiched between three minute recovery phases, wherein the device is flushed with pure dry nitrogen. The device used in this sensing experiment was Pentacene 55 BR; the results of the experiment are shown in

Figure 112.

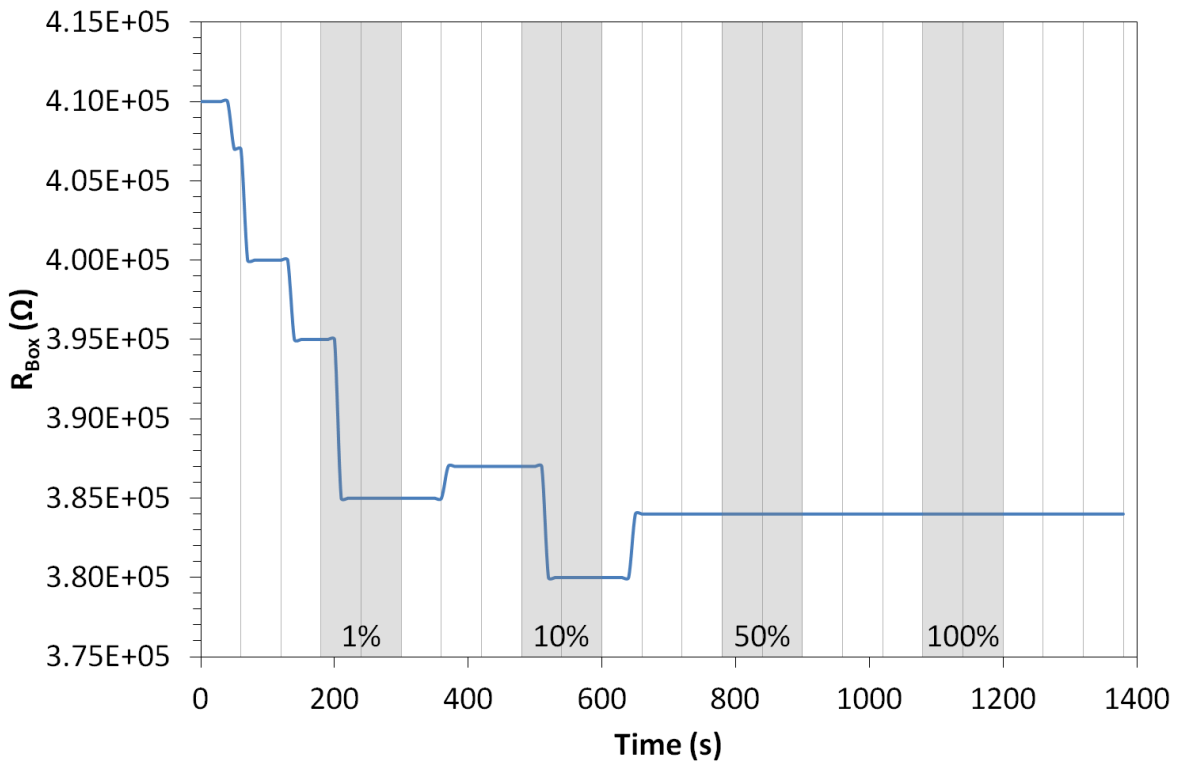


Figure 112. Pentacene 55 BR variable % octan-2-one sensing results. N.B. grey shaded areas indicate analyte exposure.

From **Figure 112** it can be seen that the device continued to “recover” from being exposed to ambient atmosphere decreasing its channel on-resistance by $150\text{k}\Omega$ (4% of its initial channel on-resistance) in the first three minute nitrogen purge, followed by a further drop of $100\text{k}\Omega$ (3% of pre-exposure value) during the first 30 seconds of 1% saturated vapour exposure perhaps indicating improved recovery under the ketone exposure rather than a sensing response, the ketone more efficiently drawing out moisture, oxygen or other ambient contaminants than dry nitrogen alone. After the initial 30 seconds of exposure, the reduction in on-resistance ceased, the on-resistance increased again slightly (by $20\text{k}\Omega$) one minute into the proceeding nitrogen purge before it reduced for a final time by $70\text{k}\Omega$ (2% of pre-exposure value) 30 seconds into the 10% saturated vapour exposure. Following the 10% exposure, the on-resistance increased once more by $40\text{k}\Omega$ before levelling off and maintaining the same value throughout the remaining 50% and 100% saturated vapour exposures and their associated recovery phases. It appears that pentacene alone has no real sensing response to octan-2-one when not out-gassing absorbed ambient contaminants.

5.2.1.7 Aldehyde Sensing Results

Again this sensing experiment was performed as a control experiment to the calixarene : porphyrin blend sensitised pentacene OFET discussed later (see section 5.2.2.2.4). The aldehyde used was octanal, used at four different concentrations: 1% saturation (1% of nitrogen to the bubbler, submerged in ice-water), 10% saturation (10% of nitrogen to the bubbler, submerged in ice-water), 50% saturation (50% of nitrogen to the bubbler, submerged in ice-water) and 100% saturation (100% of nitrogen to the bubbler, submerged in ice-water); the theoretical concentration of octanal at 100% saturation is 649ppm at 0°C. The exposure windows are two minutes in duration sandwiched between two minute recovery phases, wherein the device is flushed with pure dry nitrogen. The device used in this sensing experiment was Pentacene 55 BR; the results of the experiment are shown in **Figure 113**.

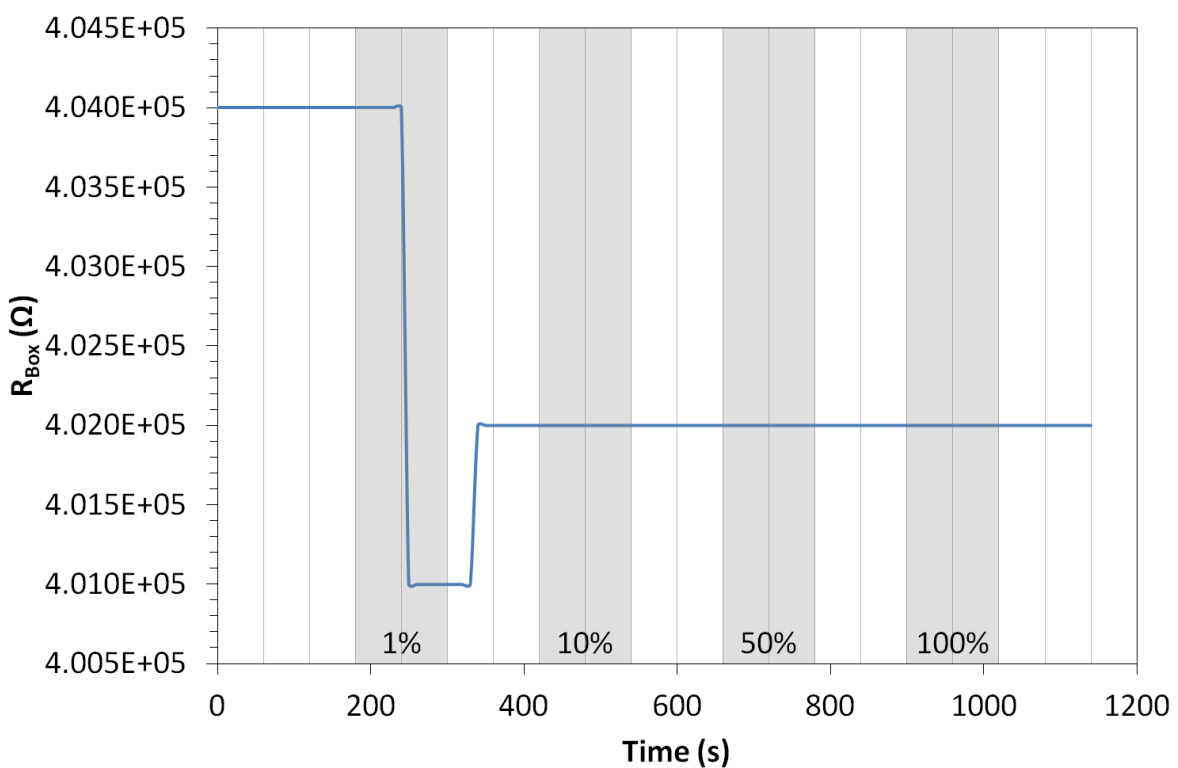


Figure 113. Pentacene 55 BR variable % octanal sensing results. N.B. grey shaded areas indicate analyte exposure.

It can be seen from **Figure 113** that the on resistance of the device did not change by a great amount throughout the experiment, the largest change was a reduction of 30kΩ, 1% of the

original channel on-resistance. Although the reduction occurred half way through the 1% saturated octanal vapour exposure and a small $10k\Omega$ increase occurred in the nitrogen purge following the exposure, the magnitude of the changes and the fact that there was no further response in the proceeding 10%, 50% and 100% saturated vapour exposure phases suggests that this was a fluctuation in the device rather than a vapour response.

5.2.1.8 Ethylene Sensing Results

The vapour exposure in this section was performed on my behalf by Dr. Delia Puzzovio using the exposure equipment at the University of Tübingen.

Ethylene was decided upon as a sensing target material due to its importance in agriculture; ethylene is a naturally occurring plant hormone that causes (amongst other things) fruit to ripen, therefore the ability to accurately monitor airborne ethylene concentration would be very useful. Generally most fruits require a concentration of between 0.1 and 1ppm to initiate ripening, attempts have already been made to sense ethylene in this concentration.^[104]

The vapour exposure apparatus consisted of computer controlled mass-flow controllers and PTFE piping connected to an exposure chamber, nitrogen was used as the carrier gas for the analyte. During this investigation, concentrations of 0.3ppm, 1ppm, 3ppm, 10ppm and 25ppm were used.

The un-sensitised device used in Tübingen was characterised in the conventional manner before transport, output and transfer characteristics for the device can be seen in **Figure 114**.

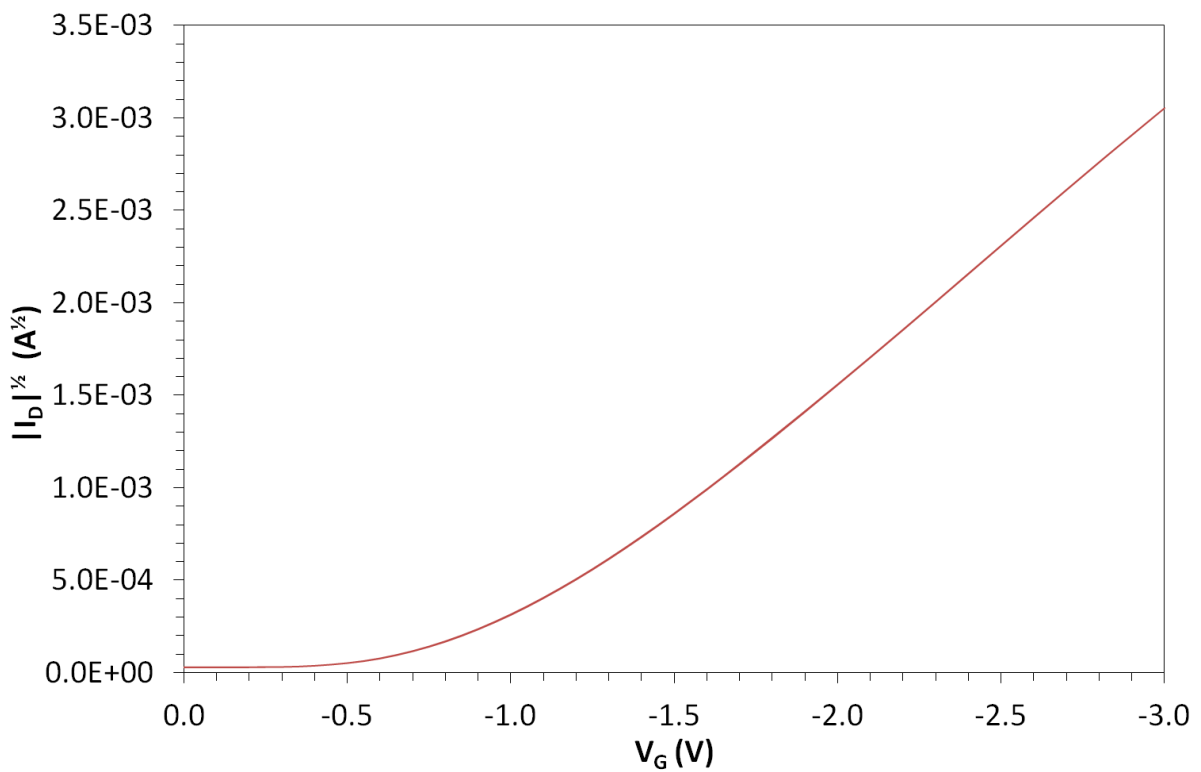
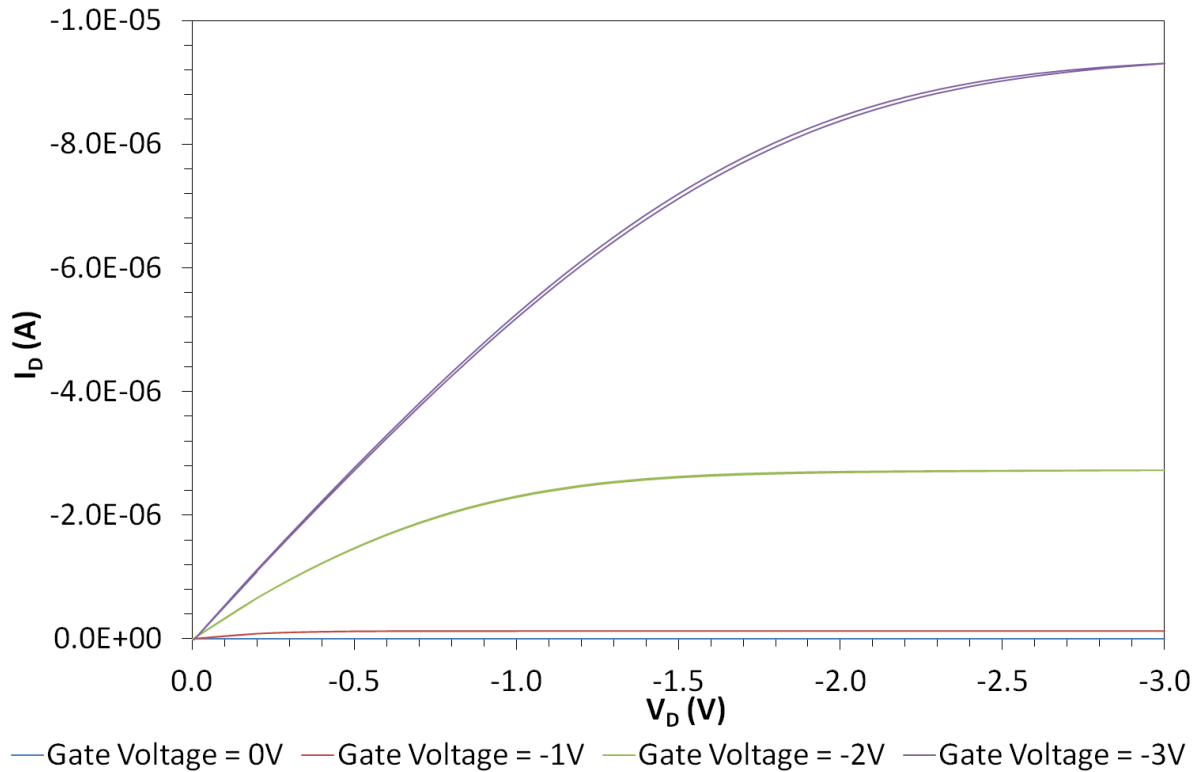


Figure 114. Pentacene 7 TL output and transfer characteristics.

It can be seen from the output characteristic of Pentacene 7 TL (**Figure 114**) that the device has no obvious contact problems, negligible doping and very little hysteresis; the transfer

characteristic shows no visible hysteresis and a high degree of linearity, carrier mobility and threshold voltage extracted from the device have values of $(3.36 \pm 0.05) \times 10^{-2} \text{ cm}^2 \text{V}^{-1} \text{s}^{-1}$ and $-0.96 \pm 0.01 \text{ V}$ respectively. The peak drain current of the device is $-9.32 \times 10^{-6} \text{ A}$, leading to a channel on-resistance of $3.22 \times 10^{-5} \Omega$.

The vapour sensing data was collected using the current-to-voltage converter circuit. The data collected from the exposure run is shown in its raw form in **Figure 115** and due to the data being quite noisy it is presented after being smoothed through the use of a five-point median in **Figure 116**.

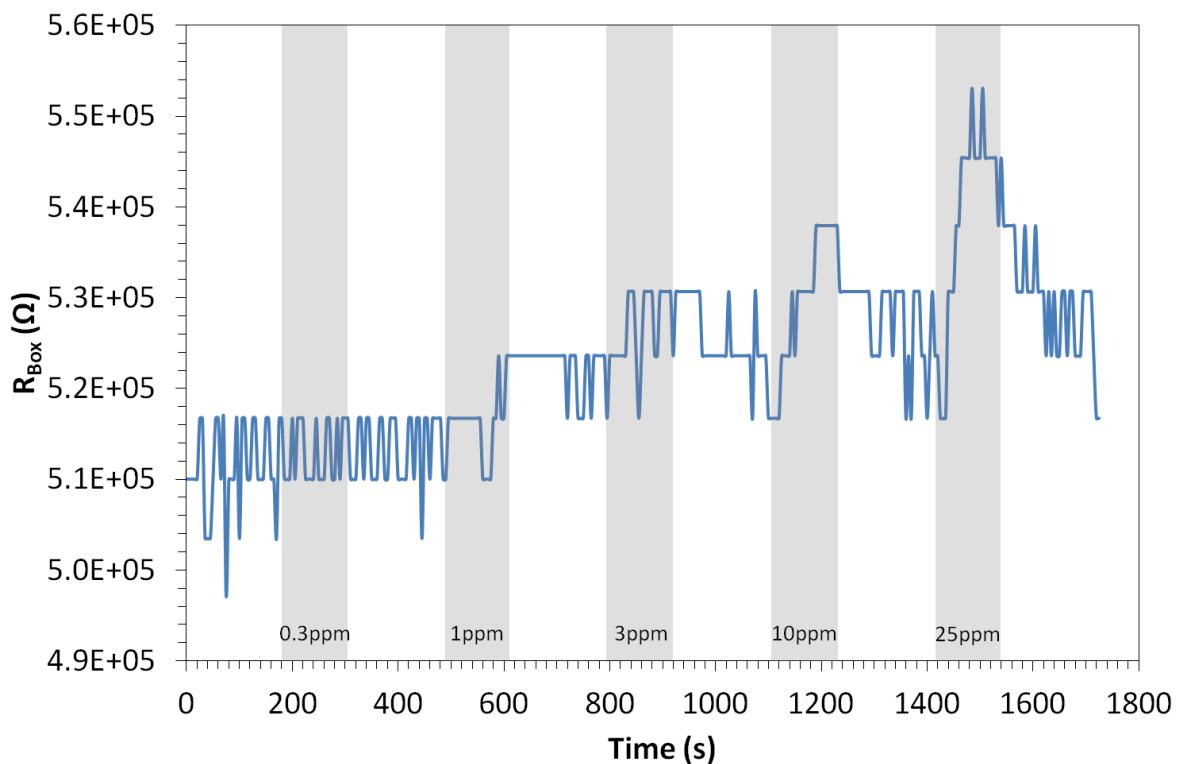


Figure 115. Pentacene 7 TL variable ppm ethylene sensing results. N.B. grey shaded areas indicate analyte exposure.

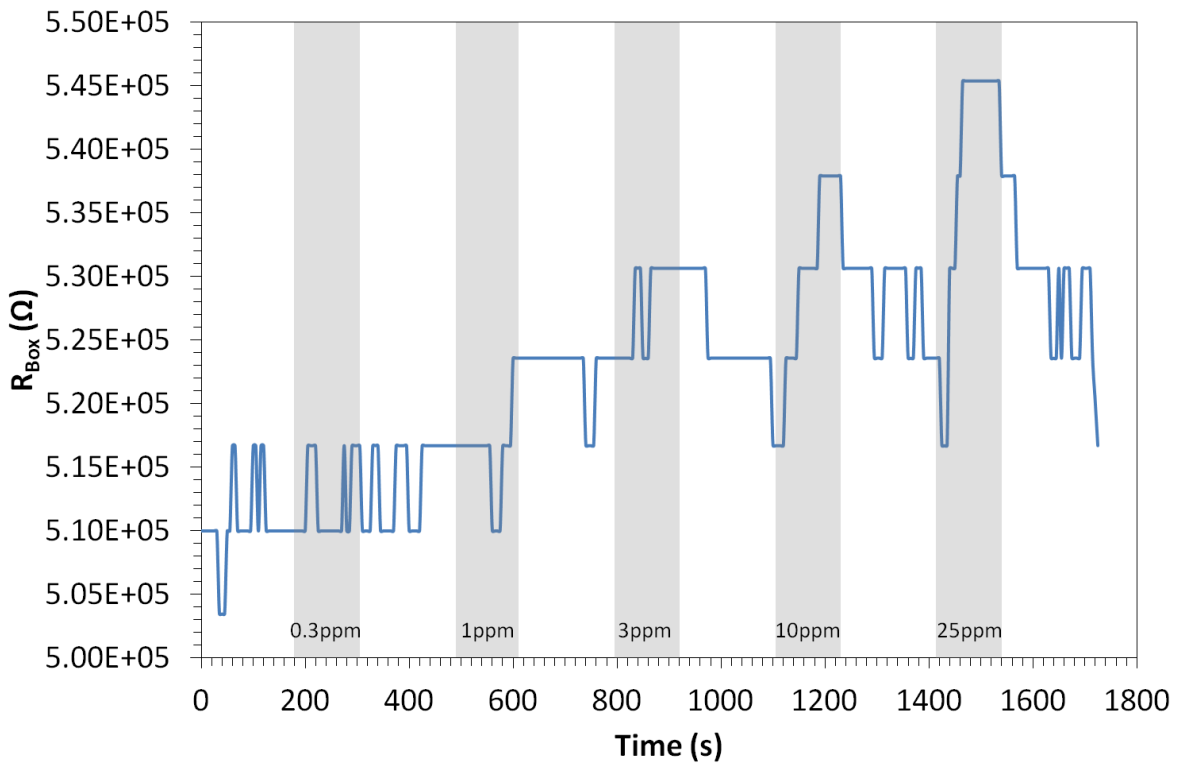


Figure 116. Pentacene 7 TL variable ppm ethylene sensing results five-point median. N.B. grey shaded areas indicate analyte exposure.

From **Figure 115** and **Figure 116** it can be seen that the device shows no obvious response to 0.3ppm ethylene but does begin to respond to the 1ppm concentration; after an initial drop from 516.71kΩ to 510.00kΩ 65 seconds into the exposure, the channel on-resistance increases to a value of 523.60kΩ by the end of the two minute exposure window, corresponding to an increase of 6.89kΩ (1% of pre-exposure) from the start of exposure to the end. Upon exposure to 3ppm an increase of 7.08kΩ (1%) is observed, beginning approximately 35 seconds after the start of exposure. The 10ppm exposure results in a much greater change of 21.24kΩ (4%), the absolute and percentage changes being roughly three times larger than the corresponding values for the 1ppm exposure. Finally the 25ppm exposure causes an increase of 36.39kΩ (7%) to the top of the “spikes” visible in **Figure 115**, which may be a product of interference in the electronics, or 28.71kΩ (6%) to the top of the plateau underneath the spikes. Recovery is observed in this device in the nitrogen flushing stages after the 1ppm, 3ppm, 10ppm and 25ppm exposures however the recovery is masked in some cases by the noisy nature of the data in **Figure 115**. As previously the increase in channel on-resistance could be due to the ethylene penetrating into the

pentacene via grain boundaries and creating traps and dipoles at the boundaries which will introduce traps that effect mobility and dipoles that can hinder accumulation layer formation, increasing threshold.

5.2.2 Sensitised Pentacene Organic Field-Effect Transistors

The transistors discussed in this section were fabricated as described in section 5.2.1, with ~6.5nm thick aluminium oxide gate insulator and top gold source and drain electrodes. The difference in the structure of the devices discussed here when compared to those in section 5.2.1, is the addition of a sensitiser layer. This layer has been introduced to allow the separation of the functions of charge transport and sensing; an advantage of using a sensitiser layer is that the material used does not have to show the slightest hint of semiconducting behaviour, it just needs to have an affinity to interact with the analyte that needs to be detected. In the case of the sensitiser layers used here, they were created from 4-6 monolayers of a calixarene, porphyrin or calixarene : porphyrin blend sensitiser material deposited via the L-B method or L-S method (see sections 2.2.3 and 2.2.4).

5.2.2.1 Calixarene Sensitised Transistors

The OFETs described in this section were coated in six monolayers of the calixarene 5,17-(34-nitrobenzylideneamino)-11,23-di-*tert*-butyl-25,27-diethoxycarbonyl-methyleneoxy-26,28dihydroxycalix[4]arene (calixarene 1, see **Figure 56**), deposited via the L-B method at a pressure of $15\text{mN}\cdot\text{m}^{-1}$, for use in amine, ester and amide sensing. The reasoning behind using calixarene 1 as a sensitiser layer is that the side groups, each containing a benzene ring and NO_2 group, should be orientated facing upwards (due to the hydrophilic OH and ester group having a high probability of being on the bottom of the ring on the water surface and Y-type L-B deposition expected), this should allow the polar NO_2 groups to interact with the amine ester and amide groups.

5.2.2.1.1 Pre-Coating Transistor Characteristics

The pentacene transistors were characterised as described in sections 2.6.1 and 2.6.2 using $V_{D,\text{Max}} = V_{G,\text{Max}} = -3\text{V}$ and $V_{G,\text{Min}} = 0\text{V}$. The characteristics of the transistors, later used in

vapour sensing, are shown in **Figure 117**, **Figure 118** and **Figure 119**. The characteristics of the transistors used for ethylene sensing will be discussed later (section 5.2.2.1.6).

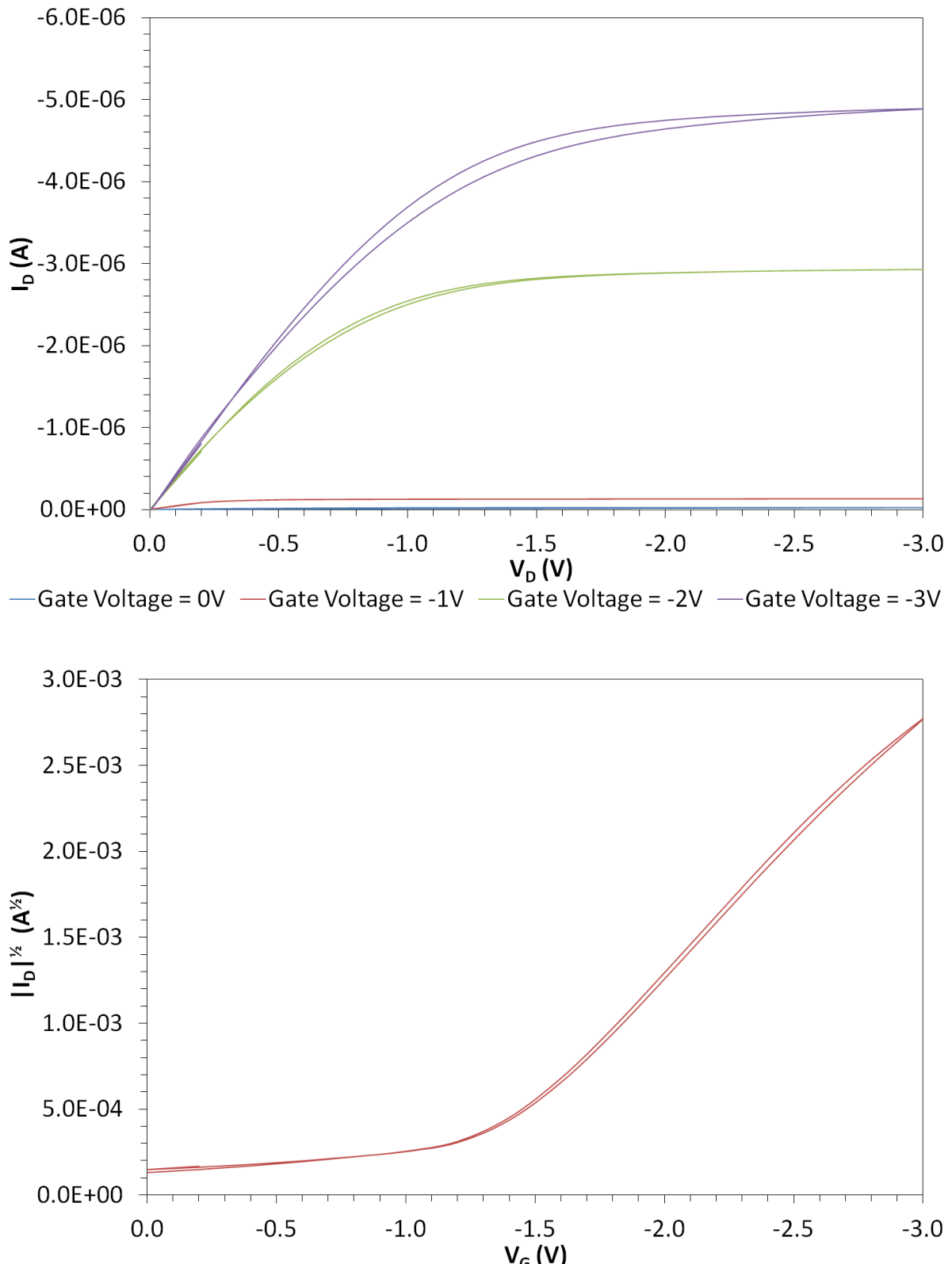


Figure 117. Pentacene 32 TR output and transfer characteristics.

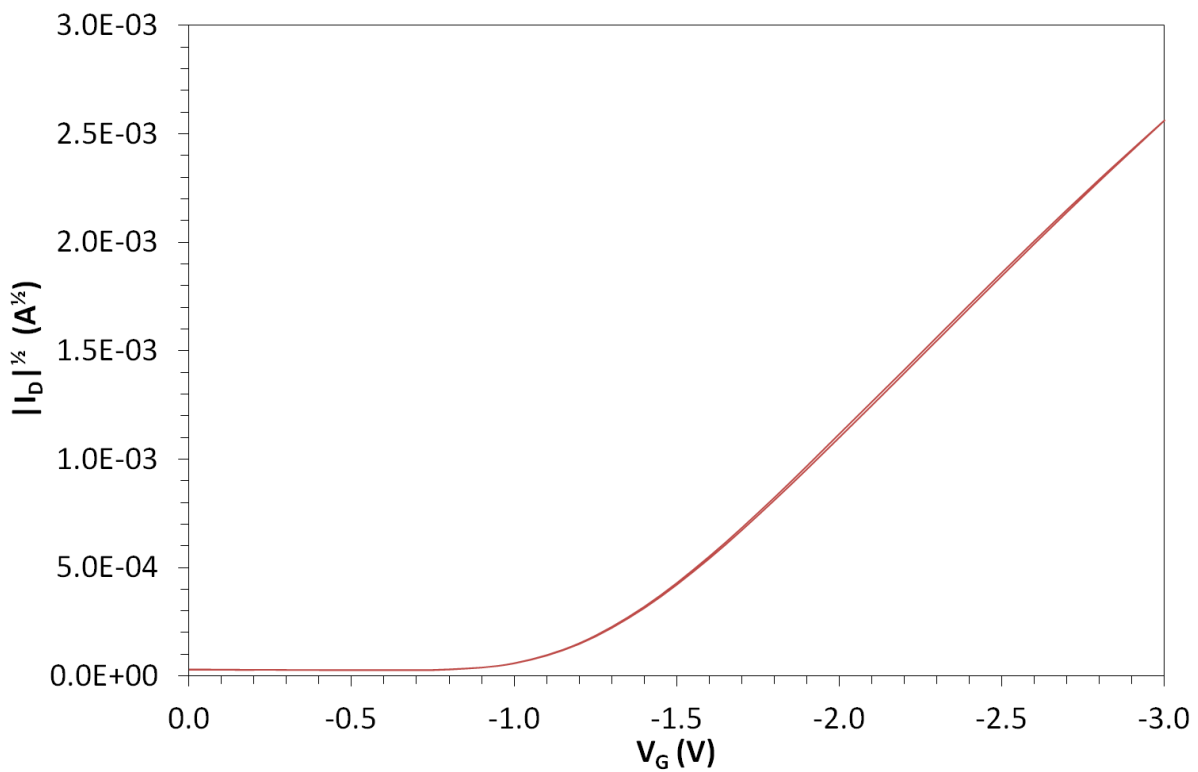
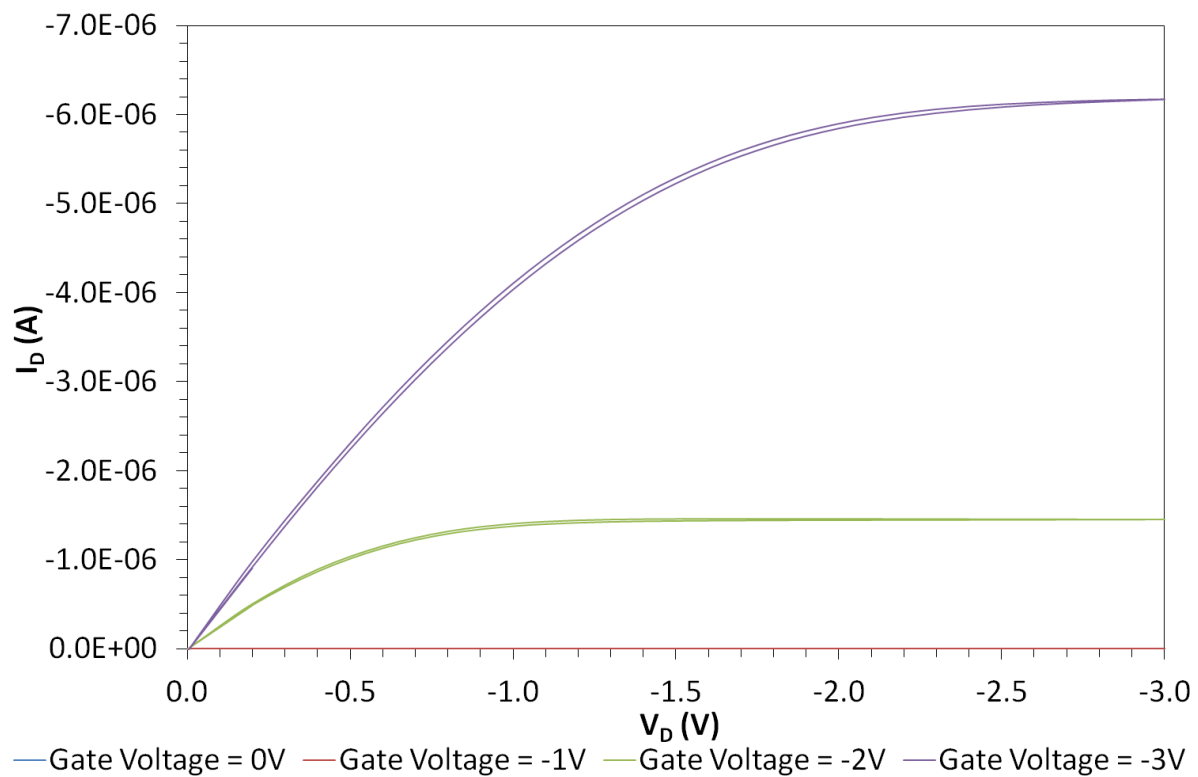


Figure 118. Pentacene 44 BR output and transfer characteristics.

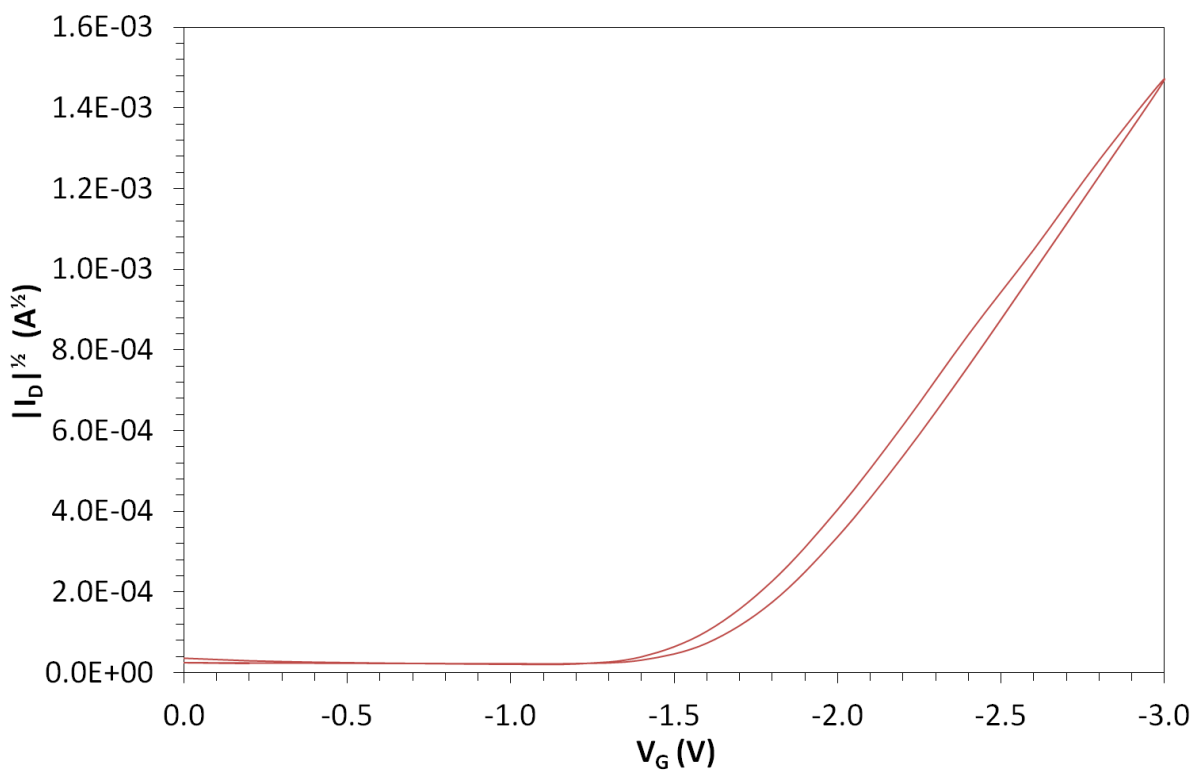
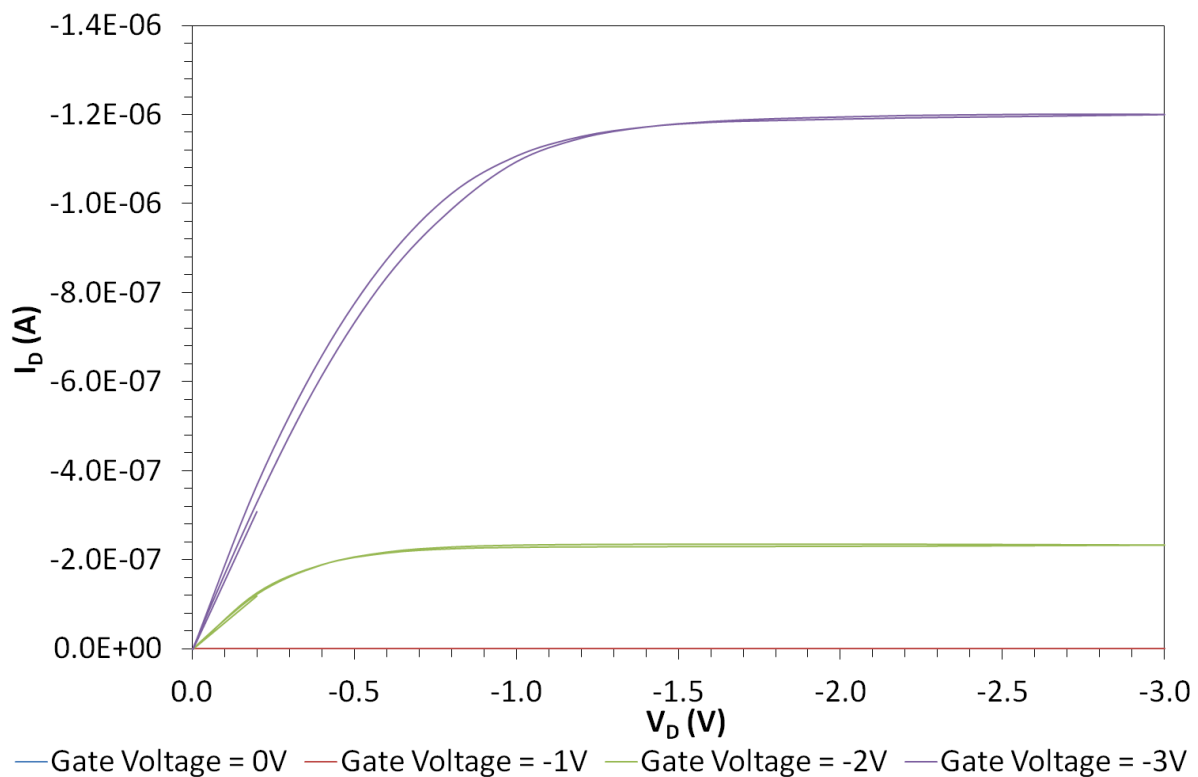


Figure 119. Pentacene 47 TL output and transfer characteristics.

From the output characteristics shown in **Figure 117**, **Figure 118** and **Figure 119** it can be seen that all three of the pre-coated OFETs have a low degree of hysteresis, the most being

shown by Pentacene 32 TR; all three transistors also have a very linear initial region indicating good ohmic contacts and show no evidence of doping.

The transfer characteristics in general show little hysteresis, Pentacene 47 TL showing the most in this case; the charge carrier mobilities of the devices are $(4.08\pm0.07)\times10^{-2}\text{cm}^2\text{V}^{-1}\text{s}^{-1}$, $(3.27\pm0.08)\times10^{-2}\text{cm}^2\text{V}^{-1}\text{s}^{-1}$ and $(2.09\pm0.04)\times10^{-2}\text{cm}^2\text{V}^{-1}\text{s}^{-1}$ for the OFETs Pentacene 32 TR, Pentacene 44 BR and Pentacene 47 TL respectively; the threshold voltages are $-1.41\pm0.02\text{V}$, $-1.26\pm0.03\text{V}$ and $-1.76\pm0.03\text{V}$ for Pentacene 32 TR, Pentacene 44 BR and Pentacene 47 TL respectively. These characteristics are summarised in **Table 3**, along with the peak drain currents and channel on-resistances.

5.2.2.1.2 Post-Coating Transistor Characteristics

As the process of depositing a sensitiser layer onto the devices causes a change in the electrical characteristics of the devices, the devices were re-tested after coating using the same methods as in section 5.2.2.1.1 above. The device characteristics are shown in **Figure 120, Figure 121 and Figure 122**.

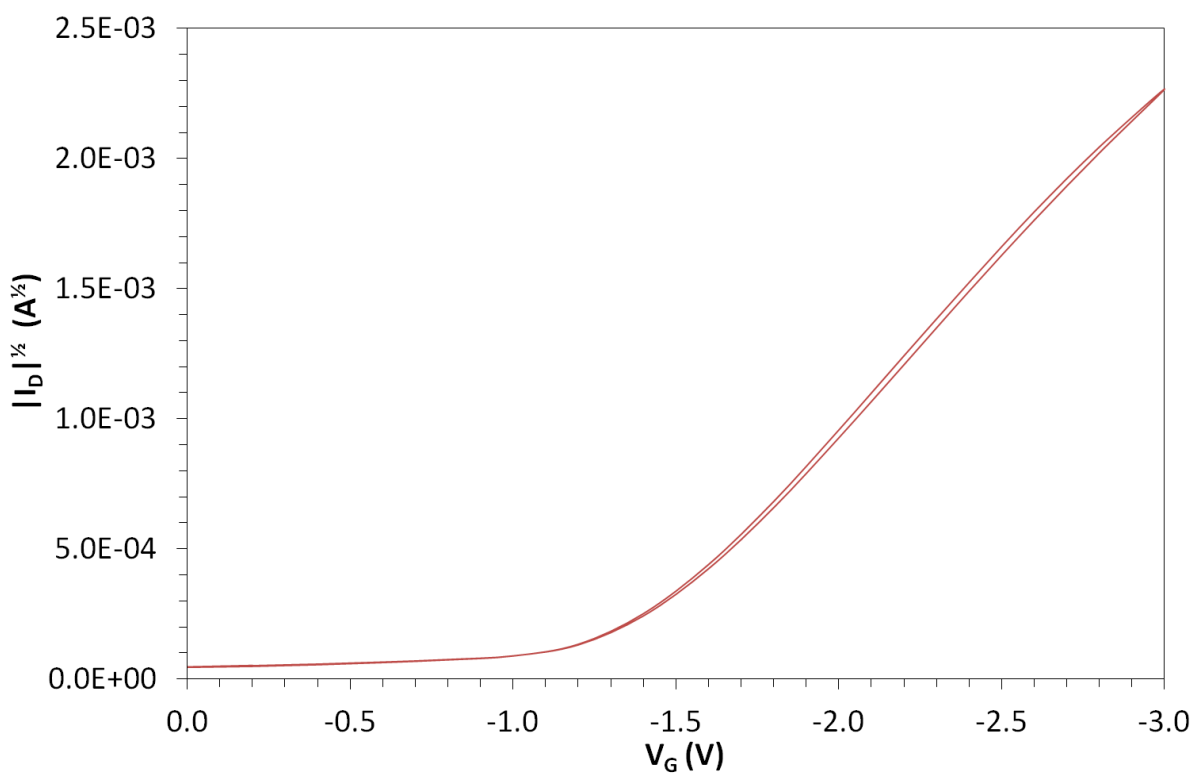
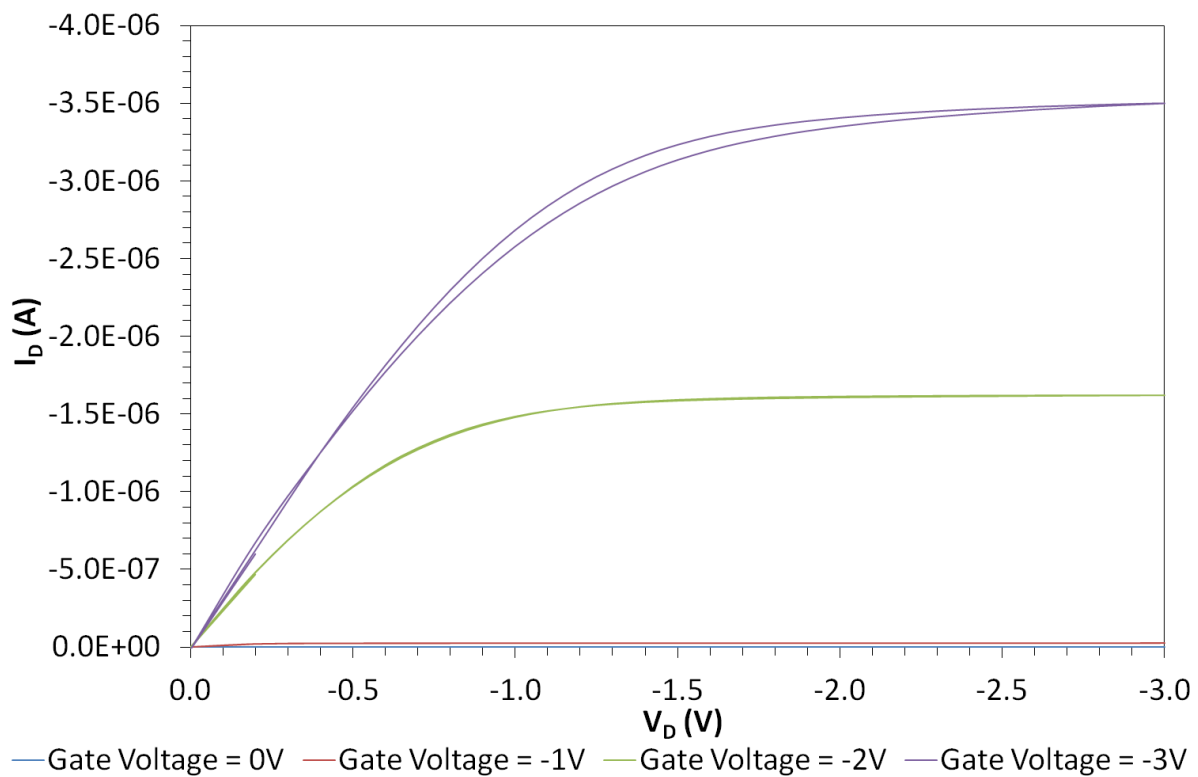


Figure 120. Pentacene 32 TR (post-coating) output and transfer characteristics.

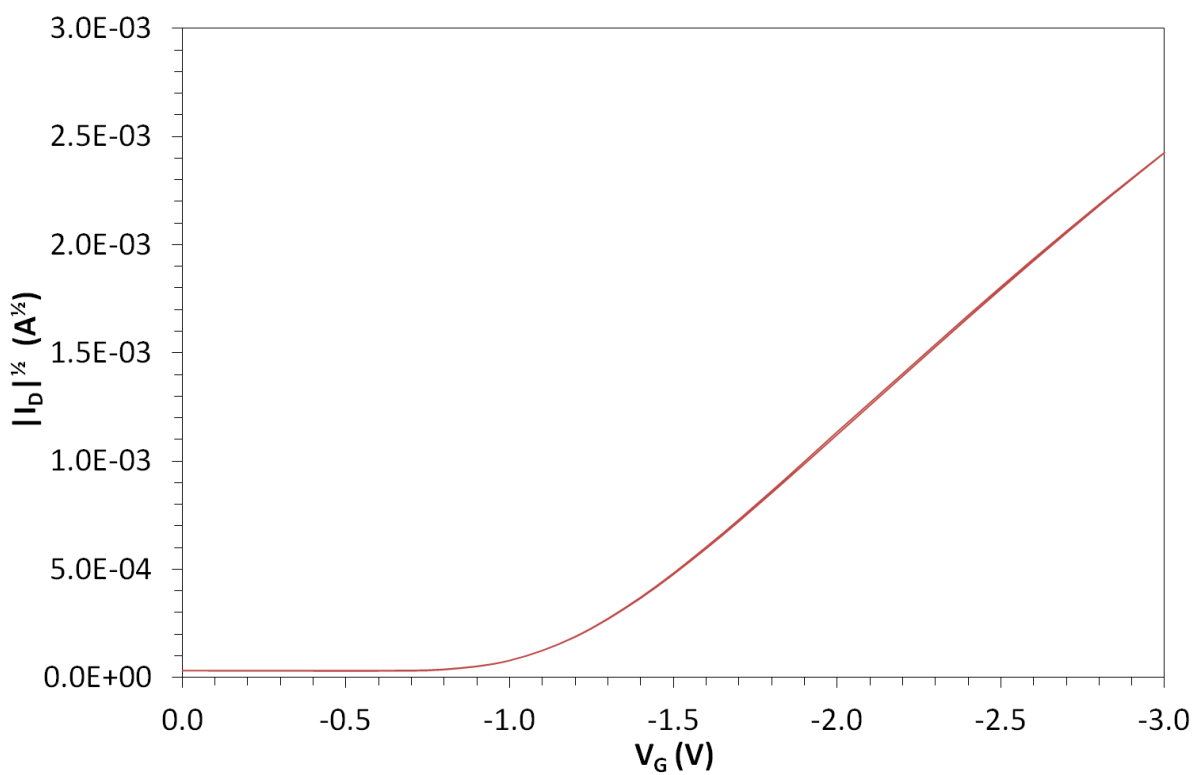
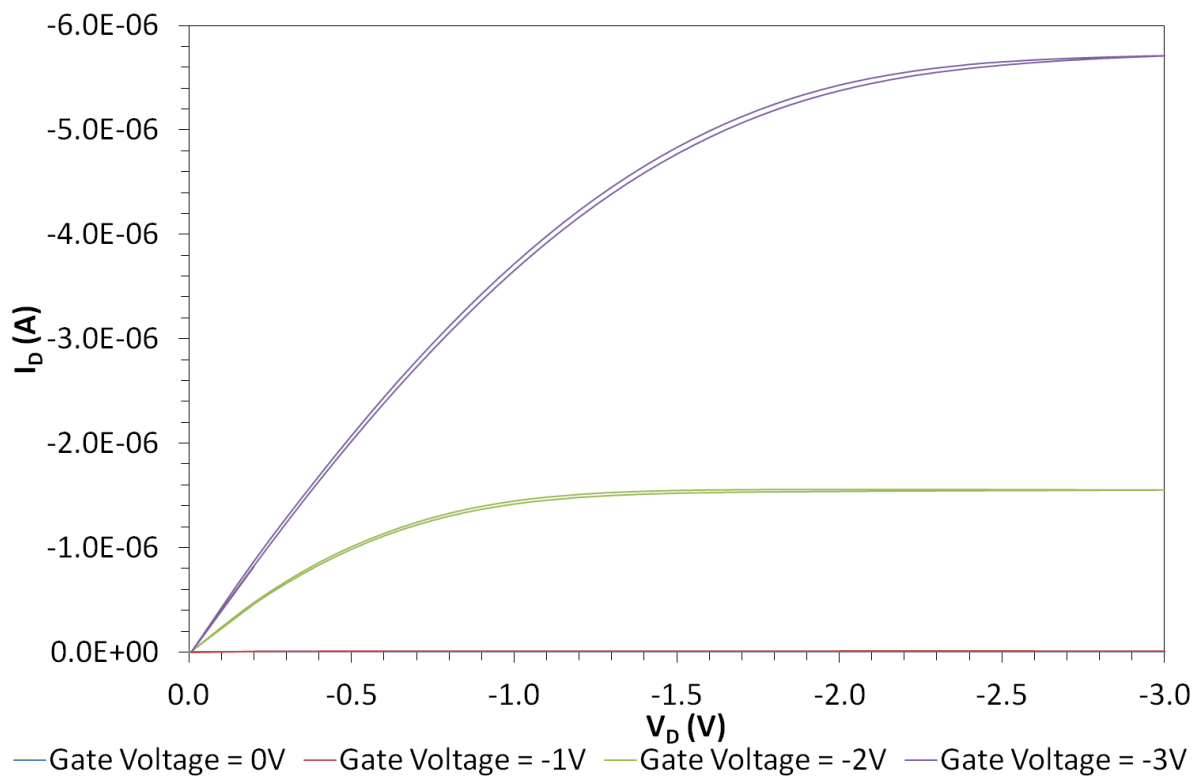


Figure 121. Pentacene 44 BR (post-coating) output and transfer characteristics.

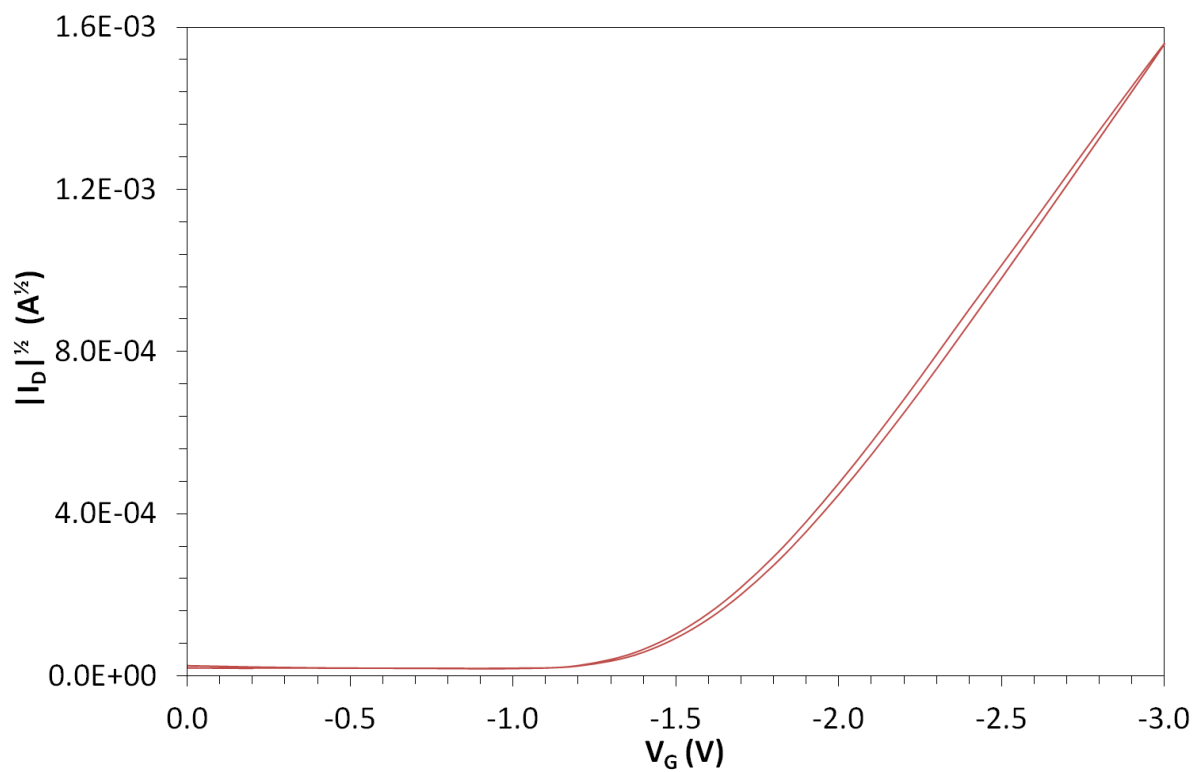
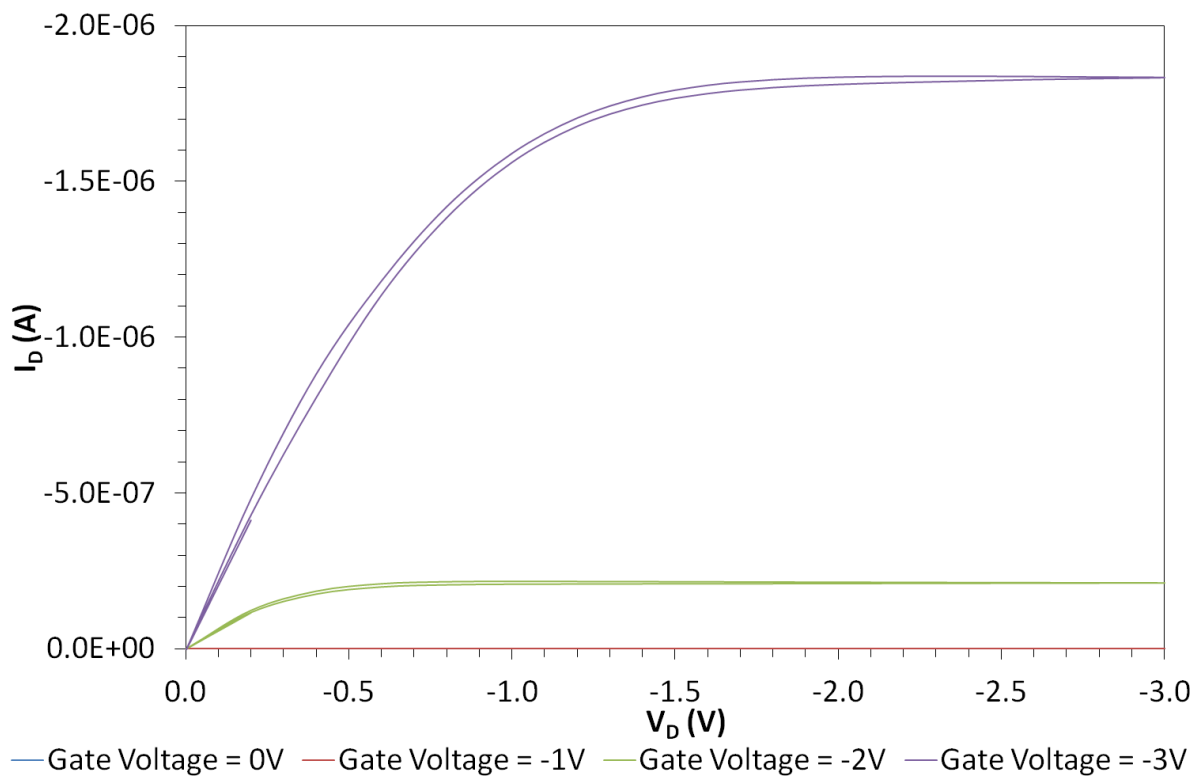


Figure 122. Pentacene 47 TL (post-coating) output and transfer characteristics.

The output characteristics in **Figure 120**, **Figure 121** and **Figure 122** all show approximately the same amount of hysteresis as they did before coating, however the saturation current of

Pentacene 32 TR and 44 BR has decreased while, unusually, the saturation current of Pentacene 47 TL has increased without the device showing any contribution from doping current.

The transfer characteristics of two of the devices show roughly the same level of hysteresis while the third device (Pentacene 47 TL) shows noticeably less hysteresis. The mobilities of the coated devices were $(2.95 \pm 0.08) \times 10^{-2} \text{ cm}^2 \text{V}^{-1} \text{s}^{-1}$, $(2.79 \pm 0.03) \times 10^{-2} \text{ cm}^2 \text{V}^{-1} \text{s}^{-1}$ and $(1.94 \pm 0.04) \times 10^{-2} \text{ cm}^2 \text{V}^{-1} \text{s}^{-1}$ for Pentacene 32 TR, 44 BR and 47 TL respectively, while the threshold voltages of these devices were $-1.39 \pm 0.03 \text{ V}$, $-1.18 \pm 0.01 \text{ V}$ and $-1.64 \pm 0.03 \text{ V}$ after coating. A summary of these characteristics as well as the peak drain currents and channel on-resistances of both the coated and uncoated devices are shown in **Table 3**.

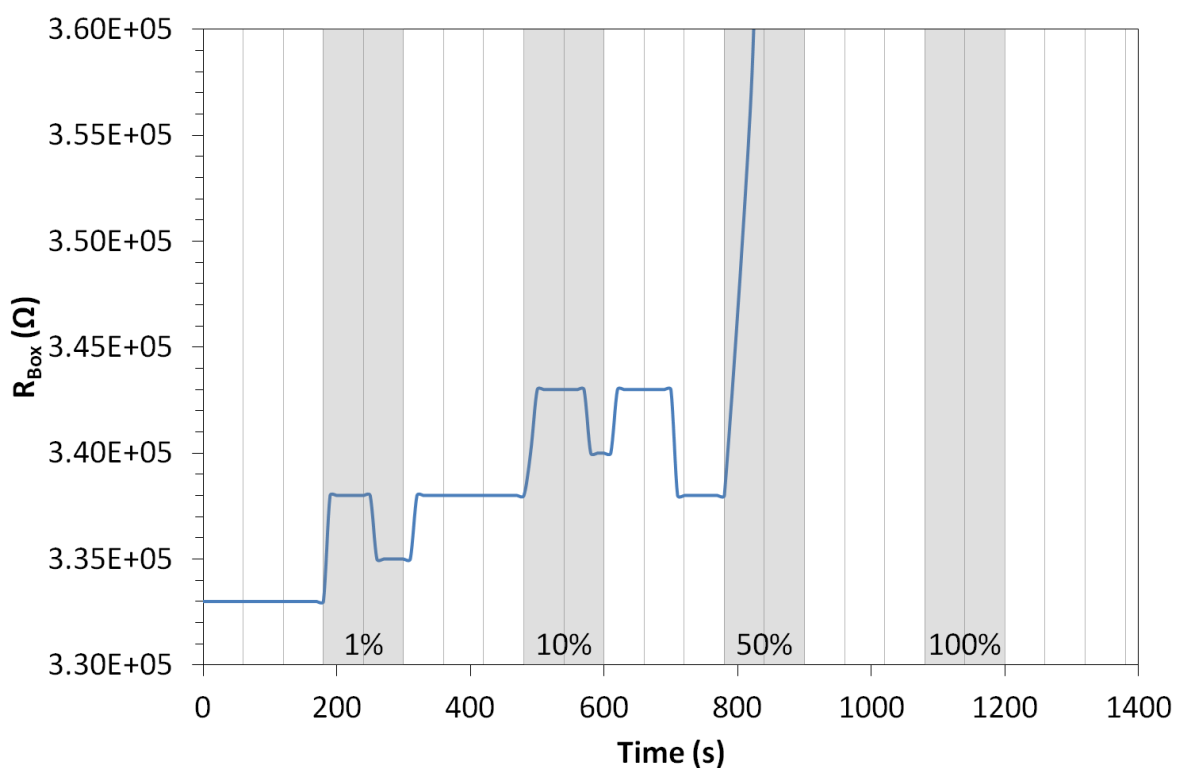
OFET	$\mu (\text{cm}^2 \text{V}^{-1} \text{s}^{-1})$	$V_T (\text{V})$	Peak $I_D (\text{A})$	$R_{on} (\Omega)$
Pentacene 32 TR	$(4.08 \pm 0.07) \times 10^{-2}$	-1.41 ± 0.02	-7.68×10^{-6}	3.91×10^5
Pentacene 32 TR (coated)	$(2.95 \pm 0.08) \times 10^{-2}$	-1.39 ± 0.03	-5.14×10^{-6}	5.84×10^5
Pentacene 44 BR	$(3.27 \pm 0.08) \times 10^{-2}$	-1.26 ± 0.03	-6.56×10^{-6}	4.57×10^5
Pentacene 44 BR (coated)	$(2.79 \pm 0.03) \times 10^{-2}$	-1.18 ± 0.01	-5.89×10^{-6}	5.09×10^5
Pentacene 47 TL	$(2.09 \pm 0.04) \times 10^{-2}$	-1.76 ± 0.03	-2.16×10^{-6}	1.39×10^6
Pentacene 47 TL (coated)	$(1.94 \pm 0.04) \times 10^{-2}$	-1.64 ± 0.03	-2.43×10^{-6}	1.23×10^6

Table 3. Mobility and threshold values for pentacene OFETs before and after coating.

When comparing the OFET devices before and after coating certain trends become obvious, firstly mobility is lowered in all devices by the addition of a sensitiser layer, this is possibly caused by the devices being in such close proximity to water during the deposition process encouraging oxidation of the pentacene; secondly the threshold voltages of all the OFET devices had decreased by $-0.02 \pm 0.04 \text{ V}$, $-0.08 \pm 0.03 \text{ V}$ and $-0.12 \pm 0.04 \text{ V}$ for 32 TR, 44 BR and 47 TL respectively, within the error for 32 TR but a clear decrease for 44 BR and 47 TL. The peak currents of the devices were reduced in the case of Pentacene 32 TR and Pentacene 44 BR but increased in the case of Pentacene 47 TL after coating; the increase is a consequence of a very small decrease in mobility but a relatively large (6.8%) decrease in the threshold voltage required by the device, the threshold shift may be a symptom of the same effect that reduced the hysteresis of the device; this effect may be the removal of mobile ions from the semiconductor bulk and/or a reduction in the number of traps.

5.2.2.1.3 Amine Sensing Results

The coated OFET used for the sensing of the amine octylamine was Pentacene 47 TL, coated in six monolayers of calixarene 1, the pre-exposure characteristics of this device can be seen in **Figure 122**. The octylamine was used in four different concentrations: 1% saturation (1% of nitrogen to the bubbler, submerged in ice-water), 10% saturation (10% of nitrogen to the bubbler, submerged in ice-water), 50% saturation (50% of nitrogen to the bubbler, submerged in ice-water) and 100% saturation (100% of nitrogen to the bubbler, submerged in ice-water); as stated previously the theoretical concentration of octylamine at 100% saturation is 354ppm at 0°C. The results of the sensing can be seen below in **Figure 123**.



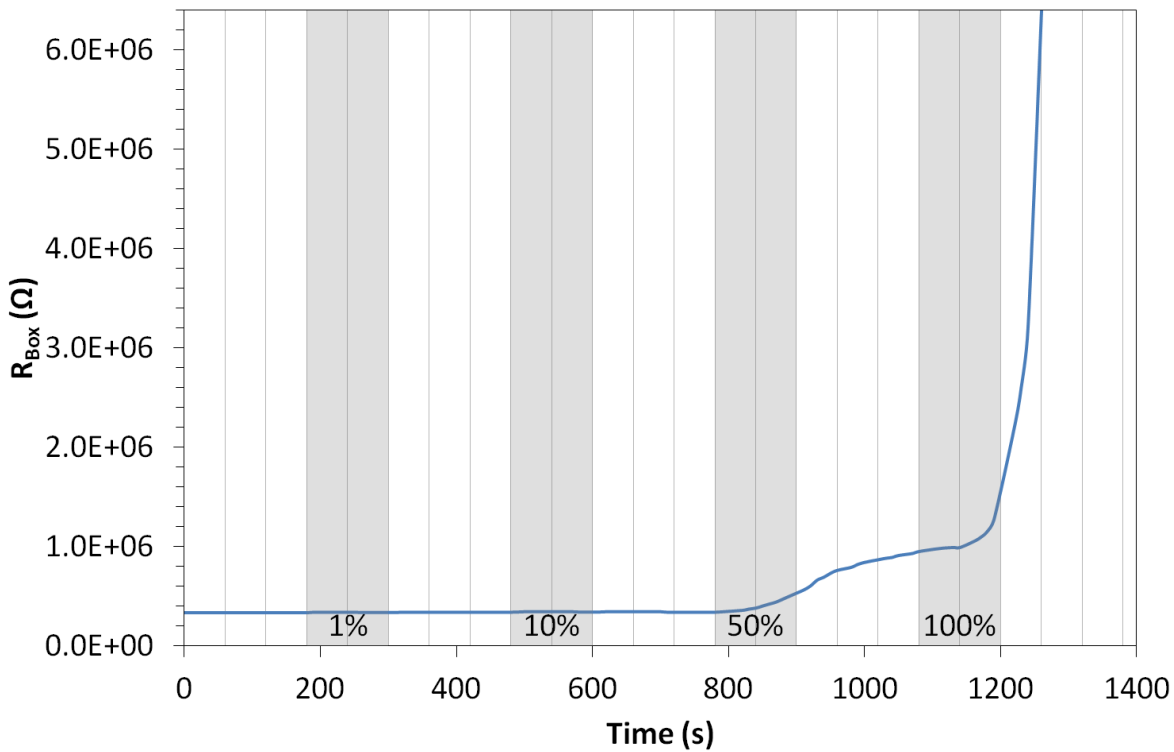


Figure 123. Pentacene 47 TL variable % octylamine sensing results. N.B. grey shaded areas indicate analyte exposure.

The sensing results presented in **Figure 123** have been split over two separate graphs as the huge resistance increase at the end of the exposure run caused the fine details at the start of the graph to become indistinguishable. The first exposure of 1% saturated vapour caused a small but immediate increase in channel on-resistance of $50\text{k}\Omega$, this corresponds to a percentage increase of 2% of the pre-exposure value; this response is dwarfed by the responses seen previously from the uncoated pentacene OFETs, which range from 33% to 42% increases in channel on-resistance. It seems from this first response that the coating of the OFET with this particular calixarene de-sensitises the OFET to octylamine. After the half-way point of the 1% exposure, the OFET also appeared to stop responding to the octylamine and recover a little before responding again, however, due to the small change this could be a natural fluctuation in the devices conduction properties or a inaccuracy in the resistance box adjustment rather than a sensing response issue. After the 1% saturated vapour exposure no recovery is seen in the device before the next exposure of 10% saturated vapour. The 10% exposure again only induced a response of $50\text{k}\Omega$ (1%), the only difference to the earlier exposure was that the device (aside from a small dip in resistance) stayed at

the elevated resistance value for almost two minutes after exposure before dropping back to its pre-exposure resistance value. The next exposure, 50% saturated vapour, showed a much larger response to the octylamine: a $1.93M\Omega$ (471%) increase in resistance within the two minutes of exposure, however, the resistance continued to increase after this exposure had ended and increased massively when exposed to the 100% saturated octylamine vapour; it was found after the exposure run had ended that the OFET now had a very large gate leakage current, possibly indicating that the responses from 50% saturated vapour onwards are actually the gate leakage manifesting in the sensing results; as the current to voltage converter measures the current coming out of the drain, it will not see gate leakage unless it becomes so severe that the device tries to draw more current than the signal generator driving the OFET's source can provide.

5.2.2.1.4 Ester Sensing Results

The ester used for this particular sensing experiment was ethylethanoate and was used in three different concentrations: 1% saturation (1% of nitrogen to the bubbler, submerged in ice-water), 10% saturation (10% of nitrogen to the bubbler, submerged in ice-water) and 100% saturation (100% of nitrogen to the bubbler, submerged in ice-water); as stated previously the theoretical concentration of ethylethanoate at 100% saturation is 2.96×10^4 ppm at 0°C. The OFET Pentacene 32 TR was used in this work, this OFET was coated in six layers of calixarene 1 (see **Figure 56**), the post-coating/pre-exposure characteristics of this device can be seen in **Figure 120**. The sensing data is presented in **Figure 124**.

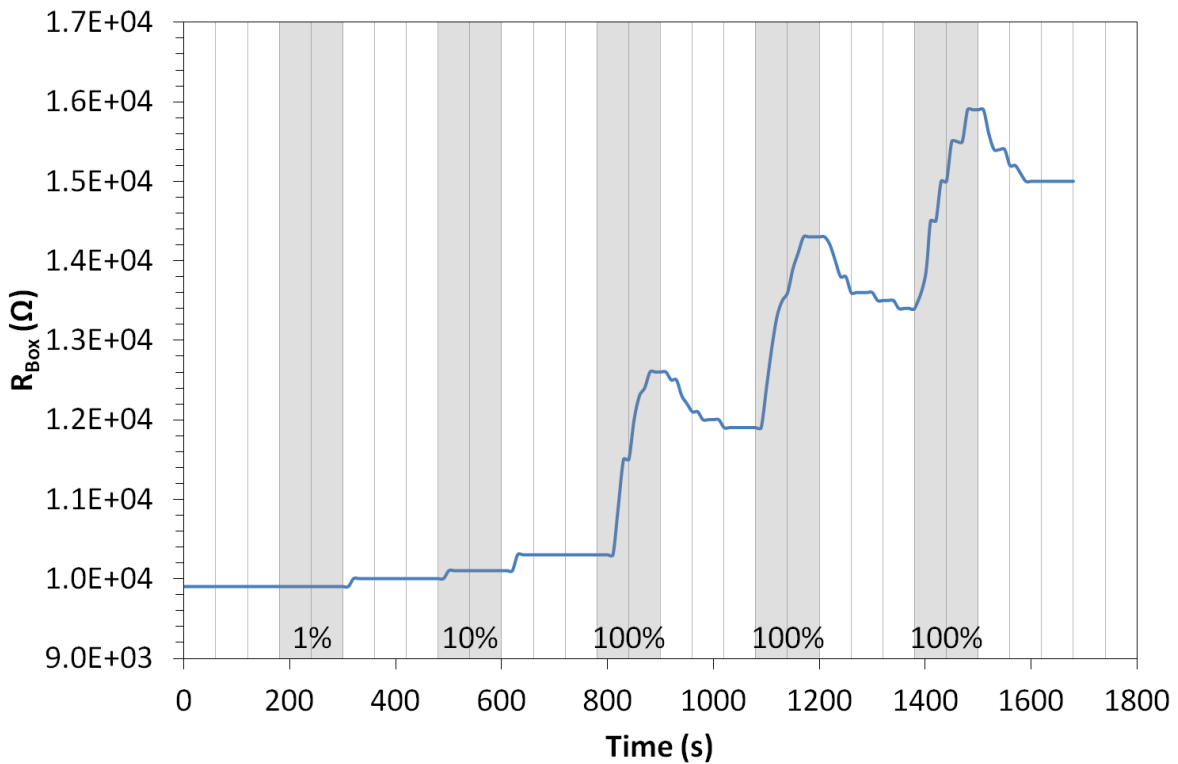


Figure 124. Pentacene 32 TR variable % ethylethanoate sensing results. N.B. grey shaded areas indicate analyte exposure.

At 1% saturated vapour exposure it can be seen from **Figure 124** that the device showed no immediate response to the ester, instead its channel on-resistance increased by 1k Ω (1%) after the two minutes of exposure had ended. Upon 10% saturated vapour exposure an initial increase of 1k Ω (1%) was observed in the channel on-resistance of the device followed by an increase of 2k Ω approximately 30 seconds after the exposure ended. Both the 1% and 10% saturated vapour exposures create a smaller response in the coated than the uncoated pentacene transistor tested earlier (see section 5.2.1.4). The final three exposures of this run were all to 100% saturated vapour, the first of which caused a response approximately 30 seconds after exposure began, the second of which caused a response approximately 20 seconds after exposure began, while the third exposure caused a response almost immediately.

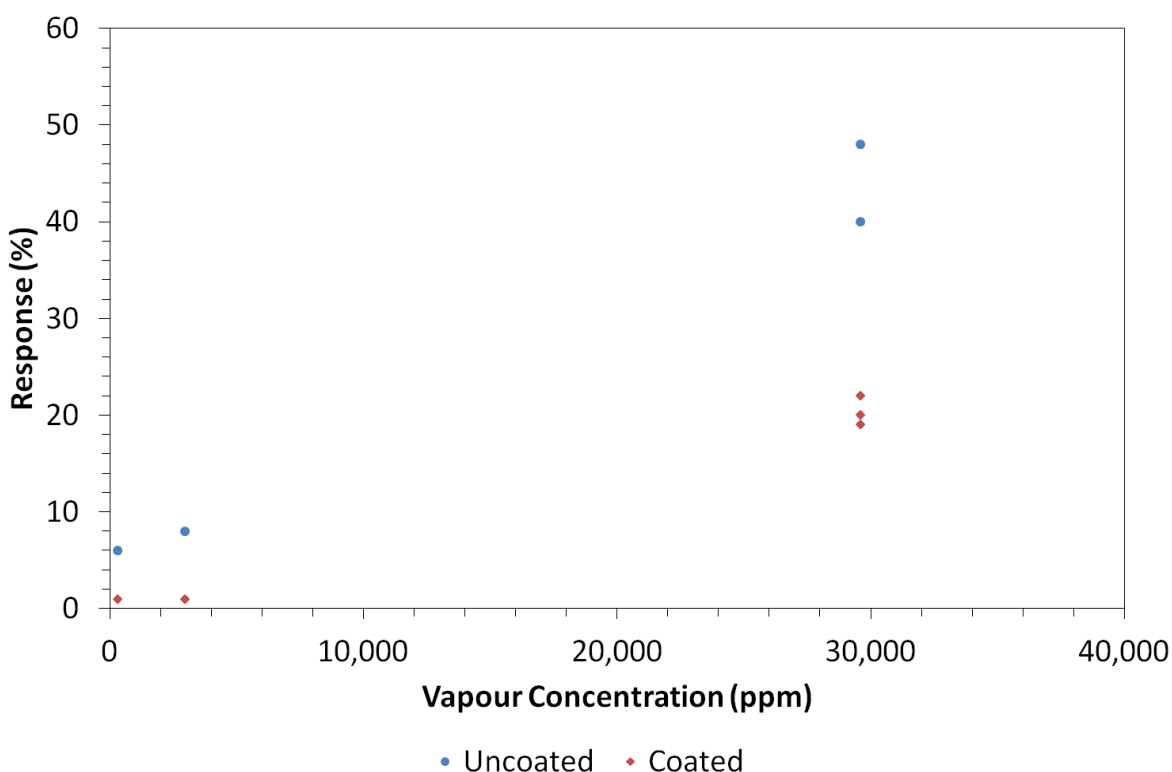


Figure 125. The percentage responses of both calixarene 1 coated and uncoated pentacene OFETs to ethylethanoate.

The absolute increase in channel on-resistance from the first, second and third exposures were $23\text{k}\Omega$, $24\text{k}\Omega$ and $25\text{k}\Omega$ respectively, leading to percentage changes of 22% for the first exposure, 20% for the second exposure and 19% for the third; these changes are less than half of the largest one observed from the uncoated sample (see **Figure 125**) showing a definite de-sensitising effect from this calixarene when the OFET is exposed to ethylethanoate vapour. This de-sensitising effect is probably due to the calixarene performing no significant binding of its own and causing the analyte to first need to penetrate the sensitiser layer before it can interact with the pentacene. It seems that the choice of calixarene sensitiser was wrong for ester sensing, maybe a material with an upper-rim side-chain containing a similar structure to the ester (such as an ester, carboxylic acid or amide group) may have been a better choice and ensured more of an interaction between analyte and sensitiser.

5.2.2.1.5 Amide Sensing Results

The coated OFET used for amide sensing was Pentacene 44 BR, coated in six monolayers of calixarene 1, the pre-exposure characteristics of this device can be seen in **Figure 121**. The amide used in the sensing experiment was formamide, used in four different concentrations: 1% saturation (1% of nitrogen to the bubbler, submerged in ice-water), 10% saturation (10% of nitrogen to the bubbler, submerged in ice-water), 50% saturation (50% of nitrogen to the bubbler, submerged in ice-water) and 100% saturation (100% of nitrogen to the bubbler, submerged in ice-water); as stated previously the theoretical concentration of formamide at 100% saturation is 3.53ppm at 0°C. The results of the sensing experiment can be seen below in **Figure 126**.

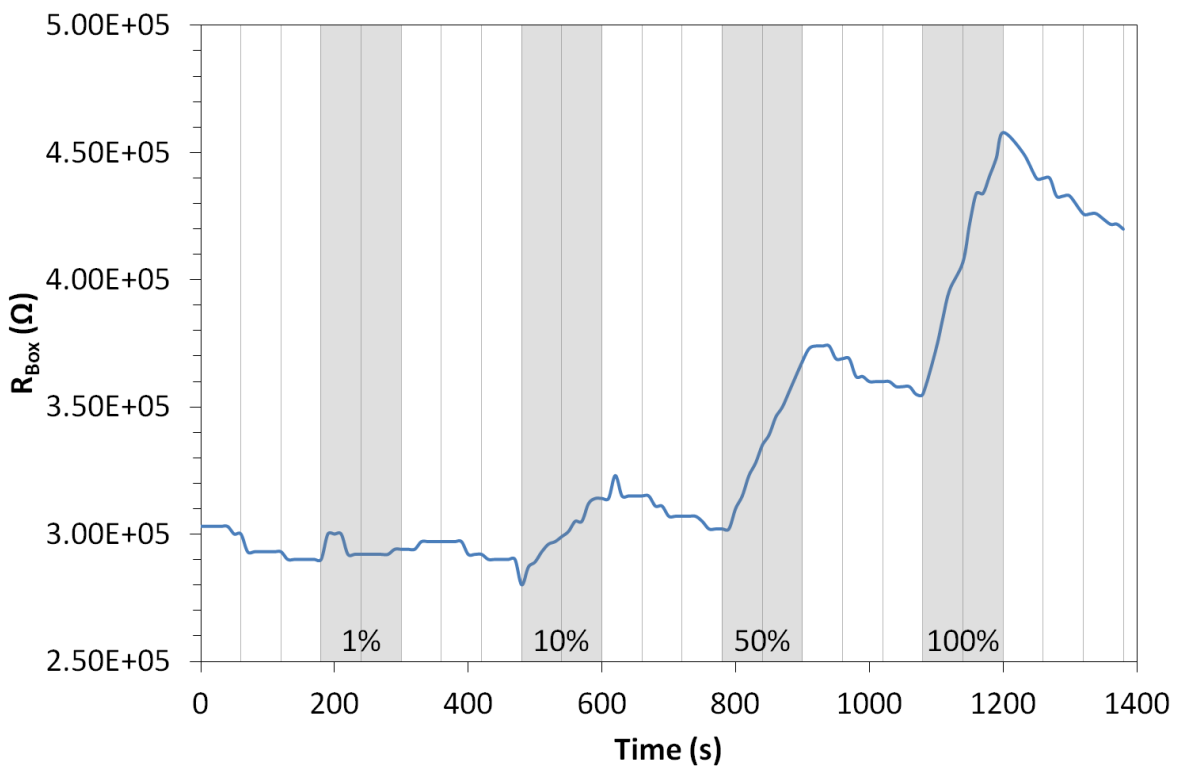


Figure 126. Pentacene 44 BR variable % formamide sensing results. N.B. grey shaded areas indicate analyte exposure.

The sensing response shown in **Figure 126** will now be discussed, it should first be noted however that this device is not as stable under nitrogen as most of the devices used previously (see the initial three minutes of **Figure 126**), possibly due to moisture or oxygen trapped during the calixarene coating process being released. The 1% saturated vapour

exposure caused a relatively small ($100\text{k}\Omega$ or 3% of pre-exposure) increase in channel on-resistance for the first 30 seconds of the two minute exposure after which the resistance dropped by $80\text{k}\Omega$, the lower percentage change, with respect to the uncoated pentacene OFET (see section 5.2.1.5), and short-lived response may hint at some sensing hindrance at lower concentrations. The 10% saturated vapour exposure shows a more obvious response to the formamide in the form of a steady rise to a channel on-resistance $340\text{k}\Omega$ higher than the pre-exposure value, this corresponds to a 12% increase and continued for 10 seconds after exposure had ended. Comparing the coated and uncoated responses (from section 5.2.1.5) it can be seen that the percentage change is still smaller than the uncoated device. Under 50% saturated vapour exposure, the coated OFET responded to the formamide with a very steady uniform increase in channel on-resistance; the response both began and ended approximately 10 seconds later than it should have, however the increase in channel on-resistance was of magnitude $710\text{k}\Omega$, corresponding to a percentage increase of 24%. Looking back at the uncoated response (section 5.2.1.5) it can be seen that the percentage change is comparable to the uncoated OFET. Finally the response to 100% saturation exposure was a huge $1.03\text{M}\Omega$ (29%) increase in channel on-resistance, comparing this to the previously tested uncoated pentacene OFET (section 5.2.1.5) the percentage change is comparable. From this data it can be safely concluded that the coating of Pentacene 44 BR has not had the desired effect and has actually reduced its response to formamide vapour, although the effect is less pronounced in higher concentration exposures. The coating, however, has an unexpected benefit in this case: it actually improves the recovery of the device during the recovery phases of the exposure run; it can be seen by comparing the two exposure graphs (**Figure 111** and **Figure 126**) that the uncoated OFET shows little to no recovery, while the recovery shown by the coated OFET in the three short minutes of the recovery phases are quite significant, especially after the larger concentration exposures; perhaps showing that rather than a sensitiser layer the calixarene acts as a way to increase the number of exposures the sensor can take before it is rendered useless. Again the calixarene layer acts as a barrier to the analyte, which needs to be penetrated before an interaction with the pentacene can occur. A comparison between the responses of the sensitiser coated and uncoated devices is given in **Figure 127**. It can be seen that the responses of both the coated and uncoated devices seem to be slowly saturating.

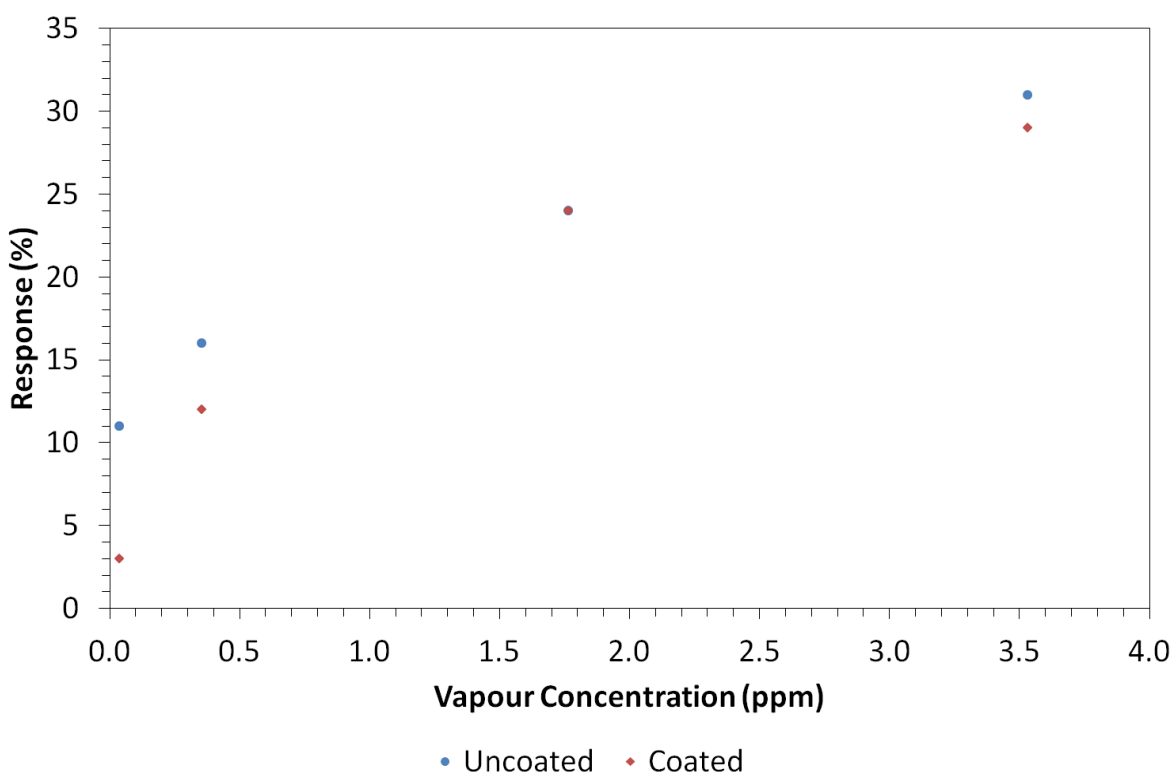


Figure 127. The percentage responses of both calixarene 1 coated and uncoated pentacene OFETs to formamide.

5.2.2.1.6 Ethylene Sensing Results

The vapour exposure in this section was performed on my behalf by Dr. Delia Puzzovio using the exposure equipment at the University of Tübingen.

As in section 5.2.1.8, concentrations of 0.3ppm, 1ppm, 3ppm, 10ppm and 25ppm ethylene were used. The device was coated in PtOEP (platinum (II) octaethyl porphyrin, see **Figure 53** for its structure) as metallic platinum is a common catalyst for reactions involving hydrogenation of unsaturated hydrocarbons (breaking carbon-carbon double bonds)^[127] and it was hoped that complexed platinum in PtOEP would show a similar affinity. The sensitiser layer was four monolayers thick and deposited via the L-S method from a Langmuir film under a surface pressure of $18\text{mN}\cdot\text{m}^{-1}$. The sensitised device used in Tübingen was characterised in the conventional manner before transport, output and transfer characteristics for the device can be seen in **Figure 128**.

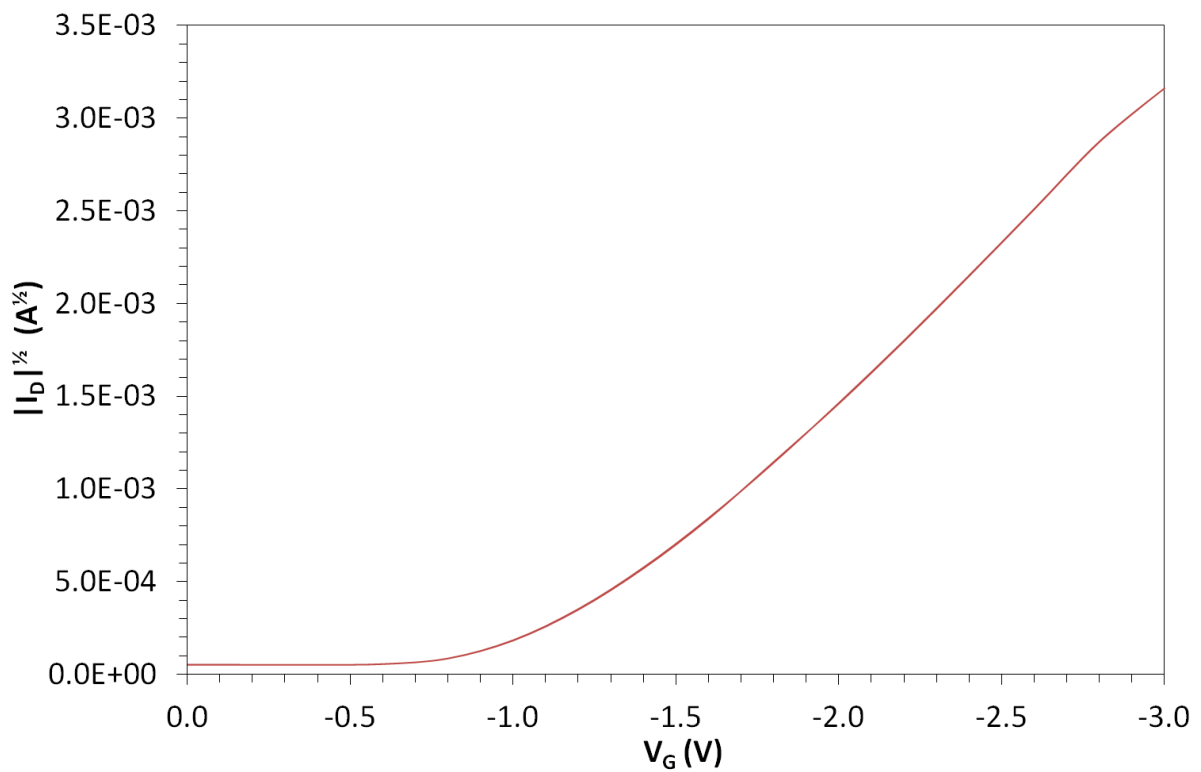
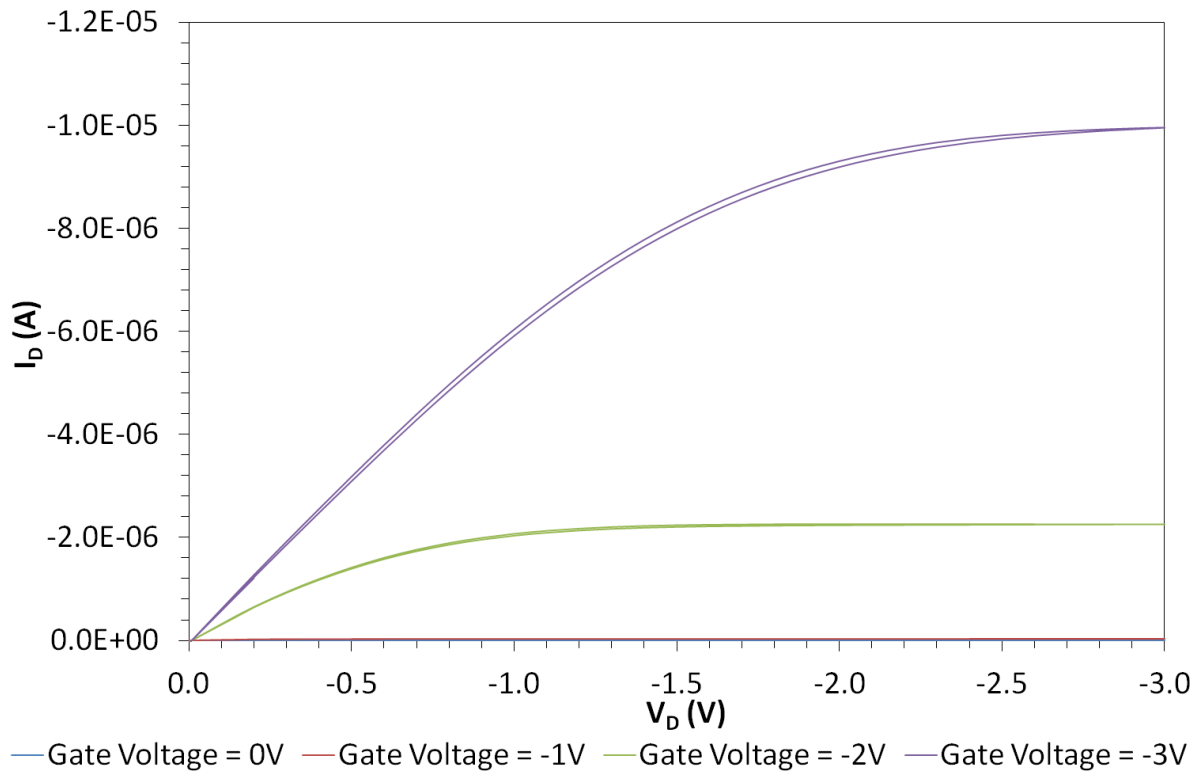


Figure 128. Pentacene-PtOEP 2 TL output and transfer characteristics.

It can be seen from the output characteristic of Pentacene-PtOEP 2 TL (Figure 128) that the device has no obvious contact problems, negligible doping and very little hysteresis, albeit

more than the uncoated device used in section 5.2.1.8 for ethylene sensing; the transfer characteristic of Pentacene-PtOEP 2 TL shows no visible hysteresis and a high degree of linearity aside from a small kink close to -3V gate voltage, carrier mobility and threshold voltage extracted from this device have values of $(4.24 \pm 0.11) \times 10^{-2} \text{ cm}^2 \text{ V}^{-1} \text{ s}^{-1}$ and $-1.15 \pm 0.03 \text{ V}$ respectively. The peak drain current of the device is $-1.00 \times 10^{-5} \text{ A}$, which corresponds to a channel on-resistance of $3.00 \times 10^5 \Omega$.

The vapour sensing data in this section was collected using the automated version of the current-to-voltage converter (as mentioned at the start of the chapter) and so the data looks less smooth than in similar graphs from other sections, due to the automated variable resistance chip only being able to be adjusted in discrete resistance steps much larger than those of the manual resistance box. The data is shown in its raw form in **Figure 129** and due to the noisiness of the data it is presented after being smoothed through the use of a five-point median in **Figure 130**.

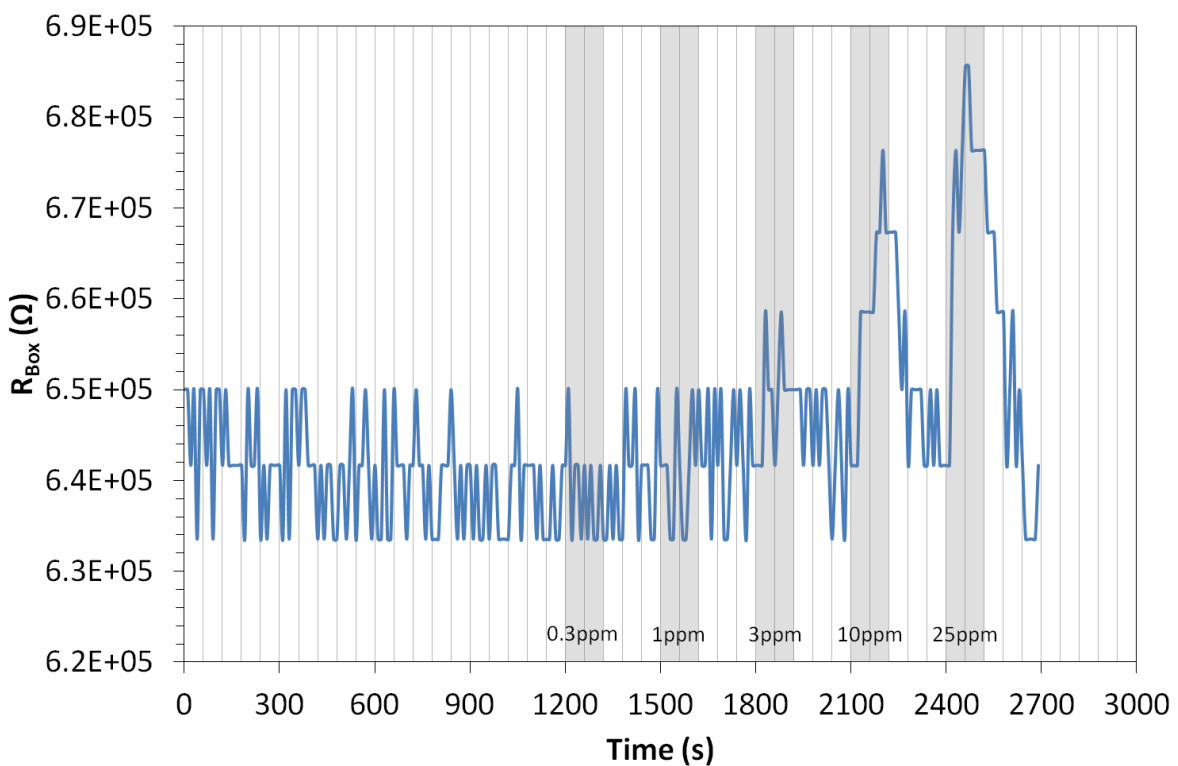


Figure 129. Pentacene-PtOEP 2 TL variable ppm ethylene sensing results. N.B. grey shaded areas indicate analyte exposure.

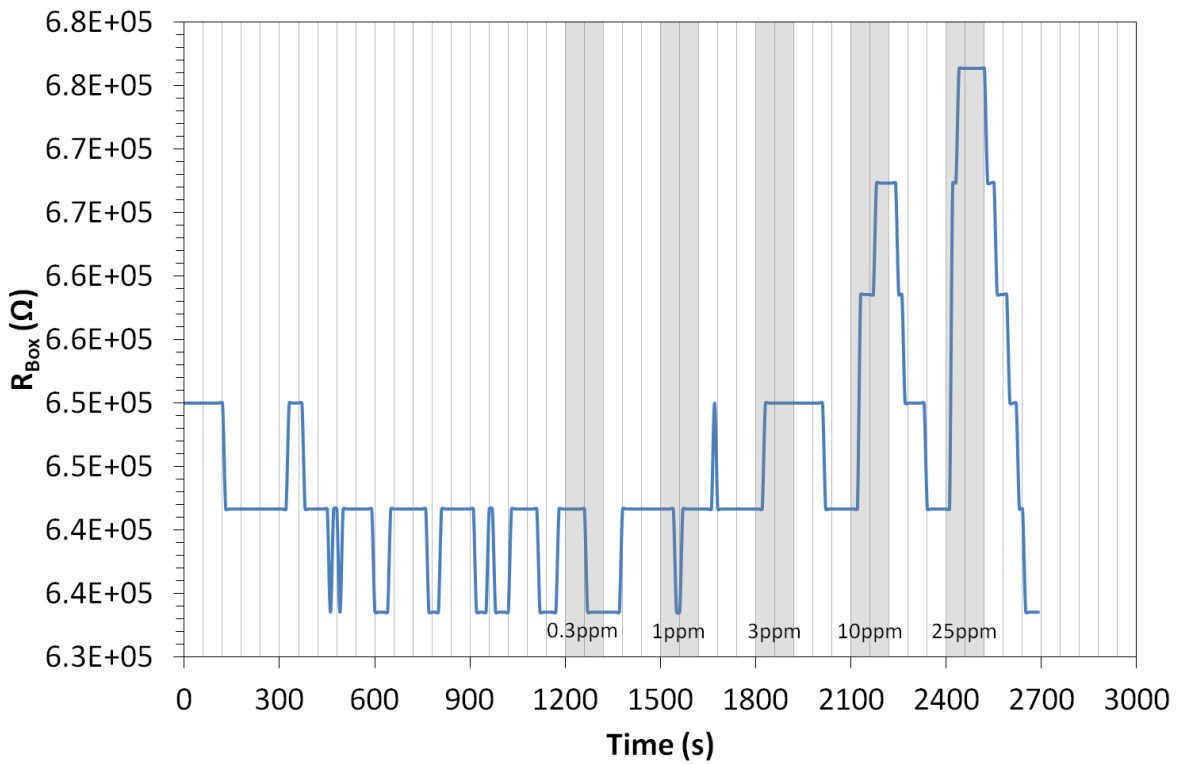


Figure 130. Pentacene-PtOEP 2 TL variable ppm ethylene sensing results five-point median.
N.B. grey shaded areas indicate analyte exposure.

The first observation that can be made from **Figure 130** is that of the OFET's channel on-resistance showing a drop under the initial nitrogen purge before exposure begins, this is possibly an effect of out-gassing a chemical the device have come into contact with prior to sensing that it shows sensitivity towards. This behaviour is not very obvious in the raw data plotted in **Figure 129**, thus highlighting the necessity of the smoothing performed on the data before it is plotted in **Figure 130**. During the initial exposure of 0.3ppm ethylene, the device seems to show no increase in resistance within the two minute exposure window; however following the exposure the resistance undergoes a small increase before approximately levelling off again, perhaps hinting at a delayed response at such dilute concentrations of ethylene. During the 1ppm exposure, the device does not respond to the ethylene within the exposure period. The 3ppm exposure causes a more noticeable increase in channel on-resistance that occurs at the very beginning of the exposure window, the magnitude of this change is approximately 10k Ω (~2%). When exposed to 10ppm the device responds much more than at 3ppm with a resistance change of ~34k Ω (~5%); the device also shows significant recovery in the nitrogen purge after the 10ppm exposure,

causing the resistance to drop back to almost the pre-exposure value. The final exposure of 25ppm causes an even larger change in resistance, within one minute the resistance increases by around $44\text{k}\Omega$ ($\sim 7\%$) before falling by $10\text{k}\Omega$ in the second minute of exposure. The device recovery after 25ppm is drastic, the resistance falls down to a value comparable to the initial resistance of the device before 0.3ppm sensing was begun.

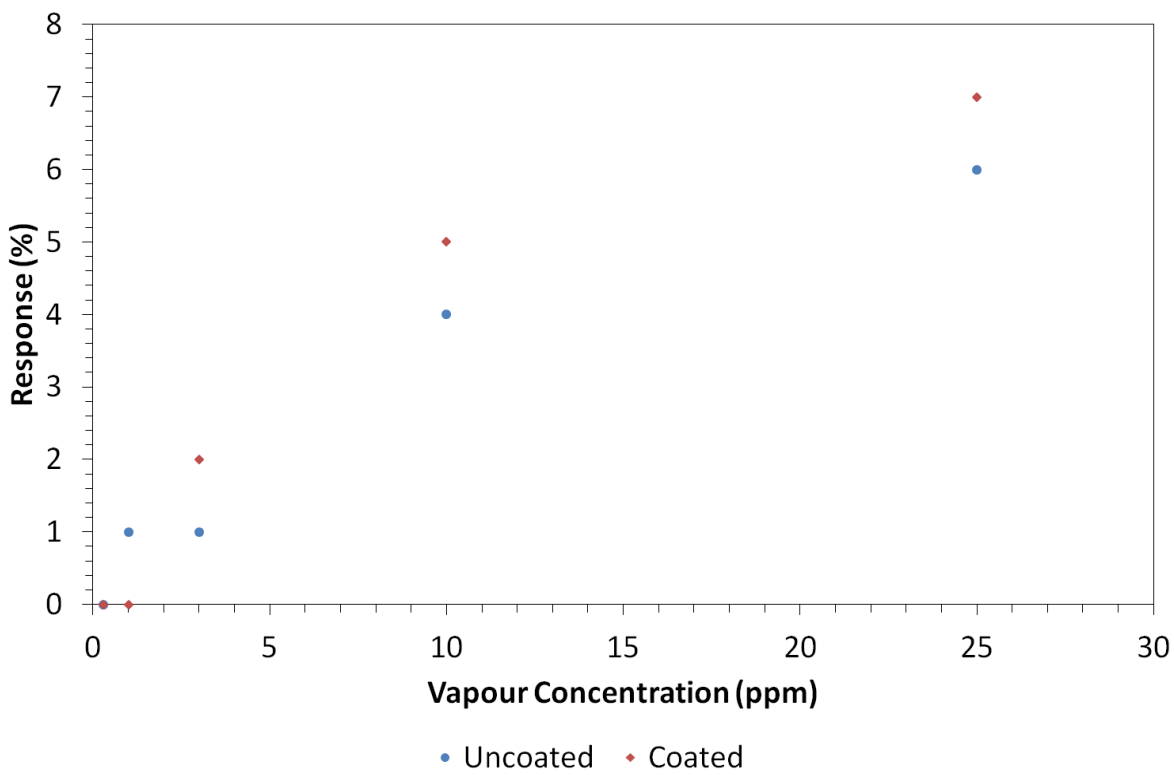


Figure 131. The percentage responses of both PtOEP coated and uncoated pentacene OFETs to ethylene.

Comparing the sensitised device's response to that of the un-sensitised device from section 5.2.1.8, it can be seen that despite the larger starting channel on-resistance of the sensitised device, the percentage changes in resistance are larger for the three largest ethylene concentrations (see **Figure 131**) (the 25ppm response being comparable only if the “spikes” are taken as the real signal and not noise). The sensitiser layer also seems to aid recovery, with faster and more dramatic recovery being shown by the sensitised device after higher concentrations of analyte exposure. This increase in response can be attributed to analyte interacting with the sensitiser layer to create dipoles that interact with the accumulation layer through the E-fields they generate, hampering carrier transport (reducing mobility) and/or hampering accumulation layer formation (increasing threshold voltage); some of the

analyte may still penetrate the PtOEP and interact as in the uncoated device in addition to the interactions of the analyte with the sensitiser layer. However, the detection limit of the sensitised device falls short of the ethylene concentration required fruit ripening (0.1ppm - 1ppm),^[104] while the un-sensitised device shows a small response to 1ppm ethylene, but this is on the very edge of its capabilities and it would therefore not make a good sensor for monitoring ethylene levels used when artificially ripening fruit or trying to prevent fruit from ripening.

5.2.2.2 Calixarene : Porphyrin Blend Sensitised Transistors

The OFET described in this section was coated in a 2:1 molar ratio blend of the calixarene calix[8]arene (calixarene 2, see **Figure 56**) and the porphyrin 5,10,15,20-Tetrakis (3,4-bis (2-ethylhexyloxy) phenyl)-21H,23H-porphyrinato cobalt (II) (Co-EHO) for use in ketone and aldehyde sensing; this particular porphyrin was chosen as it has shown some ketone and aldehyde sensitivity when used as part of an optical sensor by Dunbar *et al.*^[7] The blend was used to improve the film quality of the porphyrin, following on from the work of Dunbar *et al.*^[8]

5.2.2.2.1 Pre-Coating Transistor Characteristic

The pentacene transistor was characterised as described in sections 2.6.1 and 2.6.2 using $V_D, Max = V_{G, Max} = -3V$ and $V_{G, Min} = 0V$. The characteristics of the transistor, later used in vapour sensing, is shown in **Figure 132**.

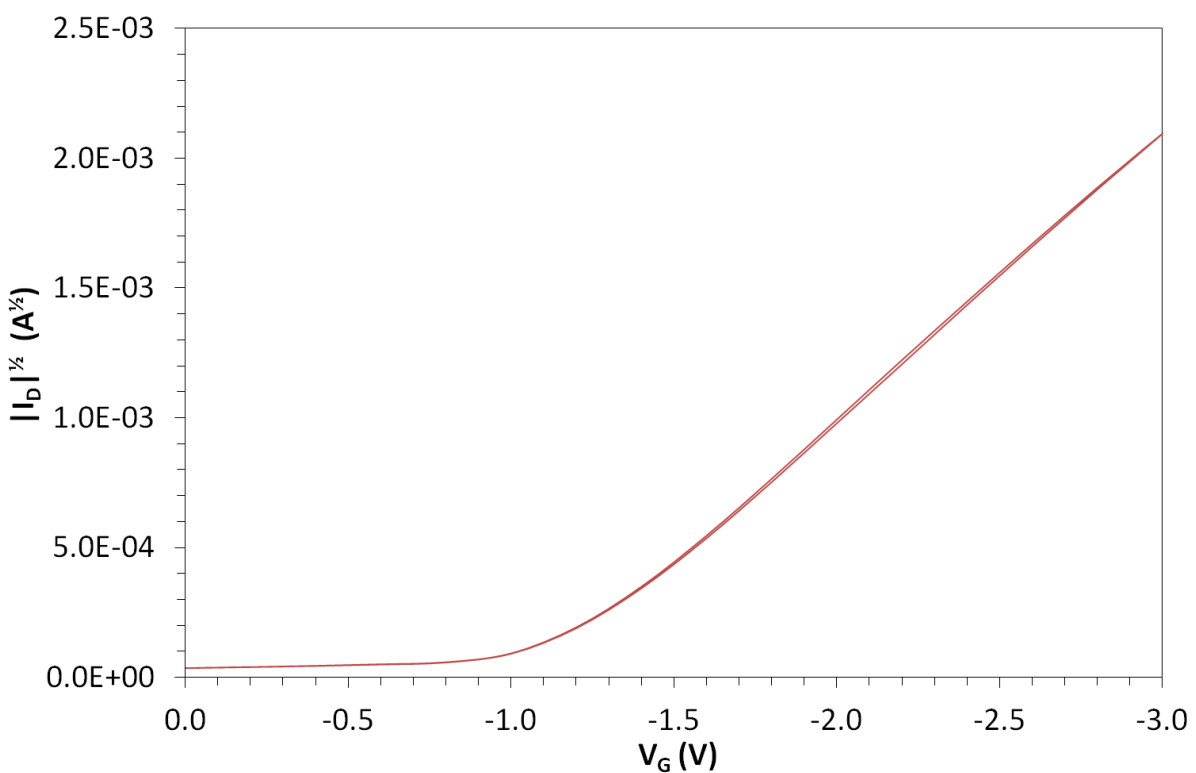
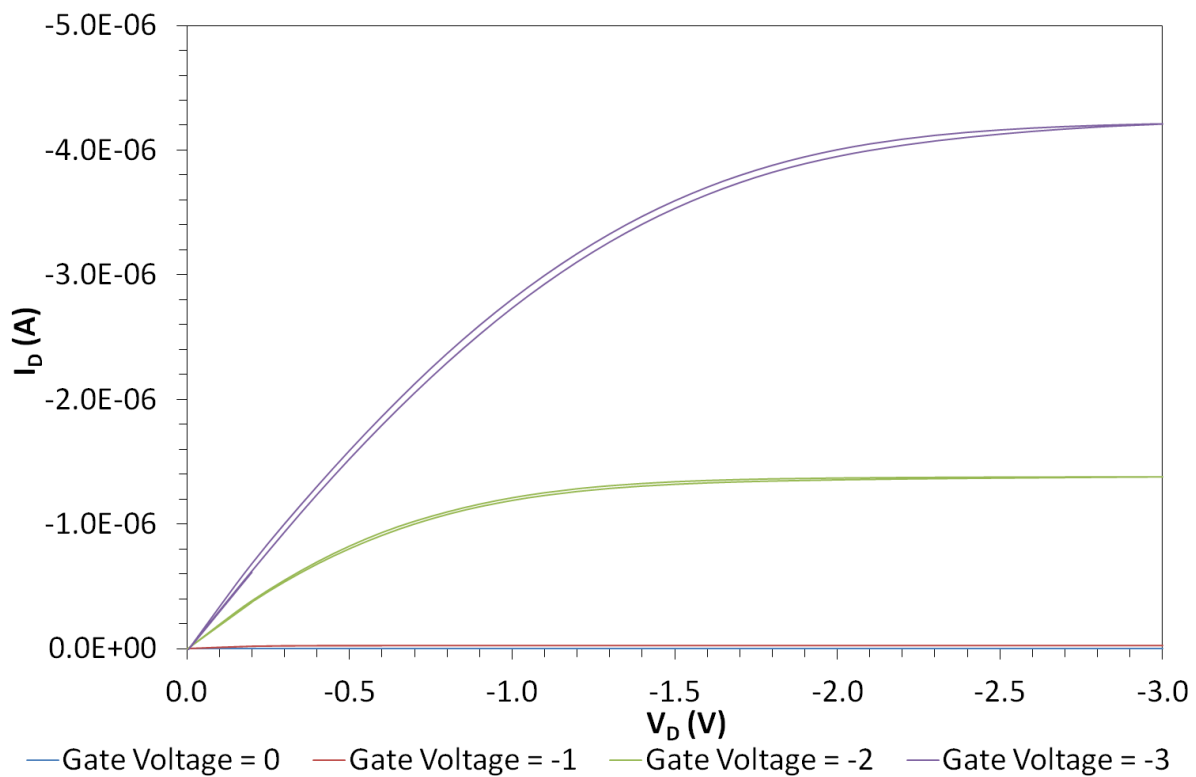


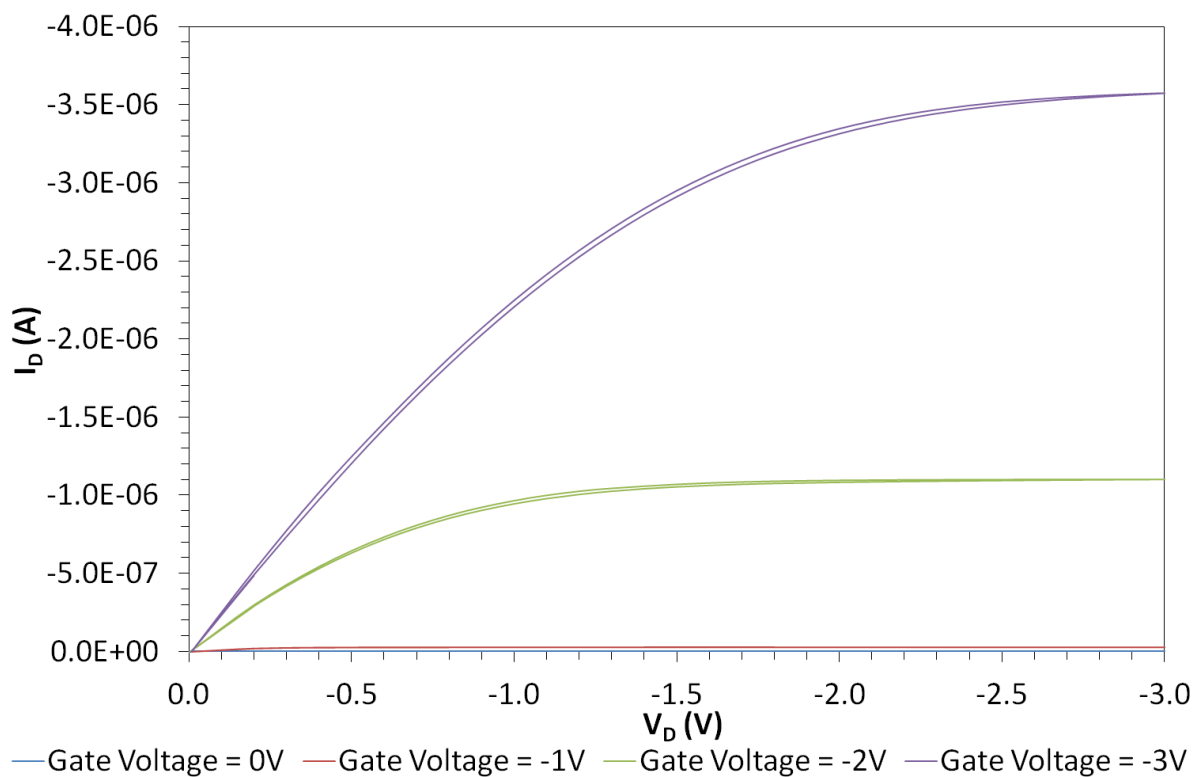
Figure 132. Pentacene 50 TR output and transfer characteristics.

The output characteristic in **Figure 132** shows that before coating Pentacene 50 TR has very little hysteresis, no apparent contact problems (indicated by the very linear initial region) and no apparent doping.

The Transfer characteristic of Pentacene 50 TR shows a tiny amount of hysteresis and its high degree of linearity allows for a very accurate fitting of the extrapolation line. Carrier mobility and threshold voltages extracted from the graph have values of $(1.98 \pm 0.02) \times 10^{-2} \text{ cm}^2 \text{V}^{-1} \text{s}^{-1}$ and $-1.19 \pm 0.01 \text{ V}$ respectively. The peak drain current of this device was $-4.36 \times 10^{-6} \text{ A}$, meaning its channel on-resistance at saturation is $6.88 \times 10^5 \Omega$.

5.2.2.2.2 Post-Coating Transistor Characteristic

As the process of depositing a sensitiser layer onto the device causes a change in the electrical characteristics of the device, the device was re-tested after coating using the same methods as in section 5.2.2.2.1 above. The device characteristics are shown in **Figure 133**.



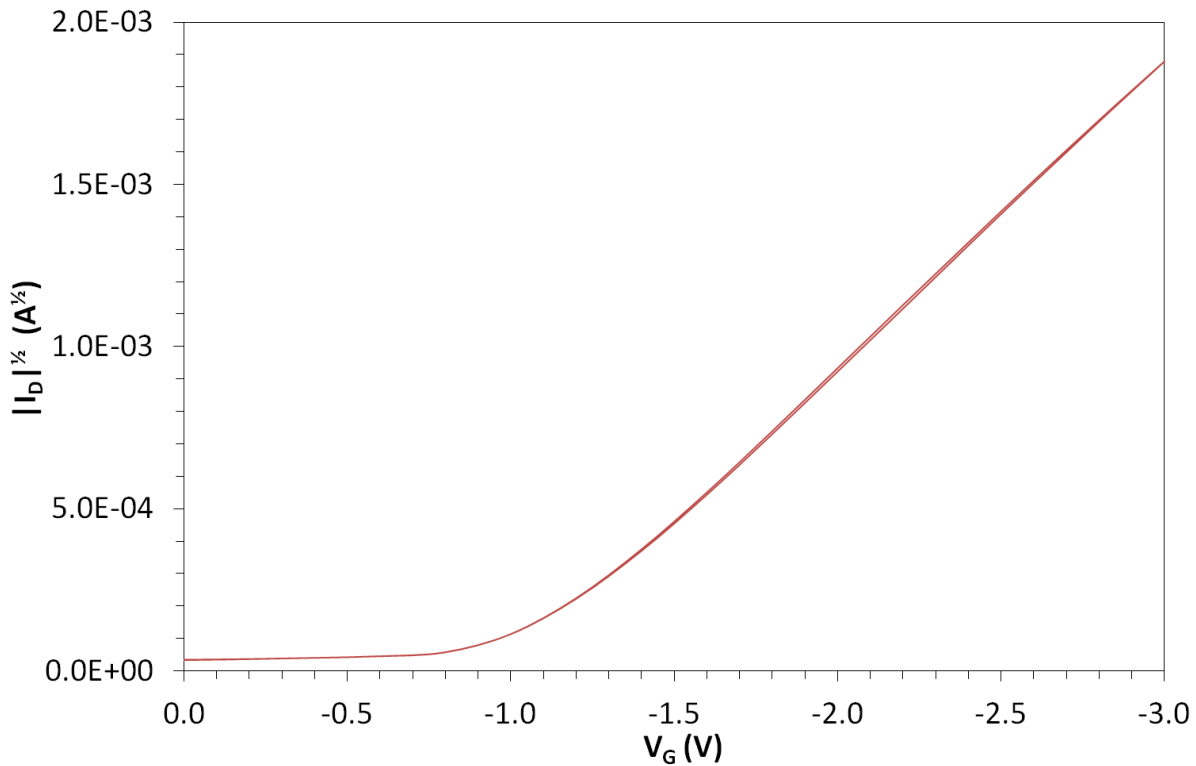


Figure 133. Pentacene 50 TR (post-coating) output and transfer characteristics.

The output characteristic after coating with the calixarene : porphyrin blend (**Figure 133**) actually shows slightly less hysteresis than the pre-coated characteristic shown previously (**Figure 132**) and still shows no contact issues and a negligible level of doping current, however, there is a decrease in the saturation current.

The transfer characteristic also shows less hysteresis than that of the uncoated OFET, however, the mobility of this device is lower than that of the uncoated device at a value of $(1.45 \pm 0.01) \times 10^{-2} \text{ cm}^2 \text{ V}^{-1} \text{ s}^{-1}$, but the threshold is also lower at a value of $-1.10 \pm 0.01 \text{ V}$. The peak drain current of this device is $3.53 \times 10^{-6} \text{ A}$, meaning that the channel on-resistance of this device is higher than it was before coating with a value of $8.50 \times 10^5 \Omega$.

5.2.2.2.3 Ketone Sensing Results

The device Pentacene 50 TR discussed in the previous sections was first exposed to a ketone, octan-2-one, in four different concentrations: 1% saturation (1% of nitrogen to the bubbler, submerged in ice-water), 10% saturation (10% of nitrogen to the bubbler, submerged in ice-water), 50% saturation (50% of nitrogen to the bubbler, submerged in ice-water) and 100% saturation (100% of nitrogen to the bubbler, submerged in ice-water); as

stated previously the theoretical concentration of octan-2-one at 100% saturation is 250ppm at 0°C. The exposure and recovery windows were the same as those used for the uncoated pentacene transistor ketone exposure experiment (see section 5.2.1.6), namely exposure windows of two minutes and recovery windows of three minutes. The results of the experiment are shown in **Figure 134**.

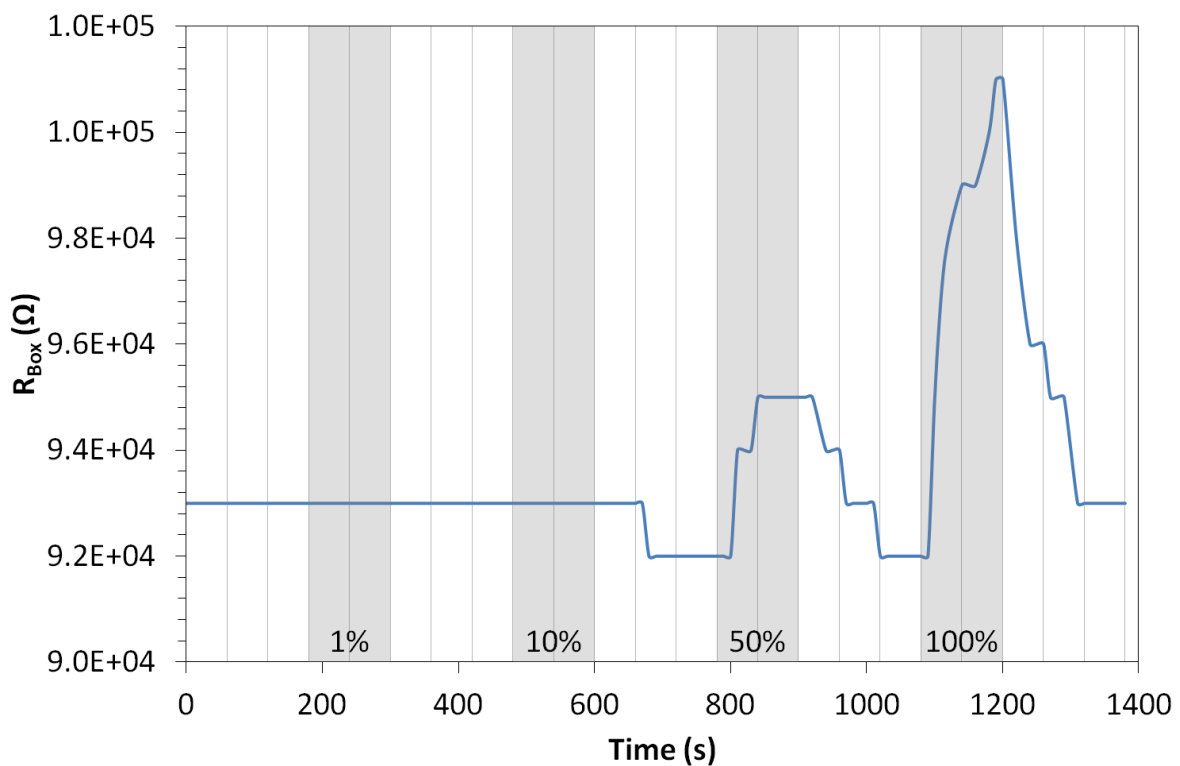


Figure 134. Pentacene 50 TR variable % octan-2-one sensing results. N.B. grey shaded areas indicate analyte exposure.

Figure 134 shows that the device Pentacene 50 TR was very stable under the initial three minute nitrogen flush and also throughout the 1% and 10% saturated octan-2-one vapour exposures. There was a slight reduction in channel on-resistance during the second minute of nitrogen flush after the 10% exposure, this was a fluctuation of the device's channel resistance taking the form of a 10k Ω (1% of initial resistance). However, approximately 10 seconds into the 50% exposure the on-resistance increased by 20k Ω (2% of the pre-exposure value), before recovering back to the pre-exposure value over the subsequent three minute nitrogen purge. During the two minutes of the 100% saturated vapour exposure the channel on-resistance rapidly increased to a peak value 90k Ω (9%) higher than

the pre-exposure value, before recovering back to the initial on-resistance, observed at the beginning of the experiment, over the first two minutes of the final nitrogen flush.

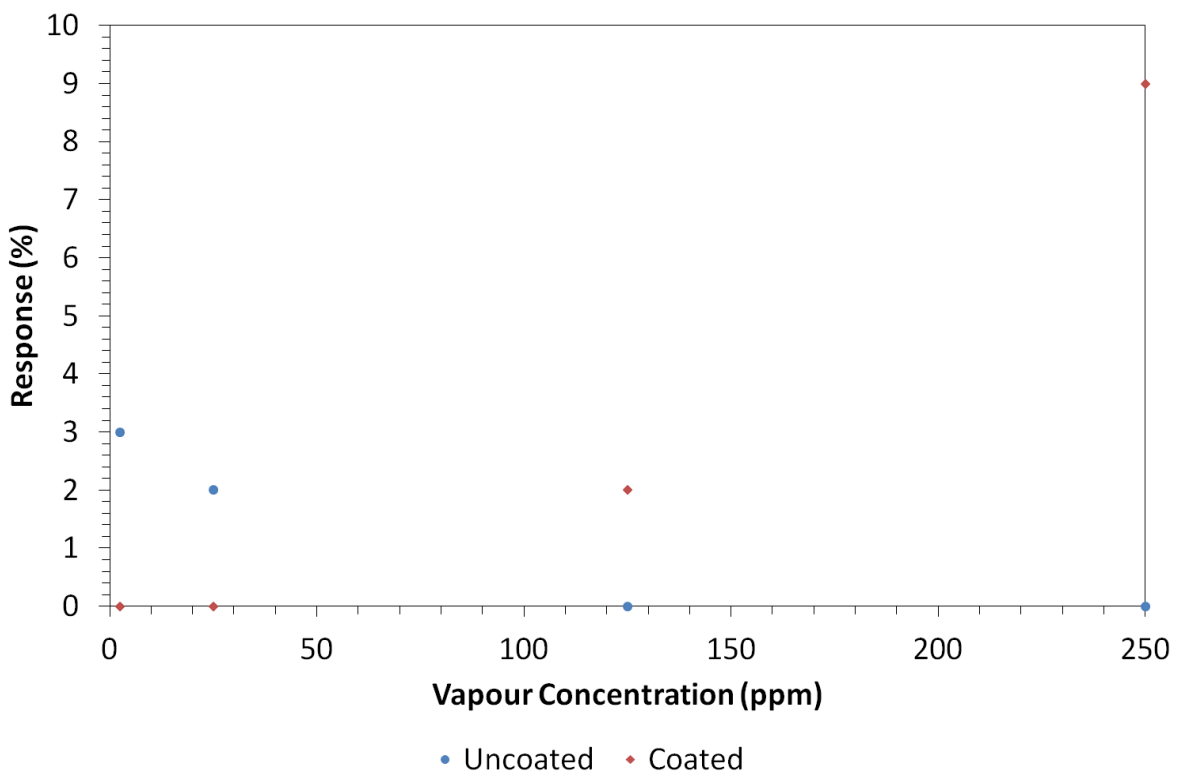


Figure 135. The percentage responses of both Co-EHO : calixarene 2 blend coated and uncoated pentacene OFETs to octan-2-one.

When comparing the coated and uncoated device responses (see **Figure 112**, **Figure 134** and **Figure 135**), it can be seen firstly that the uncoated device is a poor baseline initially; but also that even if part of the uncoated changes are due to the vapour, the addition of the sensitiser coating has blocked the pentacene's own response to the vapour essentially relegating it to the job of carrier transport (as is intended in this architecture). The sensitiser provides sensing responses of its own to the analyte (through the dipole interactions discussed previously) and shows impressive recovery meaning it is re-useable as a sensor. It appears from the data presented in **Figure 134** and **Figure 135** that the coated device appears to have a detection threshold somewhere between 25ppm (10% saturation) and 125ppm (50% saturation)..

It has been proved by this result that the optical response shown by Dunbar *et al*^[7] induces a change in the electronic structure of the film large enough to be detected by the OFET transducer.

5.2.2.2.4 Aldehyde Sensing Results

The device Pentacene 50 TR discussed was next exposed to an aldehyde, octanal, in four different concentrations: 1% saturation (1% of nitrogen to the bubbler, submerged in ice-water), 10% saturation (10% of nitrogen to the bubbler, submerged in ice-water), 50% saturation (50% of nitrogen to the bubbler, submerged in ice-water) and 100% saturation (100% of nitrogen to the bubbler, submerged in ice-water); as stated previously the theoretical concentration of octanal at 100% saturation is 649ppm at 0°C. The experiment was performed with the same exposure and recovery durations as the uncoated device in section 5.2.1.7, two minute exposure phases and two minute recovery phases. The results of the experiment are shown in **Figure 136**.

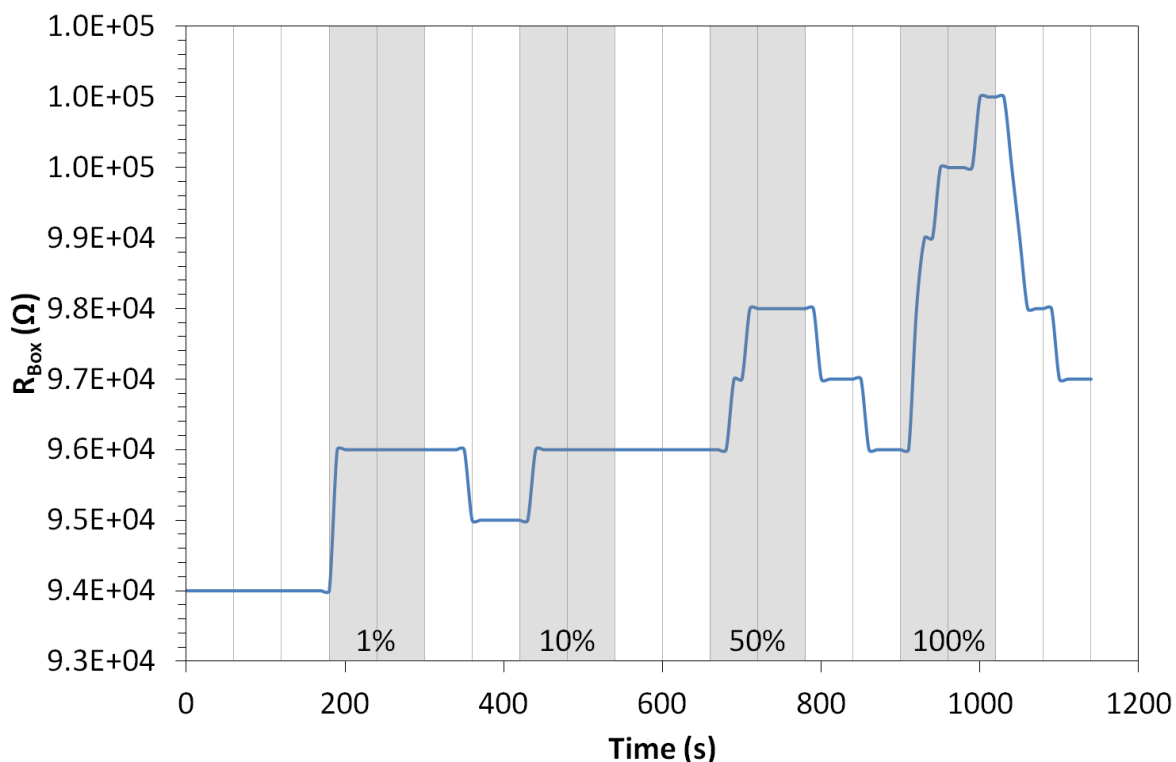


Figure 136. Pentacene 50 TR variable % octanal sensing results. N.B. grey shaded areas indicate analyte exposure.

The sensing response of the coated sample began at the lowest vapour concentration: 1% saturated vapour (see **Figure 136**), showing an immediate channel on-resistance rise of $20\text{k}\Omega$ (2% of pre-exposure) followed by a recovery of $10\text{k}\Omega$ towards the end of the first minute of the subsequent recovery stage. Upon exposure to 10% saturated octanal vapour the on-resistance rise was equal to the recovery experienced in the previous nitrogen purge, $10\text{k}\Omega$, a rise equal to 1% of the device's on-resistance prior to 10% exposure. Upon exposure to 50% saturated vapour, another rise of $20\text{k}\Omega$ (2% of pre-exposure) was observed, followed by recovery of the same magnitude during the two minute nitrogen flush. Finally, under the 100% saturated vapour exposure, the on-resistance increased by $50\text{k}\Omega$ (5% of pre-exposure) over the two minutes of exposure. In the final recovery window the device's on-resistance reduced by $40\text{k}\Omega$.

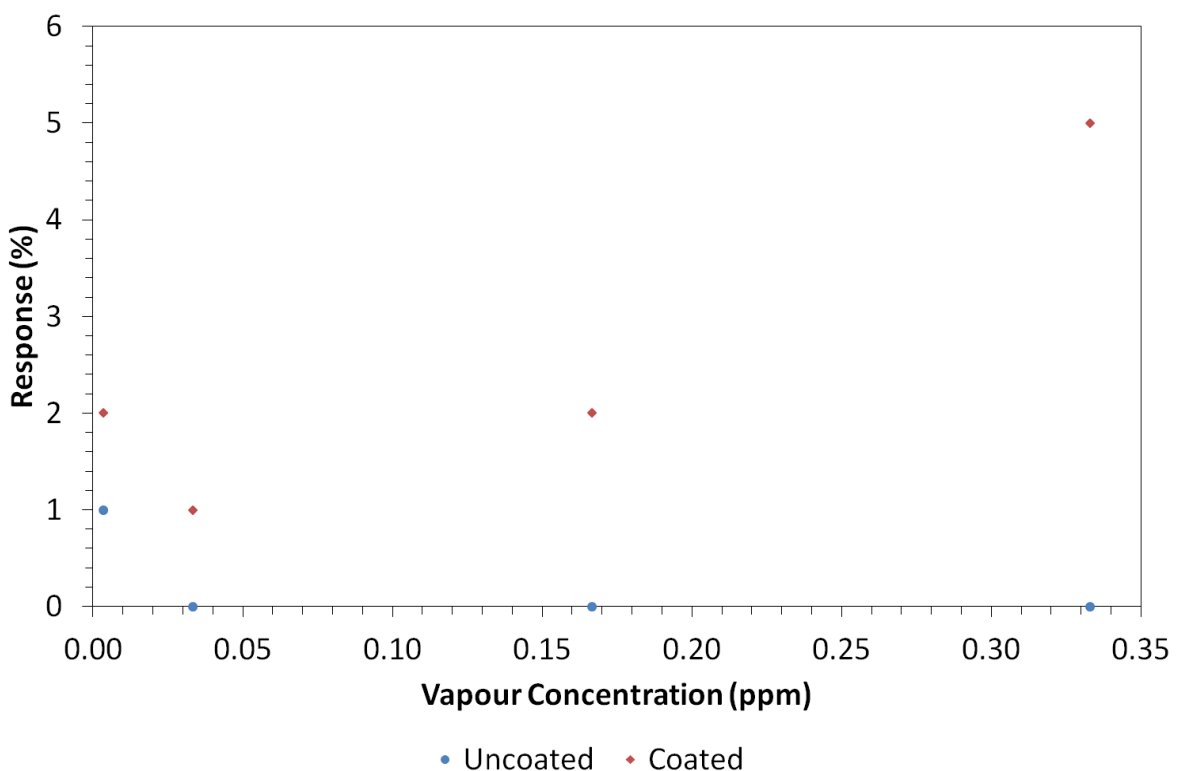


Figure 137. The percentage responses of both Co-EHO : calixarene 2 blend coated and uncoated pentacene OFETs to octanal.

When comparing the coated and uncoated pentacene transistor responses to octanal, it is obvious that the sensitiser coating has a profound effect on the device's sensing capabilities, as shown by **Figure 137**, the response of the sensitised device is greater at all concentrations; in addition the pentacene OFET shows a response to the aldehyde vapour at

the lowest concentration that actually reduces the channel on-resistance, after which it no longer responds to aldehyde exposure; this would seem to suggest that if the pentacene response is real and due to the aldehyde, then the sensitiser coating suppresses the pentacene's own response as well as enhancing the response of the device to all the concentrations tested (through the dipole generated from analyte-sensitiser interaction as mentioned previously). The sensing responses attributed to the sensitiser provide reversible responses, a very good attribute for a sensor device (see **Figure 136**).

As with the aldehyde response in section 5.2.2.2.3, it has been proved by this result that the optical response shown by Dunbar *et al*^[7] induces a change in the electronic structure of the film large enough to be detected by the OFET transducer. This allows the detection of the same analyte using the same sensor medium as the optical method but with a much smaller, simpler and cheaper measurement system.

5.2.3 Pentacene Organic Field-Effect Transistor Lifetime Studies

Real-world vapour sensors would be required to work in an ambient environment rather than the nitrogen atmosphere the devices have been within for the vapour sensing described in this work. This means that firstly the device must be moderately stable under ambient conditions and secondly that any changes in characteristics must be consistent and predictable so the changes can be dynamically “subtracted” from the data obtained from the sensor.

The device used in this experiment, Pentacene 53 TL, was fabricated as described previously in section 5.2.1. The current-to-voltage converter test circuit (see section 3.1.1) was connected to the OFET and was allowed to drive the device with a sine wave at 70Hz between +3V and -3V for 24 hours under ambient atmosphere at ~20°C under low-lighting. Screen-shots were taken periodically from the attached oscilloscope to monitor the device degradation, a plot of all the screen-shots can be seen in **Figure 138** along with the positive half-cycle of the drive voltage.

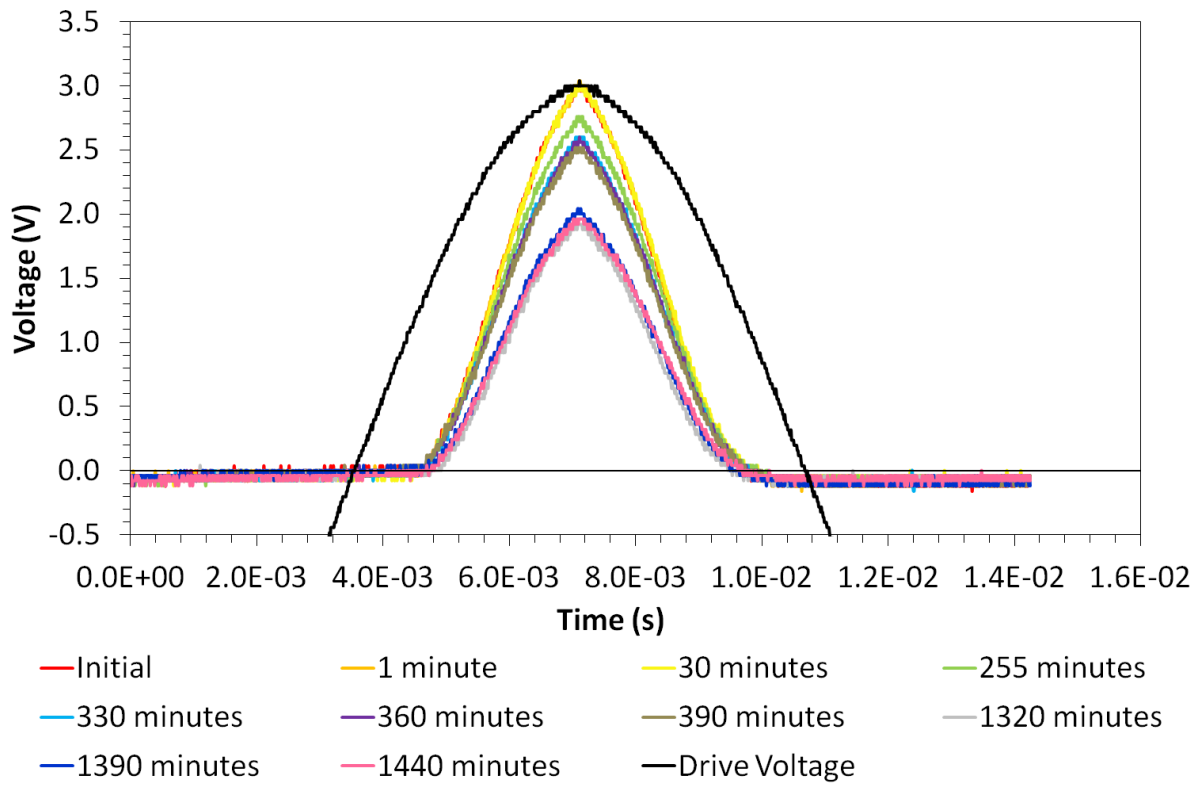


Figure 138. Pentacene 53 TL oscilloscope screen-shots.

From the screen-shots of the transistor, it can be seen that the general trend over time is for the output voltage of the current-to-voltage converter (and therefore the drain current) to drop, which is to be expected as the device degrades. Taking the channel on-resistance of the peak of each of the curves it is possible to create a plot that shows the evolution of the channel on-resistance over time, as shown in **Figure 139**.

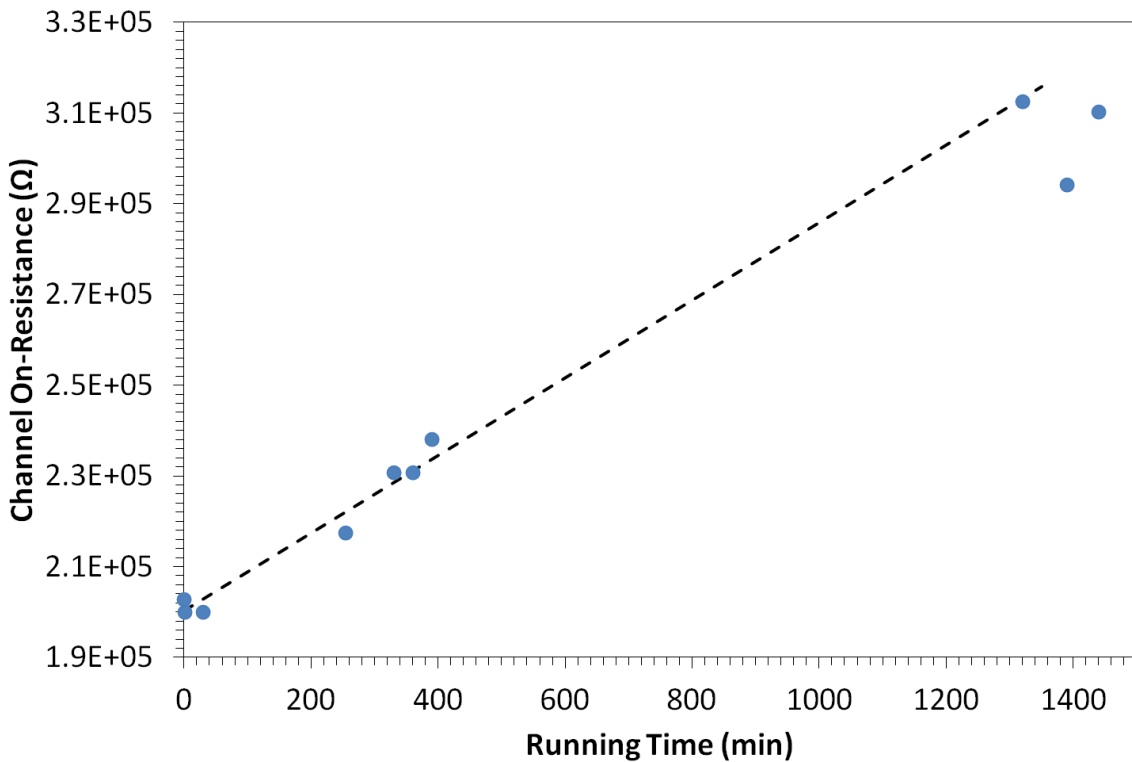


Figure 139. Pentacene 53 TL on-resistance vs. time plot.

It can be seen from **Figure 139** that after a small initial drop, the resistance steadily climbs for the first 390 minutes; when tested again after 1320 minutes the device was found to have continued the same trend gaining on average 85.6Ω every minute, this corresponds to an increase of 0.04% of initial per minute (2.57% per hour). However the next data points do not follow the trend, as the data points up to 390 minutes were taken over one day and the points from 1320 onward were taken the following day, perhaps the unusual behaviour shown by these points is a consequence of a sensing response to an airborne chemical brought into the lab on the second day.

Typically changes seen in channel on-resistance from vapour sensing experiments are at the very least of the order $10k\Omega$, which from **Figure 139** seem to occur over a period of more than 100 minutes due to aging effects alone in ambient atmosphere; so in the nitrogen environment used for sensing experiments this time-scale will be even larger meaning that aging effects are negligible to sensing experiments under nitrogen and only a minor inconvenience to experiments performed under ambient atmosphere. However, for practical real world sensors some kind of moisture removal would need to be built into

sensors and the use of protective sensitiser layers may prolong the life of the sensors as well as increasing performance.

5.3 N-Type Organic Field-Effect Transistor Vapour Sensors

As the responses of p-type organic semiconductors to a variety of analytes had now been characterised it was decided that the response of an n-type material should be investigated. The material chosen was the low molecular weight n-type material PDI8-CN₂ (*N,N'*-bis (*n*-octyl)- dicyanoperylene-3,4:9,10-bis(dicarboximide)) (see section 1.2.2.1.2) from Polyera corporation as the material has an unusually high LUMO level, meaning that gold contacts can be used to efficiently inject carriers into the material (see section 1.1.1). The device architecture used, therefore, is almost identical to that of the pentacene devices discussed previously (section 5.2.1), with SiO₂ topped Si wafers acting as the substrate, a 100nm Al gate, ~6.5nm Al₂O₃ gate insulator, OTS surface modification, a thermally evaporated ~60nm organic semiconductor layer and top 50nm Au source-drain contacts with a 10μm channel.

5.3.1 Transistor Characteristics

The PDI8-CN₂ transistors were characterised as described in sections 2.6.1 and 2.6.2 using $V_{D, Max} = V_{G, Max} = 3V$ and $V_{G, Min} = 0V$. The output and transfer characteristics of the three transistors used in vapour sensing experiments are shown in **Figure 140**, **Figure 141** to **Figure 142**.

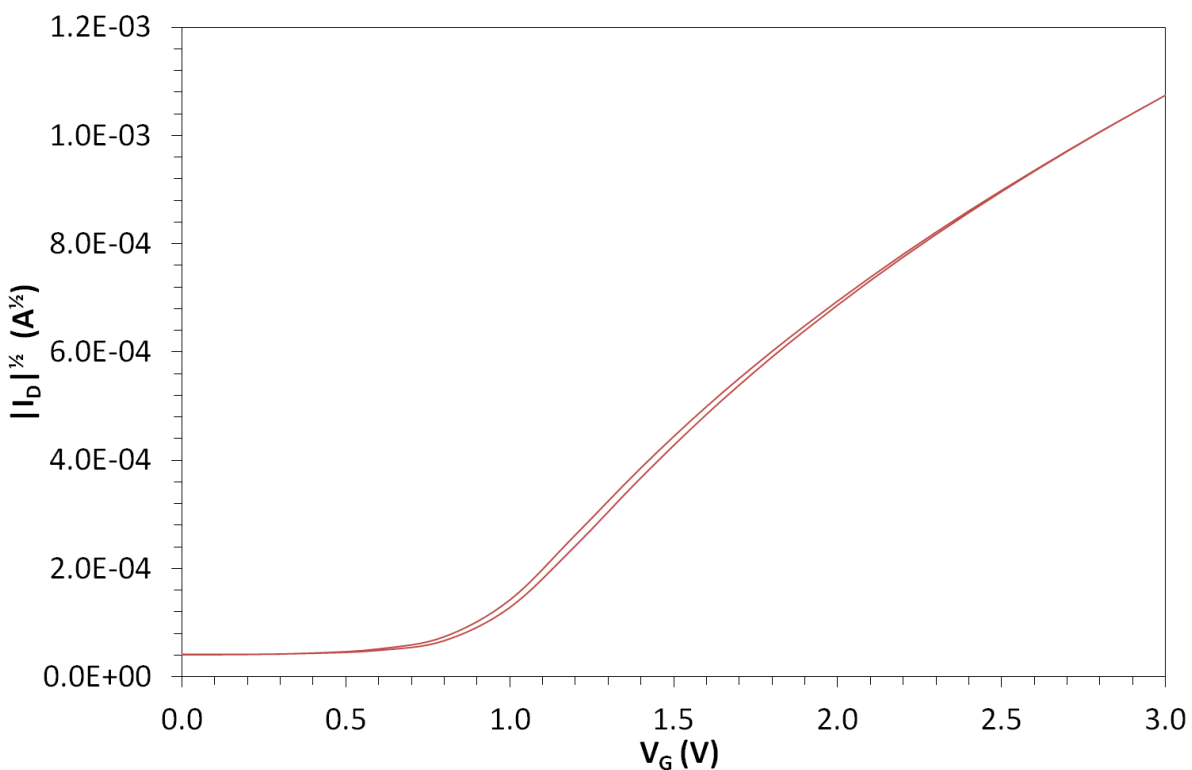
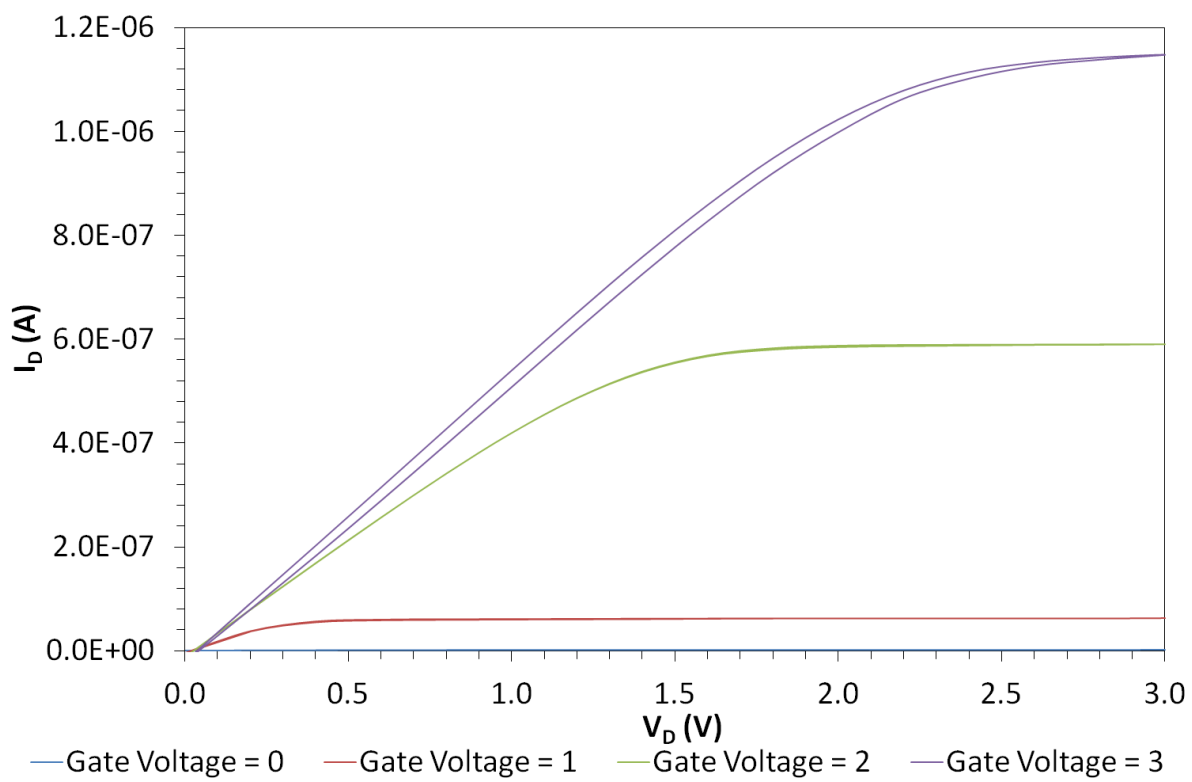


Figure 140. PDI8-CN₂ 1 TL output and transfer characteristics.

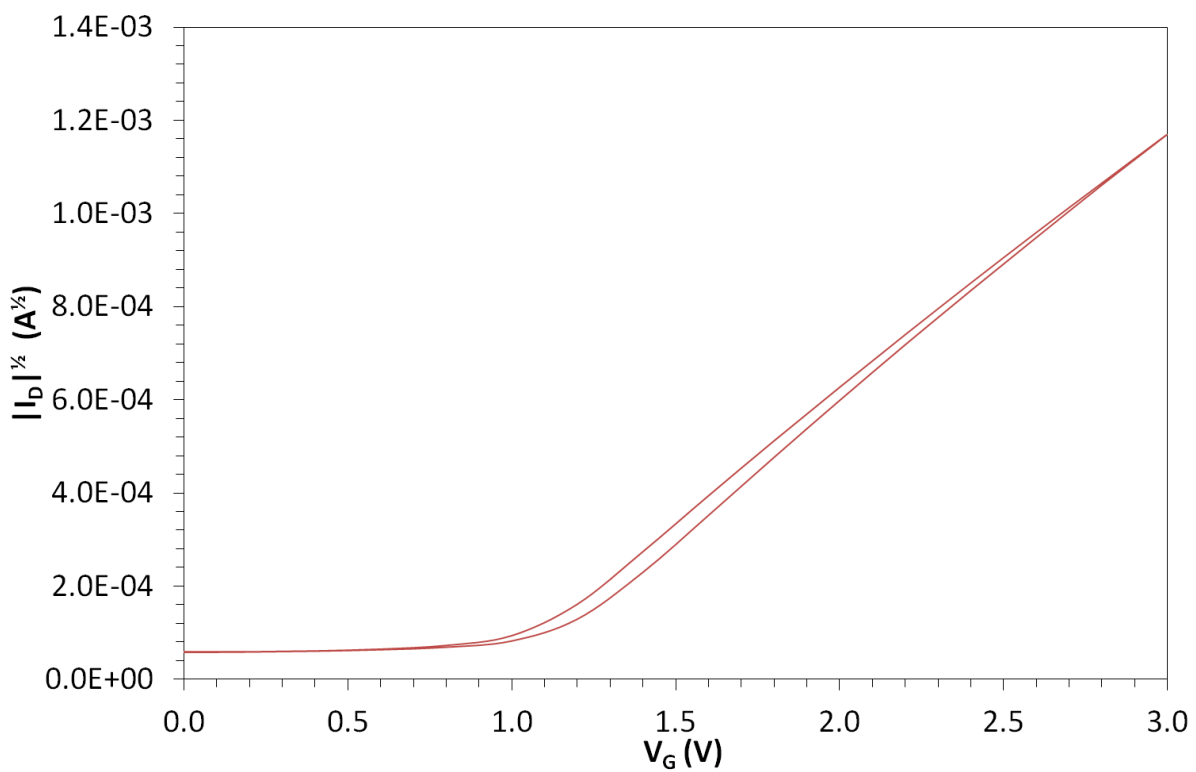
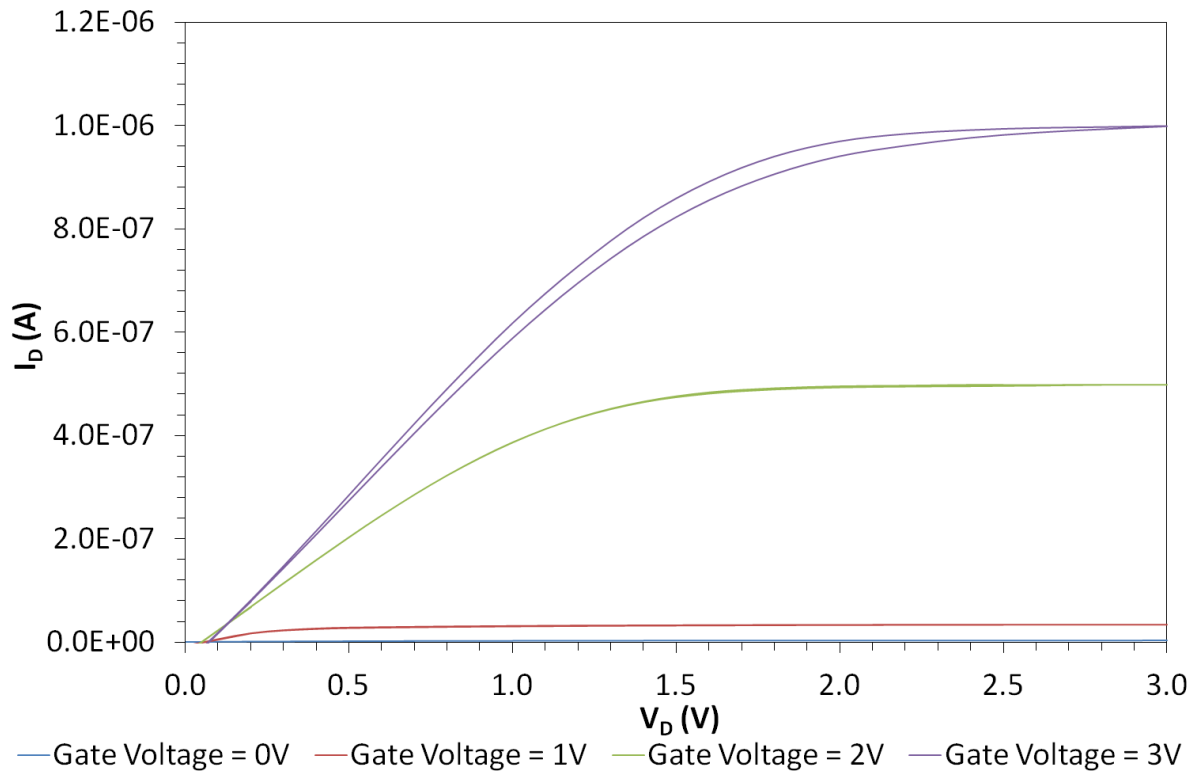


Figure 141. PDI8-CN₂ 4 BR output and transfer characteristics.

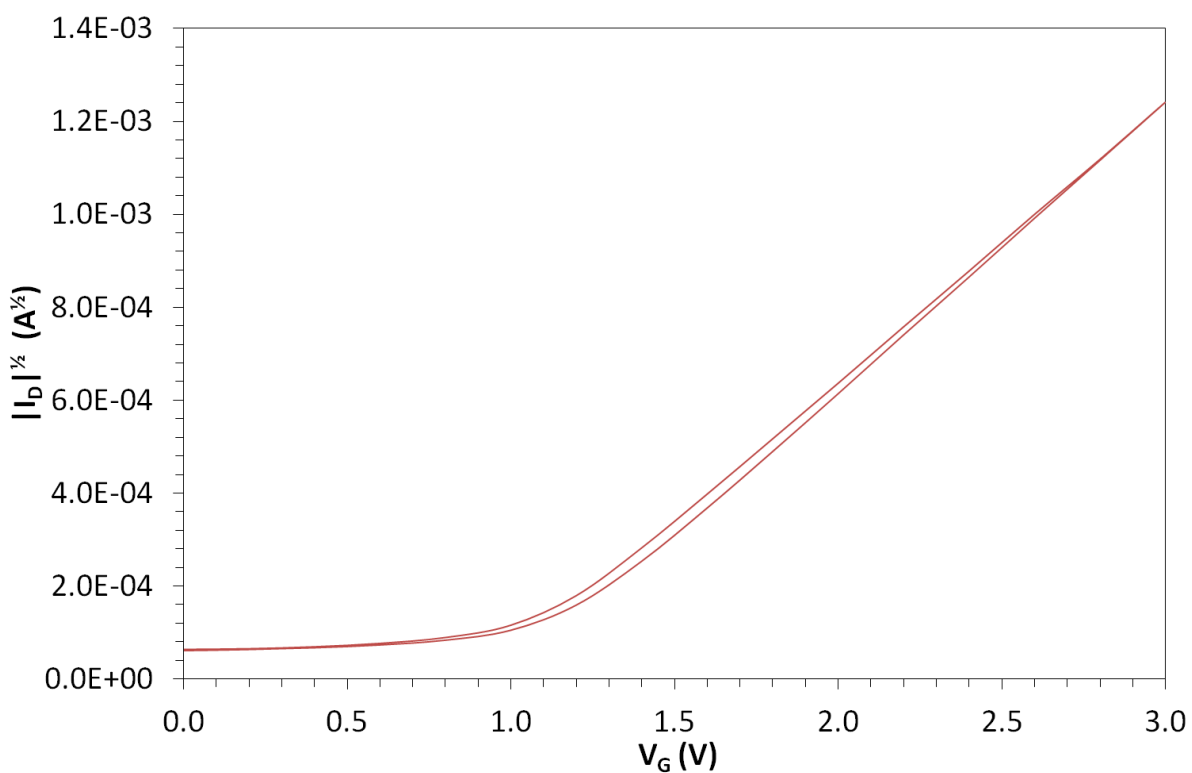
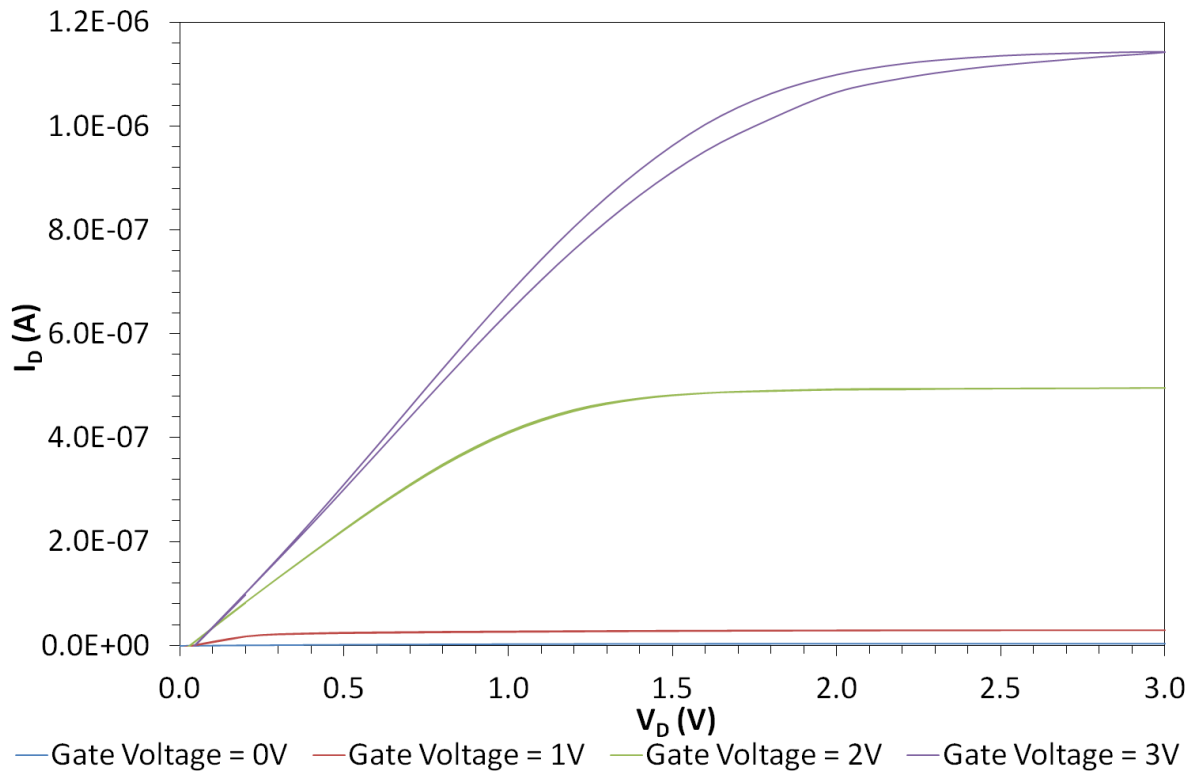


Figure 142. PDI8-CN₂ 6 BL output and transfer characteristics.

Firstly from the output characteristics of the three devices, shown in **Figure 140**, **Figure 141** and **Figure 142**, the presence of hysteresis is immediately apparent in the $V_G = 3\text{V}$ curve of

all three devices. The devices also show a small degree of gate leakage, indicated by the I-V curves beginning at a negative current at $V_G = 0V$. The device PDI8-CN₂ 1 TL shows evidence of a small amount of doping as the $V_G = 3V$ curve does not completely saturate at V_D approaching 3V. The transfer characteristics again show a small amount of hysteresis for all the devices, but whereas PDI8-CN₂ 4 BR and PDI8-CN₂ 6 BL show a high degree of linearity, PDI8-CN₂ 1 TL begins to curve at higher V_G again indicating the doping present in this device. All three of the devices also show a non-zero starting current, yet another indicator of doping. The carrier mobilities, threshold voltages, peak currents and channel on-resistances of the devices are detailed in **Table 4**.

OFET	μ (cm ² V ⁻¹ s ⁻¹)	V_T (V)	Peak I_D (A)	R_{on} (Ω)
PDI8-CN ₂ 1 TL	(5.76±0.23)x10 ⁻³	0.88±0.03	1.15x10 ⁻⁶	2.60x10 ⁶
PDI8-CN ₂ 4 BR	(5.83±0.07)x10 ⁻³	1.14±0.02	1.37x10 ⁻⁶	2.19x10 ⁶
PDI8-CN ₂ 6 BL	(6.15±0.05)x10 ⁻³	1.16±0.01	1.54x10 ⁻⁶	1.95x10 ⁶

Table 4. Mobility and threshold values for PDI8-CN₂ OFETs.

The values of mobility and threshold calculated for the PDI8-CN₂ 1 TL was taken using an extrapolation of the small linear region at the start of the rise seen in the transfer characteristics.

5.3.2 Amine Sensing Results

The vapour sensing experiment was carried out using the techniques and equipment described in section 3.2 and the transistor was monitored using the current-to-voltage converter, as described in section 3.1.1. As with the pentacene transistors the PDI8-CN₂ devices were also to be exposed to octylamine to allow comparisons to be made between the p-type and n-type responses to this analyte. As mentioned in section 1.2.1.4 an amine was chosen as the analyte due to the importance of amines in identifying food freshness; as the proteins in food break down they begin to produce amines, so the freshness of the food can be evaluated through monitoring the amine levels within the food. The device PDI8-CN₂ 1 TL was used in an exposure cycle identical to the one used for Pentacene 21 TL in section 5.2.1.3.3, with two minute exposure windows to 1% saturated octylamine (1% of nitrogen to the bubbler, with the bubbler immersed in ice water) followed by three minute recovery

phases; as stated previously the theoretical concentration of octylamine at 100% saturation is 354ppm at 0°C. The results of this exposure can be seen in **Figure 143**.

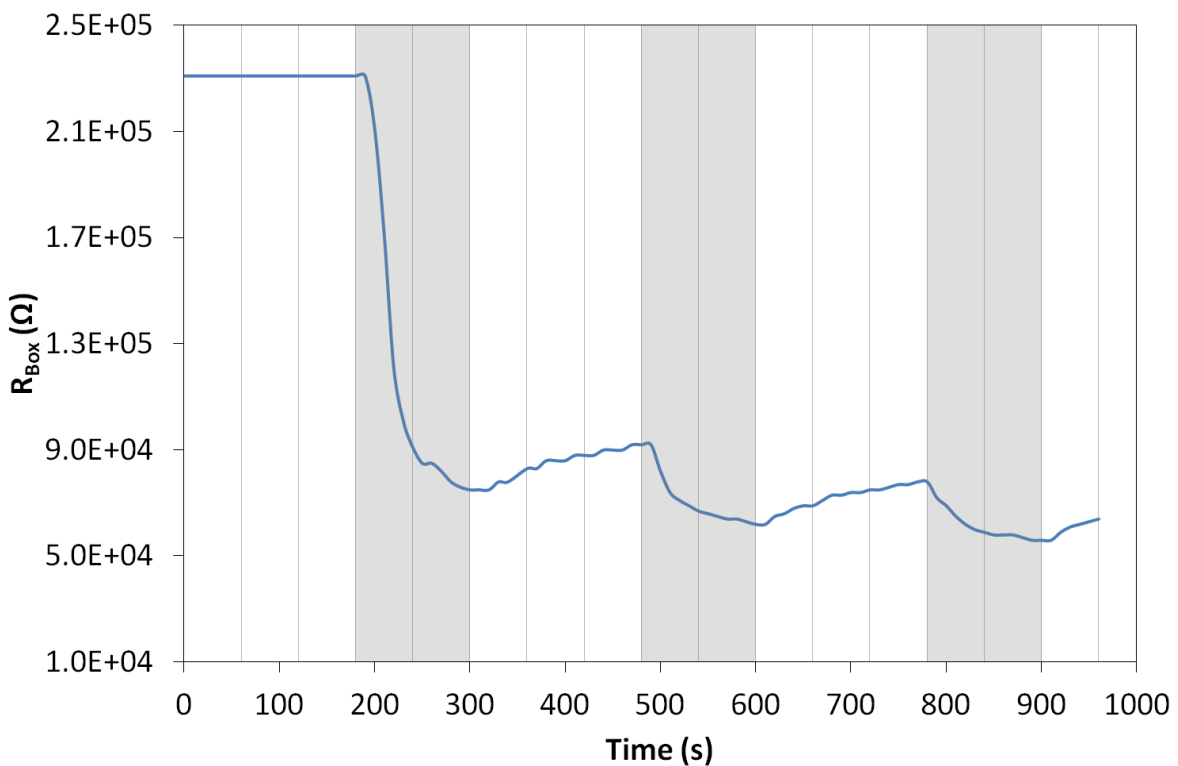


Figure 143. PDI8-CN₂ 1 TL 1% octylamine sensing cycles. N.B. grey shaded areas indicate analyte exposure.

From **Figure 143** it can be seen that initially the channel on-resistance of the device is very stable, a good attribute in a potential sensor, after which an impressive 1.56MΩ (68% of pre-exposure) drop is observed during the two minutes of 1% saturated octylamine vapour exposure; this response shows a strong interaction between the analyte and the PDI8-CN₂ semiconductor, an interaction which it appears is reversible as evidenced by the slow recovery shown in the three minute recovery phase following the initial exposure. Subsequent exposures to 1% saturated octylamine resulted in much more subdued, but still significant, reductions in channel on-resistance of 300kΩ (33%) for the second exposure and 220kΩ (28%) for the third; but recovery is seen after each of the exposures, hinting that PDI8-CN₂ has at least some suitability as a sensor material.

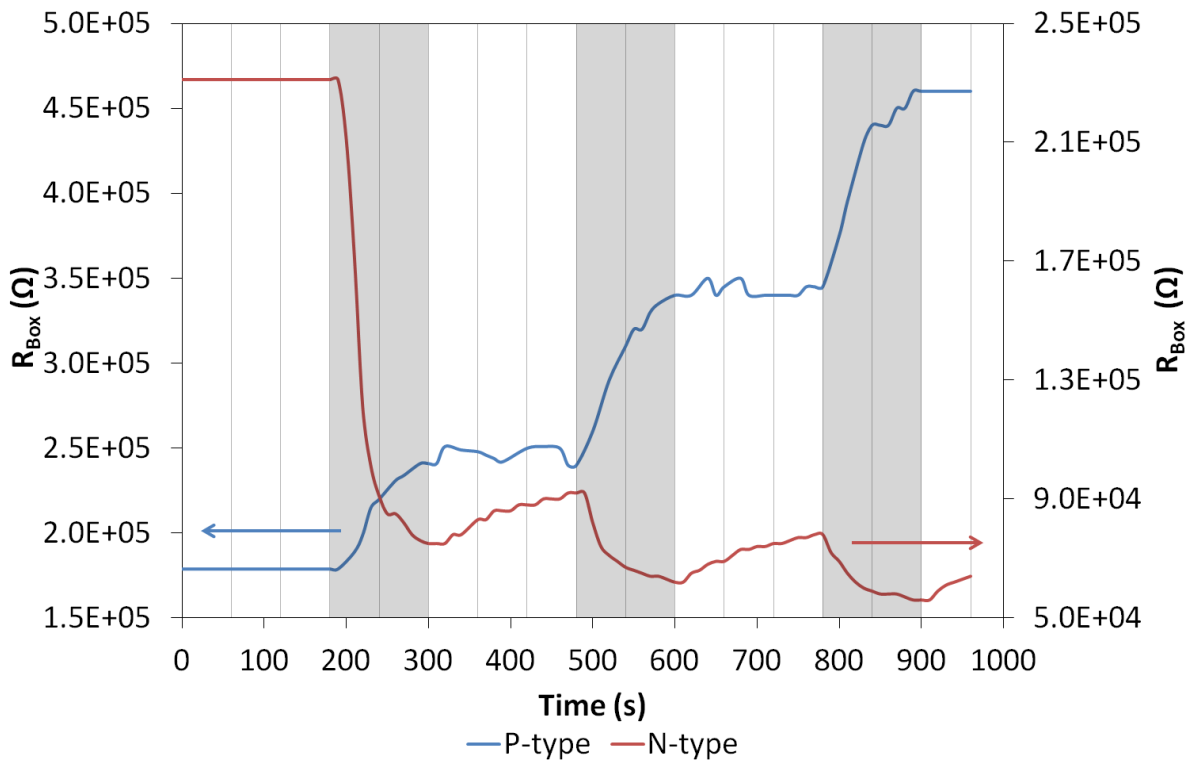


Figure 144. Pentacene 21 TL vs. PDI8-CN₂ 1 TL 1% octylamine sensing. N.B. grey shaded areas indicate analyte exposure.

Comparing the responses of a pentacene device (Pentacene 21 TL) and a PDI8-CN₂ device (PDI8-CN₂ 1 TL), as in **Figure 144**, it can be seen that the responses of these devices are the opposites of each other: exposure to octylamine causes the channel on-resistance of pentacene to increase, while it causes the channel on-resistance of PDI8-CN₂ to decrease. The resistance changes being dealt with here are for the most part an order of magnitude apart the percentage changes in the second and third exposures are within 10% of each other for both devices. In contrast to the pentacene device, however, the PDI8-CN₂ device shows a much larger initial response to octylamine and shows the ability to recover from the exposure. In contrast to the p-type pentacene, the n-type PDI8-CN₂ seems to become doped by the amine.

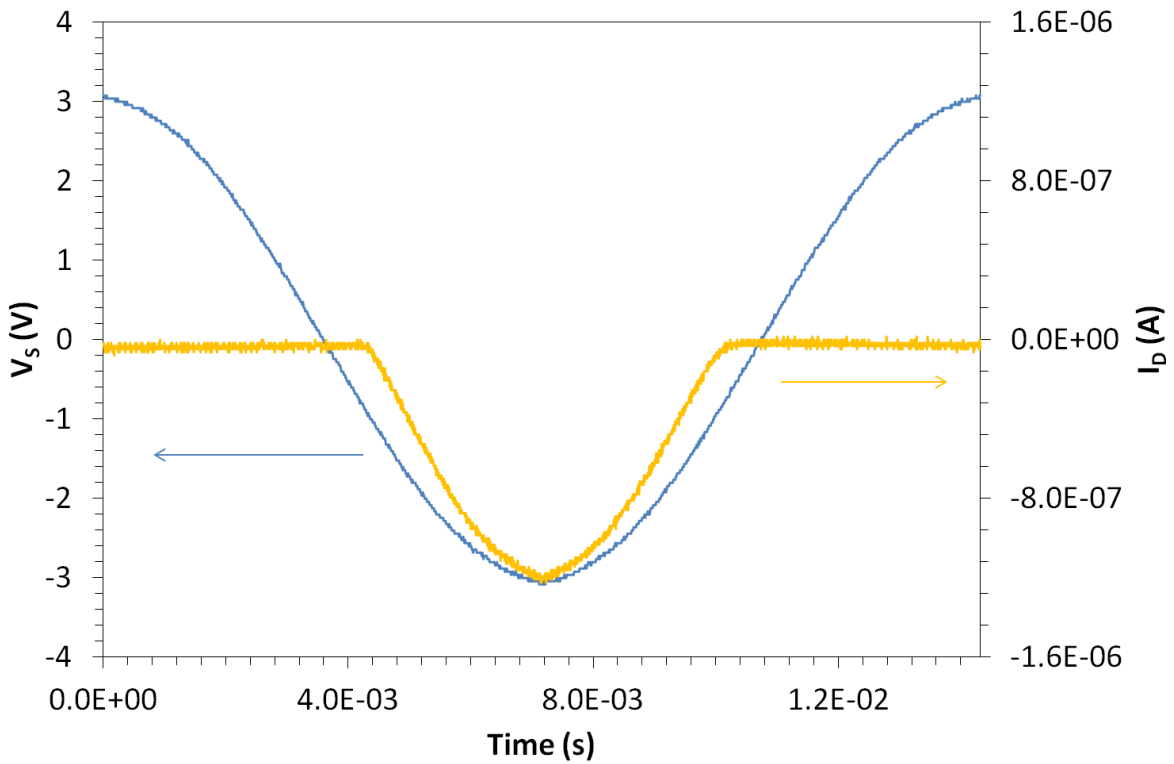


Figure 145. PDI8-CN₂ 1 TL screenshot before 1% octylamine sensing.

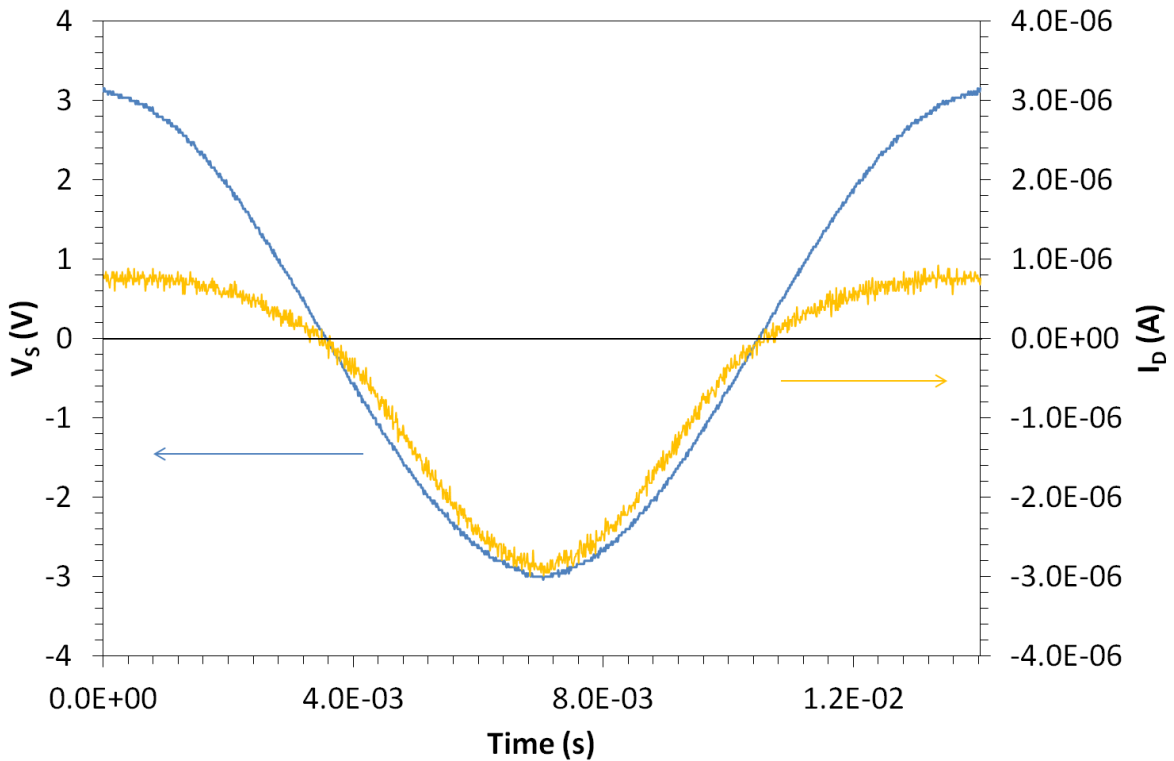


Figure 146. PDI8-CN₂ 1 TL screenshot after 1% octylamine sensing.

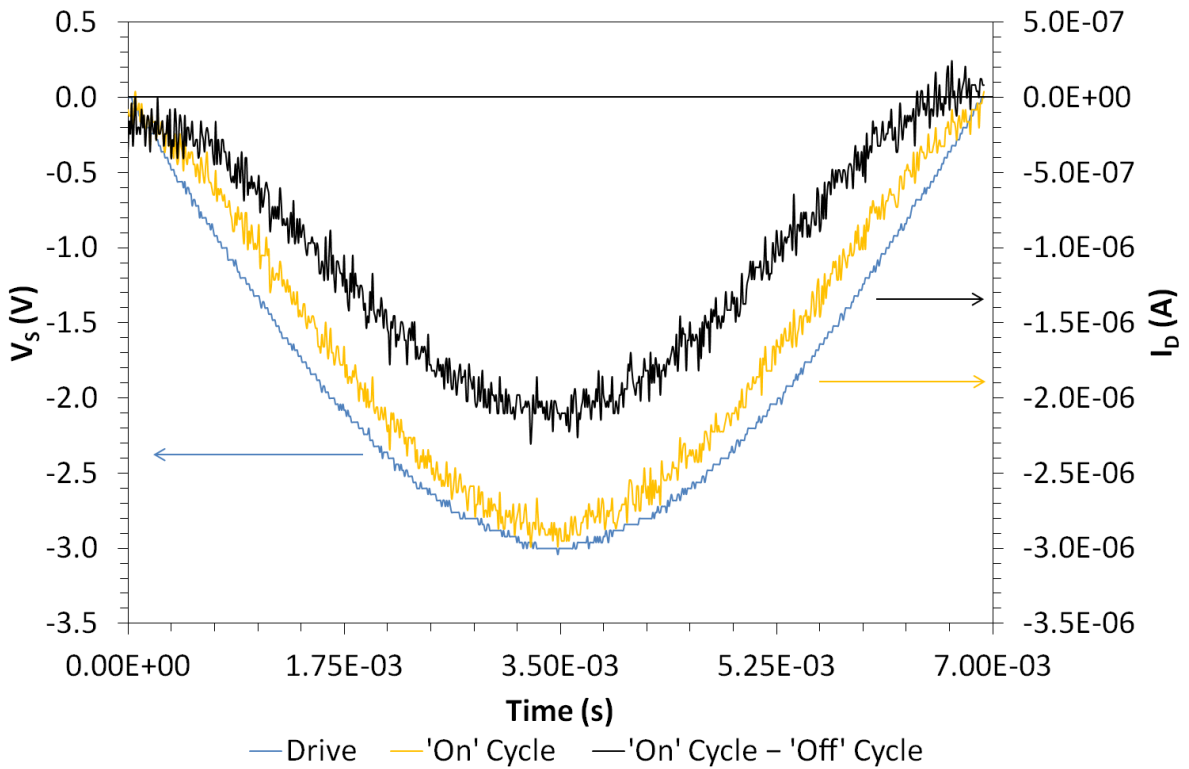


Figure 147. PDI8-CN₂ 1 TL screenshot and ‘off’ cycle subtraction directly after 1% octylamine sensing.

It can be seen in the current to voltage converter output before exposure (shown in **Figure 145**) that the device shows near zero off-current, while after exposure significant doping is displayed by the device, evidenced by the sinusoidal off current (see **Figure 146**). In an attempt to differentiate between the field-effect current and doping current a subtraction of the off-cycle data has been performed on the data from the on-cycle, the results of this can be seen in **Figure 147**; it can be seen, by comparing this to the pre-exposure screenshot (**Figure 145**), that the peak drain current due to field-effect alone has nearly doubled, proving that the response to octylamine vapour exposure has an effect on the device beyond purely doping. Due to the basicity of the amine group the logical step to take is that the PDI8-CN₂ is base-doped^[128] in a process analogous to the acid doping experienced by p-type organic semiconductors; this doping most likely occurs at the grain boundaries of the semiconductor, causing enhanced charge carrier transport across the boundaries through the formation of Schottky junctions.

Next the recovery of the PDI8-CN₂ devices was investigated, both under air and under vacuum. Firstly two devices (PDI8-CN₂ 4 BR and PDI8-CN₂ 6 BL) were exposed to 1%

saturated octylamine vapour in two separate two minute exposures separated by a three minute recovery phase; the channel on-resistance of PDI8-CN₂ 4 BR was reduced from 1.84MΩ to 920kΩ, a change of 920kΩ (50%), and the on-resistance of PDI8-CN₂ 6 BL was reduced from 1.02MΩ to 290kΩ, a change of 730kΩ (72%). The devices were then allowed to recover overnight (~16 hours) under different conditions: PDI8-CN₂ 4 BR under a dynamic ~10⁻²Torr vacuum and PDI8-CN₂ 6 BL under ambient atmosphere. Upon testing the next day the device left in vacuum had recovered by 260kΩ, 28% of the change; however the device left in ambient atmosphere had recovered by 720kΩ, 99% of the change. It seems then that some feature of the ambient environment enhances the recovery of the devices, perhaps the presence of light or some component of the atmosphere that octylamine preferentially interacts with, such as moisture or carbon dioxide. This property of the organic semiconductor with respect to octylamine does increase its suitability as a sensor material.

5.4 **Nano-Particle Based Chemi-Resistor Vapour Sensor**

In addition to the sensing carried out using organic field effect transistors, sensing was also attempted using chemi-resistor samples fabricated from custom synthesised uncoated Au nano-particles. The nano-particles were prepared by the University of Manchester's chemistry department using a controlled reaction between chloro-triphenylphosphinyl gold(I), sodium hydroxide and tetrakishydroxymethyl-phosponium chloride and the properties of the water-toluene interface;^[95] a film of the nano-particles was then dip-coated onto a mica substrate, before a pair of Au electrodes were evaporated onto the sample. The electrodes were 50nm thick with a separation of 1mm along a side 2mm long.

The sensing was performed using a square wave generator circuit (see section 2.6.4) with the sample taking the place of one of the resistors that determines the frequency of the square wave produced, in this configuration the frequency is proportional to the inverse of the sample resistance. The sample was exposed to octylamine in two concentrations, firstly three minutes of 10% saturated vapour (10% of nitrogen to the bubbler, submerged in ice-water) followed by nine minutes of 50% saturated vapour (50% of nitrogen to the bubbler,

submerged in ice-water); as stated previously the theoretical concentration of octylamine at 100% saturation is 354ppm at 0°C. The results of the exposure can be seen in **Figure 148**.

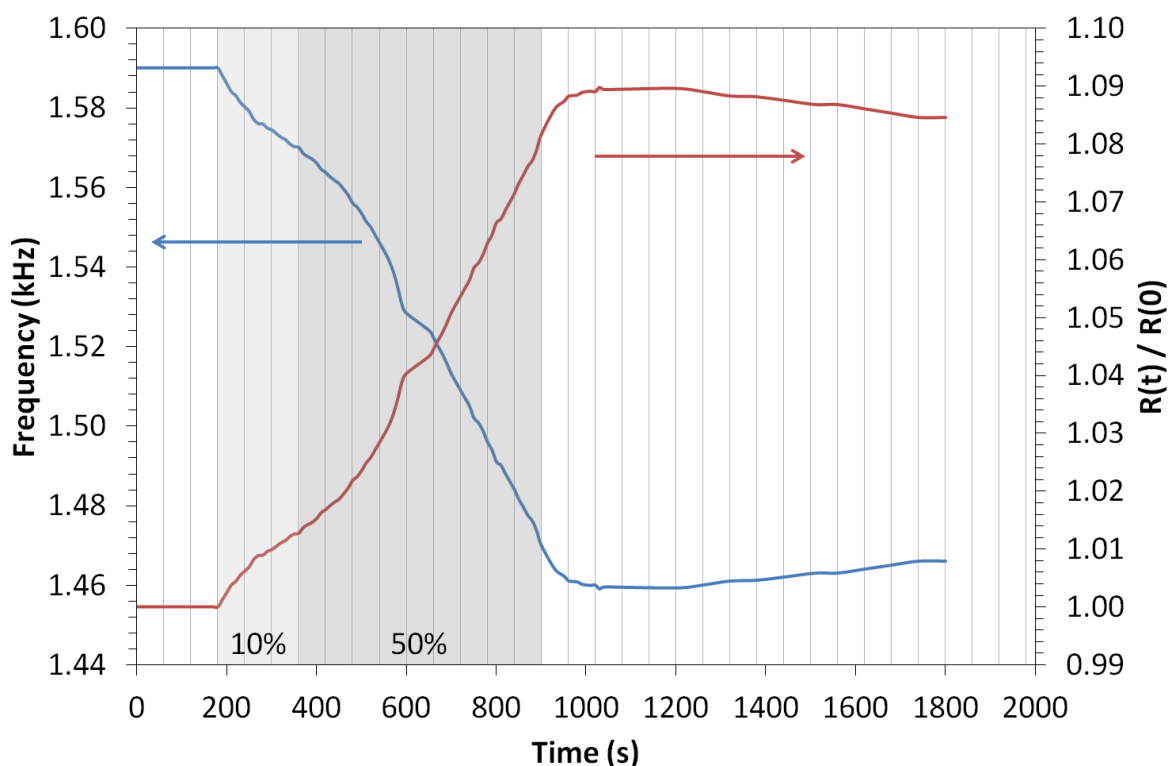


Figure 148. Nano-particle octylamine sensing results ($R(0) = 60\text{k}\Omega$). N.B. grey shaded areas indicate analyte exposure.

From **Figure 148** it can be seen that the three minutes of 10% saturated vapour exposure elicited a change of 20Hz in the square wave frequency corresponding to a change in resistance of 1.27% of the original value. The first three minutes of 50% saturated vapour exposure produced a 24Hz change in frequency (1.57% of $R(0)$ change in resistance), while the second and third sets of 3 minute exposure produced changes of 37Hz (2.52% of $R(0)$ change in resistance) and of 39Hz (2.80% of $R(0)$ change in resistance) respectively; meaning a total change of 100Hz and therefore 6.89% of $R(0)$ during the whole nine minutes.

The change in resistance caused by the amine exposure can be explained by the affinity of amine groups to bond to gold surfaces,^[126] each nano-particle will slowly become surrounded in shell of alkane chains bonded via the amine head-group, meaning that the resistance will increase due the added insulating layer and increased intermolecular separation (see section 1.2.2.4).

6

An Aqueous Sensing Platform Using Organic Field-Effect Transistors

The devices used in this chapter were made in collaboration with Dr. Delia Puzzovio and all the data was also collected in collaboration with Dr. Delia Puzzovio.

The work described so far has concentrated on sensing airborne vapour phase analytes, but could the devices described previously form part of a system capable of sensing analytes in an aqueous medium?; as described in section 1.3.1.3.1 a transistor can use an electrolyte as the gate medium due to the formation of the high capacitance electric double layer at the electrolyte / semiconductor interface, it has been shown by Kergoat *et al* that it is also possible to use water as the gate medium.^[70] Previous studies have described problems such as electrochemical doping and slow frequency response when using electrolyte gated devices,^[129, 130] here is described an attempt to address such issues and to systematically optimise performance of water gated devices towards the development of an aqueous sensing platform.

6.1 Water Gated Pentacene Based Organic Field-Effect Transistors

In keeping with the work carried out previously, pentacene was chosen as the first material to be used as the semiconductor in a water gated OFET device. The device architecture used was similar to that of a chemi-resistor: a set of 50-60nm thick Au source-drain contacts deposited onto a glass substrate before the pentacene semiconductor was evaporated on top to a thickness of 50nm. Once complete the device had the 2 μ L droplet of water placed onto its channel and contacts were made to the source, drain and into the top of the water droplet using tungsten contact needles. Unfortunately the devices, upon testing, did not show transistor behaviour, rather the output current trace matched the input voltage, indicating the current leaking through the water in the form of an ionic current. This is most likely due to water passing through the grain boundaries of the pentacene and making

contact with the source and drain electrodes beneath. For this reason single crystals or polymeric materials may be more suitable for this application.

6.2 Water Gated Poly(3-hexylthiophene-2, 5-diyl) Organic Field-Effect Transistors

To eliminate the grain boundaries seen in low molecular weight materials, it was decided to use the p-type polymer P3HT (Poly(3-hexylthiophene-2, 5-diyl)) (Sigma-Aldrich, $M_n = 30,000 - 60,000$). P3HT is a well documented and widely used p-type organic semiconductor^[44, 131] and its degradation under air is highly dependent on the solvent it is spin-coated from;^[132] high boiling point (low vapour pressure) solvents allow a more ordered and close packed film to be produced increasing the device lifetime. With this in mind 1,2-Dichlorobenzene was chosen as the solvent for the water gated devices. The device architecture used was similar to that of the pentacene device mentioned in section 6.1: a set of 50-60nm thick Au source-drain contacts deposited onto a glass substrate before the P3HT semiconductor was spin-coated on top from a $10\text{mg}\cdot\text{mL}^{-1}$ solution at 2000rpm for 1 minute; samples were dried under 10^{-2}Torr vacuum at 40°C for one hour after spinning. Once complete the devices had the $2\mu\text{L}$ droplet of water placed onto their channel and contacts were made to the source, drain and into the top of the water droplet using tungsten contact needles. The upper limit of voltage which can be applied across the devices is 1.23V, as this is the voltage at which electrolysis begins in the water; it was decided, therefore, to choose a voltage well away from 1.23V as the test voltage maximum value, preliminary testing suggested that 0.8V would be sufficient to allow the devices to switch-on but not break down the water.

It is important to mention at this point that two different mechanisms can act upon water (electrolyte) gated OFETs to produce an increase in conduction properties; the first is discussed in section 1.3.1.3.1 and involves the formation of electric double layers within the water, in effect turning the water into a high capacitance gate medium and causing conduction improvement through field-effect enhancement, as in a regular OFET; the second mechanism is the one that occurs in an organic electro-chemical transistor (OEET).^[133] The action of the gate electrode causes ions in the electrolyte to diffuse into the OEET and dope the semiconductor film, improving conduction. In the water gated OFETs

the first mechanism is desirable whilst the second is not, therefore steps must be taken to prevent electro-chemical doping of the film. It is possible to disentangle the two effects from each other when observing a device driven by a square wave voltage, the field-effect contribution to the current is typified by a relatively fast increase in drain current when the device is switched on; while the electro-chemical doping current requires a finite time to build up while the ions diffuse into the semiconductor, resulting in a gradual rise in drain current over tenths of seconds.

The first question to answer in the development of the sensing platform was that of which frequency to drive the OFETs at during testing. Due to the architecture of the devices there will be a large overlap of the water droplet and the source/drain electrodes creating a parasitic capacitance that must be charged/discharged when the voltages applied to the system change, the EDL also takes a finite time to form;^[134] it would therefore be practical to use a very low frequency to reduce the significance of the parasitic capacitance, 1Hz was chosen to allow a full sweep to be performed every second. Next the type of water used in the device had to be chosen, the obvious choice would be DI water to make sure the water was as free of any kind of contaminant as possible. But in its “real world” application the device would be required to sense an analyte from within fresh water taken from natural sources, it was therefore decided to test two devices alongside one another; the first device would have a droplet of DI water and the second ordinary tap water, the results of this experiment are shown in **Figure 149**, with the device P3HT 18 BL as the DI water sample and P3HT 10 BR as the tap water sample. The electrical testing for all the devices in this chapter were carried out using the current to voltage converter described in section 3.1.1, with a dial-up resistance box (R_{Box}) in the place of R_f . Each device had a drive voltage of frequency 1Hz and magnitude $\pm 0.8V$ (as mentioned above) applied to its source electrode and had its gate electrode on ground, the only difference in the drive voltage is that some of the experiments used a sine wave drive and some used a square wave drive.

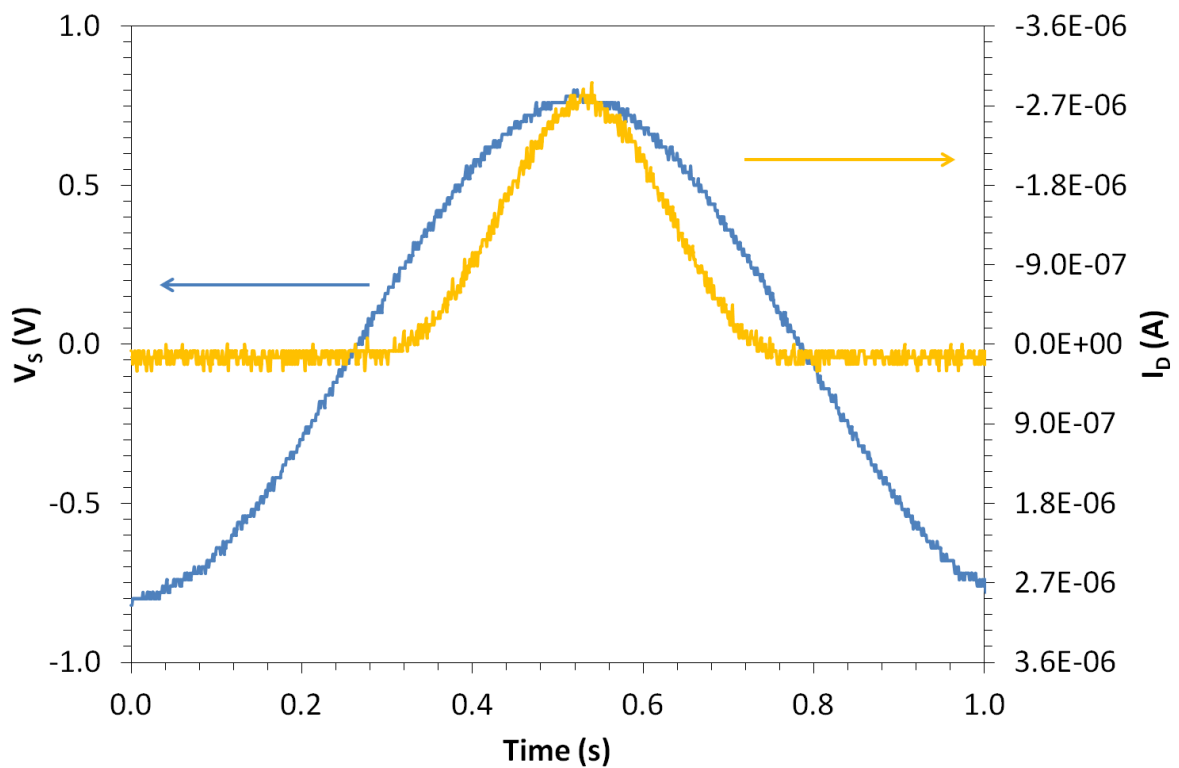
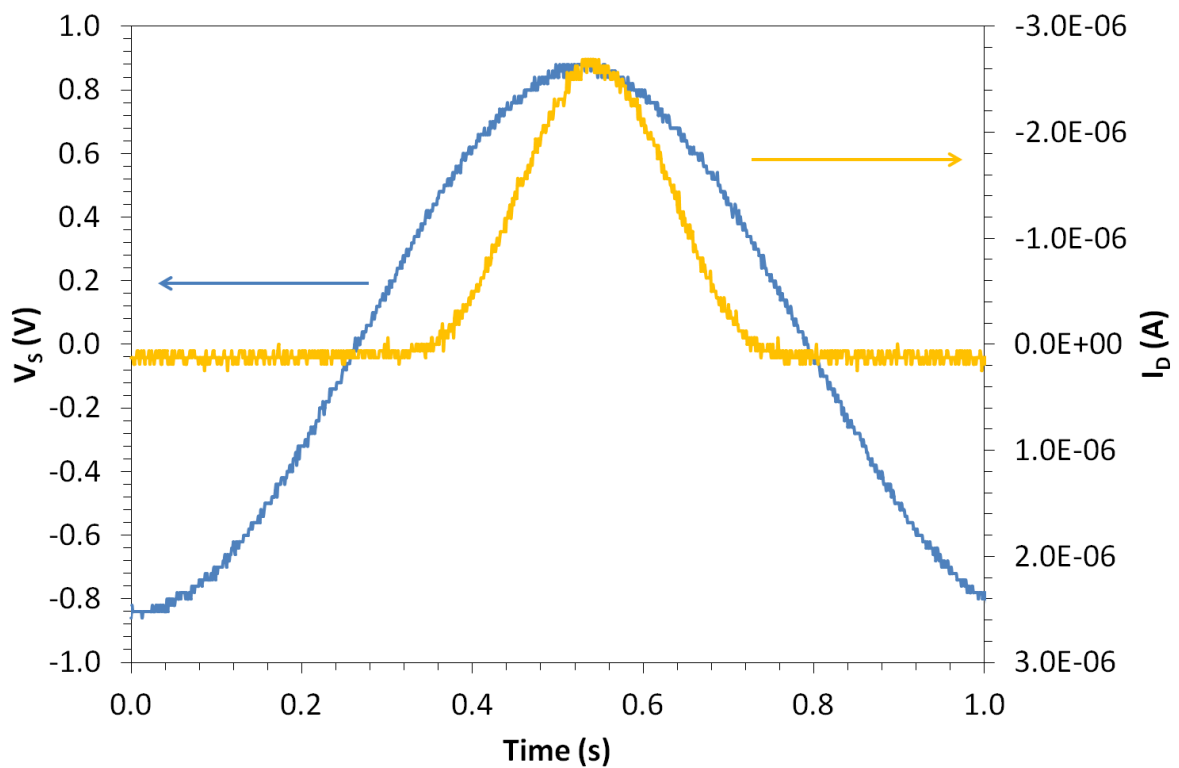


Figure 149. P3HT 18 BL and P3HT 10 BR screenshots, DI (top, $R_{Box} = 27\text{k}\Omega$) vs. tap water (bottom, $R_{Box} = 32\text{k}\Omega$).

From **Figure 149** it can be seen that the difference in device performance as a consequence of using tap water over DI water is minimal, the small differences there are between the two samples may also be more a consequence of differences in the semiconductor layers of the devices rather than the difference in the type of water. When a square wave drive voltage is used for the devices it highlights a problem experienced previously by Inganäs *et al.*^[129] in that the device begins to behave as an organic electro-chemical transistor (OEET) (as discussed above) and a secondary electro-chemical doping current is present alongside the field-effect current, this slow rise could also be partially due to the finite time taken for the EDL to establish. Two further currents that may be seen when using a water gated OFET are those that arise from permanent doping in the semiconductor and ionic currents through the water due to incomplete coverage of the electrodes by the semiconductor. Plots of the device P3HT 10 BR under both sine and square wave drives are shown in **Figure 150**.

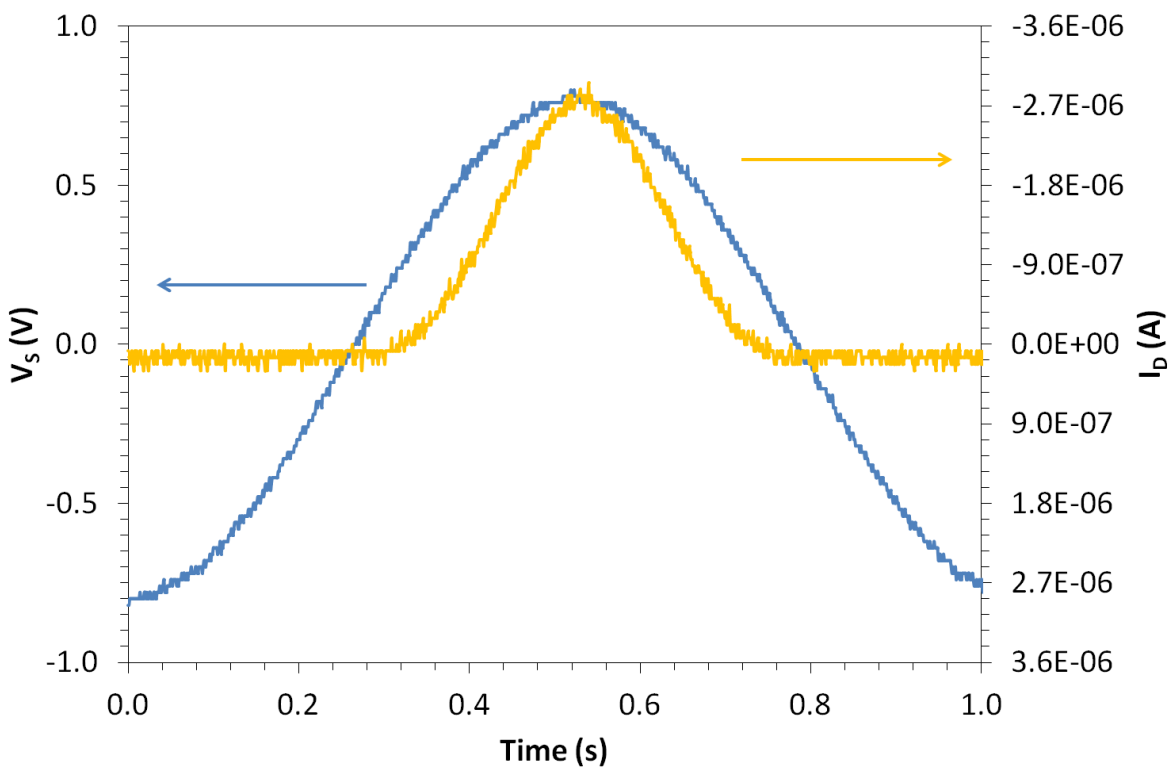
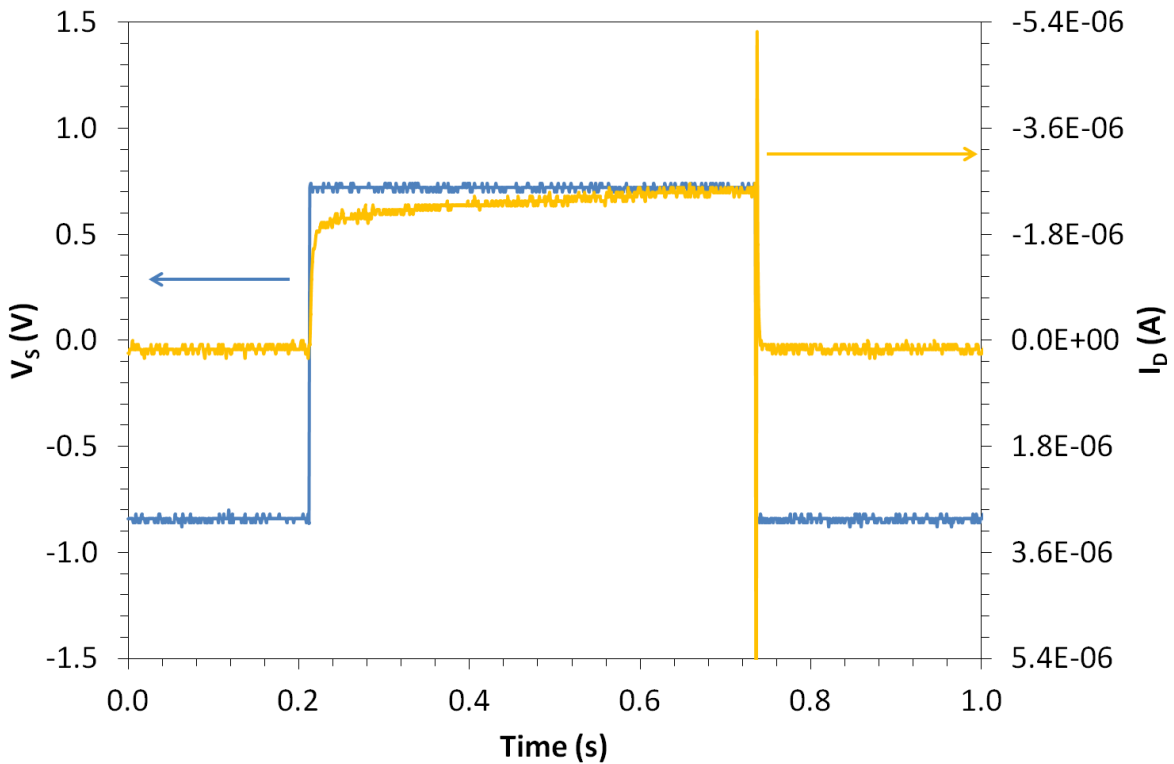


Figure 150. P3HT 10 BR screenshots, square wave and sine driven ($R_{\text{Box}} = 27\text{k}\Omega$).

From the square wave drive shown in **Figure 150** the contributions of both the field-effect and electro-chemical doping currents can be clearly seen; the field effect contribution gives

the initial spike of current as the device switches on, tracking the drive voltage on the plot, after which the inexorable slow rise caused by the gradual build-up of electro-chemical doping current and possibly the formation of the EDL. Clearly to make this a viable sensing technology a method to eliminate the electro-chemical doping current is required, towards this end it was decided to use the same calixarene sensitiser layers used on vapour sensing devices previously (calixarene 1) to act as both sensitisers and a form of encapsulation to block the electro-chemical dopant ions from entering the device. Preliminary experimentation showed that due to the orientation of molecules on the Langmuir trough, dipping an even number of Langmuir-Blodgett (L-B) layers onto the devices caused the upper layer to be the most hydrophobic, meaning the water droplet would not remain in place on the device; the answer, of course, was to use the Langmuir- Schaefer technique instead (see section 2.2.4) as this would cause the most hydrophilic side of the deposited molecules to always face upwards. To minimise the impact on the capacitance of the now composite insulator layer only four L-S monolayers of calixarene were used on devices. As a first attempt to test the principle, four L-S layers of the calixarene 5,17-(34-nitrobenzylideneamino)-11,23-di-*tert*-butyl-25,27-diethoxycarbonyl-methyleneoxy-26,28-dihydroxy-calix[4]arene (calixarene 1, see **Figure 56**) were deposited onto the device P3HT 11 BR. Comparisons of coated and non-coated samples are shown in **Figure 151** under a square wave drive and in **Figure 152** under a sine wave drive.

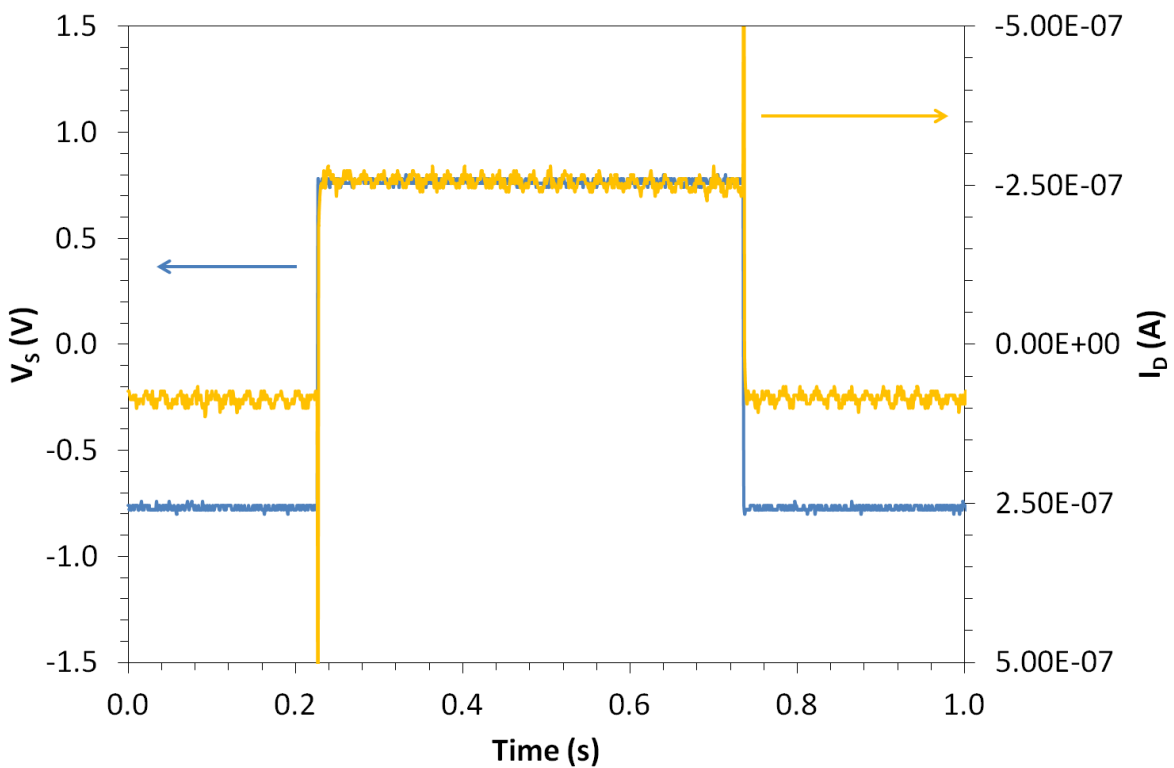
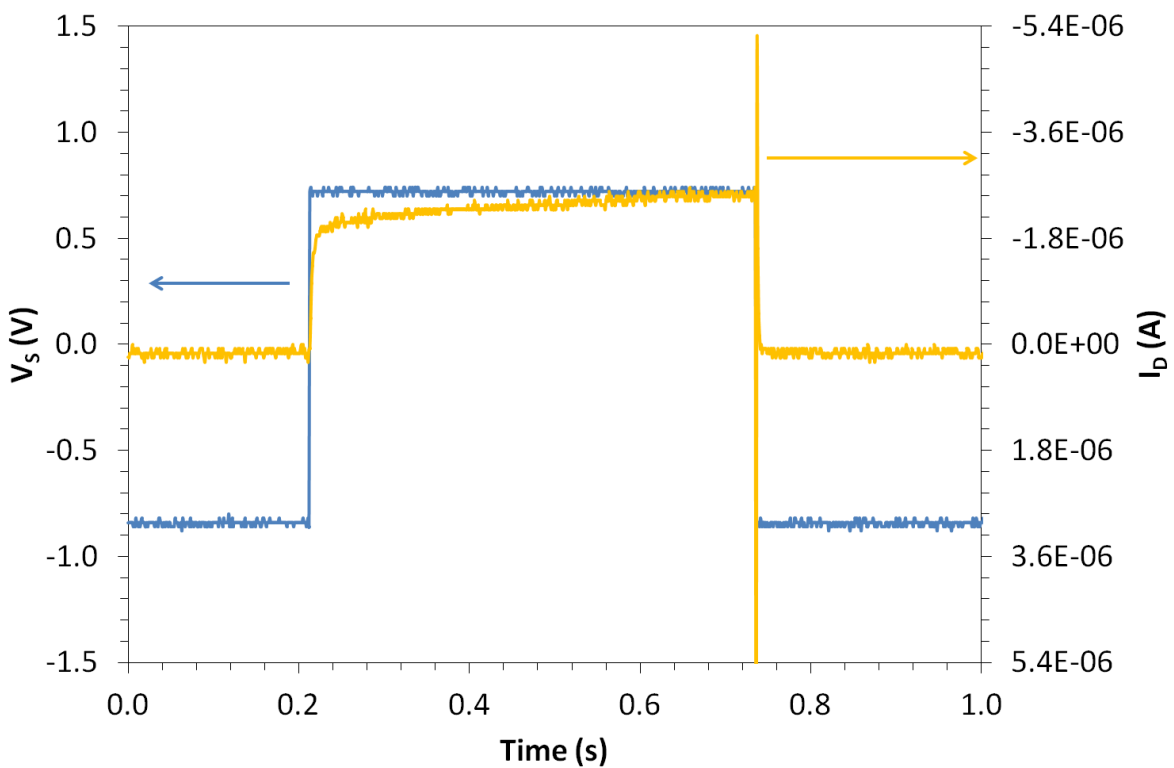


Figure 151. P3HT 10 BR (top, $R_{\text{Box}} = 27\text{k}\Omega$) and P3HT 11 BR (coated) ($R_{\text{Box}} = 300\text{k}\Omega$) screenshots, square wave drive.

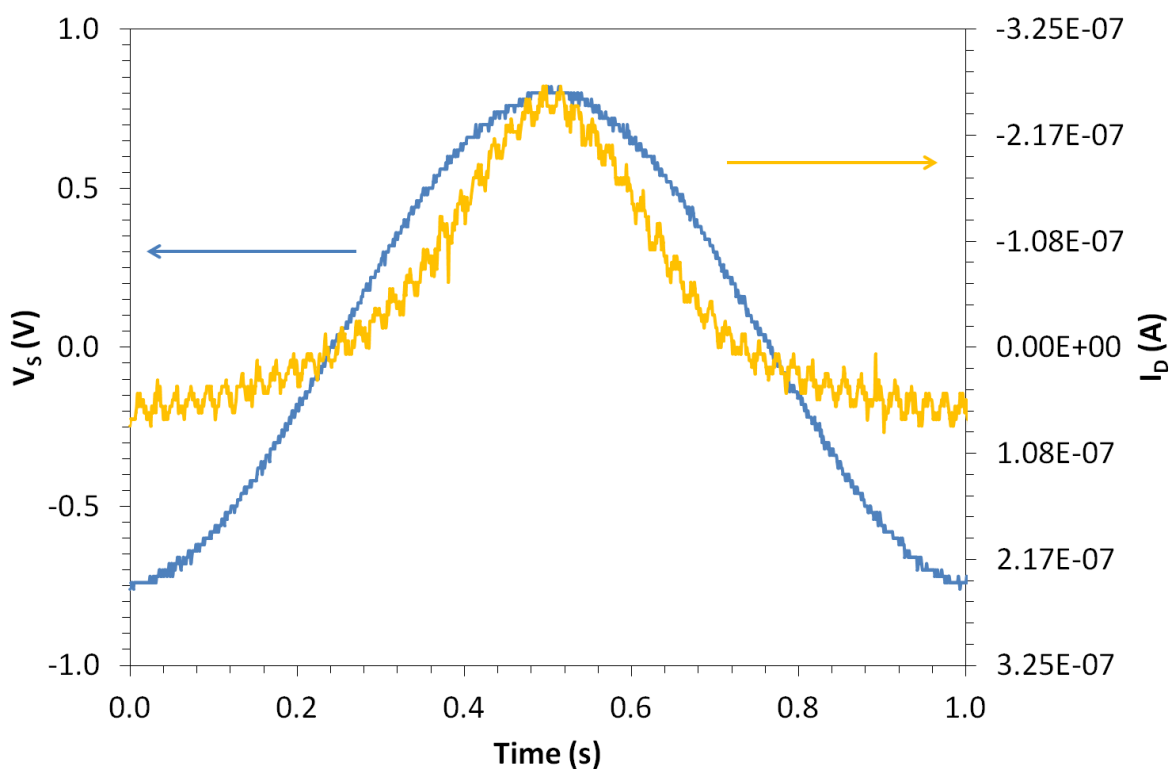
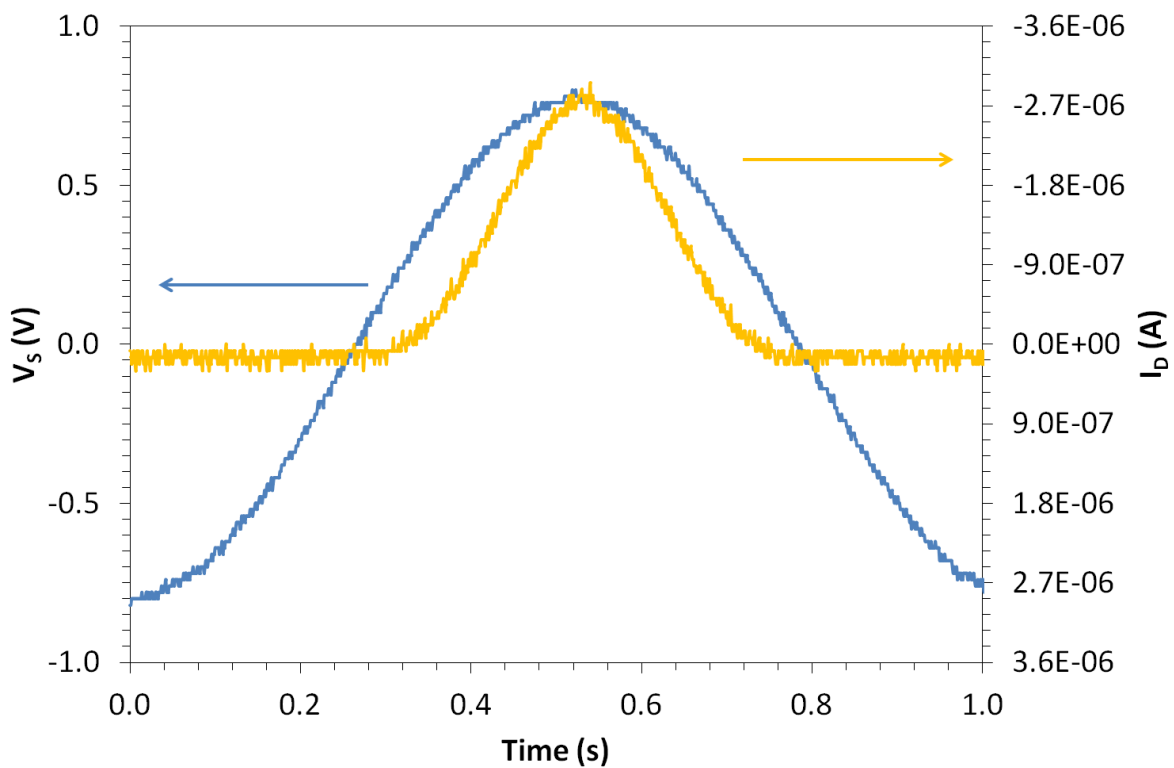


Figure 152. P3HT 10 BR (top, $R_{\text{Box}} = 27\text{k}\Omega$) and P3HT 11 BR (coated) (bottom, $R_{\text{Box}} = 300\text{k}\Omega$) screenshots, sine wave drive.

From the square wave drive (**Figure 151**) it can be seen that the slowly rising component of current seen in the previous square wave driven devices has been eliminated by the addition of the calixarene layers, meaning that this current must have been due to electro-chemical doping and not the formation of the EDL. But the effect of adding these layers is to reduce the current to approximately a tenth it's uncoated value (making 50Hz mains voltage noticeable in the output signal), making the permanent doping and any ionic currents in the water more significant, as evidenced by the more noticeable off-current shown by P3HT 11 BR in both **Figure 151** and **Figure 152**. The cause of this drop in current may be due to the reduction of capacitance of the "insulator" caused by the addition of the calixarene layers, but further measurements and knowledge of the dielectric constant of a monolayer of calixarene 1 would be needed to confirm this. Further work^[135] has shown that the lowest number of L-S monolayers of calixarene 1 that can still prevent OECT behaviour is two, one layer is not sufficient to block the electro-chemical doping current; it was also found that four LB layers of the calixarene 1 not only made it difficult to keep the water droplet over the channel where it was needed, but it also did nothing to prevent the electro-chemical doping of the transistor.

While not an ideal solution to the prevention of OECT behaviour, the sensitiser layer may provide the selectivity needed for this type of device, however, more work is needed to ascertain the effectiveness of the sensitiser layers in this application.

7

Summary Conclusions and Future Work

A summary will now be made of the findings of this thesis, including comparisons and patterns not discussed in previous chapters. This section will begin with the platinum core porphyrin materials used in the sensing work, PtOEP (platinum (II) octaethyl porphyrin) and PtEP-I (Etioporphyrin-I); both PtOEP and PtEP-I have been successfully used as organic semiconductors in their own rights, producing devices with carrier mobilities of the order $10^{-4}\text{cm}^2\text{V}^{-1}\text{s}^{-1}$ and threshold voltages around -1V. PtOEP showed a response to both IPA (albeit a slightly delayed response) and to acetone vapours, it was also used to successfully enhance the response of a pentacene OFET to ethylene vapour when used as a sensitiser layer. PtEP-I was used to attempt to sense propylamine vapours but unfortunately showed no significant response.

The un-sensitised (uncoated) p-type pentacene OFETs (with Au contacts) made for this work had carrier mobilities of the order $10^{-2}\text{cm}^2\text{V}^{-1}\text{s}^{-1}$ and threshold voltages between -1V and -2V; once coated with a sensitiser layer, the magnitudes of the mobilities and threshold voltages of the devices were slightly reduced, this may just be the effect of adding the layer or of the device being in close contact to water during the LS and LB processes. Uncoated pentacene OFETs are not naturally very selective with respect to the analytes they respond to; in this work pentacene has shown a response to an amine, an ester, an amide and to an alkene. The sensing responses from uncoated pentacene tend to be mostly or totally irreversible at room temperature, while coating the devices has led to improved recovery when exposed to ethylethanoate (an ester), formamide (an amide) and ethylene (an alkene). Coating pentacene OFETs with the calixarene 5,17-(34-nitrobenzylideneamino)-11,23-di-*tert*-butyl-25,27-diethoxycarbonyl-methyleneoxy-26,28dihydroxycalix[4]arene (calixarene 1) reduced the response of the OFETs towards octylamine, ethylethanoate and formamide, so it is not an appropriate sensitiser material for these vapours. However, coating pentacene OFETs in a 2:1 molar ratio blend of the calixarene calix[8]arene (calixarene 2) and the porphyrin 5,10,15,20-Tetrakis (3,4-bis (2-ethylhexyloxy) phenyl)-21H,23H-porphyrinato cobalt (II) (Co-EHO) increased their responses to both octanal (an aldehyde) and octan-2-one (a ketone); while coating pentacene OFETs with PtOEP increased their sensitivity to ethylene.

The n-type *N,N'*-bis (*n*-octyl)- dicyanoperylene-3,4:9,10-bis(dicarboximide) (PDI8-CN₂) OFETs (with Au contacts) made for this work had carrier mobilities of the order 10⁻³cm²V⁻¹s⁻¹ and threshold voltages of the order 1V. PDI8-CN₂ showed a strong response to octylamine vapour, which is at least partially reversible; the response is attributed to a base-doping effect of the amine as the response takes the form of a lowering of the OFET's channel on-resistance, in stark contrast to the response of pentacene OFETs, which showed an increase in channel on-resistance. With the exception of the large initial response, the responses of the PDI8-CN₂ device were of similar magnitudes to those of the pentacene device.

Au nano-particle chemi-resistors proved to be sensitive to octylamine vapours; but as the interaction was attributed to the bonding of the amine group to the Au, effectively insulating the individual nano-particles, it is unlikely the sensors will be reusable. Au nanoparticles are therefore unsuitable as a sensing medium for amine, except in the role as a one-use disposable sensor.

Finally from investigations into the water-gating behaviour of poly(3-hexylthiophene-2,5-diyl) (P3HT) OFET devices, it can be concluded that the P3HT devices show promise as an aqueous sensing platform when the devices are coated in a calixarene “sensitiser” layer that blocks electro-chemical doping.

Further work to lead on from that discussed in this thesis would include the testing of further materials as sensitiser layer materials, starting with that have previously shown sensitivity to the target analyte in some other sensing application; using sensitiser layers in conjunction with the n-type PDI8-CN₂ or a more inert p-type semiconductor would also be a good direction for the research to take. With respect to the water-gated devices, materials would need to be screened for their ability to block electro-chemical doping and sensitivity to water-borne analytes.

8

Acknowledgements and Publications

I would like to thank everyone who has helped and supported me throughout my degree; firstly my friends and family, I couldn't have done it without you being there to help me keep going all the times I felt like giving up.

I would like to thank my supervisors Martin and Tim, for all the help, support and the endless ideas that have allowed me to complete this mammoth task.

I would like to thank all the members of my research group(s) past and present: Faridah, Nora, Mark, Rene, Arindam, Benedek, Abdullah, Hadi, Alfredo, Adonis, Delia, Stuart and Adam. You guys have made my degree a much more enjoyable experience and been there to help me out when I've needed it.

I'd like to thank EPSRC for the funding.

Last and not least I'd like to thank the un-sung heroes: the technicians; you guys have gone above and beyond the call of duty to help me out with various problems over the years and I'd just like to say thanks to you all!!.

Publications:

- Growth of nanocrystals and thin films at the water–oil interface.^[95]
- Discovery of a New Odour Sensing Mechanism Using an n-Type Organic Transistor.^[128]
- Simplified Real-Time Organic Transistor Characterisation Schemes for Sensing Applications.^[120]
- Highly sensitive alkane odour sensors based on functionalised gold nanoparticles.^[53]
- Technology Platform for Sampling Water with Electrolyte-Gated Organic Transistors Sensitised with Langmuir-Deposited Calixarene Surface Layers.^[135]

References

- [1] J. Mabeck, G. Malliaras, *Anal. Bioanal. Chem.* **2006**, *384*, 343.
- [2] C.-W. Chu, C.-W. Chen, S.-H. Li, E. H.-E. Wu, Y. Yang, *Appl. Phys. Lett.* **2005**, *86*, 253503.
- [3] R. Tinivella, V. Camarchia, M. Pirola, S. Shen, G. Ghione, *Org. Electron.* **2011**, *12*, 1328.
- [4] B. Liu, G.-Z. Xie, X.-S. Du, X. Li, P. Sun, "Pentacene based organic thin-film transistor as gas sensor", presented at ICACIA 2009. , 23-25 Oct. 2009, **2009**; L. Torsi, M. Tanese, B. Crone, A. Dodabalapur, L. Wang, in *Organic Field-Effect Transistors*, CRC Press, **2007**, 507.
- [5] Y. Miyahara, K. Tsukada, H. Miyagi, *J. Appl. Phys.* **1988**, *63*, 2431.
- [6] M. D. Hanwell, S. Y. Heriot, T. H. Richardson, N. Cowlam, I. M. Ross, *Colloid. Surface. A* **2006**, *284-285*, 379.
- [7] A. D. F. Dunbar, S. Brittle, T. H. Richardson, J. Hutchinson, C. A. Hunter, *J. Phys. Chem. B* **2010**, *114*, 11697.
- [8] A. D. F. Dunbar, T. H. Richardson, A. J. McNaughton, J. Hutchinson, C. A. Hunter, *J. Phys. Chem. B* **2006**, *110*, 16646.
- [9] J. C. Scott, G. G. Malliaras, *Chem. Phys. Lett.* **1999**, *299*, 115.
- [10] N. Beaumont, I. Hancox, P. Sullivan, R. A. Hatton, T. S. Jones, *Energ. Environ. Sci.* **2011**, *4*, 1708; D. Boudinet, M. Benwadih, Y. Qi, S. Altazin, J.-M. Verilhac, M. Kroger, C. Serbutoviez, R. Gwoziecki, R. Coppard, G. Le Blevennec, A. Kahn, G. Horowitz, *Org. Electron.* **2010**, *11*, 227.
- [11] R. Schroeder, L. Majewski, M. Grell, *Appl. Phys. Lett.* **2004**, *84*, 1004.
- [12] W.-S. Liu, C.-C. Liu, M.-Y. Kuo, *Chem. – Eur. J.* **2009**, *15*, 5896.
- [13] F. Liscio, S. Milita, C. Albonetti, P. D'Angelo, A. Guagliardi, N. Masciocchi, R. G. Della Valle, E. Venuti, A. Brillante, F. Biscarini, *Adv. Funct. Mater.* **2012**, *22*, 943.
- [14] J. Zaumseil, H. Sirringhaus, *Chem. Rev.* **2007**, *107*, 1296.
- [15] C.-L. Song, C.-B. Ma, F. Yang, W.-J. Zeng, H.-L. Zhang, X. Gong, *Org. Lett.* **2011**, *13*, 2880.
- [16] L.-L. Chua, J. Zaumseil, J.-F. Chang, E. C. W. Ou, P. K. H. Ho, H. Sirringhaus, R. H. Friend, *Nature* **2005**, *434*, 194.
- [17] S. Scheinert, G. Paasch, in *Physics of Organic Semiconductors*, Wiley-VCH Verlag GmbH & Co. KGaA, **2006**, 343.
- [18] H. Zi, M. Senatore, M. Roberts, C. Reese, A. B. Mallik, S. Mannsfeld, Z. Bao, J. Locklin, in *Organic Field-Effect Transistors*, CRC Press, **2007**, 159.
- [19] N. Karl, J. Marktanner, R. Stehle, W. Warta, *Synth. Metal.* **1991**, *42*, 2473.
- [20] E. A. Silinsh, V. Čápek, *Organic molecular crystals: Interaction, localization, and transport phenomena*, AIP Press, New York **1994**.
- [21] G. Horowitz, in *Semiconducting Polymers: Chemistry, Physics and Engineering*, Vol. 2, Wiley-VCH Verlag GmbH & Co. KGaA, **2007**, 531.
- [22] H. Bässler, *Phys: Status Solidi B* **1993**, *175*, 15.
- [23] J. Veres, S. D. Ogier, S. W. Leeming, D. C. Cupertino, S. Mohialdin Khaffaf, *Adv. Funct. Mater.* **2003**, *13*, 199.

- [24] M. Redecker, D. D. C. Bradley, M. Inbasekaran, E. P. Woo, *Appl. Phys. Lett.* **1998**, *73*, 1565; M. Redecker, D. D. C. Bradley, M. Inbasekaran, W. W. Wu, E. P. Woo, *Adv. Mater.* **1999**, *11*, 241.
- [25] W. F. Pasveer, J. Cottaar, C. Tanase, R. Coehoorn, P. A. Bobbert, P. W. M. Blom, D. M. de Leeuw, M. A. J. Michels, *Phys. Rev. Lett.* **2005**, *94*, 206601.
- [26] U. Wolf, S. Barth, H. Bässler, *Appl. Phys. Lett.* **1999**, *75*, 2035.
- [27] M. I. Winter, in *Chemical Bonding*, Oxford University Press, Oxford **1994**, 57.
- [28] R. A. L. Jones, in *Soft Condensed Matter*, Oxford University Press, **2002**, 73.
- [29] H.-H. Hörrhold, M. Helbig, D. Raabe, J. Opfermann, U. Scherf, R. Stockmann, D. Weiß, *Z. Chem.* **1987**, *27*, 126.
- [30] T. Someya, H. E. Katz, A. Gelperin, A. J. Lovinger, A. Dodabalapur, *Appl. Phys. Lett.* **2002**, *81*, 3079.
- [31] R. A. L. Jones, in *Soft Condensed Matter*, Oxford University Press, **2002**, 129.
- [32] J. C. Kotz, P. M. Treichel, J. Townsend, in *Chemistry & Chemical Reactivity*, Brooks/Cole, **2011**, 400.
- [33] J.-M. Kim, S. K. Jha, R. Chand, D.-H. Lee, Y.-S. Kim, *Biosens. Bioelectron.* **2011**, *26*, 2264; K. Jung-Min, S. K. Jha, L. Dong-Hoon, R. Chand, J. Jon-Ho, S. Ik-Soo, K. Yong-Sang, *Micro Nano Lett.* **2011**, *6*, 745; L. Wang, D. Fine, A. Dodabalapur, *Appl. Phys. Lett.* **2004**, *85*, 6386; Z. Hsiao-Wen, T. Wu-Wei, L. Yen-ren, W. Yu-Mei, Y. Yuh-Shyong, *IEEE Sens. J.* **2012**, *12*, 594; H. U. Khan, J. Jang, J.-J. Kim, W. Knoll, *Biosens. Bioelectron.* **2011**, *26*, 4217; J. Yu, X. Yu, L. Zhang, H. Zeng, *Sensor. Actuat. B-Chem.* **2012**, *173*, 133; H. U. Khan, M. E. Roberts, W. Knoll, Z. Bao, *Chem. Mater.* **2011**, *23*, 1946.
- [34] P. Cosseddu, S. Milita, A. Bonfiglio, *IEEE Electr. Device L.* **2012**, *33*, 113.
- [35] Z. Hsiao-Wen, D. Ming-Zhi, H. Ting-Yu, L. Hung-Cheng, M. Hsin-Fei, Y. Yuh-Shyong, *IEEE Electr. Device L.* **2011**, *32*, 1143.
- [36] W. Chia-Yu, K. Shu-Hao, H. Yu-Ming, H. Wen-Chieh, F. Adriyanto, W. Yeong-Her, *IEEE Electr. Device L.* **2011**, *32*, 90.
- [37] J. Rivnay, L. H. Jimison, J. E. Northrup, M. F. Toney, R. Noriega, S. Lu, T. J. Marks, A. Facchetti, A. Salleo, *Nat. Mater.* **2009**, *8*, 952.
- [38] H. Tatsuo, T. Jun, *Sci. Technol. of Adv. Mat.* **2009**, *10*, 024314.
- [39] H. W. Kroto, J. R. Heath, S. C. O'Brien, R. F. Curl, R. E. Smalley, *Nature* **1985**, *318*, 162.
- [40] W.-B. Chen, H.-F. Xiang, Z.-X. Xu, B.-P. Yan, V. A. L. Roy, C.-M. Che, P.-T. Lai, *Appl. Phys. Lett.* **2007**, *91*, 191109; A. Opitz, M. Bronner, W. Brüting, *J. Phys. Conf. Ser.* **2008**, *100*, 082043.
- [41] J. W. Kingsley, A. Green, D. G. Lidzey, *Proc. of SPIE* **2009**, *7416*, 74160T.
- [42] G. Giri, E. Verploegen, S. C. B. Mannsfeld, S. Atahan-Evrenk, D. H. Kim, S. Y. Lee, H. A. Becerril, A. Aspuru-Guzik, M. F. Toney, Z. Bao, *Nature* **2011**, *480*, 504.
- [43] S. M. Goetz, C. M. Erlen, H. Grothe, B. Wolf, P. Lugli, G. Scarpa, *Org. Electron.* **2009**, *10*, 573; V. Seena, R. S. Dudhe, H. N. Raval, S. Patil, A. Kumar, S. Mukherji, V. R. Rao, *ECS Trans.* **2011**, *35*, 67; J. W. Jeong, Y. D. Lee, Y. M. Kim, Y. W. Park, J. H. Choi, T. H. Park, C. D. Soo, S. M. Won, I. K. Han, B. K. Ju, *Sensor. Actuat. B-Chem.* **2010**, *146*, 40; J. Kettle, S. Whitelegg, A. M. Song, D. C. Wedge, L. Kotacka, V. Kolarik, M. B. Madec, S. G. Yeates, M. L. Turner, *Nanotechnology* **2010**, *21*, 075301; R. S. Dudhe, J. Sinha, A. Kumar, V. R. Rao, *Sensor. Actuat. B-Chem.* **2010**, *148*, 158; F.-Y. Yang, K.-J. Chang, M.-Y. Hsu, C.-C. Liu, *J. Mater. Chem.* **2008**, *18*, 5927; S. W. Lee, H. J. Lee, J. H. Choi, W. G. Koh, J. M. Myoung, J. H. Hur, J. J. Park, J. H. Cho, U. Jeong, *Nano Lett.* **2009**, *10*, 347;

- M. Urien, G. Wantz, E. Cloutet, L. Hirsch, P. Tardy, L. Vignau, H. Cramail, J.-P. Parneix, *Org. Electron.* **2007**, *8*, 727.
- [44] L. A. Majewski, M. Grell, *Synth. Metal.* **2005**, *151*, 175.
- [45] D. H. Kim, Y. D. Park, Y. Jang, H. Yang, Y. H. Kim, J. I. Han, D. G. Moon, S. Park, T. Chang, C. Chang, M. Joo, C. Y. Ryu, K. Cho, *Adv. Funct. Mater.* **2005**, *15*, 77.
- [46] S. Wang, J.-C. Tang, L.-H. Zhao, R.-Q. Png, L.-Y. Wong, P.-J. Chia, H. S. O. Chan, P. K. H. Ho, L.-L. Chua, *Appl. Phys. Lett.* **2008**, *93*, 162103.
- [47] H. Yan, Z. Chen, Y. Zheng, C. Newman, J. R. Quinn, F. Dotz, M. Kastler, A. Facchetti, *Nature* **2009**, *457*, 679.
- [48] A. B. Kaiser, *Adv. Mater.* **2001**, *13*, 927.
- [49] L. Groenendaal, F. Jonas, D. Freitag, H. Pielartzik, J. R. Reynolds, *Adv. Mater.* **2000**, *12*, 481.
- [50] A. G. MacDiarmid, *Angew. Chem. Int. Edit.* **2001**, *40*, 2581.
- [51] W. Schartl, *Nanoscale* **2010**, *2*, 829.
- [52] M. Brust, D. Bethell, C. J. Kiely, D. J. Schiffrin, *Langmuir* **1998**, *14*, 5425; F. P. Zamborini, M. C. Leopold, J. F. Hicks, P. J. Kulesza, M. A. Malik, R. W. Murray, *J. Am. Chem. Soc.* **2002**, *124*, 8958; H. L. Zhang, S. D. Evans, J. R. Henderson, R. E. Miles, T. H. Shen, *Nanotechnology* **2002**, *13*, 439.
- [53] H. AlQahtani, M. Sugden, D. Puzzovio, L. Hague, N. Mullin, T. Richardson, M. Grell, *Sensor. Actuat. B-Chem.* **2011**, *160*, 399.
- [54] S. A. Brittle, T. H. Richardson, J. Hutchinson, C. A. Hunter, *Colloid. Surface. A* **2008**, *321*, 29.
- [55] C.-M. Che, H.-F. Xiang, S. S.-Y. Chui, Z.-X. Xu, V. A. L. Roy, J. J. Yan, W.-F. Fu, P. T. Lai, I. D. Williams, *Chem.-Asian J.* **2008**, *3*, 1092.
- [56] T. Yasuda, T. Tsutsui, *Chem. Phys. Lett.* **2005**, *402*, 395.
- [57] D. G. Zhu, M. C. Petty, M. Harris, *Sensor. Actuat. B-Chem.* **1990**, *2*, 265.
- [58] R. Ludwig, N. Dzung, *Sensors* **2002**, *2*, 397.
- [59] P. Maksyutenko, T. R. Rizzo, O. V. Boyarkin, *J. Chem. Phys.* **2006**, *125*, 181101.
- [60] S. J. Suresh, V. M. Naik, *J. Chem. Phys.* **2000**, *113*, 9727.
- [61] C.-H. Yu, T.-F. Lei, J.-L. Liao, J.-Y. Yan, J.-C. Ho, *J. Disp. Technol.* **2009**, *5*, 198.
- [62] S. P. Tiwari, V. R. Rao, T. Huei Shaun, E. B. Namdas, S. G. Mhaisalkar, "Pentacene Organic Field Effect Transistors on Flexible substrates with polymer dielectrics", presented at *VLSI Technology, Systems and Applications, 2007. VLSI-TSA 2007. International Symposium on*, 23-25 April 2007, **2007**.
- [63] T. G. I. Ling, M. Beck, R. Bunk, E. Forsén, J. O. Tegenfeldt, A. A. Zakharov, L. Montelius, *Microelectron. Eng.* **2003**, *67-68*, 887.
- [64] A. Maliakal, in *Organic Field-Effect Transistors*, CRC Press, **2007**, 229.
- [65] M. E. Roberts, N. Queraltó, S. C. B. Mannsfeld, B. N. Reinecke, W. Knoll, Z. Bao, *Chem. Mater.* **2009**, *21*, 2292.
- [66] Y.-Y. Noh, H. Sirringhaus, *Org. Electron.* **2009**, *10*, 174.
- [67] K. Natori, D. Otani, N. Sano, *Appl. Phys. Lett.* **1998**, *73*, 632.
- [68] E. Said, X. Crispin, L. Herlogsson, S. Elhag, N. D. Robinson, M. Berggren, *Appl. Phys. Lett.* **2006**, *89*, 143507.
- [69] S. Ono, S. Seki, R. Hirahara, Y. Tominari, J. Takeya, *Appl. Phys. Lett.* **2008**, *92*, 103313.
- [70] L. Kergoat, L. Herlogsson, D. Braga, B. Piro, M.-C. Pham, X. Crispin, M. Berggren, G. Horowitz, *Adv. Mater.* **2010**, *22*, 2565.
- [71] A. Nishino, *J. Power Sources* **1996**, *60*, 137.

- [72] H. Helmholtz, *Ann. Phys. - Leipzig* **1853**, 165, 211.
- [73] G. Gouy, *CR. Hebd. Acad. Sci.* **1909**, 149, 654; G. Gouy, *J.Phys. - Paris* **1910**, 9, 457; D. L. Chapman, *Philos. Mag.* **1913**, 25, 457.
- [74] O. Stern, *Z. Elektrochem. Angew. P.* **1924**, 30, 508.
- [75] M. Ariel, Y. Nemirovsky, *Electrochim. Acta* **1972**, 17, 1977.
- [76] E. Gileadi, E. Kirowa-Eisner, J. Penciner, *Interfacial electrochemistry : an experimental approach*, Addison-Wesley, **1975**.
- [77] J. E. McDermott, M. McDowell, I. G. Hill, J. Hwang, A. Kahn, S. L. Bernasek, J. Schwartz, *J. Phys. Chem. A* **2007**, 111, 12333.
- [78] H. Yang, T. J. Shin, M.-M. Ling, K. Cho, C. Y. Ryu, Z. Bao, *J. Am. Chem. Soc.* **2005**, 127, 11542; J.-F. Chang, B. Sun, D. W. Breiby, M. M. Nielsen, T. I. Sölling, M. Giles, I. McCulloch, H. Sirringhaus, *Chem. Mater.* **2004**, 16, 4772.
- [79] A. N. Sokolov, M. E. Roberts, O. B. Johnson, Y. Cao, Z. Bao, *Adv. Mater.* **2010**, 22, 2349.
- [80] I. A. Koshets, Z. I. Kazantseva, Y. M. Shirshov, S. A. Cherenok, V. I. Kalchenko, *Sensor. Actuat. B-Chem.* **2005**, 106, 177.
- [81] R. Schroeder, L. Majewski, M. Grell, *Appl. Phys. Lett.* **2003**, 83, 3201.
- [82] G. Horowitz, R. Hajlaoui, H. Bouchriha, R. Bourguiga, M. Hajlaoui, *Adv. Mater.* **1998**, 10, 923.
- [83] J. Collet, O. Tharaud, A. Chapoton, D. Vuillaume, *Appl. Phys. Lett.* **2000**, 76, 1941.
- [84] R. Dost, A. Das, M. Grell, *J. Appl. Phys.* **2008**, 104, 084519.
- [85] S. M. Sze, in *Physics of Semiconductor Devices*, John Wiley & Sons, Ltd, **1981**, 312.
- [86] L. Torsi, A. J. Lovinger, B. Crone, T. Someya, A. Dodabalapur, H. E. Katz, A. Gelperin, *J. Phys. Chem. B* **2002**, 106, 12563.
- [87] S. Huttner, M. Sommer, A. Chiche, G. Krausch, U. Steiner, M. Thelakkat, *Soft Matter* **2009**, 5, 4206.
- [88] E. D. Pellizzari, J. E. Bunch, R. E. Berkley, J. McRae, *Anal. Chem.* **1976**, 48, 803.
- [89] M. C. Carotta, V. Guidi, G. Martinelli, M. Nagliati, D. Puzzovio, D. Vecchi, *Sensor. Actuat. B-Chem.* **2008**, 130, 497.
- [90] M. C. Carotta, A. Cervi, A. Giberti, V. Guidi, C. Malagù, G. Martinelli, D. Puzzovio, *Sensor. Actuat. B-Chem.* **2008**, 133, 516.
- [91] F. Edelman, H. Hahn, S. Seifried, C. Alof, H. Hoche, A. Balogh, P. Werner, K. Zakrzewska, M. Radecka, P. Pasierb, A. Chack, V. Mikhelashvili, G. Eisenstein, *Mat. Sci. Eng. B-Solid* **2000**, 69–70, 386.
- [92] A. Pacquit, K. T. Lau, H. McLaughlin, J. Frisby, B. Quilty, D. Diamond, *Talanta* **2006**, 69, 515.
- [93] X. C. Zhou, L. Zhong, S. F. Y. Li, S. C. Ng, H. S. O. Chan, *Sensor. Actuat. B-Chem.* **1997**, 42, 59.
- [94] H. AlQahtani, M. Alduraibi, T. Richardson, M. Grell, *Phys. Chem. Chem. Phys.* **2012**, 14, 5558.
- [95] G. L. Stansfield, P. V. Vanitha, H. M. Johnston, D. Fan, H. AlQahtani, L. Hague, M. Grell, P. John Thomas, *Phil. Trans. R. Soc. A* **2010**, 368, 4313.
- [96] A. D. F. Dunbar, T. H. Richardson, A. J. McNaughton, A. Cadby, J. Hutchinson, C. A. Hunter, *J. Porphyr. Phthalocya.* **2006**, 10, 978.
- [97] S. A. Brittle, T. H. Richardson, L. Varley, C. A. Hunter, *J. Porphyr. Phthalocya.* **2010**, 14, 1027.
- [98] C.-H. J. Liu, W.-C. Lu, *J. Chin. Inst. of Chem. Eng.* **2007**, 38, 483.

- [99] F. Liao, S. Yin, M. F. Toney, V. Subramanian, *Sensor. Actuat. B-Chem.* **2010**, *150*, 254.
- [100] H.-B. Lin, J.-S. Shih, *Sensor. Actuat. B-Chem.* **2003**, *92*, 243.
- [101] Z. Li, Z. Xue, Z. Wu, J. Han, S. Han, *Org. Biomol. Chem.* **2011**, *9*, 7652.
- [102] S. Carquigny, N. Redon, H. Plaisance, S. Reynaud, *IEEE Sens. J.* **2012**, *12*, 1300.
- [103] P. Cabanillas-Galán, L. Farmer, T. Hagan, M. Nieuwenhuyzen, S. L. James, M. C. Lagunas, *Inorg. Chem.* **2008**, *47*, 9035.
- [104] B. Esser, J. M. Schnorr, T. M. Swager, *Angew. Chem. Int. Edit.* **2012**, *51*, 5752.
- [105] Hellmanex III Data Sheet, http://www.hellma-analytics.com/html/seiten/output_adb_file.php?id=785, **2012**
- [106] P. J. Cumpson, M. P. Seah, *Metrologia* **1996**, *33*, 507; S. Kasi, M. Liehr, *Appl. Phys. Lett.* **1990**, *57*, 2095.
- [107] M. T. Thomas, in *Vacuum Physics and Technology*, Academic Press inc., London **1979**, 521.
- [108] I. Langmuir, *Phys. Rev.* **1913**, *2*, 329.
- [109] M. C. Petty, in *Molecular Electronics*, John Wiley & Sons, Ltd, **2007**, 241.
- [110] S. M. Critchley, M. R. Willis, M. J. Cook, J. McMurdo, Y. Maruyama, *J. Mater. Chem.* **1992**, *2*, 157.
- [111] M. C. Petty, in *Langmuir-Blodgett Films: An Introduction*, Cambridge University Press, **1996**, 39.
- [112] T. Watanabe, K. Asai, K. Ishigure, *Thin Solid Films* **1998**, *322*, 188.
- [113] X. D. Dang, W. Plieth, S. Richter, M. Plötner, W. J. Fischer, *Phys. Status Solidi A* **2008**, *205*, 626.
- [114] L. A. Majewski, M. Grell, S. D. Ogier, J. Veres, *Org. Electron.* **2003**, *4*, 27.
- [115] L. A. Majewski, R. Schroeder, M. Grell, *J. Phys. D Appl. Phys.* **2004**, *37*, 21.
- [116] J. W. Schultze, M. M. Lohrengel, *Electrochim. Acta* **2000**, *45*, 2499.
- [117] R. Dost, A. Das, M. Grell, *J. Phys. D Appl. Phys.* **2007**, *40*, 3563.
- [118] Operational Amplifier AD549 Datasheet, http://www.analog.com/static/imported-files/data_sheets/AD549.pdf, **2002**
- [119] ICM7555/7556 Datasheet, <http://datasheets.maxim-ic.com/en/ds/ICM7555-ICM7556.pdf>, **1992**
- [120] L. Hague, D. Puzzovio, A. Dragoneas, M. Grell, *Sci. Adv. Mat.* **2011**, *3*, 907.
- [121] A. Niemz, K. Bandyopadhyay, E. Tan, K. Cha, S. M. Baker, *Langmuir* **2006**, *22*, 11092.
- [122] S. C. Lim, S. H. Kim, J. H. Lee, M. K. Kim, D. J. Kim, T. Zyung, *Synth. Metal.* **2005**, *148*, 75.
- [123] chemical modification and attempted polymerization of self-assembled monolayers of hexadecanedioic acid at aluminium surfaces, <http://www.dtic.mil/cgi-bin/GetTRDoc?Location=U2&docname=GetTRDoc.pdf&docid=a331712>.pdf, **1997**
- [124] N. Tasaltin, D. Sanli, A. Jonas, A. Kiraz, C. Erkey, *Nanoscale Res. Lett.* **2011**, *6*, 487.
- [125] Y. Y. Noh, J. J. Kim, Y. Yoshida, K. Yase, *Adv. Mater.* **2003**, *15*, 699.
- [126] L. Venkataraman, J. E. Klare, I. W. Tam, C. Nuckolls, M. S. Hybertsen, M. L. Steigerwald, *Nano Lett.* **2006**, *6*, 458; G. Fagas, J. C. Greer, *Nanotechnology* **2007**, *18*, 424010.
- [127] T. Ouchab, J. Massardier, A. Renouprez, *J. Catal.* **1989**, *119*, 517.
- [128] L. Hague, D. Puzzovio, T. H. Richardson, M. Grell, *Sens. Lett.* **2011**, *9*, 1692.
- [129] M. Hamed, L. Herlogsson, X. Crispin, R. Marcilla, M. Berggren, O. Inganäs, *Adv. Mater.* **2009**, *21*, 573.

- [130] O. Inganäs, *Chem. Soc. Rev.* **2010**, *39*, 2633.
- [131] H. Sirringhaus, N. Tessler, R. H. Friend, *Synth. Metal.* **1999**, *102*, 857.
- [132] L. A. Majewski, J. W. Kingsley, C. Balocco, A. M. Song, *Appl. Phys. Lett.* **2006**, *88*, 222108.
- [133] R. M. Owens, G. G. Malliaras, *MRS Bull.* **2010**, *35*, 449.
- [134] R. J. Klein, S. Zhang, S. Dou, B. H. Jones, R. H. Colby, J. Runt, *J. Chem. Phys.* **2006**, *124*, 144903.
- [135] D. Puzzovio, A. Al Naim, L. Hague, M. Deasy, J. Ward, T. Richardson, M. Grell, *J. Surf. Interfac. Mater.* **2012**, *1*, 1.
- [136] W. M. Haynes, Ed. *CRC Handbook of Chemistry and Physics*, CRC Press, **2011**.
- [137] W. V. Steele, R. D. Chirico, S. E. Knipmeyer, A. Nguyen, N. K. Smith, I. R. Tasker, *J. Chem. Eng. Data* **1996**, *41*, 1269.

Appendix 1 - Vapour Concentration Calculations

All data for the graphs in this section came from the “CRC Handbook of Chemistry and Physics”^[136] or the paper by Steele *et al.*^[137]

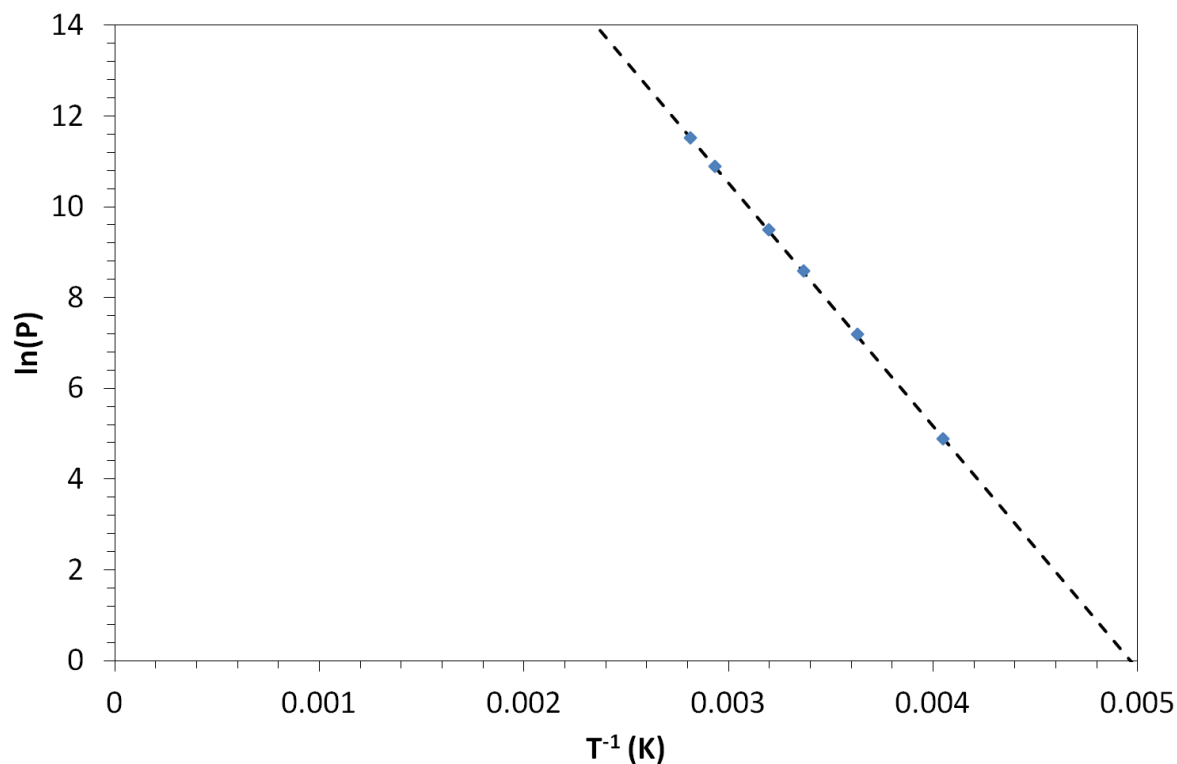


Figure 153. $\ln(\text{vapour pressure})$ against T^{-1} plot for IPA.

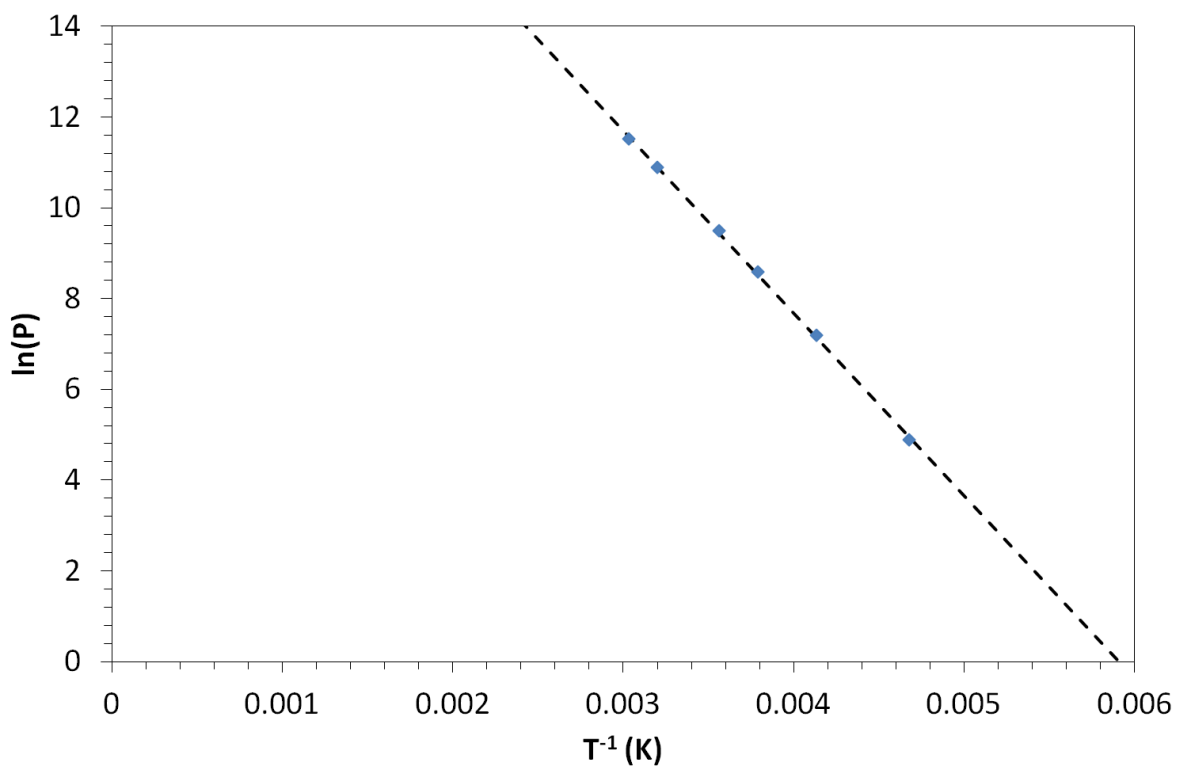


Figure 154. $\ln(\text{vapour pressure})$ against T^{-1} plot for acetone.

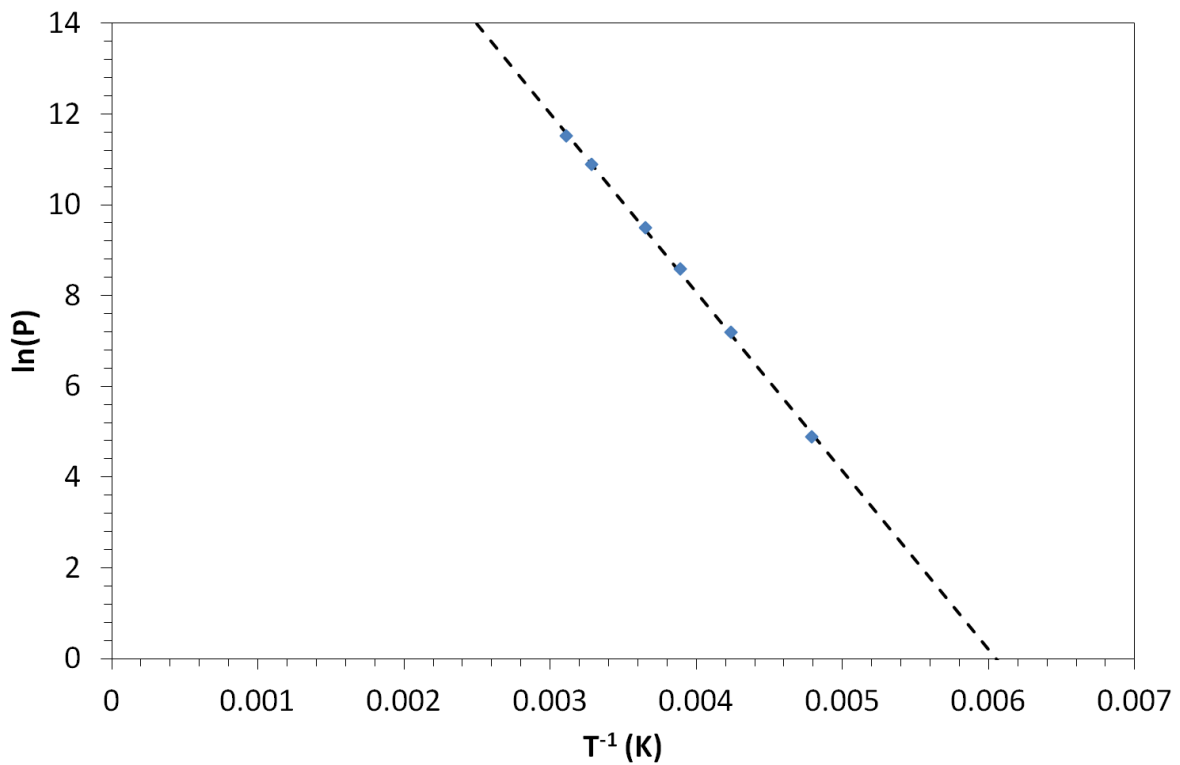


Figure 155. $\ln(\text{vapour pressure})$ against T^{-1} plot for propylamine.

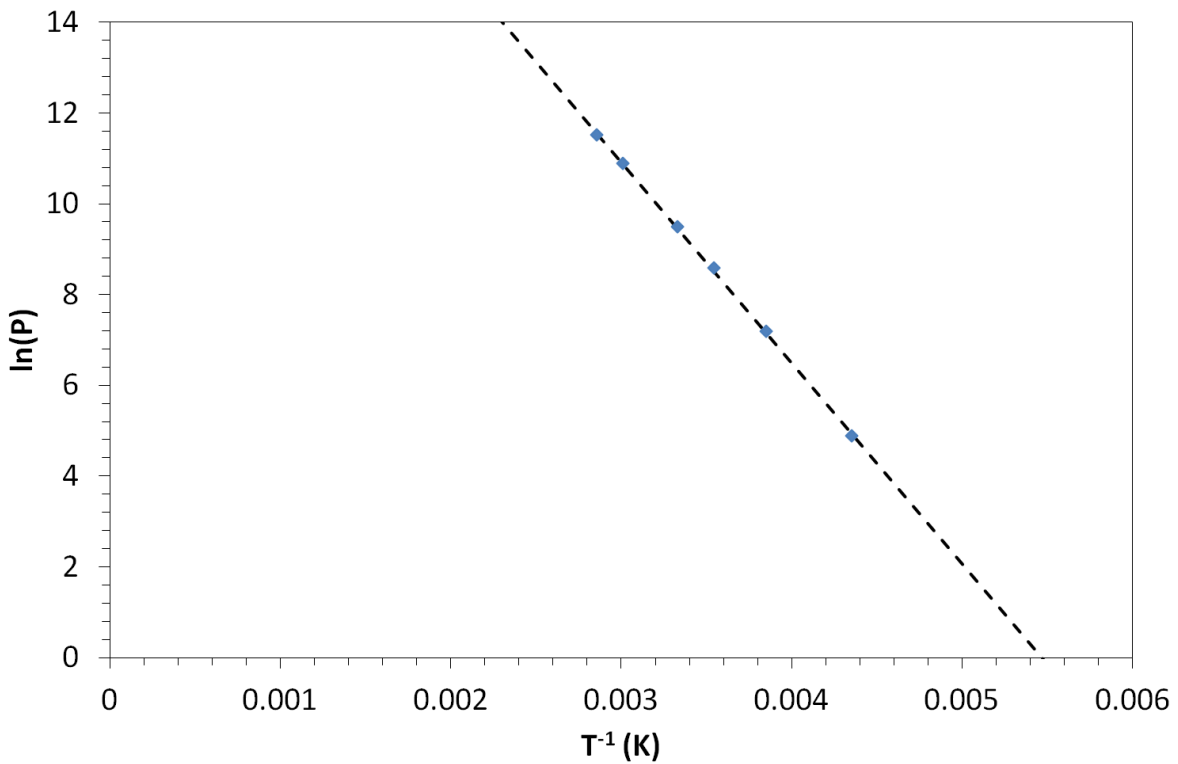


Figure 156. $\ln(\text{vapour pressure})$ against T^{-1} plot for ethylethanoate.

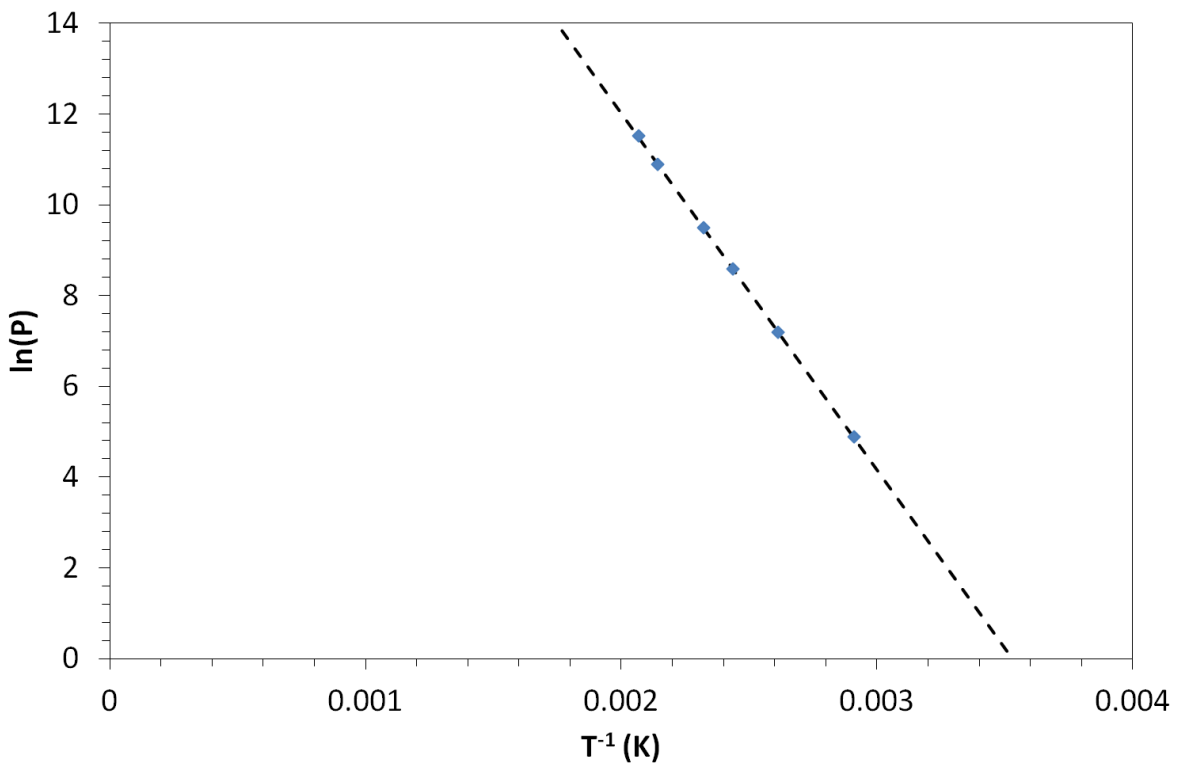


Figure 157. $\ln(\text{vapour pressure})$ against T^{-1} plot for formamide.

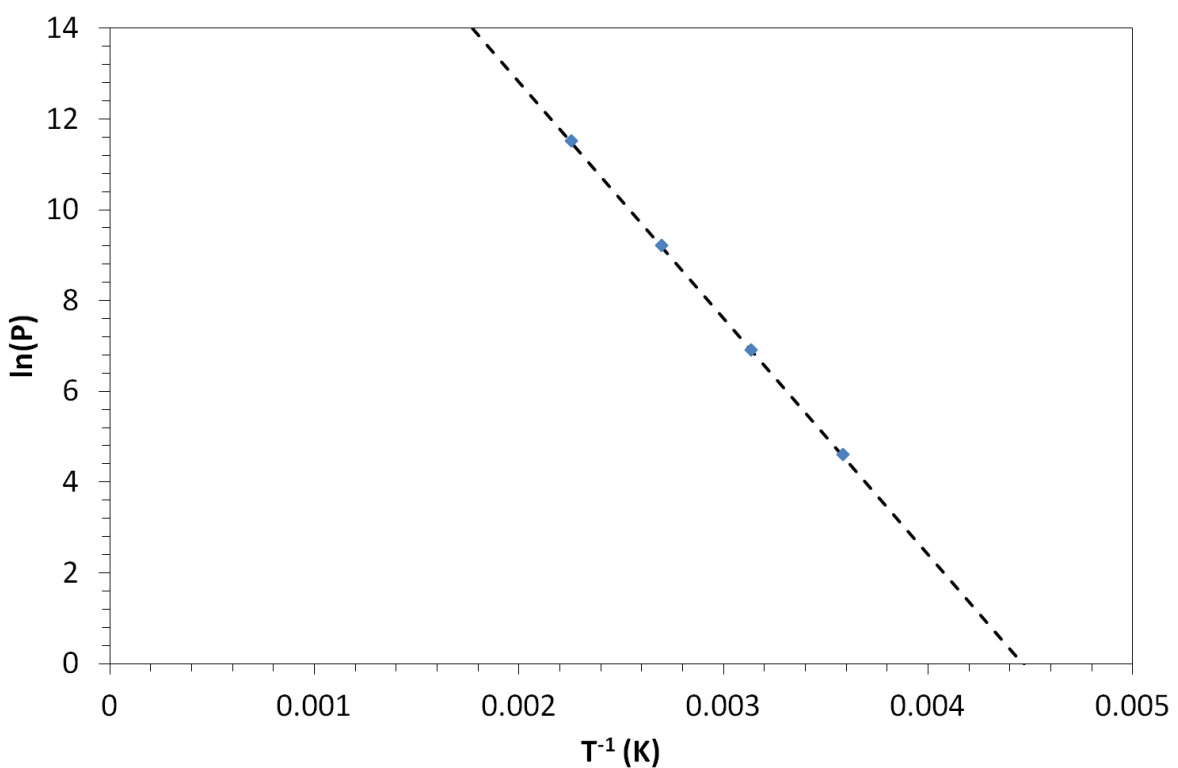


Figure 158. $\ln(\text{vapour pressure})$ against T^{-1} plot for octanal.

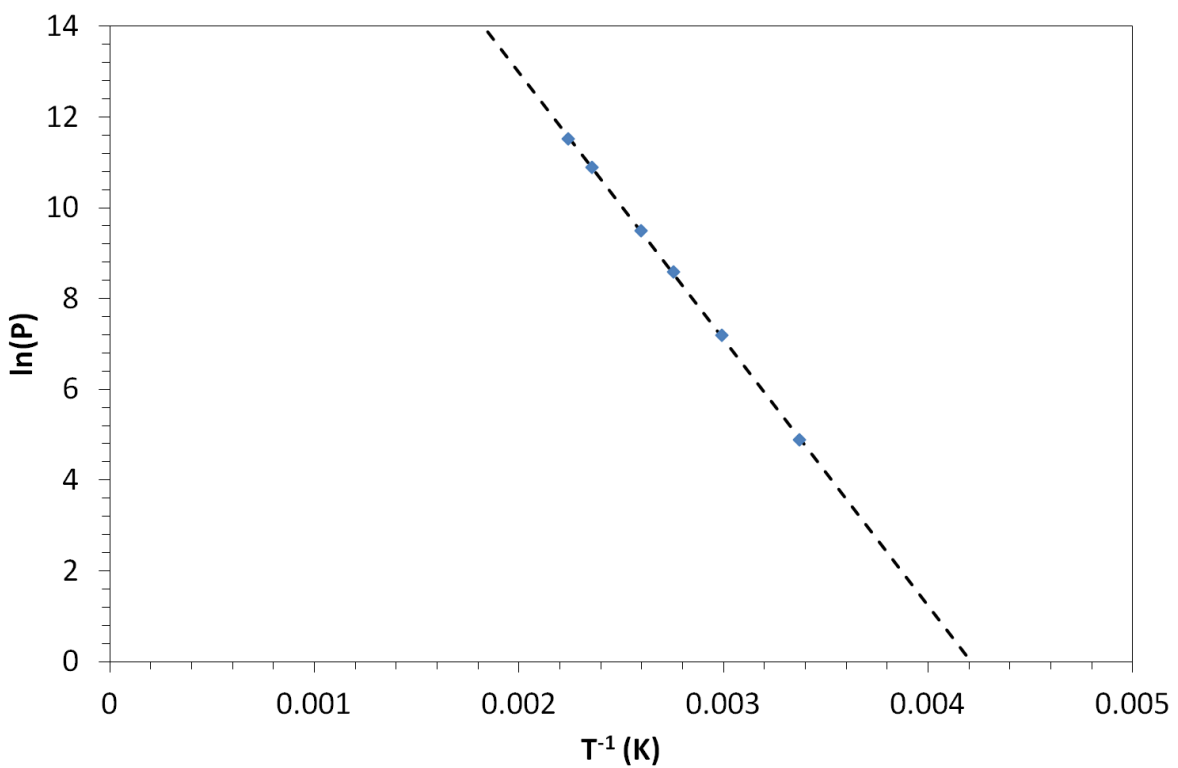


Figure 159. $\ln(\text{vapour pressure})$ against T^{-1} plot for octan-2-one.

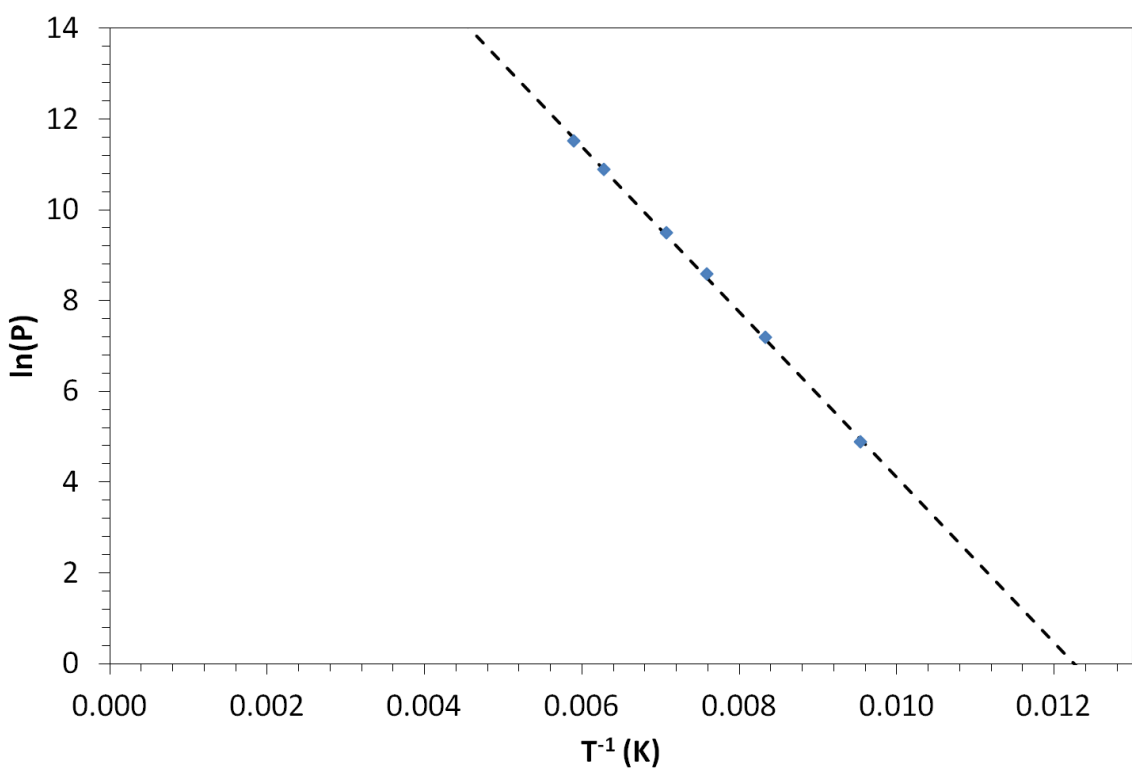


Figure 160. $\ln(\text{vapour pressure})$ against T^{-1} plot for ethylene.

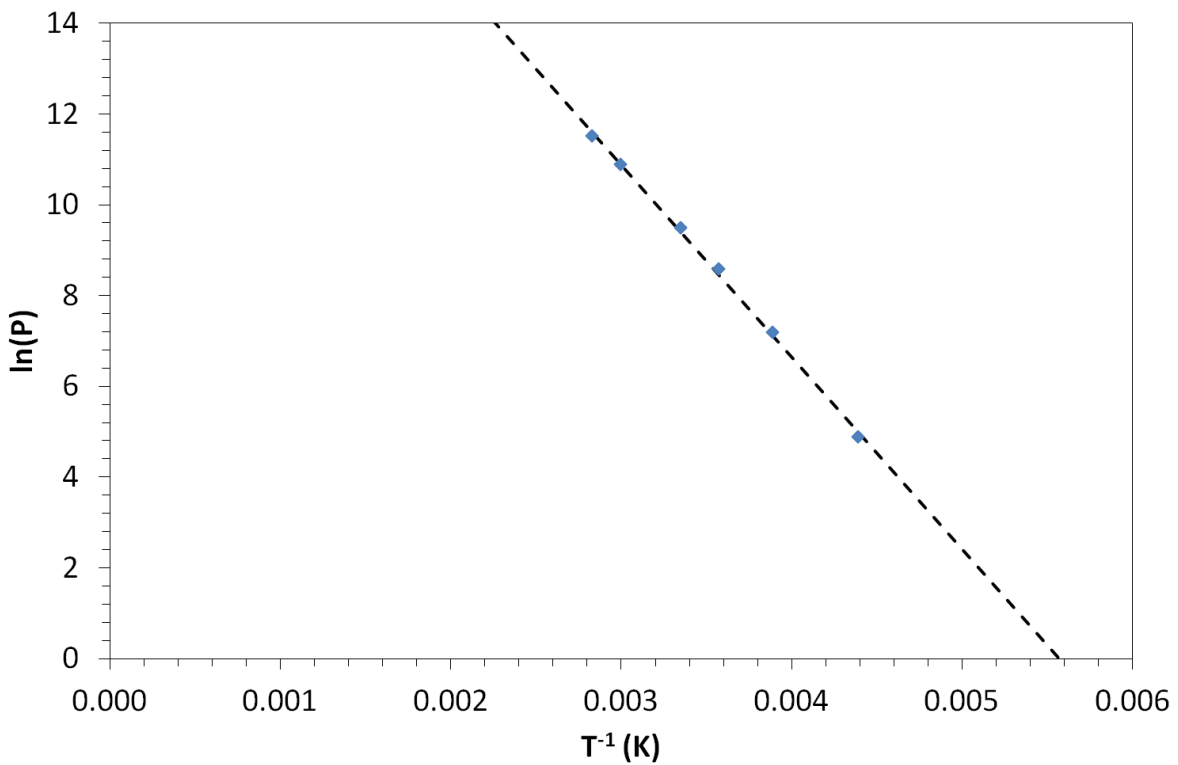


Figure 161. $\ln(\text{vapour pressure})$ against T^{-1} plot for cyclohexane.

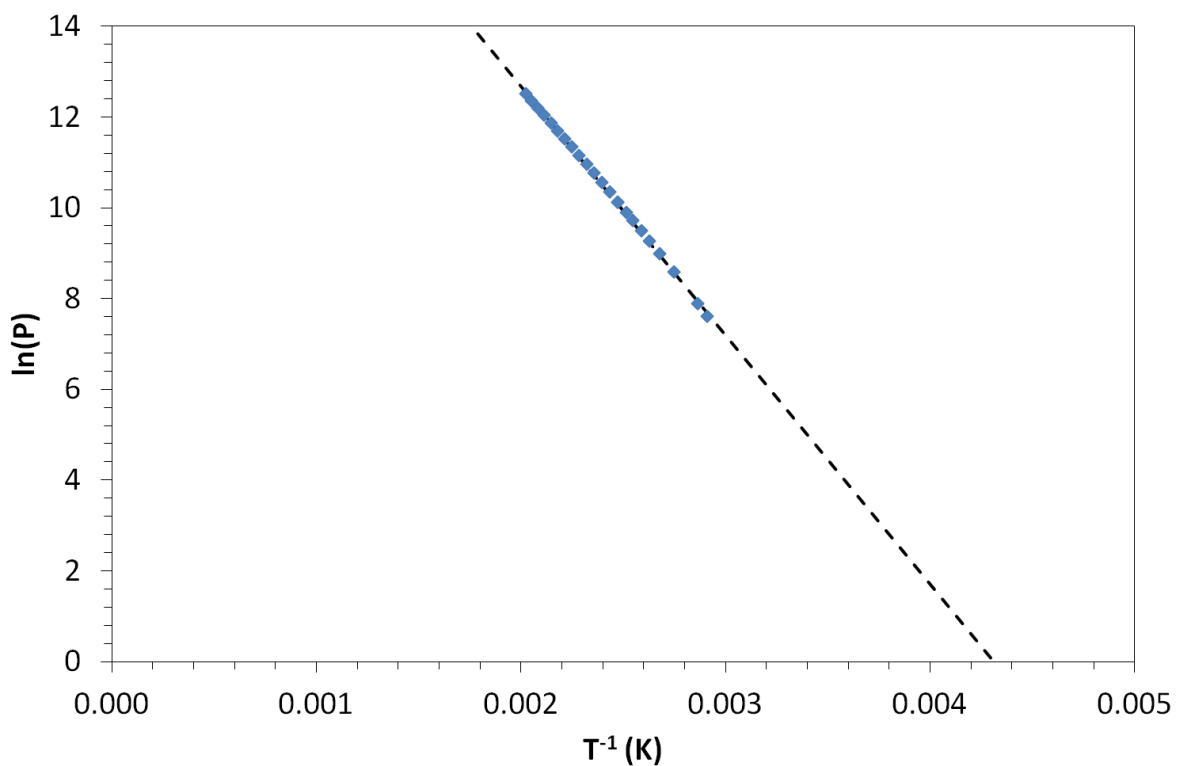


Figure 162. $\ln(\text{vapour pressure})$ against T^{-1} plot for octylamine.

Analyte	Boiling point (K)	Vapour pressure at T (Pa)	concentration at 100% saturation (ppm)	Temperature (°C)
IPA	355	4.71×10^3	4.65×10^4	22
Acetone	329	2.55×10^4	2.52×10^5	22
Propylamine	321	1.23×10^4	1.21×10^5	0
Ethylethanoate	350	3.00×10^3	2.96×10^4	0
Formamide	483	3.28×10^{-1}	3.53	0
Octanal	444	6.58×10^1	6.49×10^2	0
Octan-2-one	446	2.53×10^1	2.50×10^2	0
Ethylene	169	6.40×10^6	6.32×10^7	0
Cyclohexane	353.7	3.28×10^3	3.23×10^4	0
Octylamine	449	3.59×10^1	3.54×10^2	0

Table 5. The boiling points and concentrations of the analytes used in this thesis.